EMERGENCE OF FUNCTIONAL NEUROMUSCULAR JUNCTIONS IN AN ENGINEERED, MULTICELLULAR SPINAL CORD-MUSCLE BIOACTUATOR

BY

COLLIN D. KAUFMAN

B.S., University of Maryland at College Park, 2014

DISSERTATION

Submitted in partial fulfillment of the requirements
for the degree of Doctor of Philosophy
in the Neuroscience Program
in the Graduate College
of the University of Illinois, Urbana-Champaign, 2021

Urbana, Illinois

Doctoral Committee:

Professor Martha U. Gillette, Chair
Professor Rashid Bashir
Professor Rhanor Gillette
Professor Taher Saif

ABSTRACT

A novel, engineered platform for the co-culture of 3D muscle strips innervated by an intact spinal cord central pattern generator (CPG) is a significant advancement over traditional 2D cell culture, allocellular biological robots, and as a translational platform for pharmacological testing. Development of this platform requires an interdisciplinary approach bridging fields as diverse as tissue engineering, nanotechnology, materials science, and soft robotics. We confirmed the presence of robust neuronal and glial growth from a cultured segment of intact lumbar spinal cord. For the first time, we also demonstrated the sustained electrical activity of a cultured spinal cord out to approximately 2 weeks *in vitro*. At 0 DIV, the spinal cord was highly active at baseline and the addition of glutamate reduced the overall firing rate at both 10 µM and 200 µM doses. By ~7 DIV, the spontaneous firing at baseline was greatly reduced, but the spinal cord still became highly active in response to both low and high doses of glutamate. At ~14 DIV, spinal cords did not exhibit spontaneous firing at baseline or respond to a low dose of glutamate. However, a high dose of glutamate initiated robust electrical responses with a clear bursting pattern indicative of a pattern generating circuit. A spinal cord was co-cultured in an organotypic manner with an engineered 3D C2C12-derived skeletal muscle biobot where spinal motor neurons co-localized with post-synaptic acetylcholine receptors (AChR) clusters to form motor endplates at a time-scale developmentally similar to *in vivo*. The spinal cord is capable of inducing spontaneous contraction of the muscle via these NMJs. Glutamate stimulation of the spinal cord elicited patterned contractions from spinal central pattern generators (CPGs) which were blocked by application of glutamate receptor antagonists. Primary skeletal muscle was determined to have larger myotube diameters, AChR clusters had greater surface area, and demonstrated more consistent spontaneous contractions than their C2C12 counterparts. A new platform built for multiple 3D muscle strips was developed and optimized. These muscle cells exhibited spontaneous contractions and were capable of matching a variety of electric stimulus frequencies with differing forces of contraction. Immunoblotting revealed that though the extracted primary tissue was a mix of Type I and Type II fibers, this identity was not retained by the dissociated satellite cells when cultured on Matrigel-coated glass in 2D. When grown in mixed skeletal muscle-spinal cord conditioned media, primary skeletal muscle cultures regained a mixed

Type I/Type II fiber-type identity, which emphasizes the important role of diffusible factors released from the spinal cord in muscle development. This platform allows for the study of basic research questions about the development of each component of the neuromuscular junction through high-resolution fluorescent imaging of disease mutant models in an *in vitro* environment closer to the physiological reality than ever before. Better understanding of the neuromuscular junction and its components will inform future designs of biobots, prosthetics, pharmaceuticals, and potentially even lab-grown meats.

ACKNOWLEDGMENTS

I would like to take this opportunity to express my gratitude to my advisor, Martha Gillette. Martha's relentless positivity and support helped inspire me to be the person and scientist that I have become. I would also like to thank my committee, Dr. Rashid Bashir, Dr. Rhanor Gillette and Dr. Taher Saif for their invaluable advice and encouragement in shaping these studies.

My work would not have been possible without my collaborators and their gracious donations of time, lab space, and materials. This research was accomplished with particular thanks to expertise and assistance from the labs of Dr. Rashid Bashir, Dr. Marni Boppart, Dr. Rhanor Gillette, Dr. Hyunjoon Kong, Dr. Taher Saif, and Dr. Johnathan Sweedler.

It has been an utter joy to work with everyone in the Gillette Lab. A very special thank you to Dr. Jennifer Mitchell who was not only a major scientific inspiration throughout my graduate education, but also helped make the lab feel like a family. I would also like to thank my current and former labmates Ann Benefiel, Olivia Cangellaris, James Chu, Eman Hamed, Sam Irving, Raj Iyer, Anika Jain, Taylor Jorgensen, Chris Liu, Ghazal Naseri, Quang Nguyen, Miles Norsworthy, Amanda Weiss, and Mia Yu-Bothwell for being a constant supply of advice, encouragement, and support both in the lab and outside of it. I wish them the best in all aspects of their future lives.

To my closest friends and peers, thank you all so much for making Urbana-Champaign feel like home. Without Onur Aydin, Amogh Belagodu, Dan Bradley, Paul Camacho, Connor Courtney, Courtney Dixon, Carly Drzewiecki, Stephen Fleming, Rachel Gonzales, Kelly Hewes, Robbie Ingram, Jenna Kaempfer, Misha Knight, Payel Kundu, Colin Lee, Aaron Mahnke, Steph Matt, Elizabeth Neumann, Coltan Parker, Elli Sellinger, Ellen Qin, and Jarbo Willing, Champaign would not have been nearly so special. A special thank you to Amogh and Jari who I was able to look up to and admire both personally and professionally. I would be remiss if I did not include my many friends from before grad school, as well. An extra special thanks to Tyler Barrett, Kevin Cross, Joe Olepade, Michael Moore, Ian Reichardt, Spencer Schwartz, Jeff Shih, and Danny Silver for sticking with me for all these years.

Lastly, I would like to thank my brother, Connor, and my parents, Julie and Dan, without whom I would not be here in the first place. My weekly phone calls with my brother every Sunday were something I was always able to rely on and look forward to. The continued love, support, and encouragement from my family and friends was a firm pillar upon which I have been able to accomplish so much.

Thank you all!

TABLE OF CONTENTS

ABBREVIATIONS

1º – primary
ACh – acetylcholine
AChR – acetylcholine receptor
ADP – adenosine diphosphate
ATP – adenosine triphosphate
BTX – bungarotoxin
CCM – co-culture medium
CDM – C2C12 differentiation medium
ChAT – choline acetyltransferase
ChR2 – channel rhodopsin 2
CN – commissural neurons
CNS – central nervous system
CPG – central pattern generator
CPM – C2C12 proliferation medium
DIV – days *in vitro*
DMEM – Dulbecco's modified eagle medium
DOF – degrees of freedom
EB – embryoid body
ECM – extracellular matrix
ESC – embryonic stem cell
GFAP – glial fibrillary acidic protein
hIPSC – human induced pluripotent stem cells
HPSG – heparan sulfate proteoglycan
IZ – intermediate zone
LZ – lateral zone
mESC – mouse embryonic stem cell
MHC – myosin heavy chain
MLR – mesencephalic locomotor region
MN – motor neuron
MPZ – myelin protein zero
MZ – medial zone
NGS – normal goat serum
NMJ – neuromuscular junction
PAG – periaqueductal gray
PBS – phosphate buffered saline
PDM – primary differentiation medium
PEGDA – poly (ethylene glycol) diacrylate
PNS – peripheral nervous system

PPM – primary proliferation medium
PPN – pedunculopontine nucleus
SC – spinal cord
SCCM – spinal cord conditioned medium
SCGM – spinal cord growth medium
SCI – spinal cord injury
SkM – skeletal muscle
SLA – stereolithographic apparatus
SR – sarcoplasmic reticulum
WM – whole muscle

CHAPTER 1. AN INTRODUCTION TO THE DEVELOPMENT AND CONTROL OF VOLUNTARY NEUROMUSCULAR MOTOR FUNCTION

1.1 The Locomotor Pathway – Cerebral Initiation

1.1.1 Overview

Locomotion, the process of moving through physical space from one place to another, might appear effortless as one walks to class in the morning or sees a bird flying through the air. Nevertheless, vertebrate locomotion is a highly complex series of motor behaviors that involves the coordination of many different parts of the central and peripheral nervous systems as well as limb and body muscles. Initiation of locomotion takes place in the brain, specifically in a region known as the mesencephalic locomotor region (MLR) which resides in the midbrain and brainstem. The MLR relays this signal to the spinal cord via the reticulospinal tract where many aspects of locomotor coordination occur. The cerebellum processes both movement-generated and internal feedback to modulate the descending pathways of the spinal cord. The spinal cord outputs its commands via motor neurons which project into peripheral muscle tissues to execute motor actions. These complex and intertwined processes are highly conserved among both limbed and non-limbed vertebrates, and though there are some distinct differences, I will focus on limbed, vertebrate locomotion.

1.1.2 Substructural Functions of The Mesencephalon

The Tectum

The mesencephalon, or midbrain, is considered part of the brainstem and plays roles in many behaviors beyond locomotion including vision, audition, and aspects of sleep/wake and arousal. It is composed of two main regions: the tectum and the tegmentum. The tectum lies superior to the tegmentum and plays only a minimal role in locomotion. It is composed of the superior colliculus and the inferior colliculus which are involved with the visual and auditory systems, respectively (Rogers, 2002). There is some evidence that superior colliculus activity increases upon witnessing a visual obstacle that would require a change of locomotor pattern, which indicates a role in visuomotor adaptation (Patla, 1997).

The Periaqueductal Gray

The tegmentum, on the other hand, has many projections to and from the spinal cord that influence locomotion. The tegmental region least associated with locomotion is the periaqueductal gray (PAG), a column of grey matter that surrounds the central aqueduct and plays a key role in analgesia (Behbehani and Fields, 1979). PAG efferents excite inhibitory interneurons in dorsal spinal cord promoting the release of endogenous opioids, such as enkephalin and dynorphin, and inhibiting the release of the pain peptide, substance P (Menetrey and Basbaum, 1987). The tegmentum has also been implicated in female lordosis and maternal behavior due to its high density of vasopressin and oxytocin receptors (Figueira *et al*, 2008).

The Red Nucleus

The red nucleus of the tegmentum, so named because of its high iron content and reddish color (Hallgren and Sourander, 1958), is much more tightly associated with locomotion. Most neurons of the rubrospinal tract (projecting from red nucleus to spinal cord) demonstrate increased activity during locomotion (Orlovsky, 1972). Periodic oscillations in phase with the locomotion were also observed in the red nucleus of cats with intact cerebellums, but not in decerebellate cats (Orlovsky, 1972). The red nucleus has many afferents from the cerebellum and is used as a waystation for information transfer from the cerebellum to the spinal cord. It has been hypothesized that the red nucleus plays a role in regulating balance, maintaining gait, and adapting gait based on sensory input (Haycock, 2011). It is worth noting that in primates, the rubrospinal tract plays a diminished role due to increased cortical and corticospinal tract volume (Haycock, 2011).

The Substantia Nigra

The substantia nigra is a highly dopaminergic structure that plays important roles in reward and voluntary movement. Substantia nigra efferents to the ventral tegmental area (also a region of the tegmentum, but with no known locomotor influences) are involved in reward and motivation. There is another group of efferents, however, that project into the mesencephalic locomotor region (MLR) (Garcia-Rill *et al*, 1983). The MLR is believed to be the site in the brain where initiation of locomotion occurs (Jordan, 1998). In Parkinson's disease (PD), the substantia

nigra undergoes severe neurodegeneration resulting in many of the classic symptoms of PD such as tremors, bradykinesia, or even full akinesia (Burns *et al*, 1983). Due to the presence of substantia nigra efferents to the initiating site of locomotion, the MLR, it is unsurprising that akinesia is a side effect. However, the role of the substantia nigra in causing tremors is poorly understood.

The Mesencephalic Locomotor Region

The mesencephalic locomotor region is a relatively wide-ranging region that includes nuclei of the reticular formation such as the lateral cuneiform nucleus and the pedunculopontine nucleus (PPN), and the subthalamic fields of Forel (Garcia-Rill, 1986). However, its functions are highly specific. The MLR was originally identified as an area of the midbrain of the cat which, when electrically activated, would induce controlled locomotion on a treadmill (Shik, 1966; Nicolopoulos-Stournaras and Iles, 1984; Skinner and Garcia-Rill, 1984). It has subsequently been identified in rodents and humans (Piallat *et al*, 2009). Recently, it was found that a lesion to the PPN results in akinesia (Nandi *et al*, 2002). Also, deep brain stimulation of the MLR has been reported to effectively treat the PD symptom of gait-freezing in a small group of patients suffering from PD (Stefani *et al*, 2007). According to fMRI data, the MLR is active not only when initiating locomotion, but also when just imagining it (Jahn *et al*, 2008). Though it is still being studied, the MLR has emerged as the primary midbrain structure associated with locomotion and gait.

1.1.3 Functions of the Cerebellum

The hypothesized functions of the cerebellum have evolved over time, but the modern view is that distinct cerebellar regions play integral roles in motor behaviors such as voluntary limb movement, balance, and locomotion, as well as having a smaller role higher cognition. Cerebellar inputs from the spinal cord, brainstem, and midbrain are mediated by mossy fibers, while climbing fibers generally originate in the inferior olivary nucleus (Maekawa and Kimura, 1980; Thach, 1968). The cerebellum itself is extremely dense and has a rather uniform structure throughout. This makes it challenging to identify distinct subregions based on histological landmarks. Instead, the cerebellum can be divided into four functional zones based on

connectivity: the medial zone, the intermediate zone, the lateral zone, and the flocculonodular lobe (Voogd and Glickstein, 1998).

Medial Zone

The medial zone (MZ) can be distinguished in part based on its afferent connections from the dorsal and ventral spinocerebellar tracts which carry sensory (dorsal) and motor (ventral) information into the cerebellum (Bosco and Poppele, 2001). MZ efferents project into the vestibular nuclei and certain reticular tract nuclei such as the red nucleus. The role of the MZ is to integrate spinal and vestibular inputs via the vestibulospinal and reticulospinal tracts to maintain balance while walking and to adjust gait accordingly via the red nucleus. This has been confirmed by lesion studies which produce a unique gait phenotype with abnormal limb timings, decreased stride length, and exclusive ipsilateral flexion/contralateral extension of leg joints (Yu and Eidelberg, 1983). In summary, the cerebellar MZ plays a primary role in dynamic balance control and modulating rhythmic flexion and extension of muscles during locomotion.

Intermediate Zone

The intermediate zone (IZ) has similar afferent (from the dorsal spinocerebellar tract) and efferent (to the red nucleus) pathways to the medial zone, but functionally it plays a very different role. The IZ plays a minor role in vestibular control and instead appears to be more important for regulating the precise timing of alternating flexion-extension and calculating limb trajectory for precise limb movements.

Lateral Zone

Lateral zone (LZ) afferents are mostly from the primary motor, premotor, and somatosensory cortices while the efferents include prefrontal cortex, primary motor cortex, and the red nucleus of the midbrain (Brodal and Bjaalie, 1997; Orioli and Strick, 1989; Kakei *et al*, 1995). Lesions of the LZ do not greatly affect over-ground walking, but deficits appear in novel tasks such as walking on a narrow beam (Chambers and Sprague, 1955; Thach *et al*, 1992; Chambers and Sprague, 1955). Evidence suggests that the lateral zone of the cerebellum has a significant role in modulating the normal locomotor pattern in novel contexts.

Flocculonodular Lobe

The flocculonodular lobe plays very little role in locomotion itself and utilizes its reciprocal afferent/efferent innervation from-and-to the vestibular nuclei to prevent dizziness during gaze shifting as the head and eyes move from target to target (Clendenin et a, 1974; Kotchabhakdi and Walberg, 1978; Ito *et al*, 1976).

1.2 The Locomotor Pathway – Spinal Cord Pattern Generation

1.2.1 Overview

Over 100 years ago, Thomas Graham Brown first discovered that the rhythms and patterns of locomotion were governed by the spinal cord in cats and this initial finding has been confirmed in all tested vertebrates (Brown, 1911; Grillner, 1981). The nuclei of the reticular formation of the brainstem are responsible for activating spinal cord networks, but it is the spinal networks themselves that are responsible for generating the complex rhythms associated with locomotor movement. Quadrupedal locomotion requires the coordination of flexor-extensor muscle pairing simultaneously within a limb, and between ipsi- and contralateral pairs of limbs. This is performed by complex spinal circuits known as central pattern generators (CPGs). CPGs are roughly symmetrical circuits that generally consist of lateral excitatory interneurons and medial inhibitory interneurons which work together to output information to ventrolateral cholinergic motor neurons. The goal of a CPG is to produce patterned output from non-patterned inputs. Pattern-generating circuits are commonly believed to be used for left-right and flexor-extensor coordination. There is also another type of oscillatory circuit within the spinal cord responsible for setting the speed of locomotion known as rhythm generators; these different types of circuits work together to specify gait (reviewed by Kiehn, 2006).

1.2.2 Pattern Generation

Commissural neurons (CNs) are inhibitory interneurons that project laterally across midline of the spinal cord. These cells are thought to be primarily responsible for driving left-right and flexor-extensor pattern generation. Electrophysiology has illuminated a dual inhibitory

pathway within these cells that could lead to such patterned outputs (Jankowska, 2008; Butt and Kiehn, 2003). In recent decades, scientists have developed new tools which have reinvigorated some older questions with new purpose. Researchers began to be able to identify subpopulations of neurons within the spinal cord by differential expression of transcription factors and track these specific types of neurons from development of the neural tube to maturity in adulthood. One population identified this way is the V0 population of neurons which is characterized by early expression of the transcription factor DBX1 (Pierani *et al*, 2001). These cells make up the majority of CNs in the spinal cord (Lanuza *et al*, 2004). Selective ablations of cell populations identified in this way have provided researchers with a wealth of information about how specific subpopulations of neurons affect pattern generation and, subsequently, gait.

This new age of techniques has caused many researchers to seek to identify more precisely the cells and pathways involved in pattern generation and how they can affect gait. Wild-type mice display four basic gaits: walk, trot, gallop, and bound (in order from slowest to fastest locomotion). Walk and trot are alternating gaits wherein there is left-right alternation between hindlimbs. Bound is a synchronous gait which is attained by synchronizing the left and right hindlimbs. Gallop is an intermediate gait that has elements of both synchronous and alternating gaits (Lanuza *et al*, 2004).

The V0 CNs are subdivided into inhibitory ($V0_D$) and excitatory ($V0_V$) populations based on transcriptional markers expressed later in development (Lanuza *et al*, 2004). Genetic ablation of all V0 neurons completely abolished the left-right alternating locomotive gaits (i.e. walk, trot), but not synchronous gaits (i.e., bound) to occur (Kiehn, 2016; Talpalar *et al*, 2013). Genetic ablation of only the inhibitory $V0_D$ population was a lethal mutation and the pups did not survive to term, though the reason remains unknown. $V0_V$ ablation resulted in the loss of only the faster of the two alternating gaits (trot) while the other three (walk, bound, and gallop) were all maintained (Bellardita and Kiehn, 2015). This indicates that the $V0_D$ and $V0_V$ subpopulations of CNs are recruited in ascending order as the speed of gait increases (Figure 1.1). The precise circuit underlying the galloping remains undetermined, but it is separate from the alternating gait circuits controlled by the $V0_D$ and $V0_V$ CN populations. There is only one other known population of excitatory CNs aside from $V0_V$: V3 neurons. V3 CNs have been shown to be rhythmically active

during locomotion and project directly to contralateral motor neurons (Borowska *et al*, 2013; Zhang *et al*, 2008). Ablation of these cells does not disrupt left-right alternation but increases variability in the burst amplitude and period of locomotor rhythms. V3 neurons may play a role in synchronous gait, but this needs to be further investigated.

1.2.3 Rhythm Generation

As locomotive speed increases from walk to trot, $V0_V$ neurons are recruited alongside $V0_D$ CNs. Rhythm generation, or the control of locomotive speed, generally comes from the activity of ipsilaterally projecting glutamatergic, excitatory neurons. Blockade of glutamatergic firing leads to the cessation of all rhythmic activity, but a coordinated rhythm persists in one half of the spinal cord. This suggests that CNs are not necessary for rhythm generation (Grillner and Jessell, 2009; Roberts *et al*, 2008; Goulding, 2009).

A cardinal feature of rhythm-generating neurons is that selective activation should be able to initiate or modulate rhythmic firing. It then follows that a reduction of rhythm-generating neurons would result in slowed locomotion that cannot be sped up (Goulding, 2009). Researchers have used optogenetically-enabled mice to activate or inactive specific populations of excitatory neurons within the spinal cord (Hägglund *et al*, 2010; Hägglund *et al*, 2013). Optogenetic activation of excitatory neurons initiates locomotor-like activity, whereas inhibition blocks it. This provides evidence that excitatory neurons are both sufficient and necessary for rhythm generation in the mammalian spinal cord. Optogenetic manipulation of the spinal cord has also provided new data which may reject the classic hypothesis of a half-center oscillator as fundamental to rhythm generation (Stuart and Hultborn, 2008). Regionally specific excitation of spinal cord neurons results in rhythmic output that is limited to only flexor-related or extensor-related motor neurons (Hägglund *et al*, 2010). This evidence implies that the rhythm-generating circuits in rat are comprised of several rhythm-generating modules that are arranged structurally near the motor neurons they specifically control. However, researchers have been unsuccessful so far in determining the molecular and transcriptional identity of these subpopulations.

1.3 The Locomotor Pathway – Sensory Integration and Gait

Sensory information is integral to motor commands and can be integrated at the levels of the midbrain, spinal cord, and cerebellum. Sensory information contributes to motor control in two distinct ways. One, it can inform the CNS about errors in execution, and two, it can help the body adapt its motor output to a modified situation (Nielsen and Sinkjaer, 2002). Despite the fact that much of our understanding of the role of sensation in locomotion is experimental and very few of the actual pathways are well-characterized today, these systems are important for developing complex, multi-modal *in vitro* systems such as sensory biomachines.

Lesion and deafferentation studies form the bulk of the research into sensory modulation of gait. In nearly all cases of mass sensory nerve lesion, rhythmic motor action persists after deafferentation, but accuracy and adaptability are reduced (Prochazka, 2010). Gait is still possible after deafferentation, although it becomes irregular and uncoordinated (Giuliani and Smith, 1987; Goldberger, 1977). In the absence of sensory feedback, responses to obstacles or inclines placed in the way of over-ground locomotion are not compensated for, and if the animal is not supported, it will fall down (Goldberger, 1977; Ghezz *et al*, 1990). Other studies have found that when vision is temporarily removed, animals retain the ability to move their limbs in locomotive-like behaviors, but the movements are less coordinated (Rothwell *et al*, 1982; Sanes *et al*, 1985). Other senses, but vision in particular, can play an important role in adaptive gait (Patla, 1997). It is believed that the superior colliculus (of the mesencephalic tectum) contributes strongly to this visuomotor system (Patla, 1997).

It is believed that the cerebellum is important for longer term and more complicated adaptations of locomotion (Grillner and Wallen, 1985; Armstrong, 1986). Contralateral MZ activity increases when the top of a foot is tapped (Armstrong, 1986). Since the medial cerebellum sees increased activity, this should activate the pathway to the red nucleus, the rubrospinal tract, and then the spinal cord where it will influence the firing patterns of V0 neurons.

1.4 Skeletal Muscle Physiology and Development

1.4.1 Overview

Skeletal muscle is one of the most dynamic and plastic tissues in the human body and contributes significantly to multiple bodily functions. By weight, skeletal muscle alone makes up approximately 40% of the human body and contains more than half of its protein (Hall, 2015). Due to the inarguable importance of skeletal muscle to species across the animal kingdom, muscle contraction has been studied in great depth.

Muscle development plays a significant role in how it eventually becomes innervated by the motor neurons that carry commands from the central nervous system and in how eventual contractions occur. Once unipotency towards a muscle cell fate has been determined, these myogenic precursors differentiate into spindle-shaped myoblasts. Myoblasts then align with each other, their membranes begin to fuse, and they form multinucleated muscle cells. This fusion activates a variety of contractile and synaptic protein genes that, among other effects, cause the nuclei from the fused myoblasts to centralize along the longitudinal axis. These aligned, elongated, multi-nucleated cells with centralized nuclei are referred to as myotubes. The final step in muscle development is the conversion from myotube to muscle fiber. Muscle fibers are fully mature units of muscle that are identified primarily by the peripheralization of the nuclei and development of a sarcolemma, the external cell membrane which both contains and permeates the sarcomere (Sanes and Lichtman, 1999; Carlson, 1973). The large, singular unit that is commonly referred to as muscle (e.g., the biceps brachii), is a combination of many of these aligned muscle fibers (Schiaffino and Reggiani, 2011). Each of these fibers contains substructures highly specialized for contraction.

1.4.2 Sarcomeric Structure

The Sarcomere

Each muscle fiber contains thousands of myofibrils; each myofibril is a sequential, alternating sequence of actin, myosin, and other associated proteins. A longitudinal cut through skeletal muscle tissue reveals the presence of distinct, alternating light and dark bands with a

thick black line bisecting the lighter bands (Fig. 1.2). The lighter bands are known as I-bands because they are isotropic to polarized light while the darker A-bands are anisotropic to polarized light. Each band primarily contains one component of the myofibril: the dark A-band contains myosin (thick filaments), while the light I-band contains actin (thin filaments). The thick, dark line bisecting the I-band is a Z-disk (made primarily of α-actinin, an actin-binding protein). Actin filaments extend in opposite directions from the Z-disk and interdigitate with the myosin of the A-band. The portion of myofibrils that extends from one Z-disk to the next is a single sarcomere, the fundamental unit of contraction within a muscle fiber.

Integral Contractile Proteins

Thick myosin fibers are composed of two heavy chains and four light chains. The heavy chains form a double helical tail along most of the length of the molecule, then fold bilaterally into two oval-shaped heads. The heads are symmetrical and each is associated with a pair of two identical light chains. They are connected to the tail by a short length of an individual heavy chain referred to as an arm. Together, each head and arm form a cross-bridge resulting in a total of two cross-bridges per myosin molecule (seen as small bumps on the myosin in Figure 1.3). These cross-bridges serve a key role in sarcomere contraction (See Section 1.5.3). The head group functions as an ATPase; it can hydrolyze ATP into ADP and harness the released energy for contraction.

Thin fibers (actin filaments) are composed of double-stranded F-actin but have several characteristics specific to their role in muscle contraction. Every 2.7 nm, there is a molecule of ADP which is believed to serve as an active site for cross-bridge attachment. Wrapped around the sides of the F-actin helix are molecules of tropomyosin. In its resting state, tropomyosin is believed to rest on top of active sites on strands of F-actin. Attached to the tropomyosin molecule is a three-part troponin complex. Troponin I has a strong affinity for actin, Troponin T has a strong affinity for tropomyosin, and Troponin C interacts strongly with Ca^{2+}. It is believed that upon receiving an influx of Ca^{2+}, troponin undergoes a conformational change that pulls the tropomyosin filament away from the F-actin to expose the active sites for myosin binding. Then,

when the Ca^{2+} flux has faded, Troponin I causes the tropomyosin to revert to its resting state covering the active sites.

Titin is required to maintain the side-by-side nature of actin and myosin during both resting and contractile phases. Titin is composed of over 27,000 amino acids and weighs 4,200 kDa making it one of the largest proteins in the body. The titin molecule acts as a spring between its anchor point at the Z-disk and the tail of a myosin filament. Titin has also been hypothesized to play a role in the initial formation of the sarcomere, though the specifics remain unknown.

Other Important Components of the Muscle Cell

The external cell membrane which both contains and permeates the sarcomere is termed the sarcolemma. The sarcolemma is similar to a typical cell membrane in many ways, but it has several important muscle-specific specializations. At each end of the muscle fiber, the sarcolemma fuses with tendon fibers which eventually bundle themselves into muscle tendons that subsequently are inserted into bones. Another unique feature of the sarcolemma is the way that it penetrates the myofibrils via transverse tubules (T-tubules). Though often thought of as a separate structure, transverse tubules are actually extensions of the extracellular membrane designed to transmit the action potential signal (Refer to Section 1.4.3 for additional details).

The sarcoplasmic reticulum (SR) is a modified smooth reticulum specific to muscle cells. It rests directly on the myofibrils and along the T-tubules. A key specialization of the SR is its high concentration of $Ca2^{+}$ that is released when it is met with a membrane depolarization from either the sarcolemma or its T-tubules. This Ca^{2+} release plays an important role in muscle contraction as will be described later (Section 1.4.3).

The final component of the sarcomere is the sarcoplasm. Much as organelles are suspended in cytoplasm, so too are myofibrils suspended in sarcoplasm. Sarcoplasm has high extracellular ionic concentrations of K^{+}, Mg^{2+}, and P^{3-}, in addition to a variety of proteases. Also present in the sarcoplasm are a high number of mitochondria which produce most of the ATP required for muscle contraction (Figure 1.4).

1.4.3 Muscle Contraction

Initiation, Propagation and Transduction of the Muscle Action Potential

The muscle action potential begins with an action potential in its neuronal partner at the presynaptic terminal of the neuromuscular junction (NMJ). The presynaptic nerve releases acetylcholine (ACh) which binds to postsynaptic acetylcholine receptors (AChR) on the muscle membrane at the specialized motor endplate. AChR binding causes the opening of membrane cation channels which allow a rapid influx of Na^+ ions into the muscle. This influx travels along the membrane symmetrically in each direction opening additional voltage-gated Na^+ channels as the membrane depolarizes. The traveling depolarization activates the sarcoplasmic reticulum (SR) which leads to release of its large, sequestered Ca^{2+} stores. Ca^{2+} binds to the troponin-tropomyosin complex exposing actin active sites and promoting actin-myosin bonding. However, the signal cannot propagate in the z-direction to the deepest parts of the muscle fast enough to allow for coherent contraction without T-tubules.

T-tubules are extensions of the sarcolemma that begin at the membrane and penetrate through the muscle. T-tubules originate at the membrane at an open hole such that their lumen is open to the extracellular environment. When an action potential spreads along the sarcolemma, it also propagates down the T-tubules, fully penetrating the muscle. T-tubules are ensconced on each side by a specialized SR structure known as terminal cisternae. Together, the two terminal cisternae (one on each side) and the T-tubule form a triad. This close association is necessary so that when an electrical signal propagates along the sarcolemma and down a T-tubule, the deeper SRs also release Ca^{2+} to initiate actin-myosin binding via ryanodine-receptor channels, which govern intracellular Ca^{2+} flux in excitable cells like muscles and neurons.

Sustained Contraction and Return to Resting State

Muscle contraction will continue as long as Ca^{2+} is present in the myofibrils, but there are mechanisms that rapidly deplete the muscle cell of extraneous Ca^{2+}. Continuously active Ca^{2+}-pumps located in the walls of the SR pump Ca^{2+} ions out of the sarcoplasm and back into the SR. This pump can maintain a 10,000X lumenal concentration of Ca^{2+} within the SR. The SR also mediates Ca^{2+} reuptake by the Ca^{2+}-binding protein, calsequestrin. The mechanism behind

calsequestrin reuptake is not well understood, although there is some evidence that it also plays a role in inhibiting the time which ryanodine-receptor channels remain open in response to stimulation (Beard *et al*, 2002).

Due to these constitutively active Ca^{2+} pumps and Ca^{2+} ion recycling by the SR, sustained muscle contraction is not due to sustained release. Rather, Ca^{2+} is released in a pulsatile manner. The pulses are homotypic and contain nearly 10X more Ca^{2+} than would be required for maximum contraction of the sarcomere. Due to this mode of Ca^{2+} release and the fact that not all muscle contractions are maximal, neuronal control plays an integral role in fiber recruitment.

Actin, Myosin, and Ca^{2+} as Primary Drivers of Contraction

Prior to contraction, ATP binds to the myosin heads and is cleaved due to ATPase-like activity into its byproducts, ADP + P_i, which remain bound to the head. A rapid influx of Ca^{2+} causes the troponin-tropomyosin complex to expose active sites on the actin filaments for the myosin head (ADP + P_i still attached) to bind. This attachment causes a conformational change between the arm and head of the cross-bridge which brings the head (and attached actin filament) forward. This head movement is referred to as a power stroke. The power stroke utilizes the energy from the phosphate bond that was bound to the head of the cross-bridge. After completion of the stroke, a new molecule of ATP binds to the head causing it to release from the actin filament. On the way back to rest position, the ATPase-like activity of the myosin head once again cleaves the ATP and binds its products. The cross-bridge will once again bind to the active site and repeat the process until there is no more Ca^{2+} and the active site is covered once again. If Ca^{2+} is omnipresent, muscle contraction still faces a physical maximum that occurs at maximum compression of the spring-like titin molecules. As muscle contraction occurs, myosin pulls its adjacent actin fibers closer together until the actin fibers overlap each other, continually compressing the titin between the Z-disk and the myosin (Figure 1.3 shows a sarcomere at rest).

Skeletal Muscle Fiber Subtypes

Skeletal muscle fibers are broadly classified into two different fiber types, Type I (slow-twitch) and Type II (fast-twitch) fibers. Fiber type can have a profound impact on muscle dysregulation due to genetic muscular dystrophies or aging-induced muscle atrophy (Talbot and

Maves, 2016). Muscle fiber types are generally defined by the myosin heavy chain isoforms that they express, but many other components contribute to a fiber's physiological characteristics as well. Most vertebrate muscles contain a mix of Type I and Type II fibers, though the ratio of each is tailored to the needs of that specific muscle. Slow-twitch muscle fibers are more efficient over long periods of time and are frequently used for controlling posture (e.g., abdomen), holding up the head (neck), or endurance exercise like running or walking long distances (e.g., gastrocnemius). Type II fibers have larger diameters, contract with greater force, and tire much more quickly (e.g., biceps, quadriceps, and trapezius muscles). This variation is at least partly due to the metabolic differences between the fiber types. Type I muscle has more mitochondria than Type II and generally relies more on aerobic respiration to generate energy. Because of this increased metabolic workload, Type I-dominant muscles are more vascularized and visually appear to be red rather than white like Type II-dominant muscles. Slow- and fast-twitch muscle fibers display different contractile profiles which will influence the force production, behavior, and stimulus-response coupling of any engineered muscle tissue. Muscle fiber subtype can be determined based on which myosin heavy chain (MHC) isoforms they express. Some muscles contain only a single isoform of MHC, but others are composed of isoforms. 'Pure' skeletal muscles contain exactly one of Type I (MHC-Iβ), Type IIA (MHC-IIa), Type IIB (MHC-IIb), or Type IID (MHC-IId) fibers (Pette and Staron, 1990; Schiaffino and Reggiani, 1994, 1996). Hybrid skeletal muscle tissues co-express specific pairs of fiber subtypes, including I/IIA, IIAD, and IIBD (Pette and Staron, 1990; Schiaffino and Reggiani, 1994, 1996). There are other muscle fiber types associated with specific muscles throughout the body. For example, MHC-Iα fibers are found in extraocular and laryngeal muscles (Pette and Staron, 1997) and MHC-IIc has been implicated in the growth of neuronal processes (Wylie and Chantler, 2008).

1.4.4 Muscle Force

Relationship Between Sarcomere Contraction and Muscle Force

This maximal sarcomeric contraction that occurs when titin cannot be further compressed is not the point where the muscle most force is generated. A sarcomere that has been slightly overextended such that there is zero overlap between actin and myosin cross-bridges is

approximately 4 µm long. This position generates 0 force for the muscle, and it is completely at rest. As the sarcomere shortens towards 2.2 µm, force increases linearly as more molecules of actin and myosin begin to overlap. At 2.2 µm, all cross-bridges should be bound to actin, but the actin has not yet reached the center of the myosin (note the slight gap between cross-bridges at the myosin fiber midline in Figure 1.3). Force remains constant as this last stretch of myosin is overlapped by actin with a sarcomeric length of 2 µm. The sarcomere can be further shortened to 1.65 µm where the titin is maximal compressed and the actin fibers overlap. This causes a force reduction equivalent to approximately 80% of the maximum. Additional shortening of the sarcomere results in crumpling of titin and myosin chains and a corresponding plummeting of force until the sarcomere is irreparably broken.

Neural Control of Muscle Force Output

While the basic structural unit of muscle contraction is the sarcomere, the basic functional unit is the motor unit. A motor unit consists of a motor neuron and all the muscle fibers it innervates. Large scale, complex motor actions require recruitment of various motor units based on the task provided. Early work demonstrated a "size principle" at play which hypothesized that as stimulation increased, motor units will be recruited in an orderly fashion from smallest to largest (Henneman, 1957; Fedde *et al*, 1969; HoVer *et al*, 1987; Hogrel, 2003; Milner-Brown and Stein, 1973; Tanji and Kato, 1973). Orderly recruitment facilitates a smooth incremental increase in force that is roughly proportional to the size of the motor unit recruited (Zajac and Faden, 1985). Recent evidence is starting to show that motor recruitment in voluntary tasks can be more complicated and that the size principle does not work as a hard-and-fast rule (Gillespie *et al*, 1974; VonTscharner and Goepfert, 2006; Wakeling and Rozitis, 2004). Strain rate has shown to be one key driver of non-size principled recruitment in locomotor activities such as cycling and wheel running (Wakeling *et al*, 2006; Hodson-Tole and Wakeling, 2008). It is currently believed that while the size principle theory of motor unit recruitment provides a robust framework with which motor unit recruitment patterns can be predicted, spinal cord and brain efferents play a significant role in modulating motor unit activity based on the specific task.

1.5 The Neuromuscular Junction

1.5.1 Overview

The vertebrate neuromuscular junction (NMJ) is perhaps the most studied synapse in neuroscience. Acetylcholine (ACh) was identified at the neuromuscular junction in 1936, making it the first known neurotransmitter (Dale, 1936). In subsequent decades, the NMJ was a part of other foundational studies in neuroscience, such as the first demonstration of quantal vesicular release (Katz, 1966). The acetylcholine receptor (AChR) was also the first receptor ever cloned (Duclert and Changeux, 1995). According to Rao (1998), the vertebrate NMJ is the most studied system in neuroscience apart from the mammalian hippocampus and the Drosophila genome. Though many aspects about the formation and maintenance of the NMJ have been very well characterized, there remain many important questions to investigate.

The neuromuscular junction is formed of three cell types: motor neurons, muscle fibers, and Schwann cells (Couteaux, 1973). Motor neurons project from the ventral side of mammalian spinal cords and serve to communicate motor commands from the central nervous system to the periphery (Grillner, 2002). These cells rarely branch between their origin in the central nervous system and the site of muscle innervation and innervate only a single muscle (Frank *et al*, 1975). Upon reaching the muscle however, they branch numerous times and a single motor neuron can innervate up to several hundred muscle fibers (Frank *et al*, 1975). This combination of a single motor neuron and all the muscle fibers it innervates is called a motor unit (Buchthal and Schmalbruch, 1980).

The concept of the tripartite synapse, which includes a perisynaptic component as well as the pre- and post-synaptic components, was also pioneered in the peripheral nervous system (PNS) at the NMJ rather than in the central nervous system. The realization that Schwann cells, the myelinating glial cell of the peripheral nervous system, play an important synaptic role at the NMJ predates the idea of astrocytes playing a similar role in neuron-neuron synapses by nearly 20 years (Couteaux, 1973; Mirsky and Jessen, 1996; Araque *et al*, 1999). Part of what led to this finding was the separation of Schwann cells into two distinct types based on their structure, genetic makeup, and location: terminal and pre-terminal Schwann cells. Both arise from the same

progenitors yet are remarkably different. Terminal Schwann cells, the ones found at the NMJ, cap the nerve terminal, insulating it from the environment and providing trophic factors. They are rich in the cell adhesion molecule N-CAM while displaying low levels of myelin-associated factors such as myelin basic protein and myelin-associated glyocoprotein. Preterminal Schwann cells have the opposite phenotype (low in cell-cell adhesion, high in myelinating factors) (Mirsky and Jessen, 1996).

1.5.2 Pre-Contact Signaling Drives Early Differentiation

Before forming a neuromuscular junction, the appropriate cells must first be able to seek out, identify, and communicate with each other. Rather than following these cells all the way from the neural crest, I will be focusing on how the cells interact once already in relatively close proximity to each other. During development *in vivo*, motor neurons reach the muscle just as the myoblasts are fusing into multinucleated muscle cells and early myotubes. Very weak neuromuscular transmission begins just minutes after initial nerve-muscle contact (Chow and Poo, 1986; Xie and Poo, 1986). Over approximately a week, synaptic vesicle production increases, cytoskeletal reorganization occurs on both sides of the synapse, and AChR clustering begins, along with many other changes (Kelly and Zacks, 1969; Takahashi *et al*, 1987; Lupa and Hall, 1989). These vast differences on either side of the synapse suggest robust communication between the different cell types involved. Interestingly, all three components of the NMJ – motor neurons, muscle cells, and Schwann cells – express synaptic components even when cultured in isolation from one another. This indicates that each of the three cell types prepare themselves for synaptic transmission even without input from the others, however this communication also appears to be necessary for each cell type to reach full maturity (Sanes and Lichtman, 1999).

Motor Neuron-Derived Agrin Drives Postsynaptic Differentiation

Early investigators noticed that there was a stereotyped position of synapses on muscle fibers which suggested a coordinated interaction between the two cell types (Bennett and Pettigrew, 1976). Motor neuron axons frequently fasciculate to form a single intramuscular nerve, with myotubes extending symmetrically in each direction (Zhang and McLennan, 1995). It soon became evident that it was motor neurons organizing the clustering of AChR at sites of

nerve-muscle contact as opposed to seeking out predetermined synaptic sites on the muscle (Anderson and Cohen, 1977; Frank and Fischbach, 1979). Acetylcholine itself was unable to induce this receptor clustering, and so the mechanism by which neurons were able to mediate these changes remained unclear until McMahan (1990) identified agrin as a potential contributor.

Agrin is a heparan sulfate proteoglycan (HSPG) that is synthesized by motor neurons, transported down the axon, and released from the nerve terminal (McMahan, 19900; Reist *et al*, 1992). HSPGs are known to play a wide variety of roles but are frequently associated with cell-cell adhesion and determining cell shape, both of which are important for NMJ formation (Bernfield *et al*, 1999). Agrin has repeatedly been shown to be a critical neuron-derived organizer of postsynaptic differentiation (Frank and Fischbach, 1979; Bezakova and Ruegg, 2003; Sarrazin *et al*, 2011). In agrin knockout mice, overall levels of AChR on muscle were unchanged, but there were very few AChR clusters and a there was marked decrease in neurite arborization on the myotubes (Gautam *et al*, 1996). Even more evidence emerged for its essential role in NMJ development when investigating the role of agrin on muscle cells and motor neurons independently. When agrin was introduced to cultured motor neurons, neurites ceased growing and began to accumulate synaptic vesicles (Chang *et al*, 1997). Whereas when agrin was supplied to a monoculture of muscle cells, patches of agrin formed on the muscle fibers and nearly complete postsynaptic structures were identified directly apposed to those deposits (Jones *et al*, 1997; Cohen *et al*, 1997). Nerve-derived agrin is clearly an important, driving factor in the structural formation of postsynaptic NMJ structures.

Muscle Cells Rely on the MuSK-Rapsyn Pathway and Neuronal Activity to Form AChR Clusters

While agrin is known to be a neuronally-derived effector of postsynaptic muscle differentiation, its mechanism of action was still unknown. MuSK, a receptor tyrosine kinase, was a hypothesized receptor for agrin. MuSK is selectively expressed by skeletal muscle and co-localizes precisely with AChRs (Valenzuela *et al*, 1995). MuSK knockout-derived myotube cultures failed to form AChR clusters either spontaneously or in response to agrin, a phenotype that was reversed by the reintroduction of MuSK (DeChiara *et al*, 1996). MuSK appears to be a gateway by

which AChR clustering is mediated but is not sufficient for it to occur. Rapsyn is another protein that precisely colocalizes at the NMJ as soon as AChR clusters form. Rapsyn appears in a direct 1:1 ratio with the number of AChRs in a cluster and is hypothesized to bind there directly (Burden *et al*, 1983; Noakes, 1993). In cultures derived from rapsyn knockout mice, there is no AChR clustering, similar to the agrin and MuSK knockouts (Gautam *et al*, 1995). In these rapsyn mutants however, MuSK still clusters at synaptic sites in response to agrin, even though the AChRs remain distributed stochastically throughout the muscle cell membrane (Gautam *et al*, 1996; Apel *et al*, 1997). This strongly indicates the rapsyn acts directly downstream of MuSK to recruit other important scaffolding components of the NMJ.

As one follows the MuSK-rapsyn cascade, it eventually leads to fundamental cellular processes such as transcription. *In vivo* transcriptional work has demonstrated that the muscle nuclei directly apposed to the nerve terminal transcribe AChR subunit genes at far greater rates than non-synaptic nuclei within the same cytoplasm (Merelie and Sanes, 1985; Simon *et al*, 1992; Duclert and Changeux, 1995). This localized transcription of AChR subunits contributes greatly to the enhanced synaptic accumulation of AChRs. Another interesting finding that came out of associated work was that the muscle was also upregulating its expression of neuregulins. Neuregulin has been shown to affect both pre- and post-synaptic function at the NMJ. Presynaptically, neuregulins induce differentiation of isolated motor neurons and enhance neurotransmitter release at newly formed NMJs (Dai and Peng, 1996; Fitzsimonds and Poo, 1998). Neuregulin blockade prevents the synthesis of additional AChRs normally induced by agrin and mediated by MuSK/rapsyn (Meier *et al*, 1998; Jones *et al*, 1996). This release of retrograde trophic factors from the muscle to enhance the strength of healthy synapses supports the hypothesis that NMJ formation is a bidirectional effort between the muscle and its motor neuron counterpart.

Schwann Cells Play a Role in Guiding Motor Neurons to the Muscle

The role of Schwann cells, as it is currently understood, is quite limited at this stage of NMJ development. Schwann cells follow motor neuron axons, using the axons as a scaffold for their own migration towards the synapse (Riethmacher *et al.*, 1997). Motor neuron axons provide

both mitogenic and guidance cues to the Schwann cells *en route* to their final destination. Interestingly, this trend seems to be reversed (i.e., Schwann cells guide axons) during reinnervation (see section 1.5.3 for more detail).

1.5.3 Post-Contact Differentiation and Maturation

Elimination of Polyneuronal Innervation

Input elimination is the process by which all neuronal inputs except one retract from each muscle fiber and align their arbors with the structure of the postsynaptic apparatus (Balice-Gordon and Lichtman, 1993). This process occurs at a rate of about 5-15% of fibers per day over approximately 2 weeks in rats (Rosenthal and Taraskevich, 1977). Polyneural innervation occurs as multiple motor axons converge onto a single muscle fiber at the single site identified by the first neuronal input (Bennett and Pettigrew, 1976). This specificity indicates that the synaptic region becomes extra sensitive to innervation or that the surrounding extra-synaptic membrane is somehow aversive to it (Frank *et al*, 1976). The localization of multiple neuronal inputs to a single postsynaptic region is beneficial for muscle tissues because they are only required to invest fully in a single receptive apparatus. Each neurite undergoes a standardized process of atrophy, detachment, and withdrawal from the muscle, culminating in the separation of distinct intramuscular axon territories (Riley, 1981; Gan and Lichtman, 1998). Even though many muscle fibers undergo this process of input elimination, there is no net change in the number of motor axons innervating the muscle as a whole (Balice-Gordon and Thompson, 1988). It is worth noting that this process only occurs for fast twitch muscle that undergo muscular action potentials. Tonic, or slow-twitch, muscle fibers have multiple synaptic sites and retain multiple axons at individual sites as well (Lichtman *et al*, 1985).

The mechanism by which polyneuronal inputs are eliminated is thought to be dependent on chemicals released by both the neuronal and muscular components of the NMJ. Inhibition of synaptic release causes a drastic reduction in the rate of synaptic elimination while overstimulation expedites the process (Thompson, 1985). Additionally, if a particular neuron is more active than its neighbors, it is less likely to be eliminated (Balice-Gordon and Lichtman, 1994). This indicates that input elimination is strongly mediated by synaptic activity. However,

other work has shown that even before neurons begin atrophying at the synapse, muscles express decreased amounts of AChRs and rapsyn molecules which indicates that the muscle plays an active role in determining its neuronal partner (Balice-Gordon and Lichtman, 1993; Culican *et al*, 1998). This area is not as well studied, but the prevailing theory is that muscles release retrograde trophic factors such as synaptotrophin which are uptaken by the presynaptic neuron in an activity-dependent manner (Snider and Lichtman, 1996). This would ensure that the neuron that is best able to bring the muscle fiber to threshold would be selectively rewarded with trophic factors, further strengthening that connection.

Structural Maturation of the Postsynaptic NMJ

Acetylcholine receptor clustering is just the first step in the dramatic, post-contact differentiation that occurs for muscle cells in the two weeks post-contact. AChRs initially cluster in a relatively uniform, elliptical plaque. As neuronal inputs are eliminated, receptor density changes to match the new pattern of innervation, eventually resulting in a pretzel-like form referred to as a motor endplate (Balice-Gordon and Lichtman, 1993; Steinbach, 1981; Slater, 1982). For visualization of this process, see Figure 1.5 at the end of this chapter. The development of the motor endplate occurs over the same two-week period as input elimination and does not extend further into the life cycle of the animal. This is significant because rats, and their muscles, continue to grow for at least another 4-6 weeks before reaching full maturity (Boice and Adams, 1983). Muscle growth mostly occurs due to increases in muscle fiber length and diameter, but not fiber number (Sanes and Lichtman, 1999). The NMJ also grows in parallel with the muscle fibers, but its x-y geometry remains largely unaffected. The z-direction however gains additional complexity. The membrane starts becoming invaginated with shallow gutters underneath the nerve terminals which align with the active zones of the neuron terminal (Sanes and Lichtman, 1999). These invaginations increase the surface area of membrane available for insertion of AChRs thereby increasing receptor density and leading to enhanced muscle response (Fertuck and Salpeter, 1974).

Schwann Cells Finalize Mature NMJ

The majority of Schwann cell maturation occurs during the conclusion of input elimination when the postsynaptic apparatus is nearly complete. Terminal Schwann cells initially follow the motor neuron axon down to the muscle and form a loose cap over the terminal, but as the motor neuron boutons become more permanent, each terminal bouton is separately capped by a terminal Schwann cell (Hirata *et al*, 1997). These Schwann cells are also much more robust than their pre-differentiation counterparts and can survive independently of neurons for a relatively long period of time once established, a characteristic important for reinnervation (Trachtenberg and Thompson, 1997).

1.5.4 Long-Term Stability and Reinnervation

Long-Term Stability

The postsynaptic endplate of a neuromuscular junction is stable throughout adult mammalian life and researchers have questioned whether this is due to a high degree of inert self-sufficiency or perpetual maintenance and upkeep (Sanes and Lichtman, 1999). Time-lapse imaging in mice has shown that NMJs neither gain nor lose branches over through most of an animal's lifetime, even during the muscular hypertrophy associated with puberty (Lichtman and Thompson, 1997; Lichtman *et al*, 1987). Even axotomy leading to degeneration of the nerve terminal does not cause degradation of the elaborate postsynaptic structures (Wigston, 1990). However, there is evidence that the muscle itself plays an important role in maintaining the synaptic connection. Injection of a membrane-impermeant protein synthesis inhibitor caused nerve terminals to withdraw from muscle fibers demonstrating that the maintenance of the nerve terminals is highly dependent on proteins produced by muscle fibers (Sanes and Lichtman, 1999). Further, it could implicate these proteins as targets of inhibition during polyneuronal input elimination. Though impressively stable for much of an organism's life, NMJs do degrade significantly with age. The number of AChRs per junction gradually decreases in older muscles, extra-junctional receptors appear, empty synaptic sites become more prevalent, and some terminal Schwann cells degenerate (Frank *et al*, 1976; Courtney and Steinbach, 1981; Rosenheimer and Smith, 1985 Ludatscher *et al*, 1985; Boaro *et al*, 1998). Overall, it is not explicitly

clear why NMJs are so stable for the majority of an animal's life or why they begin to degrade with age, but there is a wealth of evidence to support that once they are formed, mature NMJs are robust over long periods of time.

Reinnervation

Reinnervating a NMJ following de-innervation is an important concept with a wide range of therapeutic and translational applications. Even though it has been shown that motor neurons dictate the location of AChR clustering on aneural muscle fibers, it is the muscle that dictates the site of re-innervation. Novel axons will form their new synapses on already existent postsynaptic sites (Cajal and Ramon, 1928; Sanes *et al*, 1978). Schwann cells play a large role in this as they serve as a guidance cue for adult axons (Son and Thompson, 1995). As was stated above, Schwann cells survive at the NMJ for a brief period after the neuron withdraws and this serves as a target for incoming neurons. During development, Schwann cells express many trophic and adhesive proteins that are downregulated in adulthood but reactivated when no longer in the presence of an axon (Taniuchi *et al*, 1988; Plantinga *et al*, 1993). The majority of regenerated NMJs look and perform very similarly to those that formed during normal development (Sanes and Lichtman, 1999).

1.6 Biological Machines

1.6.1 Overview

The driving principle behind man-made robots is force actuation that leads to a form of directed movement. Natural systems can motivate the design and development of robots that replicate or enhance many basic locomotive strategies, such as climbing (Unver *et al*, 2006), crawling, walking, jumping, or swimming (Umedachi *et al*, 2016; Cvetkovic *et al*, 2014; Kovac, 2013; Bartlett *et al*, 2015; Feinberg *et al*, 2007; Wen *et al*, 2013; Low, 2007; Herr and Dennis, 2004; Nawroth *et al*, 2012). Biological soft robotics derive inspiration and design principles from organic systems to facilitate engineering approaches to challenges that have historically plagued conventional robotic actuators. Traditional hard skeletons (made of high stiffness metals or plastics) and electromagnetic actuators can result in rigid bioactuators that exhibit few degrees

of freedom (DOF), low complexity, difficulty in grasping actions, and aggressive collisions with living tissues (Majidi, 2013).

Soft bioactuators (typically composed of gels, polymers, and fluids, sometimes with the addition of biological materials) must not only be functional in a research laboratory but also effective in situations where they may be called on to move over unstable terrain while carrying heavy loads of sensors, imagers, or samplers. These devices would also ideally be capable of untethered as well as directional locomotion, elastic deformation or stiffness modulation, efficient energy storage, and robust motion control, to be both effective and useful. Soft biorobotic manipulators generally have more degrees of freedom and are more compliant than their rigid counterparts. The lightweight and flexible polymers, hydrogels, and elastomers used to form soft robots have lower stiffnesses (moduli of 104–109 Pa) that correspond to properties of biological matter with which they interact. Due to recent manufacturing advancements, they can be rapidly produced with high spatial control and a range of properties in three dimensions (Kovac, 2013; Vincent *et al*, 2006; Full, 2001; Ricotti *et al*, 2012; Kim *et al*, 2013).

Beyond a skeletal structure, soft biorobotic systems require an actuating source and a fuel supply. It therefore follows that living biological materials would inspire and comprise a large portion of demonstrated bioactuators (Kim *et al*, 2013; Tadesse *et al*, 2016). Beyond simple biomimicry, the field of biodesign incorporates living organisms into artificial or manmade systems (Bernabei and Power, 2016). The addition of living biological actuator sources (e.g., muscle tissues) can increase the efficiency and responsiveness of soft actuators, as many of these living components have evolved with efficient standard processes for force production, energy consumption, or net movement (Zolfagharian *et al*, 2016; Lee *et al*, 2017; Chan *et al*, 2014). Depending on the ecosystem, there are numerous methods of potential locomotion among species in both the plant and animal kingdoms, including crawling, running, jumping, swimming, flying, etc. (Burgert and Fratzl, 2009). Considering the many methods of propulsion, it is unsurprising that there are many ways for these robots to generate locomotive forces, from molecular (*e.g.,* motor proteins; nm) to cellular (*e.g.,* individual microorganisms or cells; µm) to tissue (*e.g.*, muscles or cell clusters; mm) length scales (Chan *et al*, 2014). In addition to locomotors, there are also biorobots that imitate peristalsis to act as pumps or valves, transport

cargo, actuate a joint, sense a signal, or perform as microgrippers, rotors, mixers, or manipulators to achieve other tasks (Kabumoto *et al*, 2013; Carlsen and Sitti, 2014; Bowers *et al*, 2011; Cho and Wood, 2016; Li *et al*, 2019). It is apparent that the development of soft bioactuators necessitates the intersection and integration of advancements in diverse fields such as nanotechnology, tissue engineering, and developmental biology (Kamm and Bashir, 2013).

1.6.2 Living Bioactuators

Overview

The use of biological materials (including DNA, motor proteins, myosin-actin complexes, bacteria, algae, single cells or clusters, and natural or engineered tissues) as the primary actuators of locomotive force is still an extremely young field, but has resulted in some interesting possibilities (Chan *et al*, 2014; Feinberg, 2015). The basic requirements of an ideal living biological actuation source include the ability to generate a controllable or repeatable force, operate under a range of environments, and be easily maintained (Carlsen and Sitti, 2014). Evolution has produced optimal living actuators that can operate long-term at physiological conditions (favorable for bio-medical applications), wirelessly convert chemical energy to mechanical work (from glucose or fats with up to 100 times the energy density of a battery (Majidi, 2013)), produce nontoxic and biodegradable byproducts from fuel conversion, and be stimulated electrically, optically, or pharmacologically thereby eliminating the need for an attached energy source. Additionally, they are proficient at self-assembly and replication, protein synthesis, rapid adaptation (responses as short as tens of milliseconds), and high sensitivity to environmental conditions. They are also biodegradable, biocompatible, and can dynamically interact with other living or non-living components (Kim *et al*, 2013; Dennis and Herr, 2005; Feinberg, 2015).

In general, when exploiting the innate contractility of cells or tissue to power a bioactuator, it is critical to consider the stimuli (mechanical, electrical, and biochemical) necessary for differentiation, development, or maintenance (Uzel *et al*, 2014; Dennis and Herr, 2005). A stereolithography apparatus (SLA) can print hydrogels with tissue-like stiffness values that are mechanically similar to cells' *in vivo* extracellular environment, providing important mechanical queues for the engineered tissue. The elastic modulus of the extracellular matrix

(ECM) not only affects viability and proliferation, but also dictates the differentiation bias of cultured stem cells (Engler *et al*, 2004); for this reason, stereolithography has been used to fabricate a variety of matrices that can realistically simulate cellular microenvironments and aid in engineered tissue development (Arcaute *et al*, 2011).

Engineered molecular and bacterial bioactuators are capable of cargo transport and fluidic pumping and can thrive in a range of environmental temperatures or pH (Chan *et al*, 2014; Carlsen and Sitti, 2014; Knoblauch and Peters, 2004; Stanton *et al*, 2017). The production of a multi-cellular tissue can allow for a collective output that is greater than the sum of its parts. Moreover, complexity and functionality both increase when progressing from single cells to cell clusters to tissues and systems (Carlsen and Sitti, 2014; Kamm and Bashir, 2013). Functional bioactuators have been devised using whole explanted tissues, cells differentiated within a scaffold or gel, or self-organized engineered tissue (Herr and Dennis, 2004; Akiyama *et al*, 2012; Goebel and Wahlster, 2015; Hinds *et al*, 2011; Dennis and Kosnik, 2000). It is worth noting that although smooth muscle is capable of force production, the relatively slow rate of contraction has largely prohibited its employment in bio-robots that require rapid actuation (Duan *et al*, 2012; Feinberg, 2015).

Benefits of 3-Dimensional Culture

For over a century, 2D cell cultures have been used as *in vitro* models to study biological phenomena. Although these approaches are well-accepted and have significantly advanced our understanding of cell behavior, growing evidence now indicates that 2D systems often cause irregular cell behaviors. Specific behaviors of cancer cells, muscle fibers, and hepatocytes have all been more closely aligned with *in vivo* knowledge when cultured in 3D rather than 2D (Choi *et al*, 2010; Mudera *et al*, 2010; Gieseck III *et al*, 2014). Recent advances in 3D culture such as sandwich culture, micropatterning, porous hydrogels, and 3D printing have contributed to a rapid rise in the number of publications studying cell populations in 3D, further improving upon older 2D data in these systems (Bi *et al*, 2006; Chaubey *et al*, 2008; Lee *et al*, 2015; Cvetkovic *et al*, 2014). The production of mature muscle fibers in 2D cultures has always been difficult due to the spontaneous twitching that is intrinsic to healthy myotubes during development (Lewis, 1915).

On a stiff substrate, such as the traditional hard glass or plastic of a petri dish or cell culture flask, spontaneous contractions can often cause the myotubes to pull themselves off the substrate. This results in a selection bias for fibers that either contract weakly or not at all as culture time increases. There is also strong evidence that muscle cells reach later stages of development and do so more quickly in 3D culture systems than in 2D (Langelaan *et al*, 2010; Grabowska *et al*, 2011).

Cardiac Muscle

Cardiomyocytes provide an excellent source for bioactuation due to their intrinsic, synchronous contractions which makes external stimulation unnecessary. The cells produce spontaneous contractions by forming a syncytium through cell-cell adhesion and gap junctions (Chan *et al*, 2014; Kamm and Bashir, 2013). The original developments in cardiac-based bioactuators included locomotive machines such as walking micro-robots and swimming robots modeled after spermatozoa and jellyfish (Feinberg *et al*, 2007; Park *et al*, 2005; Kim *et al*, 2007; Williams *et al*, 2014; Nawroth *et al*, 2012).

Skeletal Muscle

The behavioral complexity and degree of external control that can be imposed on cardiac muscle is limited by its intrinsic spontaneous contractility. The ability to regulate an actuator through the application and modulation of a stimulus not only allows for precise control over locomotion, but also opens avenues for greater functionality. Skeletal muscle is the primary generator of animal locomotion and these biological systems exhibit a greater force-to-weight ratio than many rigid mechanical actuators (Chan *et al*, 2014; Carlsen and Sitti, 2014; Kamm and Bashir, 2013; Feinberg, 2015). A high degree of spatial and temporal control over actuation, even of single fibers, is possible via external sources such as optical or neural stimulation, as is larger-scale control through electrical or chemical stimulation (Park *et al*, 2016; Raman *et al*, 2016; Uzel *et al*, 2016; Cvetkovic *et al*, 2017; Cvetkovic *et al*, 2014; Aydin *et al*, 2019).

A skeletal muscle-powered biobot developed by Cvetkovic and her colleagues mimicked the mammalian musculoskeletal system, wherein muscle contraction drives the articulation of bones across flexible joints (Cvetkovic *et al*, 2014; Raman *et al*, 2017). A 3D printed skeleton

(comprised of a flexible beam connected to two stiff pillars) was fabricated using a stereolithographic apparatus and subsequently anchored to an engineered muscle strip containing differentiating C2C12 myoblasts. The 3D muscle strip contained fibrin and Matrigel to serve as an artificial ECM to support the densely embedded cells. To induce the locomotion-driving contraction of the muscle strip, the biobot was positioned within an electric field and subjected to pulse stimulations of 1, 2, or 4 Hz, resulting in a global response of the excitable cells. The introduction of deliberate asymmetry in the pillars allowed the biobot to move in a unidirectional trajectory along a surface in a fluid.

Although the muscle strip successfully induced net locomotion, the muscle was permanently tethered to the skeleton, preventing the adaptation of the muscle to other skeleton structures (Cvetkovic *et al*, 2014). A second iteration by Raman *et al* was devised with a muscle ring structure, formed in a separate 3D printed mold before being transferred to the skeleton (Raman *et al*, 2016). Muscle rings exhibited higher myofiber alignment as well as increased viability (Raman *et al*, 2017). The C2C12s were also genetically modified to express Channel rhodopsin (ChR2), a membrane protein which causes muscle contraction when stimulated with blue light (Sakar *et al*, 2012). This allowed for the control of locomotion through an optical stimulus, which could be positioned with spatial resolution on localized regions of the biobot, thus enabling the development of a symmetrical yet multi-directional bioactuator whose direction of locomotion was determined by which ring the light stimulated. Similarly, a single device could also be forced to rotate by stimulating only one half of a single muscle ring. To maximize force production, the biobots underwent an “exercise regimen” of daily optical stimulation throughout muscle differentiation. Exercise was shown to improve myotube formation, leading to increased tension and locomotive speed. Further adaptations to this platform were performed by reshaping the muscle strip to include two rings connected by a muscular bridge resulting in locomotive speeds nearly two-fold greater than without exercise.

Using skeletal muscle in developing biobots allows for broader applications than just locomotion – such as mimicking peristaltic pumping. Li *et al* (2019) designed and fabricated a biohybrid valve-less pumping bot utilizing a closed-loop tube filled with liquid. Periodic compression at the junction of soft and rigid tubes generated unidirectional flow. By wrapping a

skeletal muscle ring around the tube at this location, muscle contraction was used to compress the hydrogel tube along the circumferential direction in the radial direction to drive unidirectional flow.

1.6.3 Applications

The extreme diversity of fabrication approaches, material compositions, and actuation methods means that soft robots can be used in a wide variety of ways. Soft robots have many useful capabilities, including the abilities to deform their shape, to manipulate delicate objects, to conform to their surroundings, and to move in cluttered and/or unstructured environments. (Martinez *et al*, 2013). Small robots at the millimeter scale also offer several advantages over larger robots. For example, their small size enables them to be operated in environments where large robots would be impractical or impossible. In large numbers, soft robots might be networked to form highly mobile and robust sensor and communication networks (Jung and Bae, 2013). This allows them to assist work in 3D environments such as rubble fields, utility conduits, the ocean floor, or outer space for many applications, including by the military (Umedachi *et al*, 2016).

Human-related applications are also being explored with fluidically-powered soft actuators demonstrating their potential in wearable prosthetics and orthotics (Wirekoh and Park, 2017). These devices, compared with their motor-driven counterparts, are lighter, undergo continuous and more natural deformation with simple control inputs, and are more easily mass-produced (Zhao *et al*, 2016). Humanoid robots could assist human beings in numerous ways, from military applications and firefighting to entertainment, socially assistive devices, medical studies, and education. Soft actuators lay the groundwork for the development of these humanoid robots for cognitive studies or for training medical professionals. In addition, facially expressive robots are demonstrating encouraging results as therapeutic tools for children with Autism Spectrum Disorder (Tadesse *et al*, 2016).

Both living and nonliving bioactuators must be designed such that the form matches the intended function (Uzel *et al*, 2014; Feinberg, 2015; Kim *et al*, 2014). When building with muscle, the devices might need to closely match the performance of their *in vivo* equivalents, especially

if their intended use is to mimic a native tissue for drug testing or regenerative applications, or to provide a novel platform for understanding fundamental biological phenomena. It is expected that custom-printed 3D soft robots and actuator structures will start to appear in areas as diverse as medical implants, devices for human-computer interaction, and even children's toys (Rossiter *et al*, 2009). Soft robotics is a rapidly growing field with almost unlimited potential to universally impact human life.

1.7 Figures

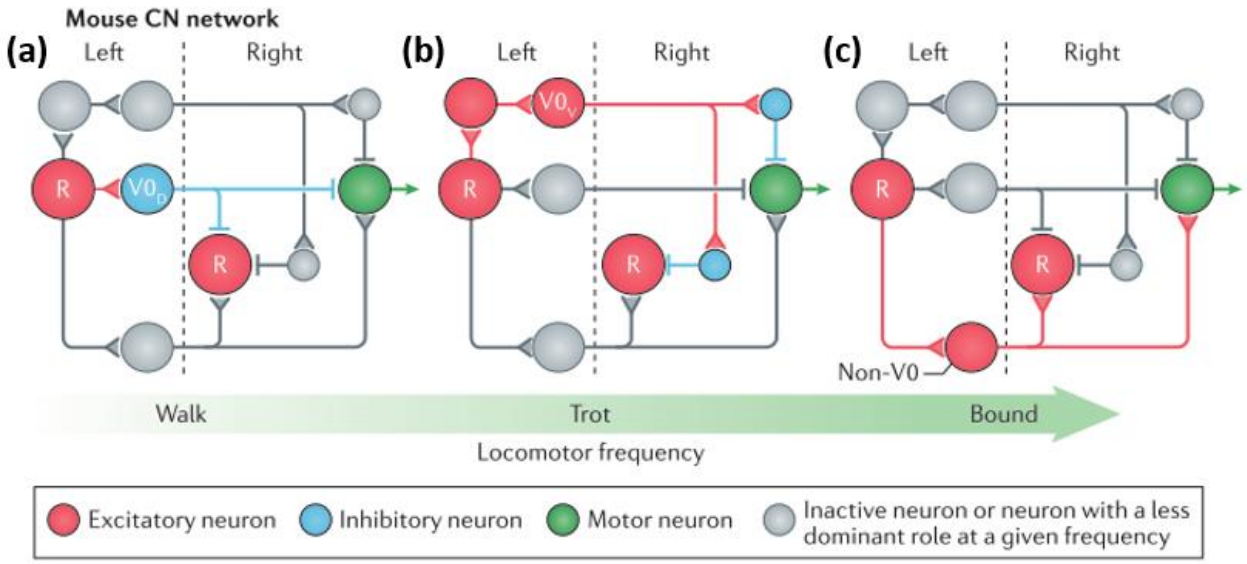

Figure 1.1 Proposed recruitment of V0D and V0V commissural neurons (CNs) during increased speed of gait. **(a)** Low frequency locomotion (walk). Inhibitory V0D CNs are activated by rhythm-generating neurons (R) on the ipsilateral side. This leads to the inhibition of contralateral locomotor networks, including motor neurons. **(b)** Trot. V0V commissural neurons are being activated causing the contralateral inhibition. **(c)** Bound. Left–right synchrony is secured by excitatory non-V0 (possibly V3) neurons (red). Adapted from a review by Kiehn, 2016.

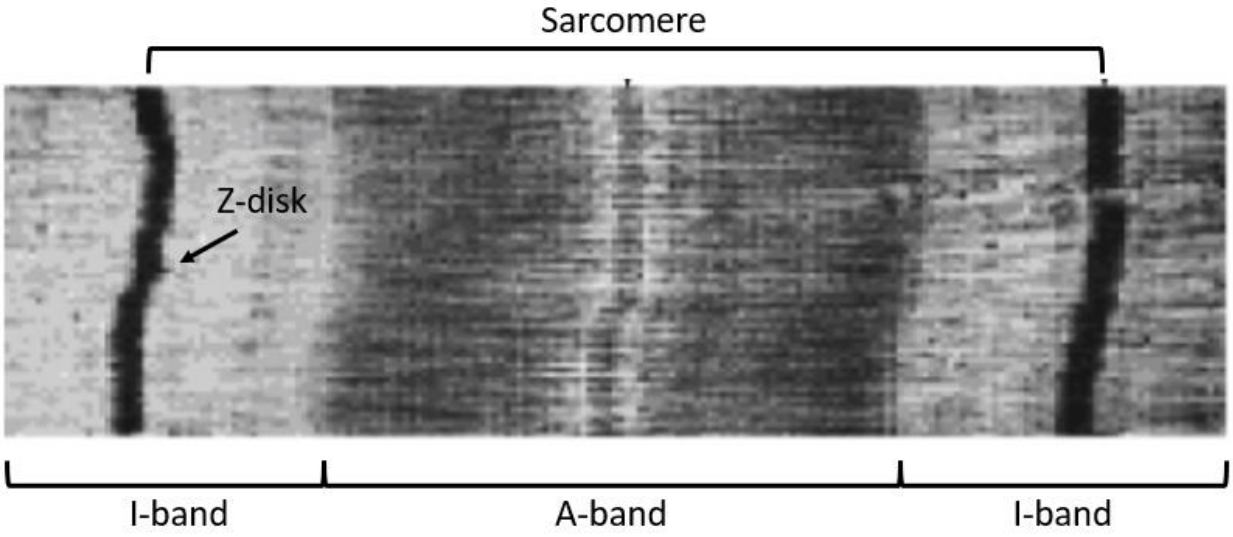

Figure 1.2. Image of a single sarcomere. Light bands contain actin and are known as I-bands. The dark bands are myosin-rich A-bands. The thick, dark line bisecting the I-band is a Z-disk (made from a separate type of myofilament). The copyright holder of this work allows anyone to use it for any purpose including unrestricted redistribution, commercial use, and modification.

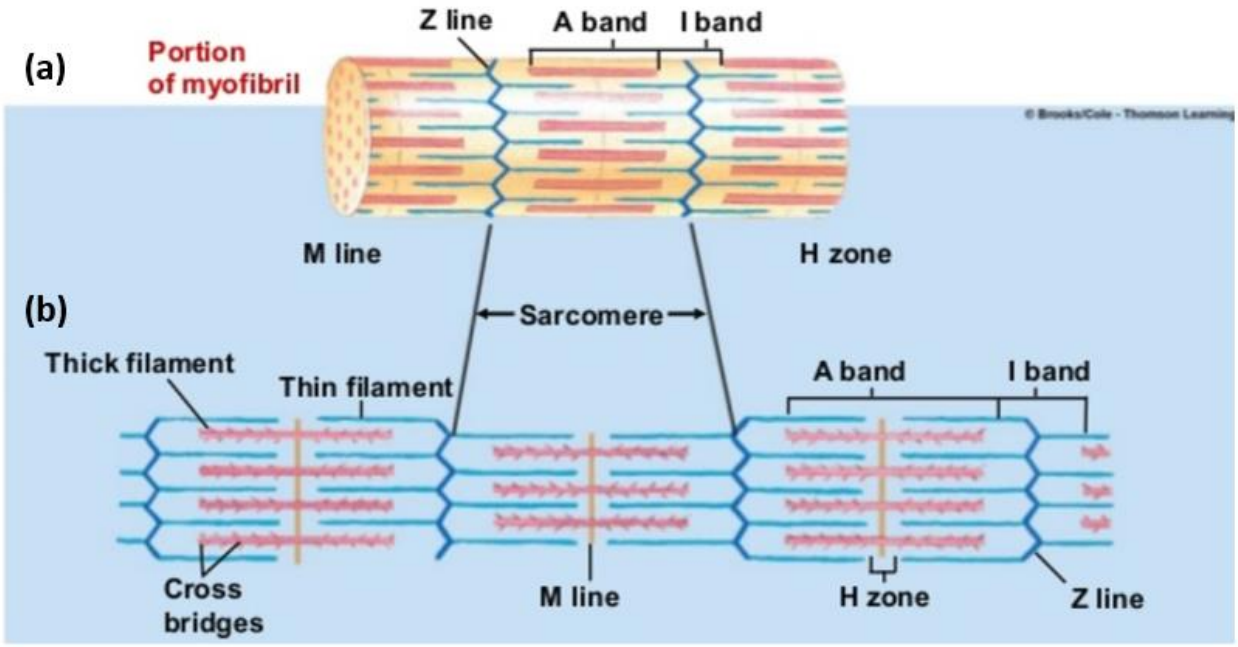

Figure 1.3. Diagram of contractile units within a sarcomere. **(a)** Diagramatic representation of the A-band, I-band, and Z-disk. **(b)** Shows organization of my actin (thin) and myosin (thick) filaments within a sarcomere. Sequential sarcomeres form a myofibril. Adapted from Hall, 2015.

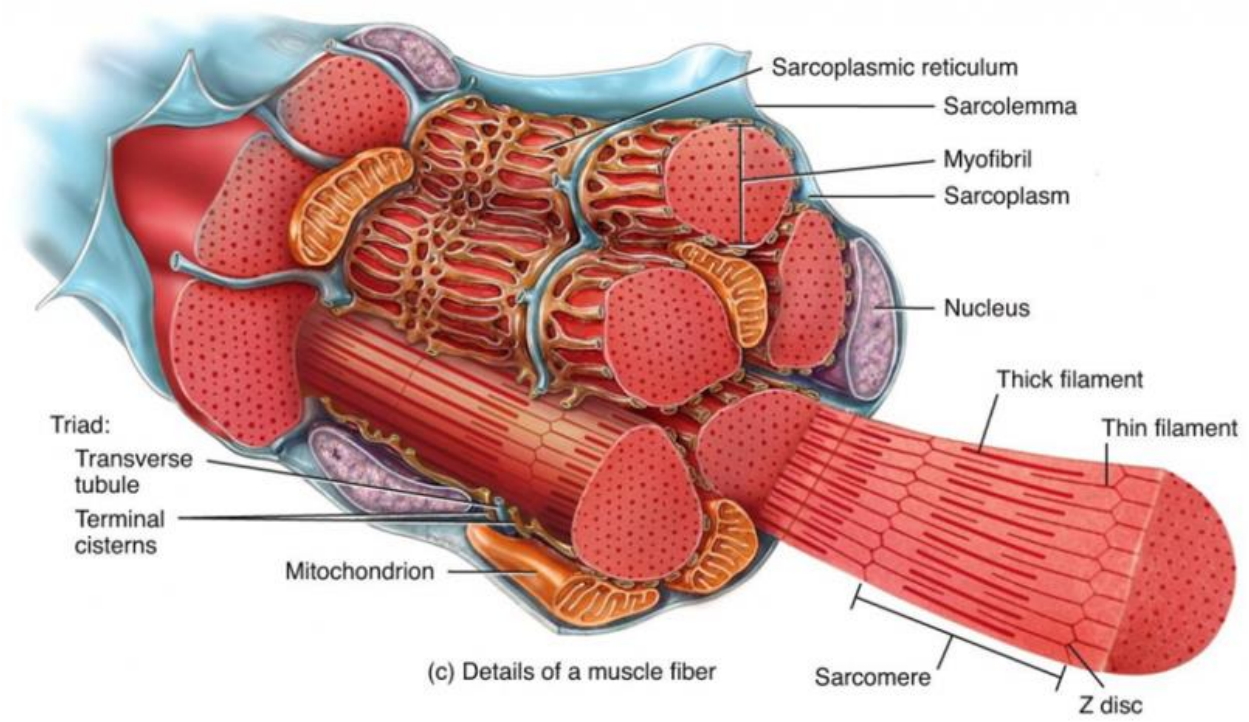

Figure 1.4. Visual representation of relative organization of sarcolemma, sarcoplasmic reticulum, transverse tubules, triads, mitochondria, and myofibrils. Adapted from Hall, 2015.

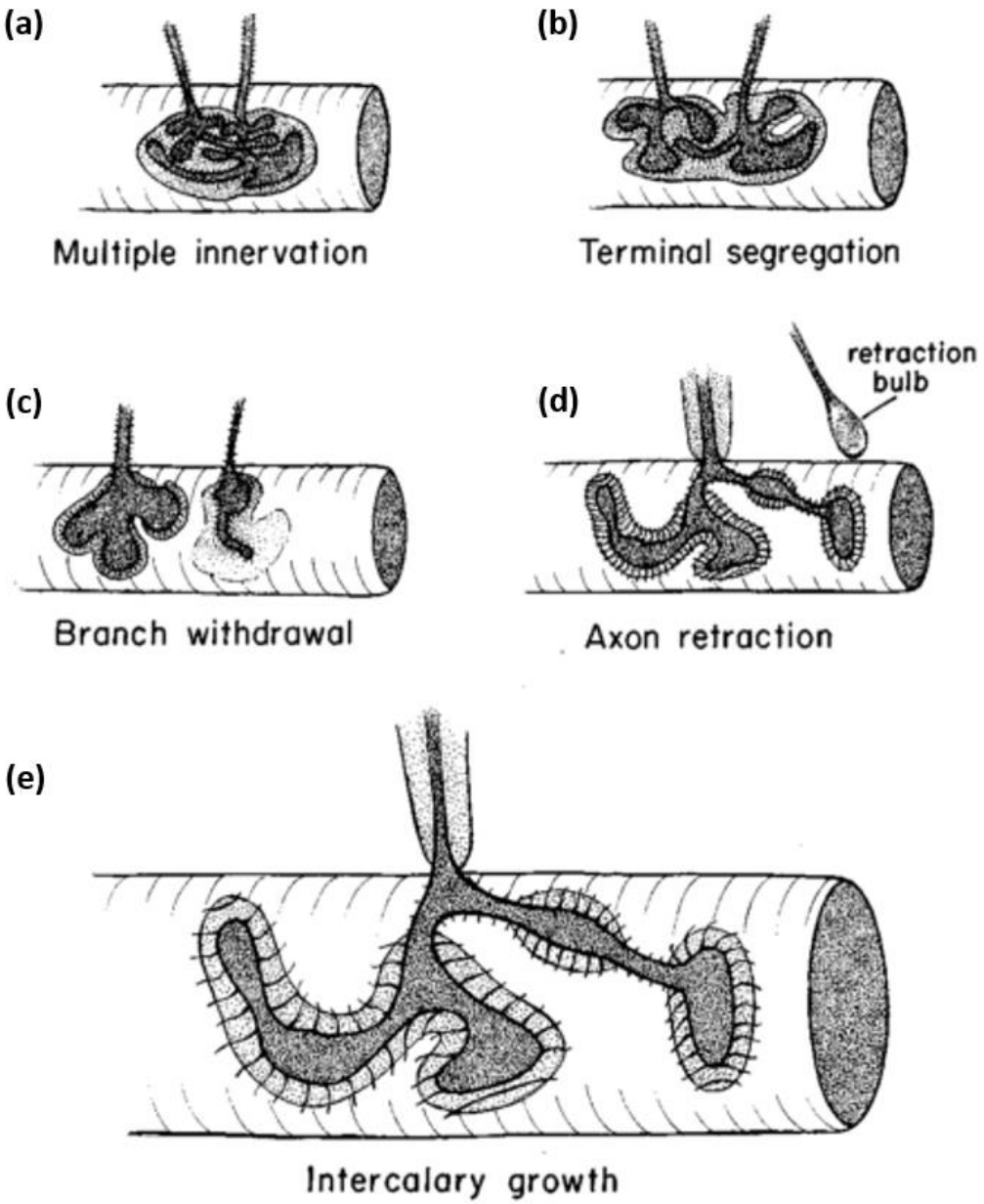

Figure 1.5. A depiction of the stages of AChR clustering on muscle. **(a)** AChRs cluster in a relatively uniform, elliptical plaque. **(b)-(d):** As neuronal inputs are eliminated, receptor density changes to match the new pattern of innervation. **(e)** A mature, innervated AChR cluster with a pretzel-like shape. Adapted from McComas *et al*, 1984.

1.8 References

1. Rogers, K. (2002). Midbrain. In *Encyclopedia Brittanica*. Encyclopædia Britannica, inc.
2. Patla, A. E. (1997). Understanding the roles of vision in the control of human locomotion. *Gait & Posture*, *5*(1), 54-69.
3. Behbehani, M. M., & Fields, H. L. (1979). Evidence that an excitatory connection between the periaqueductal gray and nucleus raphe magnus mediates stimulation produced analgesia. *Brain research*, *170*(1), 85-93.
4. Menetrey, D., & Basbaum, A. I. (1987). The distribution of substance P-, enkephalin-and dynorphin-immunoreactive neurons in the medulla of the rat and their contribution to bulbospinal pathways. *Neuroscience*, *23*(1), 173-187.
5. Figueira, R. J., Peabody, M. F., & Lonstein, J. S. (2008). Oxytocin receptor activity in the ventrocaudal periaqueductal gray modulates anxiety-related behavior in postpartum rats. *Behavioral neuroscience*, *122*(3), 618.
6. Hallgren, B., & Sourander, P. (1958). The effect of age on the non-haemin iron in the human brain. *Journal of neurochemistry*, *3*(1), 41-51.
7. Orlovsky, G. N. (1972). Activity of vestibulospinal neurons during locomotion. *Brain research*, *46*, 85-98.
8. *Being and Perceiving*. Manupod Press, 2011.
9. Garcia-Rill, E., Skinner, R. D., Gilmore, S. A., & Owings, R. (1983). Connections of the mesencephalic locomotor region (MLR) II. Afferents and efferents. *Brain research bulletin*, *10*(1), 63-71.
10. Jordan, L. M. (1998). Initiation of locomotion in mammals. *Annals of the New York Academy of Sciences*, *860*(1), 83-93.
11. Burns, R. S., Chiueh, C. C., Markey, S. P., Ebert, M. H., Jacobowitz, D. M., & Kopin, I. J. (1983). A primate model of parkinsonism: selective destruction of dopaminergic neurons in the pars compacta of the substantia nigra by N-methyl-4-phenyl-1, 2, 3, 6-tetrahydropyridine. *Proc. Nat. Acad. Sci. 80*(14), 4546-4550.
12. Garcia-Rill, E. (1986). The basal ganglia and the locomotor regions. *Brain Research Reviews*, *11*(1), 47-63.
13. Shik, M. L. (1966). Control of walking and running by means of electrical stimulation of the mid-brain. *Biophysics*.
14. Nicolopoulos-Stournaras, S., & Iles, J. F. (1984). Hindlimb muscle activity during locomotion in the rat (Rattus norvegicus)(Rodentia: Muridae). *Journal of Zoology*, *203*(3), 427-440.
15. Skinner, R. D., & Garcia-Rill, E. (1984). The mesencephalic locomotor region (MLR) in the rat. *Brain research*, *323*(2), 385-389.
16. Piallat, B., Chabardès, S., Torres, N., Fraix, V., Goetz, L., Seigneuret, E., ... & Yelnik, J. (2009). Gait is associated with an increase in tonic firing of the sub-cuneiform nucleus neurons. *Neuroscience*, *158*(4), 1201-1205.
17. Nandi, D., Aziz, T. Z., Giladi, N., Winter, J., & Stein, J. F. (2002). Reversal of akinesia in experimental parkinsonism by GABA antagonist microinjections in the pedunculopontine nucleus. *Brain*, *125*(11), 2418-2430.

18. Stefani, A., Lozano, A. M., Peppe, A., Stanzione, P., Galati, S., Tropepi, D., ... & Mazzone, P. (2007). Bilateral deep brain stimulation of the pedunculopontine and subthalamic nuclei in severe Parkinson's disease. *Brain*, *130*(6), 1596-1607.
19. Jahn, K., Deutschländer, A., Stephan, T., Kalla, R., Hüfner, K., Wagner, J., ... & Brandt, T. (2008). .20-Supraspinal locomotor control in quadrupeds and humans. *Progress in brain research*, *171*, 353-362.
20. Maekawa, K., & Kimura, M. (1980). Mossy fiber projections to the cerebellar flocculus from the extraocular muscle afferents. *Brain research*, *191*(2), 313-325.
21. Thach, W. T. (1968). Discharge of Purkinje and cerebellar nuclear neurons during rapidly alternating arm movements in the monkey. *Journal of neurophysiology*, *31*(5), 785-797.
22. Voogd, J., & Glickstein, M. (1998). The anatomy of the cerebellum. *Trends in cognitive sciences*, *2*(9), 307-313.
23. Bosco, G., & Poppele, R. E. (2001). Proprioception from a spinocerebellar perspective. *Physiological reviews*, *81*(2), 539-568.
24. Yu, J., & Eidelberg, E. (1983). Recovery of locomotor function in cats after localized cerebellar lesions. *Brain research*, *273*(1), 121-131.
25. Brodal, P., & Bjaalie, J. G. (1997). Salient anatomic features of the cortico-ponto-cerebellar pathway. *Progress in brain research*, *114*, 227-249.
26. Orioli, P. J., & Strick, P. L. (1989). Cerebellar connections with the motor cortex and the arcuate premotor area: an analysis employing retrograde transneuronal transport of WGA-HRP. *Journal of Comparative Neurology*, *288*(4), 612-626.
27. Kakei, S., Yagi, J., Wannier, T., Na, J., & Shinoda, Y. (1995). Cerebellar and cerebral inputs to corticocortical and corticofugal neurons in areas 5 and 7 in the cat. *Journal of neurophysiology*, *74*(1), 400-412.
28. Chambers, W. W., & Sprague, J. M. (1955). Functional localization in the cerebellum: Somatotopic organization in cortex and nuclei. *AMA Archives of Neurology & Psychiatry*, *74*(6), 653-680.
29. Thach, W. T., Goodkin, H. P., & Keating, J. G. (1992). The cerebellum and the adaptive coordination of movement. *Annual review of neuroscience*, *15*(1), 403-442.
30. Clendenin, M., Ekerot, C. F., Oscarsson, O., & Rose, I. (1974). Functional organization of two spinocerebellar paths relayed through the lateral reticular nucleus in the cat. *Brain research*, *69*(1), 140-143.
31. Kotchabhakdi, N., & Walberg, F. (1978). Primary vestibular afferent projections to the cerebellum as demonstrated by retrograde axonal transport of horseradish peroxidase. *Brain research*, *142*(1), 142-146.
32. Ito, M., Nisimaru, N., & Yamamoto, M. (1976). Pathways for the vestibulo-ocular reflex excitation arising from semicircular canals of rabbits. *Experimental brain research*, *24*(3), 257-271.
33. Brown, T. G. (1911). The intrinsic factors in the act of progression in the mammal. *Proceedings of the Royal Society of London. Series B, containing papers of a biological character*, *84*(572), 308-319.
34. Grillner, S. in Handbook of Physiology (ed. Brooks, V.) 1179–1236 (American Physiological Society, 1981)

35. Kiehn, O. (2006). Locomotor circuits in the mammalian spinal cord. *Annu. Rev. Neurosci.*, *29*, 279-306.
36. Jankowska, E. (2008). Spinal interneuronal networks in the cat: elementary components. *Brain research reviews*, *57*(1), 46-55.
37. Butt, S. J., & Kiehn, O. (2003). Functional identification of interneurons responsible for left-right coordination of hindlimbs in mammals. *Neuron*, *38*(6), 953-963.
38. Pierani, A., Moran-Rivard, L., Sunshine, M. J., Littman, D. R., Goulding, M., & Jessell, T. M. (2001). Control of interneuron fate in the developing spinal cord by the progenitor homeodomain protein Dbx1. *Neuron*, *29*(2), 367-384.
39. Lanuza, G. M., Gosgnach, S., Pierani, A., Jessell, T. M., & Goulding, M. (2004). Genetic identification of spinal interneurons that coordinate left-right locomotor activity necessary for walking movements. *Neuron*, *42*(3), 375-386.
40. Kiehn, O. (2016). Decoding the organization of spinal circuits that control locomotion. *Nature Reviews Neuroscience*, *17*(4), 224-238.
41. Talpalar, A. E., Bouvier, J., Borgius, L., Fortin, G., Pierani, A., & Kiehn, O. (2013). Dual-mode operation of neuronal networks involved in left-right alternation. *Nature*, *500*(7460), 85-88.
42. Bellardita, C., & Kiehn, O. (2015). Phenotypic characterization of speed-associated gait changes in mice reveals modular organization of locomotor networks. *Current Biology*, *25*(11), 1426-1436.
43. Borowska, J., Jones, C. T., Zhang, H., Blacklaws, J., Goulding, M., & Zhang, Y. (2013). Functional subpopulations of V3 interneurons in the mature mouse spinal cord. *Journal of Neuroscience*, *33*(47), 18553-18565.
44. Zhang, Y., Narayan, S., Geiman, E., Lanuza, G. M., Velasquez, T., Shanks, B., ... & Fan, C. M. (2008). V3 spinal neurons establish a robust and balanced locomotor rhythm during walking. *Neuron*, *60*(1), 84-96.
45. Grillner, S., & Jessell, T. M. (2009). Measured motion: searching for simplicity in spinal locomotor networks. *Current opinion in neurobiology*, *19*(6), 572-586.
46. Roberts, A., Li, W. C., Soffe, S. R., & Wolf, E. (2008). Origin of excitatory drive to a spinal locomotor network. *Brain research reviews*, *57*(1), 22-28.
47. Goulding, M. (2009). Circuits controlling vertebrate locomotion: moving in a new direction. *Nature Reviews Neuroscience*, *10*(7), 507-518.
48. Hägglund, M., Borgius, L., Dougherty, K. J., & Kiehn, O. (2010). Activation of groups of excitatory neurons in the mammalian spinal cord or hindbrain evokes locomotion. *Nature neuroscience*, *13*(2), 246-252.
49. Hägglund, M., Dougherty, K. J., Borgius, L., Itohara, S., Iwasato, T., & Kiehn, O. (2013). Optogenetic dissection reveals multiple rhythmogenic modules underlying locomotion. *Proceedings of the National Academy of Sciences*, *110*(28), 11589-11594.
50. Stuart, D. G., & Hultborn, H. (2008). Thomas Graham Brown (1882–1965), Anders Lundberg (1920–), and the neural control of stepping. *Brain research reviews*, *59*(1), 74-95.
51. Nielsen, J. B., & Sinkjaer, T. (2002). Afferent feedback in the control of human gait. *Journal of electromyography and kinesiology*, *12*(3), 213-217.

52. Prochazka, A. (2010). Proprioceptive feedback and movement regulation. *Comprehensive Physiology*.
53. Giuliani, C. A., & Smith, J. L. (1987). Stepping behaviors in chronic spinal cats with one hindlimb deafferented. *Journal of Neuroscience*, *7*(8), 2537-2546.
54. Goldberger, M. E. (1977). Locomotor recovery after unilateral hindlimb deafferentation in cats. *Brain research*, *123*(1), 59-74.
55. Ghez, C., Gordon, J., Ghilardi, M. F., Christakos, C. N., & Cooper, S. E. (1990, January). Roles of proprioceptive input in the programming of arm trajectories. In *Cold spring harbor symposia on quantitative biology* (Vol. 55, pp. 837-847). Cold Spring Harbor Laboratory Press.
56. Rothwell, J. C., Traub, M. M., Day, B. L., Obeso, J. A., Thomas, P. K., & Marsden, C. D. (1982). Manual motor performance in a deafferented man. *Brain*, *105*(3), 515-542.
57. Sanes, J. N., Mauritz, K. H., Dalakas, M. C., & Evarts, E. V. (1985). Motor control in humans with large-fiber sensory neuropathy. *Human neurobiology*, *4*(2), 101-114.
58. Giuliani, C. A., & Smith, J. L. (1985). Development and characteristics of airstepping in chronic spinal cats. *Journal of Neuroscience*, *5*(5), 1276-1282.
59. Forssberg, H., Grillner, S., Halbertsma, J., & Rossignol, S. (1980). The locomotion of the low spinal cat. II. Interlimb coordination. *Acta Physiologica*, *108*(3), 283-295.
60. Udo, M., Kamei, H., Matsukawa, K., & Tanaka, K. (1982). Interlimb coordination in cat locomotion investigated with perturbation. *Experimental brain research*, *46*(3), 438-447.
61. Grillner, S., & Wallen, P. (1985). Central pattern generators for locomotion, with special reference to vertebrates. *Annual review of neuroscience*, *8*(1), 233-261.
62. Armstrong, D. M. (1986). Supraspinal contributions to the initiation and control of locomotion in the cat. *Progress in neurobiology*, *26*(4), 273-361.
63. Hall, J. E. (2015). *Guyton and Hall Textbook of Medical Physiology E-Book*. Elsevier Health Sciences.
64. This book, particularly "Unit II: Excitation of Skeletal Muscle" was instrumental in writing sections 1.5.2 and 1.5.3.
65. Sanes J, Lichtman J. 1999. Development of the vertebrate neuromuscular junction. *Annu. Rev. Neurosci.* 22: 389-442
66. Carlson B. 1973. The Regeneration of Skeletal Muscle – A Review. *Am. J. Anat.* 137: 119-150
67. Schiaffino S, Reggiani C. 2011. Fiber types in mammalian skeletal muscles. *Physiol. Rev.* 91: 1447-1531
68. Beard, N. A., Sakowska, M. M., Dulhunty, A. F., & Laver, D. R. (2002). Calsequestrin is an inhibitor of skeletal muscle ryanodine receptor calcium release channels. *Biophysical journal*, *82*(1), 310-320.
69. Talbot, J., & Maves, L. (2016). Skeletal muscle fiber type: using insights from muscle developmental biology to dissect targets for susceptibility and resistance to muscle disease. *Wiley Interdisciplinary Reviews: Developmental Biology*, *5*(4), 518-534.
70. Pette, D., & Staron, R. S. (1990). Cellular and molecular diversities of mammalian skeletal muscle fibers. *Reviews of Physiology, Biochemistry and Pharmacology, Volume 116*, 1-76.

71. Schiaffino, S. T. E. F. A. N. O., & Reggiani, C. A. R. L. O. (1994). Myosin isoforms in mammalian skeletal muscle. *Journal of applied physiology*, *77*(2), 493-501.
72. Schiaffino, S., & Reggiani, C. (1996). Molecular diversity of myofibrillar proteins: gene regulation and functional significance. *Physiological reviews*, *76*(2), 371-423.
73. Pette, D., & Staron, R. S. (2000). Myosin isoforms, muscle fiber types, and transitions. *Microscopy research and technique*, *50*(6), 500-509.
74. Pette, D., & Staron, R. S. (1997). Mammalian skeletal muscle fiber type transitions. *International review of cytology*, *170*, 143-223.
75. Wylie, S. R., & Chantler, P. D. (2008). Myosin IIC: a third molecular motor driving neuronal dynamics. *Molecular biology of the cell*, *19*(9), 3956-3968.
76. Henneman E (1957) Relation between size of neurons and their sus- ceptibility to discharge. *Science* 126:1345–1347
77. Fedde MR, DeWet PD, Kitchell RL (1969). Motor unit recruitment pat- tern and tonic activity in respiratory muscles of Gallus domesticus. *J Neurophysiol* 32:995–1004
78. HoVer JA, Loeb GE, Marks WB, O'Donovan MJ, Pratt CA, Sugano N (1987). Cat hindlimb motoneurons during locomotion. I. Destination, axonal conduction velocity, and recruitment threshold. *J Neurophysiol* 57:510–529
79. Hogrel JY (2003) Use of surface EMG for studying motor unit recruitment during isometric linear force ramp. *J Electromyogr Kinesiol* 13:417–423
80. Milner-Brown HS, Stein RB, Yemm R (1973). The orderly recruitment of human motor units during voluntary isometric contractions. *J Physiol* 230:359–370
81. Tanji J, Kato M (1973). Recruitment of motor units in voluntary contraction of a finger muscle in man. E*xp Neurol* 40:759–770
82. Zajac FE, Faden JS (1985). Relationship among recruitment order, axonal conduction velocity and muscle-unit properties of type-identified motor units in cat plantaris muscle. *J Neurophysiol* 53:1303–1322
83. Gillespie CA, Simpson DR, Edgerton VR (1974). Motor unit recruitment as reflected by muscle fibre glycogen loss in a prosimian (bushbaby) after running and jumping. *J Neurol Neurosurg Psychiatry* 37:817–824
84. Von Tscharner V, Goepfert B (2006). Estimation of the interplay between groups of fast and slow muscle fibers of the tibialis anterior and gastrocnemius muscle while running. *J Electromyogr Kinesiol* 16:188–197
85. Wakeling JM, Rozitis AI (2004). Spectral properties of myoelectric signals from different motor units in the leg extensor muscles. *J Exp Biol* 207:2519–2528
86. Wakeling JM, Uehli K, Rozitis AI (2006). Muscle fibre recruitment can respond to the mechanics of the muscle contraction. *J R Soc Interface* 3:533–544
87. Hodson-Tole EF, Wakeling JM (2008). Motor unit recruitment patterns 2: the influence on myoelectric intensity and muscle fascicle strain rate. *J Exp Biol* 211:1893–1902
88. Dale HH, Feldberg W, Vogt M. 1936. Release of acetylcholine at voluntary motor nerve endings. *J. Physiol*. 86: 353–80
89. Katz B. 1966. *Nerve, Muscle and Synapse*. New York: McGraw-Hill
90. Duclert A, Changeux JP. 1995. Acetylcholine receptor gene expression at the developing neuromuscular junction. *Physiol. Rev*. 75: 339–68

91. Rao A, Kim E, Sheng M, Craig AM. 1998. Heterogeneity in the molecular composition of excitatory postsynaptic sites during development of hippocampal neurons in culture. *J. Neurosci.* 18: 1217–29
92. Couteaux R. 1973. Motor endplate structure. In *Structure and Function of Muscle*, Vol. 2, ed. GH Bourne, p. 483–530. New York
93. Grillner, S. in *Fundamental Neuroscience* (eds. Zigmond, M. J., Bloom, F. E., Landis, S. C., Roberts, J. L. & Squire, L. R.) 755–767 (Academic, San Diego, 2002). A general review of the motor system, from simple to complex.
94. Frank E, Jansen JKS, Lomo T, Westgaard R. 1975. The interaction between foreign and original motor nerves innervating the soleus muscle of rats. *J. Physiol.* 247: 725-743
95. Buchthal F, Schmalbruch H. 1980. Motor Unit of Mammalian Muscle. *Physiol. Rev.*60: 91-131
96. Sanes J, Lichtman J. 1999. Development of the vertebrate neuromuscular junction. *Annu. Rev. Neurosci.* 22: 389-442
97. Carlson B. 1973. The Regeneration of Skeletal Muscle – A Review. *Am. J. Anat.* 137: 119-150
98. Schiaffino S, Reggiani C. 2011. Fiber types in mammalian skeletal muscles. *Physiol. Rev.* 91: 1447-1531
99. Mirsky R, Jessen KR. 1996. Schwann cell development, differentiation and myelination. *Curr. Opin. Neurobiol.* 6: 89–96
100. Araque A, Parpura V, Sanzgiri RP, Haydon PG. 1999. Tripartite synapses: glia, the unacknowledged partner. *Trends in Neurosci*. 22: 208-214
101. Chow I, Poo MM. 1985. Release of acetyl- choline from embryonic neurons upon con- tact with muscle cell. *J. Neurosci.* 5:1076–82
102. Xie ZP, Poo MM. 1986. Initial events in the formation of neuromuscular synapse: rapid induction of acetylcholine release from embryonic neuron. *Proc. Natl. Acad. Sci.* USA 83:7069–73
103. Kelly AM, Zacks SI. 1969. The fine structure of motor endplate morphogenesis. *J. Cell Biol.* 42:154–69
104. Takahashi T, Nakajimi Y, Hirosawa K, Nakajimi S, Onodera K. 1987. Structure and physiology of developing neuromuscular synapses in culture. *J. Neurosci.* 7:473–81
105. Lupa MT, Hall ZW. 1989. Progressive restriction of synaptic vesicle protein to the nerve terminal during development of the neuro- muscular junction. *J. Neurosci.* 9:3937–45
106. Bennett MR, Pettigrew AG. 1976. The formation of neuromuscular synapses. *Cold Spring Harbor Symp. Quant. Biol.* 40: 409–24
107. Zhang M, McLennan IS. 1995. During secondary myotube formation, primary, myotubes preferentially absorb new nuclei at their ends. *Dev. Dynam.* 204: 168–77
108. Anderson MJ, Cohen MW. 1977. Nerve-induced and spontaneous redistribution of acetylcholine receptors on cultured muscle cells. *J. Physiol.* 268: 757–73
109. Frank E, Fischbach GD. 1979. Early events in neuromuscular junction formation *in vitro*: induction of acetylcholine receptor clusters in the postsynaptic membrane and morphology of newly formed synapses. *J. Cell Biol.* 83: 143–58

110. McMahan UJ. 1990. The agrin hypothesis. *Cold Spring Harbor Symp. Quant. Biol.* 55: 407–18
111. Reist NE, Werle MJ, McMahan UJ. 1992. Agrin released by motor neurons induces the aggregation of acetylcholine receptors at neuromuscular junctions. *Neuron.* 8: 865–68
112. Bernfield M, Gotte M, Park PW, Reizes O, Fitzgerald ML, Lincecum, Zako M. 1999. Functions of Cell Surface Heparan Sulfate Proteoglycans. *Ann. Rev. Biochem.* 68: 729-777
113. Bezakova G, Ruegg MA. 2003. New insights into the roles of agrin. *Nat. Rev. Mol. Cell Biol.* 4: 295-308
114. Sarrazin S, Lamanna WC, Esko JD. 2011. Heparan sulfate proteoglycans. *Cold Spring Harb Perspect Biol.* 3:
115. Gautam M, Noakes PG, Moscoso L, Rupp F, Scheller RH, *et al*. 1996. Defective neuromuscular synaptogenesis in agrin-deficient mutant mice. *Cell.* 85:525–35
116. Chang D, Woo JS, Campanelli J, Scheller RH, Ignatius MJ. 1997. Agrin inhibits neurite out- growth but promotes attachment of embryonic motor and sensory neurons. *Dev. Biol.* 181: 21–35
117. Jones G, Meier T, Lichtsteiner M, Witzemann V, Sakmann B, Brenner HR. 1997. Induction by agrin of ectopic and functional postsynaptic-like membrane in innervated muscle. *Proc. Natl. Acad. Sci.* 94: 2654–59
118. Cohen I, Rimer M, Lomo T, McMahan UJ. 1997. Agrin-induced postsynaptic-like apparatus in skeletal muscle fibers *in vivo*. *Mol. Cell. Neurosci.* 9: 237–53
119. Valenzuela DM, Stitt TN, DiStefano PS, Rojas E, Mattsson K, *et al*. 1995. Receptor tyrosine kinase specific for the skeletal muscle lineage: expression in embryonic muscle, at the neuromuscular junction, and after injury. *Neuron.* 15: 573–84
120. DeChiara TM, Bowen DC, Valenzuela DM, Simmons MV, Poueymirou WT, *et al*. 1996. The receptor tyrosine kinase MuSK is required for neuromuscular junction formation *in vivo*. *Cell*. 85: 501–12
121. Burden SJ, DePalma RL, Gottesman GS. 1983. Crosslinking of proteins in acetylcholine receptor-rich membranes: associated between the β-subunit and the 43 kD subsynaptic protein. *Cell.* 35: 687–92
122. Noakes PG, Phillips WD, Hanley TA, Sanes JR, Merlie JP. 1993. 43K protein and acetylcholine receptors colocalize during the initial stages of neuromuscular synapse formation *in vivo*. *Dev. Biol.* 155: 275–80
123. Gautam M, Noakes PG, Mudd J, Nichol M, Chu GC, *et al*. 1995. Failure of postsynaptic specialization to develop at neuromuscular junctions of rapsyn-deficient mice. *Nature.* 377: 232–36
124. Apel E, Glass DJ, Moscoso LM, Yancopoulos GD, Sanes JR. 1997. Rapsyn is required for MuSK signaling and recruits synaptic components to a MuSK-containing scaffold. *Neuron.* 18: 623–35
125. Merlie JP, Sanes JR. 1985. Concentration of acetylcholine receptor mRNA in synaptic regions of adult muscle fibers. *Nature.* 317: 66– 68
126. Simon AM, Hoope P, Burden SJ. 1992. Spatial restriction of AChR gene expression to subsynaptic nuclei. *Development.* 114: 545– 53

127. Duclert A, Changeux JP. 1995. Acetylcholine receptor gene expression at the developing neuromuscular junction. Physiol. Rev. 75: 339–68
128. Dai Z, Peng HB. 1996. From neurite to nerve terminal: induction of presynaptic differentiation by target-derived signals. *Semin. Neurosci.* 8:97–106
129. Fitzsimonds RM, Poo MM. 1998. Retrograde signaling in the development and modification of synapses. *Physiol. Rev.* 78: 143–70
130. Meier T, Masciulli F, Moore C, Schoumacher F, Eppenberger U, *et al*. 1998. Agrin can mediate acetylcholine receptor gene expression in muscle by aggregation of muscle-derived neuregulins. *J. Cell Biol.* 141: 715–26
131. Jones G, Herczeg A, Ruegg MA, Lichsteiner M, Kroger S, Brenner HR. 1996. Substrate-bound agrin induces expression of acetylcholine receptor ε-subunit gene in cultured mammalian muscle cells. *Proc. Natl. Acad. Sci.*
132. Riethmacher D, Sonnenbergriethmacher E, Brinkmann V, Yamaai T, Lewin GR, Birchmeier C. 1997. Severe neuropathies in mice with targeted mutations in the ERBB3 receptor. *Nature.* 389: 725–30
133. Balice-Gordon RJ, Lichtman JW. 1993. *In vivo* observations of pre-and postsynaptic changes during the transition from multiple to single innervation at developing neuromuscular junctions*. J. Neurosci.* 13: 834–55
134. Rosenthal JL, Taraskevich PS. 1977. Reduction of multiaxonal innervation at the neuromuscular junction of the rat during development. *J. Physiol*. 270: 299–310
135. Frank E, Gautvik K, Sommerschild H. 1976. Persistence of junctional acetylcholine receptors following denervation. *Cold Spring Har- bor Symp. Quant. Biol.* 40: 275–81
136. Riley DA. 1981. Ultrastructural evidence for axon retraction during the spontaneous elimination of polyneuronal innervation of the rat soleus muscle*. J. Neurocytol.* 10: 425–40
137. Gan W-B, Lichtman JW. 1998. Synaptic segregation at the developing neuromuscular junction. *Science.*
138. Balice-Gordon RJ, Thompson WJ. 1988. Synaptic rearrangements and alterations in motor unit properties in neonatal rat ex- tensor digitorum longus muscle. *J. Physiol.* 398: 191–210
139. Lichtman JW, Wilkinson RS, Rich MD. 1985. Multiple innervation of tonic endplates revealed by activity-dependent uptake of fluorescent probes. *Nature.* 314: 357–59
140. Thompson WJ. 1985. Activity and synapse elimination at the neuromuscular junction. *Cell. Mol. Neurobiol*. 5: 167–82
141. Balice-Gordon RJ, Lichtman JW. 1994. Long-term synapse loss induced by focal blockade of postsynaptic receptors. *Nature.* 372: 519– 24
142. Culican SM, Nelson CC, Lichtman JW. 1998. Axon withdrawal during synapse elimination at the neuromuscular junction is accompanied by disassembly of the postsynaptic specialization and withdrawal of Schwann cell processes*. J. Neurosci.* 18: 4953–65
143. Snider WD, Lichtman JW. 1996. Are neurotrophins synaptotrophins? *Mol. Cell. Neurosci.* 7: 433–42

144. Steinbach JH. 1981. Developmental changes in acetylcholine receptor aggregates at rat skeletal neuromuscular junctions. *Dev. Biol.* 84: 267–76
145. Slater CR. 1982. Postnatal maturation of nerve- muscle junctions in hindlimb muscles of the mouse. *Dev. Biol.* 94: 11–22
146. Boice R, Adams N. 1983. Degrees of captivity and aggressive behavior in domestic Norway rats. *Bull. Psychonom. Soc.* 21: 149-152.
147. Fertuck HC, Salpeter MM. 1974. Localization of acetycholine receptor by 125I-Labeled alpha-bungarotoxin binding at mouse motor endplates. *Proc. Nat. Acad. Sci.* 71: 1376-1378
148. Hirata K, Zhou C, Nakamura K, Kawabuchi M. 1997. Postnatal development of Schwann cells at neuromuscular junctions, with special reference to synapse elimination. *J. Neurocytol.* 26: 799–809
149. Trachtenberg JT, Thompson WJ. 1997. Nerve terminal withdrawal from rat neuromuscular junctions induced by neuregulin and Schwann cells. *J. Neurosci.* 17: 6243–55
150. Lichtman JW, Magrassi L, Purves D. 1987. Visualization of neuromuscular junctions over periods of several months in living mice. *J. Neurosci.* 7: 1215–22
151. Wigston DJ. 1990. Repeated *in vivo* visualization of neuromuscular junctions in adult mouse lateral gastrocnemius. *J. Neurosci*. 10: 1753–61
152. Frank E, Gautvik K, Sommerschild H. 1976. Persistence of junctional acetylcholine receptors following denervation. *Cold Spring Harbor Symp. Quant. Biol.* 40: 275–81
153. Courtney J, Steinbach JH. 1981. Age changes in neuromuscular junction morphology and acetylcholine receptor distribution on rat skeletal muscle fibers. *J. Physiol.* 320: 435– 47
154. Rosenheimer JL, Smith DO. 1985. Differential changes in the end-plate architecture of functionally diverse muscles during aging. *J. Neurophysiol*. 53: 1567–81
155. Ludatscher RM, Silbermann M, Gershon D, Reznick A. 1985. Evidence of Schwann cell degeneration in the aging mouse motor end- plate region. *Exp. Gerontol.* 20: 81–91
156. Boaro SN, Soares JC, Konig B. 1998. Comparative structural analysis of neuromuscular junctions in mice at different ages. *Ann. Anat.* 180: 173–79
157. Cajal S, Ramon Y. 1928. Reprinted 1991. *Degeneration and Regeneration of the Nervous System.* London: Oxford Univ. Press
158. Sanes JR, Marshall LM, McMahan UJ. 1978. Reinnervation of muscle fiber basal lamina after removal of myofibers. Differentiation of regenerating axons at original synaptic sites. *J. Cell Biol.* 78: 176–98
159. Son YJ, Thompson WJ. 1995. Schwann cell processes guide regeneration of peripheral axons. *Neuron.* 14: 125–32
160. Taniuchi M, Clark HB, Schweitzer JB, Johnson EM Jr. 1988. Expression of nerve growth factor receptors by Schwann cells of axotomized peripheral nerves: ultrastructural location, suppression by axonal contact, and binding properties. *J. Neurosci.* 8: 664–81
161. Plantinga LC, Verhaagen J, Edwards PM, Hol EM, Bar PR, Gispen WH. 1993. The expression of B-50/GAP-43 in Schwann cells is upregulated in degenerating peripheral nerve stumps following nerve injury. *Brain Res.* 602: 69–76

162. Unver, O., Uneri, A., Aydemir, A., & Sitti, M. (2006, May). Geckobot: a gecko inspired climbing robot using elastomer adhesives. In *Proceedings 2006 IEEE International Conference on Robotics and Automation, 2006. ICRA 2006.* (pp. 2329-2335). IEEE.
163. Umedachi, T., Vikas, V., & Trimmer, B. A. (2016). Softworms: the design and control of non-pneumatic, 3D-printed, deformable robots. *Bioinspiration & biomimetics*, *11*(2), 025001.
164. Cvetkovic, C., Raman, R., Chan, V., Williams, B. J., Tolish, M., Bajaj, P., ... & Bashir, R. (2014). Three-dimensionally printed biological machines powered by skeletal muscle. *Proceedings of the National Academy of Sciences*, *111*(28), 10125-10130.
165. Kovač, M. (2014). The bioinspiration design paradigm: A perspective for soft robotics. *Soft Robotics*, *1*(1), 28-37.
166. Bartlett, N. W., Tolley, M. T., Overvelde, J. T., Weaver, J. C., Mosadegh, B., Bertoldi, K., ... & Wood, R. J. (2015). A 3D-printed, functionally graded soft robot powered by combustion. *Science*, *349*(6244), 161-165.
167. Feinberg, A. W., Feigel, A., Shevkoplyas, S. S., Sheehy, S., Whitesides, G. M., & Parker, K. K. (2007). Muscular thin films for building actuators and powering devices. *Science*, *317*(5843), 1366-1370.
168. Wen, L., Wang, T., Wu, G., & Liang, J. (2012). Quantitative thrust efficiency of a self-propulsive robotic fish: Experimental method and hydrodynamic investigation. *IEEE/ASME Transactions on Mechatronics*, *18*(3), 1027-1038.
169. Low, K. H. (2007). Design, development and locomotion control of bio-fish robot with undulating anal fins. *International Journal of Robotics & Automation*, *22*(1), 88.
170. Herr, H., & Dennis, R. G. (2004). A swimming robot actuated by living muscle tissue. *Journal of neuroengineering and rehabilitation*, *1*(1), 6.
171. Nawroth, J. C., Lee, H., Feinberg, A. W., Ripplinger, C. M., McCain, M. L., Grosberg, A., ... & Parker, K. K. (2012). A tissue-engineered jellyfish with biomimetic propulsion. *Nature biotechnology*, *30*(8), 792.
172. Majidi, C. (2014). Soft robotics: a perspective—current trends and prospects for the future. *Soft Robotics*, *1*(1), 5-11.
173. Vincent, J. F., Bogatyreva, O. A., Bogatyrev, N. R., Bowyer, A., & Pahl, A. K. (2006). Biomimetics: its practice and theory. *Journal of the Royal Society Interface*, *3*(9), 471-482.
174. Full, R. J. (2001, October). Using biological inspiration to build artificial life that locomotes. In *International Symposium on Evolutionary Robotics* (pp. 110-120). Springer, Berlin, Heidelberg.
175. Ricotti, L., & Menciassi, A. (2012). Bio-hybrid muscle cell-based actuators. *Biomedical microdevices*, *14*(6), 987-998.
176. Kim, S., Laschi, C., & Trimmer, B. (2013). Soft robotics: a bioinspired evolution in robotics. *Trends in biotechnology*, *31*(5), 287-294.
177. Tadesse, Y., Wu, L., & Saharan, L. K. (2016). Musculoskeletal system for bio-inspired robotic systems. *Mechanical Engineering Magazine Select Articles*, *138*(03), S11-S16.

178. Bernabei R, Power J. On Three Categories of Conscious Machines. In: Lepora NF, Mura A, Mangan M, Verschure PFMJ, Desmulliez M, Prescott TJ (eds). *Biomimetic and Biohybrid Systems: Proceedings of the 5th International Conference, Living Machines 2016, Edinburgh, UK*. Springer International Publishing, 2016, pp 40–47.
179. Zolfagharian, A., Kouzani, A. Z., Khoo, S. Y., Gibson, I., & Kaynak, A. (2016, November). 3D printed hydrogel soft actuators. In *2016 IEEE Region 10 Conference (TENCON)* (pp. 2272-2277). IEEE.
180. Lee, C., Kim, M., Kim, Y. J., Hong, N., Ryu, S., Kim, H. J., & Kim, S. (2017). Soft robot review. *International Journal of Control, Automation and Systems*, *15*(1), 3-15.
181. Chan, V., Asada, H. H., & Bashir, R. (2014). Utilization and control of bioactuators across multiple length scales. *Lab on a Chip*, *14*(4), 653-670.
182. Burgert, I., & Fratzl, P. (2009). Actuation systems in plants as prototypes for bioinspired devices. *Philosophical Transactions of the Royal Society A: Mathematical, Physical and Engineering Sciences*, *367*(1893), 1541-1557.
183. Kabumoto, K. I., Hoshino, T., Akiyama, Y., & Morishima, K. (2013). Voluntary movement controlled by the surface EMG signal for tissue-engineered skeletal muscle on a gripping tool. *Tissue Engineering Part A*, *19*(15-16), 1695-1703.
184. Carlsen, R. W., & Sitti, M. (2014). Bio-hybrid cell-based actuators for microsystems. *Small*, *10*(19), 3831-3851.
185. Bowers, A. E., Rossiter, J. M., Walters, P. J., & Ieropoulos, I. A. (2011, March). Dielectric elastomer pump for artificial organisms. In *Electroactive Polymer Actuators and Devices (EAPAD) 2011* (Vol. 7976, p. 797629). International Society for Optics and Photonics.
186. Cho, K. J., & Wood, R. (2016). Biomimetic robots. In *Springer Handbook of Robotics* (pp. 543-574). Springer, Cham.
187. Li, Z., Seo, Y., Aydin, O., Elhebeary, M., Kamm, R. D., Kong, H., & Saif, M. T. A. (2019). Biohybrid valveless pump-bot powered by engineered skeletal muscle. *Proceedings of the National Academy of Sciences*, *116*(5), 1543-1548.
188. Kamm, R. D., & Bashir, R. (2014). Creating living cellular machines. *Annals of biomedical engineering*, *42*(2), 445-459.
189. Rus, D., & Tolley, M. T. (2015). Design, fabrication and control of soft robots. *Nature*, *521*(7553), 467-475.
190. Mosadegh, B., Polygerinos, P., Keplinger, C., Wennstedt, S., Shepherd, R. F., Gupta, U., ... & Whitesides, G. M. (2014). Pneumatic networks for soft robotics that actuate rapidly. *Advanced functional materials*, *24*(15), 2163-2170.
191. Wei, T., Stokes, A., & Webb, B. (2016, July). A soft pneumatic maggot robot. In *Conference on Biomimetic and Biohybrid Systems* (pp. 375-386). Springer, Cham.
192. Martinez, R. V., Branch, J. L., Fish, C. R., Jin, L., Shepherd, R. F., Nunes, R. M., ... & Whitesides, G. M. (2013). Robotic tentacles with three-dimensional mobility based on flexible elastomers. *Advanced materials*, *25*(2), 205-212.
193. Schulte HF. The Characteristics of the McKibben Artificial Muscle. In: *The Application of External Power in Prosthetics and Orthotics*. National Acadamey of Sciences-National Research Council: Washington DC, 1961, pp 94–102.

194. Caldwell, D. G., Tsagarakis, N., & Medrano-Cerda, G. A. (2000). Bio-mimetic actuators: polymeric pseudo muscular actuators and pneumatic muscle actuators for biological emulation. *Mechatronics*, *10*(4-5), 499-530.
195. Daerden, F., & Lefeber, D. (2002). Pneumatic artificial muscles: actuators for robotics and automation. *European journal of mechanical and environmental engineering*, *47*(1), 11-21.
196. Wirekoh, J., & Park, Y. L. (2017). Design of flat pneumatic artificial muscles. *Smart Materials and Structures*, *26*(3), 035009.
197. Shepherd, R. F., Ilievski, F., Choi, W., Morin, S. A., Stokes, A. A., Mazzeo, A. D., ... & Whitesides, G. M. (2011). Soft multigait robot. *Proceedings of the National Academy of Sciences of the USA*, *108*, 20400-20403.
198. Ilievski F, Mazzeo AD, Shepherd RF, Chen X, Whitesides GM. Soft robotics for chemists. *Angew Chemie - Int Ed* 2011; **50**: 1890–1895.
199. Suzumori K, Iikura S, Tanaka H. Applying a Flexible Microactuator to Robotic Mechanisms. *IEEE Control Syst* 1992; **February**: 21–27.
200. Shepherd, R. F., Stokes, A. A., Freake, J., Barber, J., Snyder, P. W., Mazzeo, A. D., ... & Whitesides, G. M. (2013). Using explosions to power a soft robot. *Angewandte Chemie International Edition*, *52*(10), 2892-2896.
201. Polygerinos, P., Wang, Z., Galloway, K. C., Wood, R. J., & Walsh, C. J. (2015). Soft robotic glove for combined assistance and at-home rehabilitation. *Robotics and Autonomous Systems*, *73*, 135-143.
202. Katzschmann, R. K., Marchese, A. D., & Rus, D. (2016). Hydraulic autonomous soft robotic fish for 3D swimming. In *Experimental Robotics* (pp. 405-420). Springer, Cham.
203. Gul, J. Z., Yang, B. S., Yang, Y. J., Chang, D. E., & Choi, K. H. (2016). In situ UV curable 3D printing of multi-material tri-legged soft bot with spider mimicked multi-step forward dynamic gait. *Smart Materials and Structures*, *25*(11), 115009.
204. Jin, H., Dong, E., Xu, M., Liu, C., Alici, G., & Jie, Y. (2016). Soft and smart modular structures actuated by shape memory alloy (SMA) wires as tentacles of soft robots. *Smart Materials and Structures*, *25*(8), 085026.
205. Haines, C. S., Lima, M. D., Li, N., Spinks, G. M., Foroughi, J., Madden, J. D., ... & Göktepe, Ö. (2014). Artificial muscles from fishing line and sewing thread. *science*, *343*(6173), 868-872.
206. Umedachi T, Vikas V, Trimmer BA. Softworms: the design and control of non-pneumatic, 3D-printed, deformable robots. *Bioinspir Biomim* 2016; **11**. doi:10.1088/1748-3190/11/2/025001.
207. Cvetkovic C, Raman R, Chan V, Williams BJ, Tolish M, Bajaj P *et al.* Three-dimensionally printed biological machines powered by skeletal muscle. *Proc Natl Acad Sci USA* 2014; **111**: 10125–10130.
208. Kovač M. The Bioinspiration Design Paradigm: A Perspective for Soft Robotics. *Soft Robot* 2013; **1**: 28–37.
209. Bartlett NW, Tolley MT, Overvelde JTB, Weaver JC, Mosadegh B, Bertoldi K *et al.* A 3D-printed, functionally graded soft robot powered by combustion. *Science (80-)* 2015; **349**: 161–165.

210. Feinberg AW, Feigel A, Shevkoplyas SS, Sheehy S, Whitesides GM, Parker KK. Muscular thin films for building actuators and powering devices. *Science (80-)* 2007; **317**: 1366–1370.
211. Wen L, Wang T, Wu G, Liang J. Quantitative thrust efficiency of a self-propulsive robotic fish: Experimental method and hydrodynamic investigation. *IEEE/ASME Trans Mechatronics* 2013; **18**: 1027–1038.
212. Low KH. Design, development and locomotion control of bio-fish robot with undulating anal fins. *Int J Robot Autom* 2007; **22**: 88–99.
213. Herr H, Dennis RG. A swimming robot actuated by living muscle tissue. *J Neuroeng Rehabil* 2004; **1**: 1–9.
214. Nawroth JC, Lee H, Feinberg AW, Ripplinger CM, McCain ML, Grosberg A *et al.* A tissue-engineered jellyfish with biomimetic propulsion. *Nat Biotechnol* 2012; **30**: 792–797.
215. Majidi C. Soft Robotics: A Perspective—Current Trends and Prospects for the Future. *Soft Robot* 2013; **1**: 5–11.
216. Vincent JF V, Bogatyreva OA, Bogatyrev NR, Bowyer A, Pahl A-K. Biomimetics: its practice and theory. *J R Soc Interface* 2006; **3**: 471–82.
217. Full RJ. Using Biological Inspiration to Build Artificial Life That Locomotes. *EvoWorkshops* 2001; **2217**: 110–120.
218. Ricotti L, Menciassi A. Bio-hybrid muscle cell-based actuators. *Biomed Microdevices* 2012; **14**: 987–998.
219. Kim S, Laschi C, Trimmer B. Soft robotics: a bioinspired evolution in robotics. *Trends Biotechnol* 2013; : 1–8.
220. Tadesse Y, Wu L, Saharan LK. Musculoskeletal System for Bio-Inspired Robotic Systems. *Focus Dyn Syst Control* 2016; : 11–17.
221. Bernabei R, Power J. On Three Categories of Conscious Machines. In: Lepora NF, Mura A, Mangan M, Verschure PFMJ, Desmulliez M, Prescott TJ (eds). *Biomimetic and Biohybrid Systems: Proceedings of the 5th International Conference, Living Machines 2016, Edinburgh, UK*. Springer International Publishing, 2016, pp 40–47.
222. Zolfagharian A, Kouzani AZ, Khoo SY, Gibson I, Kaynak A. 3D Printed Hydrogel Soft Actuators. In: *IEEE Region 10 Conference (TENCON)*. 2016, pp 2274–2279.
223. Lee C, Kim M, Kim YJ, Hong N, Ryu S, Kim HJ *et al.* Soft Robot Review. *Int J Control Autom Syst* 2017; **15**: 3–15.
224. Inoue D, Kabir AR, Sada K, Gong JP. Tissue Engineering Approach to Making Soft Actuators. 2014; : 475–487.
225. Chan V, Asada HH, Bashir R. Utilization and control of bioactuators across multiple length scales. *Lab Chip* 2014; **14**: 653–70.
226. Burgert I, Fratzl P. Actuation systems in plants as prototypes for bioinspired devices. *Philos Trans A Math Phys Eng Sci* 2009; **367**: 1541–57.
227. Kabumoto, K. I., Hoshino, T., Akiyama, Y., & Morishima, K. (2013). Voluntary movement controlled by the surface EMG signal for tissue-engineered skeletal muscle on a gripping tool. *Tissue Engineering Part A*, *19*(15-16), 1695-1703.
228. Carlsen RW, Sitti M. Bio-hybrid cell-based actuators for microsystems. *Small* 2014; **10**: 3831–51.

229. Bowers AE, Rossiter JM, Walters PJ, Ieropoulos IA. Dielectric elastomer pump for artificial organisms. *Proc SPIE* 2011; **7976**: 797629-797629–7.
230. Cho K-J, Wood R. Biomimetic Robots. In: *Springer Handbook of Robotics*. 2016, pp 543–574.
231. Kamm RD, Bashir R. Creating Living Cellular Machines. *Ann Biomed Eng* 2013; **42**: 445–59.
232. Rus D, Tolley MT. Design, fabrication and control of soft robots. *Nature* 2015; **521**: 467–475.
233. Mosadegh B, Polygerinos P, Keplinger C, Wennstedt S, Shepherd RF, Gupta U *et al.* Pneumatic networks for soft robotics that actuate rapidly. *Adv Funct Mater* 2014; **24**:
234. Wei T, Stokes A, Webb B. A Soft Pneumatic Maggot Robot. *Living Mach* 2016; **1**: 375–386.
235. Martinez R V., Branch JL, Fish CR, Jin L, Shepherd RF, Nunes RMD *et al.* Robotic tentacles with three-dimensional mobility based on flexible elastomers. *Adv Mater* 2013; **25**: 205–212.
236. Kim S, Laschi C, Trimmer B. Soft robotics: a bioinspired evolution in robotics. *Trends Biotechnol* 2013; : 1–8.
237. Schulte HF. The Characteristics of the McKibben Artificial Muscle. In: *The Application of External Power in Prosthetics and Orthotics*. National Acadamey of Sciences-National Research Council: Washington DC, 1961, pp 94–102.
238. Caldwell DG, Tsagarakis N, Medrano-Cerda GA. Bio-mimetic actuators: polymeric Pseudo Muscular Actuators and pneumatic Muscle Actuators for biological emulation. *Mechatronics* 2000; **10**: 499–530.
239. Daerden F, Lefeber D. Pneumatic artificial muscles: actuators for robotics and automation. *Eur J Mech Environ Eng* 2002; **47**: 11–21.
240. Wirekoh H, Park Y-L. Design of flat pneumatic artificial muscles. *Smart Mater Struct* 2017; **26**: 1–10.
241. Shepherd RF, Ilievski F, Choi W, Morin SA, Stokes AA, Mazzeo AD *et al.* Multigait soft robot. *Proc Natl Acad Sci U S A* 2011; **108**: 20400–20403.
242. Ilievski F, Mazzeo AD, Shepherd RF, Chen X, Whitesides GM. Soft robotics for chemists. *Angew Chemie - Int Ed* 2011; **50**: 1890–1895.
243. Suzumori K, Iikura S, Tanaka H. Applying a Flexible Microactuator to Robotic Mechanisms. *IEEE Control Syst* 1992; **February**: 21–27.
244. Shepherd, R. F., Stokes, A. A., Freake, J., Barber, J., Snyder, P. W., Mazzeo, A. D., ... & Whitesides, G. M. (2013). Using explosions to power a soft robot. *Angewandte Chemie International Edition*, *52*(10), 2892-2896.
245. Polygerinos P, Wang Z, Galloway KC, Wood RJ, Walsh CJ. Soft robotic glove for combined assistance and at-home rehabilitation. *Rob Auton Syst* 2015; **73**: 135–143.
246. Katzschmann RK, Marchese AD, Rus D. Hydraulic Autonomous Soft Robotic Fish for 3D Swimming. In: Kumar V, Khatib O, Hsieh MA (eds). *Experimental Robotics*. Springer Tracts in Advanced Robotics, 2000, pp 149–163.
247. Gui JZ, Yang B-S, Yang YJ, Chang DEE, Choi KH, Gul JZ *et al.* In situ UV curable 3D printing of multi-material tri-legged soft bot with spider mimicked multi- step forward dynamic gait. *Smart Mater Struct* 2016; **25**: 1–12.

248. Martinez R V., Branch JL, Fish CR, Jin L, Shepherd RF, Nunes RMD *et al.* Robotic tentacles with three-dimensional mobility based on flexible elastomers. *Adv Mater* 2013; **25**: 205–212.
249. Jin H, Dong E, Xu M, Liu C, Alici G, Jie Y. Soft and smart modular structures actuated by shape memory alloy (SMA) wires as tentacles of soft robots. *Smart Mater Struct* 2016; **25**: 85026.
250. Haines, C. S., Lima, M. D., Li, N., Spinks, G. M., Foroughi, J., Madden, J. D., ... & Göktepe, Ö. (2014). Artificial muscles from fishing line and sewing thread. *science*, *343*(6173), 868-872.
251. Tadesse Y, Wu L, Saharan LK. Musculoskeletal System for Bio-Inspired Robotic Systems. *Focus Dyn Syst Control* 2016; : 11–17.
252. Feinberg AW. Biological Soft Robotics. *Annu Rev Biomed Eng* 2015; **17**: 243–65.
253. Dennis RG, Herr H. Engineered muscle actuators: cells and tissues. In: Bar-Cohen Y (ed). *Biomimetics: Biologically Inspired Technologies*. CRC Press, 2005, pp 243–266.
254. Uzel SGM, Pavesi A, Kamm RD. Microfabrication and microfluidics for muscle tissue models. *Prog Biophys Mol Biol* 2014; **115**: 279–293.
255. Engler AJ, Griffin M a, Sen S, Bönnemann CG, Sweeney HL, Discher DE. Myotubes differentiate optimally on substrates with tissue-like stiffness: pathological implications for soft or stiff microenvironments. *J Cell Biol* 2004; **166**: 877–87.
256. Arcaute K, Mann BK, Wicker RB. Practical Use of Hydrogels in Stereolithography for Tissue Engineering Applications. In: Bártolo PJ (ed). *Stereolithography: Materials, Processes and Applications*. Springer US: Boston, MA, 2011, pp 299–331.
257. Knoblauch M, Peters WS. Biomimetic actuators: Where technology and cell biology merge. *Cell Mol Life Sci* 2004; **61**: 2497–2509.
258. Stanton MM, Park B-W, Miguel-López A, Ma X, Sitti M, Sánchez S. Biohybrid Microtube Swimmers Driven by Single Captured Bacteria. *Small* 2017; : 1603679.
259. Akiyama Y, Hoshino T, Iwabuchi K, Morishima K. Room temperature operable autonomously moving bio-microrobot powered by insect dorsal vessel tissue. *PLoS One* 2012; **7**: e38274.
260. Goebel R, Wahlster W. Aplysia Californica as a Novel Source of Material for Biohybrid Robots and Organic Machines. 2015; **1**: 268–279.
261. Hinds S, Bian W, Dennis RG, Bursac N. The role of extracellular matrix composition in structure and function of bioengineered skeletal muscle. *Biomaterials* 2011; **32**: 3575–3583.
262. Dennis RG, Kosnik PE. Excitability and isometric contractile properties of mammalian skeletal muscle constructs engineered *in vitro*. *Vitr Cell Dev Biol - Anim* 2000; **36**: 327–335.
263. Duan B, Hockaday LA, Kang KH, Butcher JT. 3D Bioprinting of heterogeneous aortic valve conduits with alginate / gelatin hydrogels. *J Biomed Mater Res Part A* 2012; : 1–10.
264. Choi, S. W., Yeh, Y. C., Zhang, Y., Sung, H. W., & Xia, Y. (2010). Uniform beads with controllable pore sizes for biomedical applications. *Small*, *6*(14), 1492-1498.
265. Mudera, V., Smith, A. S. T., Brady, M. A., & Lewis, M. P. (2010). The effect of cell density on the maturation and contractile ability of muscle derived cells in a 3D tissue-

engineered skeletal muscle model and determination of the cellular and mechanical stimuli required for the synthesis of a postural phenotype. *Journal of cellular physiology*, *225*(3), 646-653.

266. Gieseck III, R. L., Hannan, N. R., Bort, R., Hanley, N. A., Drake, R. A., Cameron, G. W., ... & Vallier, L. (2014). Maturation of induced pluripotent stem cell derived hepatocytes by 3D-culture. *PloS one*, *9*(1), e86372.
267. Bi, Y. A., Kazolias, D., & Duignan, D. B. (2006). Use of cryopreserved human hepatocytes in sandwich culture to measure hepatobiliary transport. *Drug Metabolism and Disposition*, *34*(9), 1658-1665.
268. Chaubey, A., Ross, K. J., Leadbetter, R. M., & Burg, K. J. (2008). Surface patterning: tool to modulate stem cell differentiation in an adipose system. *Journal of Biomedical Materials Research Part B: Applied Biomaterials*, *84*(1), 70-78.
269. Lee, M. K., Rich, M. H., Baek, K., Lee, J., & Kong, H. (2015). Bioinspired tuning of hydrogel permeability-rigidity dependency for 3D cell culture. *Scientific reports*, *5*, 8948.
270. Lewis, M. R. (1915). Rhythmical contraction of the skeletal muscle tissue observed in tissue cultures. *American Journal of Physiology-Legacy Content*, *38*(1), 153-161.
271. Langelaan, M. L., Boonen, K. J., Rosaria-Chak, K. Y., van der Schaft, D. W., Post, M. J., & Baaijens, F. P. (2011). Advanced maturation by electrical stimulation: Differences in response between C2C12 and primary muscle progenitor cells. *Journal of tissue engineering and regenerative medicine*, *5*(7), 529-539.
272. Grabowska, I., Szeliga, A., Moraczewski, J., Czaplicka, I., & Brzóska, E. (2011). Comparison of satellite cell-derived myoblasts and C2C12 differentiation in two-and three-dimensional cultures: changes in adhesion protein expression. *Cell biology international*, *35*(2), 125-133.
273. Park J, Ryu J, Choi SK, Seo E, Cha JM, Ryu S *et al.* Real-time measurement of the contractile forces of self-organized cardiomyocytes on hybrid biopolymer microcantilevers. *Anal Chem* 2005; **77**: 6571–6580.
274. Kim J, Park J, Yang S, Baek J, Kim B, Lee SH *et al.* Establishment of a fabrication method for a long-term actuated hybrid cell robot. *Lab Chip* 2007; **7**: 1504–1508.
275. Williams BJ, Anand S V, Rajagopalan J, Saif MTA. A self-propelled biohybrid swimmer at low Reynolds number. *Nat Commun* 2014; **5**: 3081.
276. Chan V, Jeong JH, Bajaj P, Collens MB, Saif T, Kong H *et al.* Multi-material bio-fabrication of hydrogel cantilevers and actuators with stereolithography. *Lab Chip* 2012; **12**: 88–98.
277. Chan V, Park K, Collens MB, Kong H, Saif TA, Bashir R. Development of miniaturized walking biological machines. *Sci Rep* 2012; **2**: 1–8.
278. Chan V, Asada HH, Bashir R. Utilization and control of bioactuators across multiple length scales. *Lab Chip* 2014; **14**: 653–70.
279. Raman R, Cvetkovic C, Uzel SGM, Platt RJ, Sengupta P, Kamm RD. Optogenetic skeletal muscle-powered adaptive biological machines. *Proc Natl Acad Sci* 2016. doi:10.1073/pnas.1516139113.

280. Uzel SGM, Platt RJ, Subramanian V, Pearl TM, Rowlands CJ, Chan V *et al.* Microfluidic device for the formation of optically excitable, three-dimensional, compartmentalized motor units. *Sci Adv* 2016; **2**: e1501429.
281. Cvetkovic C, Rich MH, Raman R, Kong H, Bashir R. A 3D-printed platform for modular neuromuscular motor units. *Microsystems Nanoeng* 2017; **3**. doi:10.1038/micronano.2017.15.
282. Aydin, O., Zhang, X., Nuethong, S., Pagan-Diaz, G. J., Bashir, R., Gazzola, M., & Saif, M. T. A. (2019). Neuromuscular actuation of biohybrid motile bots. *Proceedings of the National Academy of Sciences*, *116*(40), 19841-19847.
283. Raman R, Cvetkovic C, Bashir R. A modular approach to the design, fabrication, and characterization of muscle-powered biological machines. *Nat Protoc* 2017; **12**: 519–533.
284. Sakar MS, Neal D, Boudou T, Borochin MA, Li Y, Weiss R *et al.* Formation and optogenetic control of engineered 3D skeletal muscle bioactuators. *Lab Chip* 2012; **12**: 4976–4985.
285. Jung Y, Bae J. A Six-Legged Walking Robot Bio-Inspired Walking Pattern : Kinematic Analysis. 2013; : 257–264.
286. Wirekoh H, Park Y-L. Design of flat pneumatic artificial muscles. *Smart Mater Struct* 2017; **26**: 1–10.
287. Zhao H, O'Brien K, Li S, Shepherd RF, O 'brien K, Li S *et al.* Optoelectronically innervated soft prosthetic hand via stretchable optical waveguides. *Sci Robot* 2016; **7529**: eaai7529.
288. Kim J, Kim HN, Lang Y, Pandit A. Biologically Inspired Micro- and Nanoengineering Systems for Functional and Complex Tissues. *Tissue Eng Part A* 2014; **19**: 1–4.
289. Rossiter J, Walters P, Stoimenov B. Printing 3D dielectric elastomer actuators for soft robotics. In: Bar-Cohen Y, Wallmersperger T (eds). *Electroactive Polymer Actuators and Devices (EAPAD) 2009*. SPIE, 2009 doi:10.1117/12.815746.
290. McComas, A. J., Kereshi, S., & Manzano, G. (1984). Multiple innervation of human muscle fibers. *Journal of the neurological sciences*, *64*(1), 55-64.

CHAPTER 2. EFFECT OF ORGANOTYPIC CELL CULTURE ON SPINAL CORD GROWTH AND ELECTROPHYSIOLOGY

2.1 Introduction

Over 100 years ago, Thomas Graham Brown first discovered that the rhythms and patterns of locomotion were governed by the spinal cord in cats and this finding has been confirmed in all tested vertebrates (Brown, 1911; Grillner, 1981). Research has shown that these oscillatory periodic circuits, called central pattern generators (CPGs) are present in animals from birth (Cazalets *et al*, 1995). CPGs are complex neural circuits that produce self-sustained patterns without requiring sensory input, though they can be modulated by such inputs (Grillner, 1986; Anderson and Grillner 1983; Pearson and Rossignol 1991). Pattern-generating circuits are commonly believed to be used for left-right and flexor-extensor coordination in locomotion. There is also another type of oscillatory circuit within the spinal cord responsible for setting the speed of locomotion known as rhythm generators; these different types of circuits work together to specify gait (reviewed by Kiehn, 2006). The majority of early work on CPGs was done in lamprey, fish, and invertebrates (Grillner, 1975; Poon, 1980; Grillner and Wallen, 1985; Poon 1980; Cohen and Wallen, 1978; Coehn and Wallen 1980; Skinner *et al*, 1997; Yu *et al*, 1999; Buschges *et al*, 1995). The data collected on invertebrates and other lower vertebrates (e.g., Xenopus tadpoles, lamprey) might not translate well to mammalian locomotion however since the researched locomotor behavior studied is swimming as opposed to multi-limbed gait. These swimming behaviors result from the longitudinal transmission of a metachronal wave, which is transmitted through a multisegmented system and is unlike anything observed in land mammals (Kahn and Roberts, 19X2; Cohen, 1987; Grillner and Matsushima, 1991; Tunstall and Sillar, 1993). Despite the large amount of research fully and directly characterizing the pattern generating circuits of invertebrates, nothing of comparable depth has been done with mammals – especially humans (Dietz, 2003). The majority of early mammalian central pattern generator findings came from observing how spinal injuries to cats and dogs affected their locomotive gaits and relatively less has been done on rodent locomotion (Duysens and Van de Crommert, 1998; Cruse and Warnecke, 1992; Grillner and Zangger, 1979; Naito *et al*, 1990).

The best way of demonstrating the existence of pattern-generating networks is to directly remove the nervous system from the animal and record the activity in these isolated conditions (Cazalet *et al*, 1995). Although this has been achieved in many preparations from invertebrates and lower vertebrates (Kristan and Calabrese, 1976; Sillar and Skorupski1986; Chrachri and Clarac, 1990; Cohen and Wallen, 1978; Grillner *et al*, 1981; Roberts *et al*, 1983), locomotor-like activity was only quite recently recorded in mammals in an *in-vitro* isolated spinal cord preparation (Kudo and Yamada, 1987; Smith *et al*, 1987; Cazalets *et al*, 1990, 1992). It was not until 1995 that Cazalets *et al* were able to conclude that, in the rat, the spinal network producing rhythmic activity is located between segments T13 and L2, while the lower lumbar segments (L3-L5), which contain most of the motor neurons innervating the hindlimbs, do not have a significant role in rhythm genesis (Cazalets *et al*, 1995).

More recently, it has been discovered that commissural neurons (CNs), interneurons that project laterally across midline of the spinal cord, are primarily responsible for driving left-right and flexor-extensor pattern generation. The V0 sub-population of CNs make up the majority of CNs in the spinal cord and are characterized by early expression of the transcription factor DBX1 (Lanuza *et al*, 2004; Pierani *et al*, 2001). The V0 CNs are subdivided into inhibitory ($V0_D$) and excitatory ($V0_V$) populations based on transcriptional markers expressed later in development (Lanuza *et al*, 2004). Genetic ablation of all V0 neurons completely abolished left-right alternating locomotive gaits like walking, but not synchronous gaits like bounding (Kiehn, 2016; Talpalar *et al*, 2013). Similar ablation and transcriptome studies have determined that CNs are not necessary for rhythm generation (Borowska *et al*, 2013; Zhang *et al*, 2008; Grillner and Jessell, 2009; Roberts *et al*, 2008; Goulding, 2009). This work laid the groundwork for the growing consensus that mammalian CPGs do not follow the same half-center oscillator model as their invertebrate counterparts.

Researchers have also used optogenetic mouse models to control the activity of specific populations of excitatory neurons within the spinal cord (Hägglund *et al*, 2010; Hägglund *et al*, 2013). Optogenetic activation of excitatory neurons initiates locomotor-like activity, whereas inhibition blocks it. This provides evidence that excitatory neurons are both sufficient and necessary for rhythm generation in the mammalian spinal cord. Optogenetic manipulation of the

spinal cord has also provided new data which rejects the classic hypothesis of a half-center oscillator as fundamental to rhythm generation (Stuart and Hultborn, 2008). Regionally specific excitation of spinal cord neurons results in rhythmic output that is limited to only flexor-related or extensor-related motor neurons (Hägglund *et al*, 2010). This evidence implies that the rhythm-generating circuits in rat are comprised of several rhythm-generating modules that are arranged structurally near the motor neurons they specifically control. It has been concluded that, in the cat, the bursting capacity is distributed along the spinal cord (Deliagnia *et al*, 1983). However, researchers have been unsuccessful so far in determining the molecular and transcriptional identity of these subpopulations.

Traditionally, studies of spinal cord CPGs are performed *in vivo* or immediately after dissection (Skinner *et al*, 1997; Yu *et al*, 1999; Busetto *et al*, 2000; Pearson, 1995; Brownstone and Wilson, 2008; Rybak *et al*, 2015). Motor patterns in acute spinal cord recordings are comparable in terms of both periodic and phasic relationships to those observed in newborn and adult animals (Cazalets *et al*. 1990). Because of its small size, the spinal cord can survive *in vitro* for several hours under the proper conditions (Cazalets *et al*, 1995). Additionally, the action of neurotransmitters or pharmaceuticals can be directly studied because of the lack of a blood-brain barrier which provides easy access to neuronal components.

There is no prior work that has performed organotypic 2.5-D cultures of an intact spinal cord and assessed its electrical activity over time. Previous studies on organotypic slice cultures of the hippocampus, visual cortex, and subthalamic nuclei have demonstrated minimal differences between *in-situ* electrophysiology and organotypic cultures, but it is unknown how spinal cord circuits will behave in such a culture environment (Muller *et al*, 1993; Uesaka *et al*, 2005; Rohrbacher *et al*, 2000). By comparing the degree of long-term potentiation (LTP) at the CA3-CA1 junction between 2-day old pups plus 10 DIV and 8-day old pups plus 4 DIV to 12-day old pups, researchers have shown that development proceeds in hippocampal slice cultures with a comparable time course to *in situ* (Muller *et al*, 1993). Organotypic cultures from the rat visual cortex similarly time-matched *in vivo* development in terms of axonal branching and electrophysiological recordings on a MEA (Uesaka *et al*, 2005). Even more complex cultures that involve organotypic slices of three different brain regions – the substantia nigra, tegmental

pedunculopontine nucleus, and the subthalamic nucleus – demonstrate that the morphological and electrophysiological characteristics are generally similar to those reported in in vitro slice and in vivo studies (Rohrbacher *et al*, 2000).

The culture of intact lumbar spinal cords will allow for greater accessibility and more in-depth measurements of the complex circuitry that underlies mammalian locomotion. Here, we investigate how spinal cords react to culture conditions over a 2-week period at cellular, histological, and electrophysiological levels. Immunohistochemistry of cleared whole spinal cords and of lumbar cross-sections revealed the presence of interneurons, motor neurons, astrocytes, and Schwann cells which are associated with central pattern generator activity and motor outputs. When cultured on Matrigel-coated glass, spinal cords produce a complex arbor of motor neurons and astrocytes that extends over a 1 mm away from the spinal cord. These outgrowths do not exhibit electrical activity immediately, but electrical activity is detectable as the processes mature by 7 DIV. Acute lumbar spinal cord recordings demonstrate both spontaneous and stimulated activity in response to glutamate. Pin electrode recordings from lumbar spinal cords cultured for one week demonstrate infrequent spontaneous activity and a slightly reduced sensitivity to glutamate stimulation compared to acute conditions. Recordings from lumbar spinal cords cultured for two weeks exhibit very little spontaneous activity and only respond to a high dose of glutamate. By 14 DIV, spinal cords do not exhibit spontaneous firing at baseline or respond to a low dose of glutamate. However, a high dose of glutamate initiates robust electrical activity with a clear bursting pattern indicative of a pattern generating circuit. Overall, these data are the first to demonstrate that spinal cords extend a complex, multicellular arbor of motor neurons and glia and that they retain the ability to generate robust electrical potentials for up to two weeks *in vitro*.

2.2 Materials and Methods

2.2.1 Animal Welfare

Animal procedures were developed in accordance with Public Health Service Policy on Humane Care and Use of Laboratory Animals and reviewed and approved by the University of Illinois at Urbana-Champaign Institutional Animal Care and Use Committee. Rat spinal cords were

isolated from postnatal day 3-5 Long-Evans BluGill rats from an inbred colony maintained by our laboratory, according to previously established protocols (Millet *et al*, 2007).

2.2.2 Spinal Cord Extraction and Seeding for 2.5-D Culture

A 35 mm Petri dish with a 14 mm glass coverslip bottom (MatTek Corporation, Ashland, MA) was coated for a minimum of 1 h in 0.1% gelatin (EMD Millipore, Burlington, MA). The gelatin was rinsed 3-5 times with sterile PBS, followed by the addition of 100 µL of 1% Matrigel onto each glass coverslip. The Petri dishes were then placed in the incubator for 60-90 mins to allow for Matrigel polymerization. For each dish, a single BluGill rat pup between postnatal day 1-5 (P1-P5) was decapitated. The vertebral column was rapidly dissected from the pup and cleaned to expose the vertebrae. A small section of the spinal column from the T13 to L2 vertebrae was isolated using a pair of small scissors. Then, making two diagonal cuts at ± 45 degrees from the ventral midline, the ventral bone was removed thereby exposing the spinal cord. The spinal cord was then rapidly and gently dissected with a pair of fine-tipped tweezers.

The spinal cord was placed on ice in 5 mL HibernateA (Life Technologies, Gaithersburg, MD) where the dorsal root ganglia were removed. The spinal cord was moved to a laminar flow hood where it was rinsed in fresh HibernateA. Using forceps, the spinal cord was seeded with the ventral side facing down directly onto the polymerized Matrigel. The spinal cords were placed back in the incubator for 45 mins to allow the spinal cord to settle before adding 5 mL Spinal Cord Growth Medium (SCGM) consisting of 96.825% NeurobasalA (Life Technologies) without L-glutamine or phenol red (Life Technologies), 2% GS21 (MTI-GlobalStem, Gaithersburg, MD), 1% penicillin-streptomycin (Cellgro Mediatech, Inc., Herndon, VA), 0.125% Glutamax (Life Technologies), 0.025% Brain Derived Neurotrophic Factor (10 ng/mL, EMD Millipore), and 0.025% Nerve Growth Factor (1 ng/mL, EMD Millipore). All cells were maintained at 37 °C and 5% CO2. The first media change was a full media replacement 24 h after seeding, with half media replacement every 2-4 days following the first one. The full media change was implemented to remove any released apoptotic factors and from cells that did not survive immediately following seeding. Subsequent half media changes were meant to maintain the presence of beneficial secreted extracellular cues while still providing a fresh source of nutrients.

2.2.3 Immunofluorescence and Histology

Tissues were rinsed in PBS and fixed in 4% (vol/vol) paraformaldehyde. Prior to immunostaining, tissues were permeabilized with 0.3% (vol/vol) Triton X-100 (EMD Millipore) and blocked with 5% Normal Goat Serum (NGS, Abcam, Cambridge, UK) for 60 min. Tissues were incubated with alpha-actinin (1:2000, Abcam), Beta-III Tubulin (1:2000, Abcam), conjugated alpha bungarotoxin (1:1000, EMD Millipore), myelin protein zero (1:2000, Abcam), and glial fibrillary acidic protein (1:20000, Abcam) antibodies for 48 h at 4^{o} C and washed with PBS. Tissues were incubated with Alexa Fluor 488 goat anti-mouse IgG, Alexa Fluor 568 goat anti-chicken IgG, and Alexa Fluor 647 goat anti-rabbit IgG secondary antibodies (1:1000, Invitrogen, Walktam, MA) in PBS for 2 h at room temperature in the dark.

2.2.4 Clear Lipid-exchanged Acrylamide-hybridized Rigid Imaging Tissue-hYdrogel (CLARITY)

Prior to clearing, tissues were rinsed in PBS and fixed in 4% (vol/vol) paraformaldehyde. The tissues were submerged in a hydrogel monomer solution (composition of 400 mL: 210 mL dH_2O, 100 mL 16% paraformaldehyde, 40 mL 40% acrylamide, 40 mL 10X PBS, 10 mL 2% Bis, 1 g VA-044 initiator, 200 mg saponin, stored in 40 mL aliquots at -20° C) and de-gassed in a desiccation chamber to replace all gas in the tube with nitrogen. The solution (with the sample inside) was submerged in a 37° C water bath for 3 hours, or until the solution polymerized. The embedded sample was extracted from the gel and extra gel pieces were removed with gloved fingers. The sample was then submerged in 50 mL passive clearing solution (composition of 10 L: 10 L dH_2O, 123.66 g boric acid, 400 g sodium dodecyl sulfate, adjusted to pH 8.5) and gently shaken for 24 h at room temperature. Sample was then transferred to a fresh 50 mL of passive clearing solution and submerged for 24 h in a water bath at 37° C. Replace clearing solution every 24 h, alternating between room temperature and 37° C until sample was sufficiently cleared.

2.2.5 Spinal Cord Electrophysiology

Each neonatal spinal cord was extracted as described above. The isolated spinal cord was submerged in physiological saline (composition in mM: NaCl, 129; KCl, 4; $CaCl_2$, 2.5; $MgCl_2$, 1.14; NaH_2PO_4, 0.5; $NaHCO_3$, 25, glucose, 10, adjusted to pH = 7.4 with HCl) that was constantly superfused with oxygen (95% O_2/5% CO_2) before recording. The bath temperature was kept

constant at 24° C. Locomotor-like activity was induced by bath applying glutamate (10 mM stock, frozen, and stored at -20^{o} C). Neurons in the ventral horns were recorded with inspect pin electrodes connected to a differential A/C amplifier (Model1700, A-M Systems, Sequim, WA) and a data acquisition system (PowerLab 8/30, ADInstruments, Dunedin, New Zealand). The tissues were allowed to rest on the recording rig for 25-30 mins before recording began. Records were digitized and recorded in LabChart 7.3 (ADInstruments) at a sampling rate of 20 kHz.

2.3 Results

2.3.1 Histology and cell characterization of a rat spinal cord

The structure of mammalian locomotor CPGs is largely unknown (Kiehn, 2006), but recent breakthroughs in microscopy techniques have enabled researchers to image ever larger and optically dense tissues. The first and second lumbar (L1-L2) vertebrae of neonatal (P1-5) rat spinal cord (SC) were selected because an intact SC is approximately 23.5 mm in length (Fig. 2.1a) and 1.5 mm in diameter, over 4-fold longer than the average inchworm biobot skeleton (Fig. 4.1). Previous work had also shown that this was the localization of the hindlimb locomotor CPG (Cazalets *et al*, 1993). In order to view the internal structures of an intact rat spinal cord, the tissue needed to undergo a passive clearing process (Fig. 2.1b). The thickness of the tissue prevented either the light or the antibodies from fully penetrating the interior of the spinal cord (Fig. 2.1a,c), but the multicellular complexity of the spinal cord is apparent (Fig. 2.1c,d). Schwann cells (MPZ) and astrocytes (GFAP) encase the spinal cord in a protective sheath and Schwann cells are observed surrounding bundles of neural projections (Tuj1) out of the spinal cord (Fig. 2.1d). Deep to the protective glial sheath, there is also a complex, 3D web of astrocytes which are known to play integral and wide-ranging functions within the CNS. Figure 2.1e shows a spinal cord cross-section with a simplified diagram of a locomotor central pattern generator. In vertebrates, the motor neurons of the ventral horn serve as CPG outputs that innervate and control muscle contraction (Fig. 2.1e). The motor neurons of the ventral horn (Fig. 2.1e,f) are responsible for driving the muscle contraction outputs of spinal cord activity.

2.3.2 Neonatal rat spinal cords extend a robust arbor of glia and cholinergic neurons *in vitro*

To determine how a spinal cord explant responds to being cultured on Matrigel-coated glass, we isolated and cultured a segment of neonatal SC from within the L1-L2 vertebrae. When cultured on Matrigel-coated glass, the spinal cord extended robust process outgrowths (Fig. 2.2b,c,d,f). In all cases, the spinal cord was cultured ventral side down with the goal of inducing the motor neurons of the ventral horn (Fig. 2.1f) to extend out of the spinal cord. First, we measured the maximum distance outgrowths extended from the spinal cord in a 2.5-D organotypic monoculture at 1, 7, 14, and 21 DIV (Fig. 2.2a-c). The cultured spinal cords rapidly extended outgrowths up to 504 µm even by 1 DIV (Fig. 2.2d). This explosive growth continued past 1.18 mm by 7 DIV before reaching a peak of 1.6 mm at 14 DIV (Fig. 2.2d). The outgrowths began to slightly retract in length by 21 DIV to 1.49 mm (Fig. 2.2d). This complex arbor of extensions was composed of many cell types, including not only neurons but also glia (Fig. 2.1e), which are important for the formation and maintenance of functional synapses (Volterra *et al*, 2002). Of the neuronal processes that extended by 7 DIV, a large majority expressed choline acetyltransferase (ChAT), an enzyme found exclusively in ACh-producing neurons (Fig. 2.1f). Additionally, electrophysiological recordings reveal that cultured spinal cords produce electrical activity both spontaneously and when stimulated with glutamate (Figures 2.4-2.7). Thus, spinal cords extend a robust arbor of electrically active, cholinergic neurons that are likely to be motor neurons due to their location within the spinal cord, as well as the robust presence of ChAT. This confirms that a spinal cord explant can serve as a viable system for muscular interaction and control.

2.3.3 Electrical activity in cultured spinal cord outgrowths is not detected before 7 DIV

To generate synchronous contractions of muscle tissues, we needed to determine whether the pattern generating circuit within the spinal cord is altered by long-term culture. First, we isolated and cultured intact segments of lumbar spinal cord from neonatal rats on a Matrigel-coated substrate and electrical potentials were recorded at 0, 4, 7, and 10 DIV. At each time point, spontaneous and elicited firings were recorded in 30 second batches. In preparation for seeding, each MEA was prepared according to the protocol previously established in Chapter 2

for spinal cord culture on glass. Each MEA has 64 nodes (60 electrodes, 4 grounds) arranged in an 8 x 8 grid (Fig. 2.3a). The spinal cord was seeded with its ventral side adjacent to the electrodes (Fig. 2.3b), and cultured for 0, 4, or 7 days. Culture of a spinal cord on an MEA results in outgrowths that approach the electrodes on both sides of the spinal cord. By 4 DIV, some outgrowths have reached the electrodes (Fig. 2.3c), but the MEA was unable to pick up any signal. By 7 DIV, we began to see spontaneous bursts of action potentials in the cultures over several minutes (Fig. 2.3e). The raw data shows a burst-like firing pattern in these spontaneous recordings (Fig. 2.3f), indicative of healthy neuronal circuitry. The consistent size and shape of the action potentials registered by a single electrode (Fig. 2.3g) is representative of normal neural firing in healthy and electrically active outgrowths. One downside to using an MEA is that we need to wait for these outgrowths to extend out of the spinal cord and begin exhibiting electrical activity.

2.3.4 Acute lumbar spinal cords spontaneously express electrical activity which is altered by the application of neurotransmitters

To produce patterned muscle contractions, we first must demonstrate an intact pattern generating circuit and determine how it changes its behavior *in vitro*. We isolated an upper lumbar segment of neonatal rat spinal and immediately transferred it to the electrophysiological recording apparatus. Acute lumbar spinal cord recordings demonstrate that spinal cord neurons are highly active at baseline (Fig. 2.4a). When a single dose of glutamate (10 µM) is applied, the firing pattern of the spinal cord is altered (Fig. 2.4b). The firing increases in frequency and distinct burst-like patterns of activity are observed (Fig. 2.4b). After multiple doses of glutamate (final concentration 100 µM) are applied, the spinal cord exhibits robust action potentials similar to the 10 µM glutamate condition (Fig. 2.4c). The simultaneous application of glutamate (100 µM) and 5-HT (100 µM) elicits burst firing activity (Fig. 2.4d). Upon washing out the glutamate (5 full replacement washes), activity is reduced below what is observed at baseline, but can still be observed (Fig. 2.4e).

2.3.5 After one week, cultured spinal cords demonstrate infrequent spontaneous activity and a slightly reduced sensitivity to glutamate stimulation

There are no prior studies that have assessed the electrical activity of organotypic 2.5-D cultures of intact spinal cords. Recordings from neonatal L1-L2 spinal cord segments cultured for one week demonstrate infrequent spontaneous activity at baseline (Fig. 2.5a). Spinal cord activity at baseline occurs in small random bursts with occasional large potentials (Fig. 2.5a). Approximately five minutes after one dose of glutamate (10 µM), the firing rate of the spinal cord increases. The firing of both large and small units can be detected (Fig. 2.5b). When the glutamate rises to a final concentration 100 µM, spinal cord neurons display robust, sustained action potentials (Fig. 2.5c). After fully washing out the glutamate, activity dissipates almost completely (Fig. 2.5d).

2.3.6 Lumbar spinal cords cultured for two weeks exhibit very little spontaneous activity and only respond to high doses of neurotransmitter

Neuromuscular junction maturation requires the muscle to be in close apposition with motor neurons for approximately 2 weeks (Rosenthal and Taraskevich, 1977), so it is imperative that cultured spinal cords remain electrically active for a similar timespan to allow for maximal neuromuscular development. Lumbar spinal cords cultured for two weeks exhibit very little spontaneous electrical activity at baseline, though small unit firings occur sporadically (Fig. 2.6a). 14+ DIV spinal cords do not always respond to a low dose of glutamate (10 µM), but they will sometimes demonstrate weak activity above baseline levels (Fig. 2.6b). As the glutamate concentration approaches 100 µM, robust, sustained action potentials are elicited from these cultured spinal cords (Fig. 2.6c). Activity in response to this high concentration of glutamate appears rhythmic compared to baseline, indicating that the pattern-generating circuitry within the spinal cord remains largely intact (Fig. 2.6c). This is further supported by the presence of burst firing activity of multiple spinal cords in response to joint stimulation with glutamate and 5-HT (Fig. 2.6d). After washing out the glutamate with fresh ACSF, no activity is recorded (Fig. 2.6e).

Spontaneous firing and sensitivity to glutamate decrease in cultured spinal cords over time

The spontaneous activity of the spinal cord and its sensitivity to glutamate both decrease as time in culture increases out to two weeks. Under baseline conditions, the spinal cord is initially highly active during acute recordings. The amplitude, frequency, and number of spontaneous potentials all decline the longer the spinal cord is cultured (Fig. 2.7a). When a 10 µM bolus of glutamate is applied to the bath, spinal cord activity is elicited across all three time points (Fig. 2.7b). The effect is greatest on acute spinal cords and the least consistent at 14+ DIV (Fig. 2.7b). As glutamate concentrations reach 100 µM, electrical activity peaks at 0, 7, and 14 DIV (Fig. 2.7c). The activity is visually indistinguishable at this dose and continues until the glutamate is washed out (Fig. 2.7c,e). Dual application of glutamate and 5-HT stimulates patterned bursts of electrical activity at both 0 DIV and 7 DIV (Fig. 2.7d). Upon washout of the glutamate, activity drops below baseline levels and remains low for more than 15 minutes after the wash has been completed (Fig. 2.7e).

2.4 Discussion

Organotypic lumbar spinal cord cultures provide researchers with a more easily accessible, controllable, and quantifiable system than *in vivo* work or dissociative *in vitro* studies. We confirmed that many of the cell types found in central pattern generators (CPGs) were present in lumbar spinal cords, including populations of interneurons (Lanuza *et al*, 2004; Fig. 1d,e,f), motor neurons (Hägglund *et al*, 2010; Fig. 1f; Fig. 2f), and multiple glial subtypes (Couteaux, 1973; Fig. 2.1d,e,f; Fig. 2.2e). We demonstrated for the first time that spinal cords could be cultured on glass and kept alive for at least three weeks (Fig. 2.2). Under these conditions, spinal cords extend a robust, heterogenous arbor of neurons and glia that extend for over 1 mm and become electrically active within 7 DIV. The sustained electrical activity observed in response to tonic glutamate stimulation of organotypic spinal cords demonstrates that while the L1-L2 segment becomes less sensitive to glutamate over time, the neurons still responded similarly when stimulation reached the threshold. This work demonstrates the first example of intact, organotypic spinal cord circuitry generating electrical activity for multiple weeks *in vitro*.

Many structures that are difficult to access physically, optically, or pharmaceutically, can best be studied in organotypic slice culture *in vitro* (Prosser and Gillette, 1989). Previous work on organotypic CNS cultures have shown minimal differences between *in situ* electrophysiology and the organotypic brain slice cultures (Muller *et al*, 1993; Uesaka *et al*, 2005; Rohrbacher *et al*, 2000; Gillette and Tischkau, 1999). Contrary to previous findings, our study determined that cultured spinal cords have a decreased sensitivity to glutamate (Fig. 2.7b,c) and reduced basal activity (Fig. 2.7a), though this does not prevent the tissue from generating patterned bursting activity (Fig. 2.7d). However, many of these previous studies investigated shorter time windows ranging from 24 h to 4 DIV, and only a few of the studies with hippocampal brain slices extended beyond 10 DIV. There are no published electrical recording data from rat spinal cords beyond postnatal day 3, so we are unable to compare our results to previous findings at a chronologically similar timescale. Therefore, it will be important to perform additional electrophysiological recordings of acute spinal cords from older animals to compare them with our organotypic spinal cord cultures.

In some organotypic hippocampal slice cultures, it has been shown that the timecourses of electrophysiological maturation and axonal branching complexity are comparable between *in vivo* and *in situ* hippocampal brain slices (Muller *et al*, 1993; Uesaka *et al*, 2005). However, dissociated hippocampal cultures have demonstrated reduced levels of spontaneous activity as well as reduced sensitivity to stimulation when cultured for up to 5 weeks which more closely aligns with our observations in the spinal cord (Odawara *et al*, 2014; Fig. 2.7). It has also been reported that neuronal activity is heavily modulated by the presence of other cells (e.g., skeletal muscle), and we hypothesize that passive spinal cord activity would be heavily modulated by being co-cultured with muscle (Odawara *et al*, 2014; Balice-Gordon and Lichtman, 1993; Rosenthal and Taraskevich, 1977; Bennett and Pettigrew, 1976).

The lack of obvious patterned bursts in both our acute (Fig. 2.4a-d) and cultured (Fig. 2.5, Fig. 2.6, Fig. 2.7) spinal cords is likely due to the stimulus consisting only of glutamate when it is known that other neurotransmitters are also present in the spinal cord and brainstem that significantly modulate the pattern of electrical activity. The use of an NMDA and serotonin cocktail to stimulate oscillatory firing is common practice in these acute electrical recordings of

CPG activity (Cazalets *et al*, 1995; Kiehn, 2006; Brownstone and Wilson, 2008; Ghosh and Pearse, 2015). When we applied both glutamate and 5-HT simultaneously, we observed the patterned bursts previously reported and hypothesized (Figs. 2.4d, 2.6d, 2.7d). In future experiments, antagonistic blockade of receptors would be an important method of experimental control to isolate and determine the effects of NMDA/glutamate and 5-HT/serotonin. APV is a well-known antagonist for NMDA receptors that will work well for blockade of the NMDA stimulation, but blockade of serotonin receptors is far more complex. Researchers have determined that the 5-$HT_{1,2A,2C,3,7}$ receptors are important for the regulation of spinal locomotor networks, but that the 5-HT_2 receptors play the largest role in driving the K^+-linked inhibitory rebound (Courtine *et al*, 2009; Guertin and Steuer, 2005; Liu *et al*, 2009; Jacobs and Fornal, 1993; Harvey *et al*, 2006; Li *et al*, 2007; Perrier *et al*, 2013; Gackière and Vinay, 2014). Clozapine is an atypical antipsychotic in humans that also acts as an antagonist for each of the 5-HT receptor subtypes associated with locomotion (Saber et al, 2019). Therefore, we expect that a cocktail of APV and clozapine would provide a sufficient blockade from stimulation by NMDA and serotonin to serve as controls. By stimulating with, and blocking against, a mixed glutamate and serotonin cocktail, we hypothesize that more classical bursting activity would be observed.

Rodent spinal cord cultures with sustainable, characterized patterns of electrical activity could provide researchers with improved access to and knowledge about one of the most understudied mammalian circuits. It would provide a unique platform on which researchers can investigate the pathology of neuromuscular diseases and the modes of action for drugs against ALS, spinal muscular atrophy, Duchenne's muscular dystrophy, and peripheral neuropathies. Future experiments could also prove instructive about how complex neuronal circuits behave in medium-to-long-term culture conditions. Currently, the precise circuitry underlying mammalian CPGs is unknown (Kiehn, 2006), but enhancing our understanding of these locomotive circuits is an important step towards improving clinical rehabilitation of patients with spinal cord injury (SCI; Edgerton *et al,* 2004; Rossignol *et al,* 1998). The treatments physicians can offer to SCI patients are very limited and largely ineffective (MacDonald and Sadowsky, 2002). Through better understanding of spinal cord circuits like CPGs, clinicians and researchers will be able to design better therapies to improve patients suffering from a variety of SCIs. Continuing advances

in biorobotics are pushing the boundaries of science and sustained long-term growth and re-innervation of motor pathways is an important step in the creation of biologically based prosthetics (Rossiter *et al*, 2009; Albalaihid *et al*, 2017; Park *et al*, 2014).

2.5 Figures

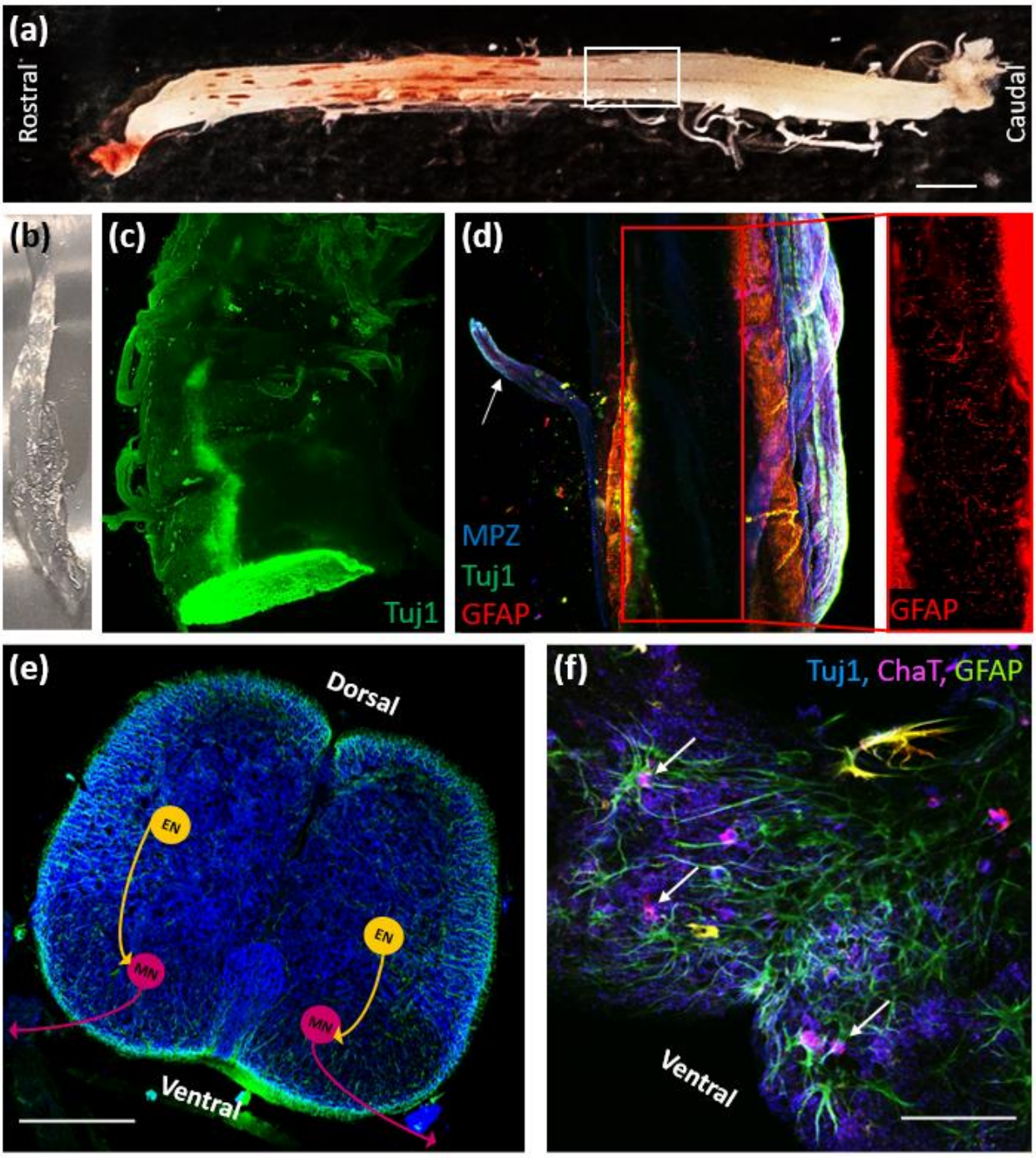

Figure 2.1. (a) A fully intact rat spinal cord is shown, with a white box outlining the first and second lumbar (L1-L2) region, which houses the hindlimb locomotor central pattern generator (CPG). **(b)** Performing passive CLARITY on a rat spinal cord causes the spinal cord to become nearly transparent. **(c)** Neurons (Tuj1, green) are seen making up the major structures of the

Fig. 2.1 (cont.). exterior of an intact lumbar rat spinal. **(d)** Light sheet imaging allows for imaging of both external structures such as the dorsal root ganglion (indicated by a white arrow) and internal organization. We see the presence of Schwann cells (MPZ, blue), neurons (Tuj1, green), and astrocytes (GFAP, red) in both the internal and external structures. The inset to the right shows *in situ* astrocytes deep within the spinal cord. **(e)** Horizontal cross-section of lumber spinal cord shows the presence of neurons (Tuj1, blue) and glia (GFAP, green) within the spinal cord. Excitatory interneurons (EN) stimulate lower motor neurons (MN) in the ventrolateral spinal cord. (f) Choline acetyltransferase (ChAT, magenta) co-localizes with Tuj1 and appears ventrolaterally in the cross section, confirming the presence of the cholinergic neurons at the output of the CPG.

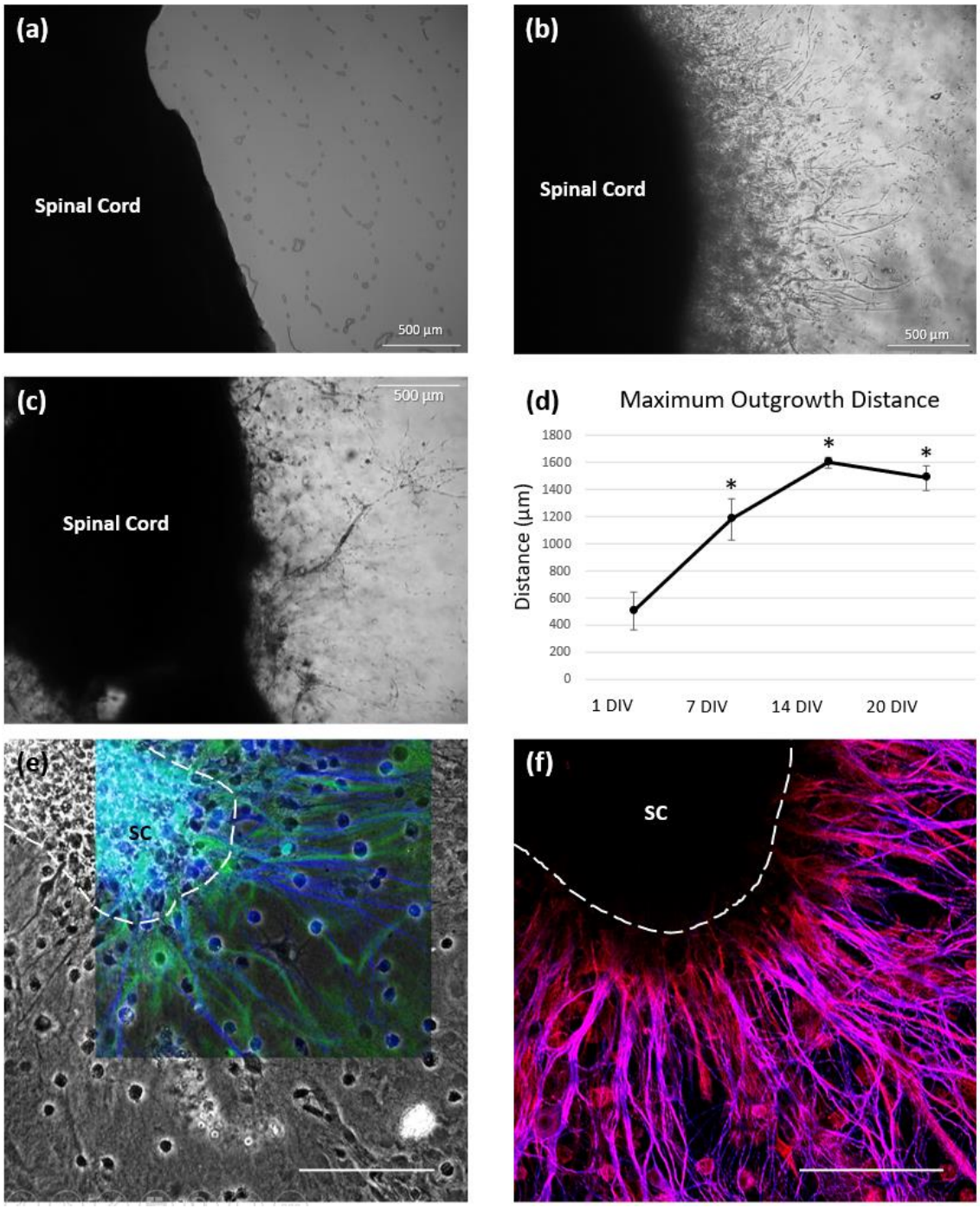

Figure 2.2. (a) Image of a cultured spinal cord 2 h after being seeded before any outgrowths extend onto the glass substrate. **(b)** By 7 DIV, robust outgrowths have extended from the spinal cord. **(c)** Fasciculation of the outgrowths into more well-defined nerve-like structures begins to occur by 14 DIV. **(d**) Processes that grow out from cultured spinal cords grow demonstrate significant extension between at all time points after 1 DIV, but there are no significant changes in maximal outgrowth length between 7 and 20 DIV. **(e)** Neuronal outgrowths radiate from a 7

Fig. 2.2 (cont.). DIV rat spinal cord (SC) cultured on Matrigel-coated glass. These outgrowths contained large populations of both neurons (Tuj-1, blue) and astrocytes (GFAP, green). **(f)** The colocalization of ChAT (red) and Tuj-1 tubulin immunohistochemistry indicates that these processes are nearly entirely cholinergic. The dark area is SC that is out of the plane of focus.

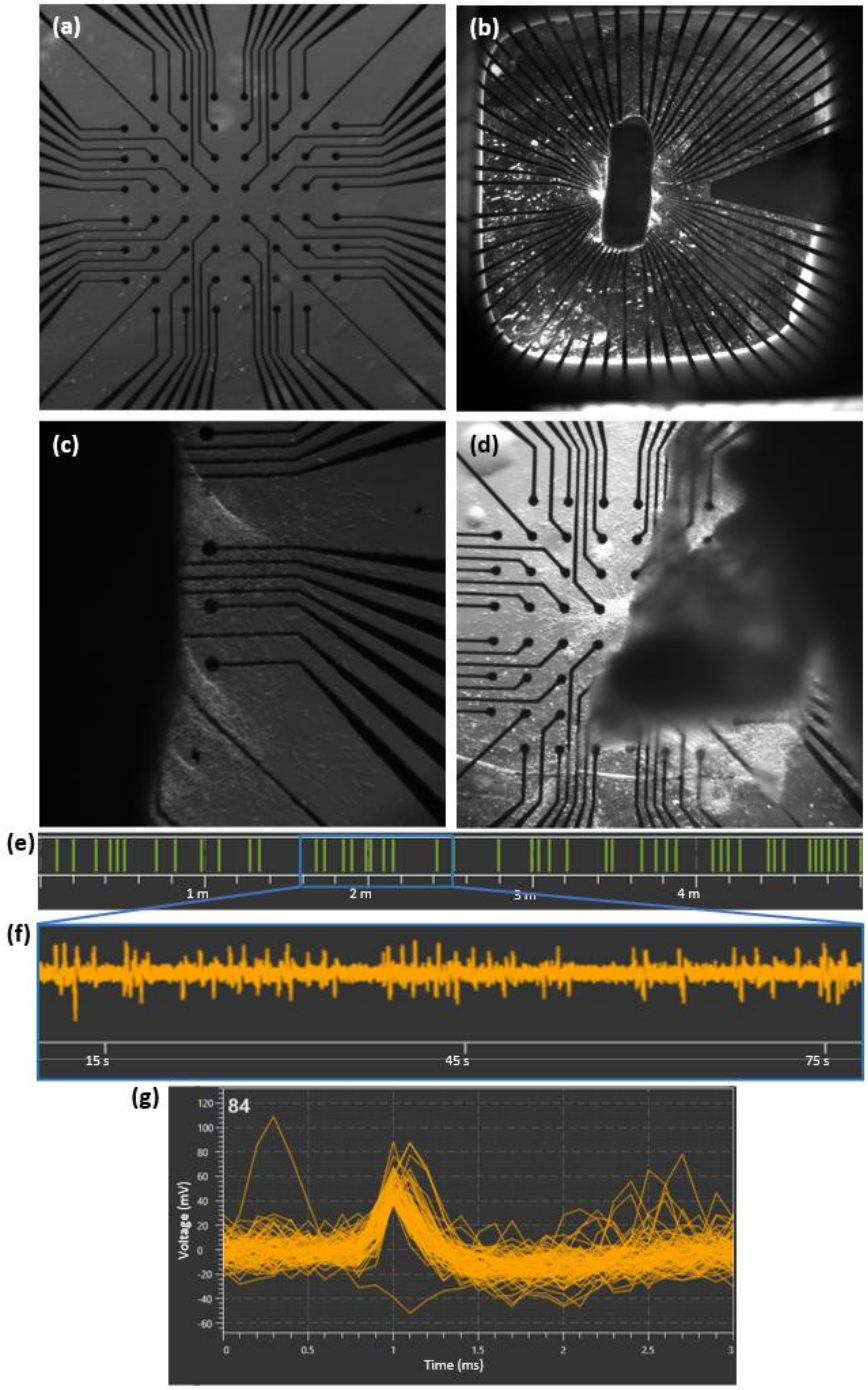

Figure 2.3. Multi-electrode array recordings of outgrowths from an organotypic spinal cord culture. **(a)** Image of the 64-electrode array on which the spinal cord is cultured. **(b)** Lumbar spinal cord is seeded with its ventral side facing the electrodes. The MEA is coated with 1% Matrigel before seeding. **(c)-(d**) Magnified view of two different spinal cord cultures where early outgrowths reach nearby electrodes. **(e)** Raster plot of action potentials fired at a single electrode of a 7 DIV spinal cord over 5 m. **(f)** Raw electrical data from 60 s shows that action potentials

Fig. 2.3 (cont.). come in multi-second long bursts. **(g)** Overlay of all action potentials recorded by a single electrode over a 10 min interval.

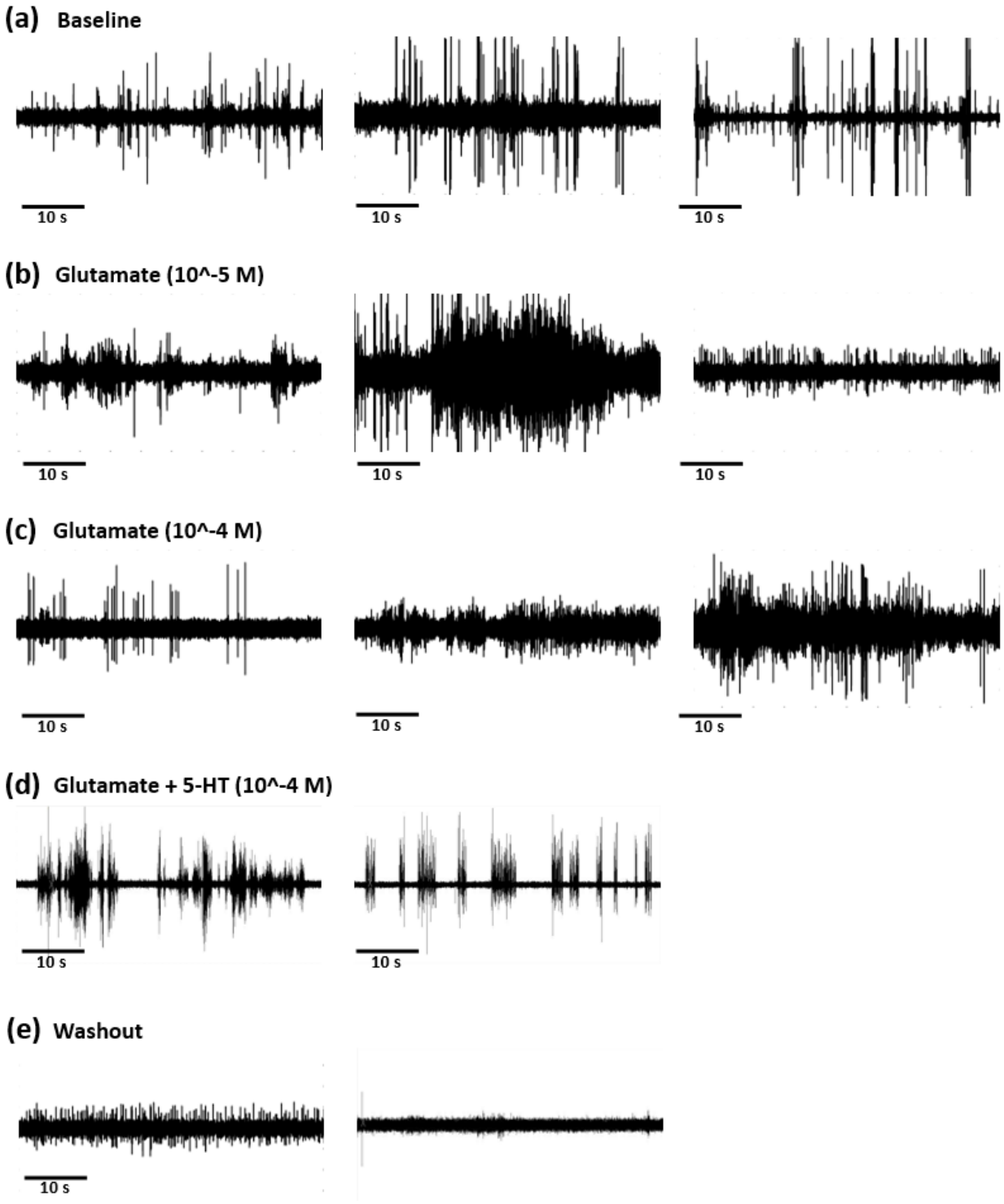

Figure 2.4. Acute lumbar spinal cord recordings demonstrate both spontaneous and stimulated activity in response to glutamate. **(a)** The spinal cord is highly active at baseline. **(b)** A single dose of glutamate (10 µM) is sufficient to alter the firing pattern of the spinal cord. **(c)** After multiple doses of glutamate (final concentration 100 µM), the spinal cord exhibits robust action potentials similar to the 10 µM glutamate condition. **(d)** Simultaneous application of 100 µM glutamate and

Fig. 2.4 (cont.). 100 μM 5-HT elicited burst firing patterns from acute spinal cord tissues. **(e)** After washing out the glutamate (5 full replacement washes), activity is reduced below what is observed at baseline, but is still present. Voltages are relative values, and therefore not displayed.

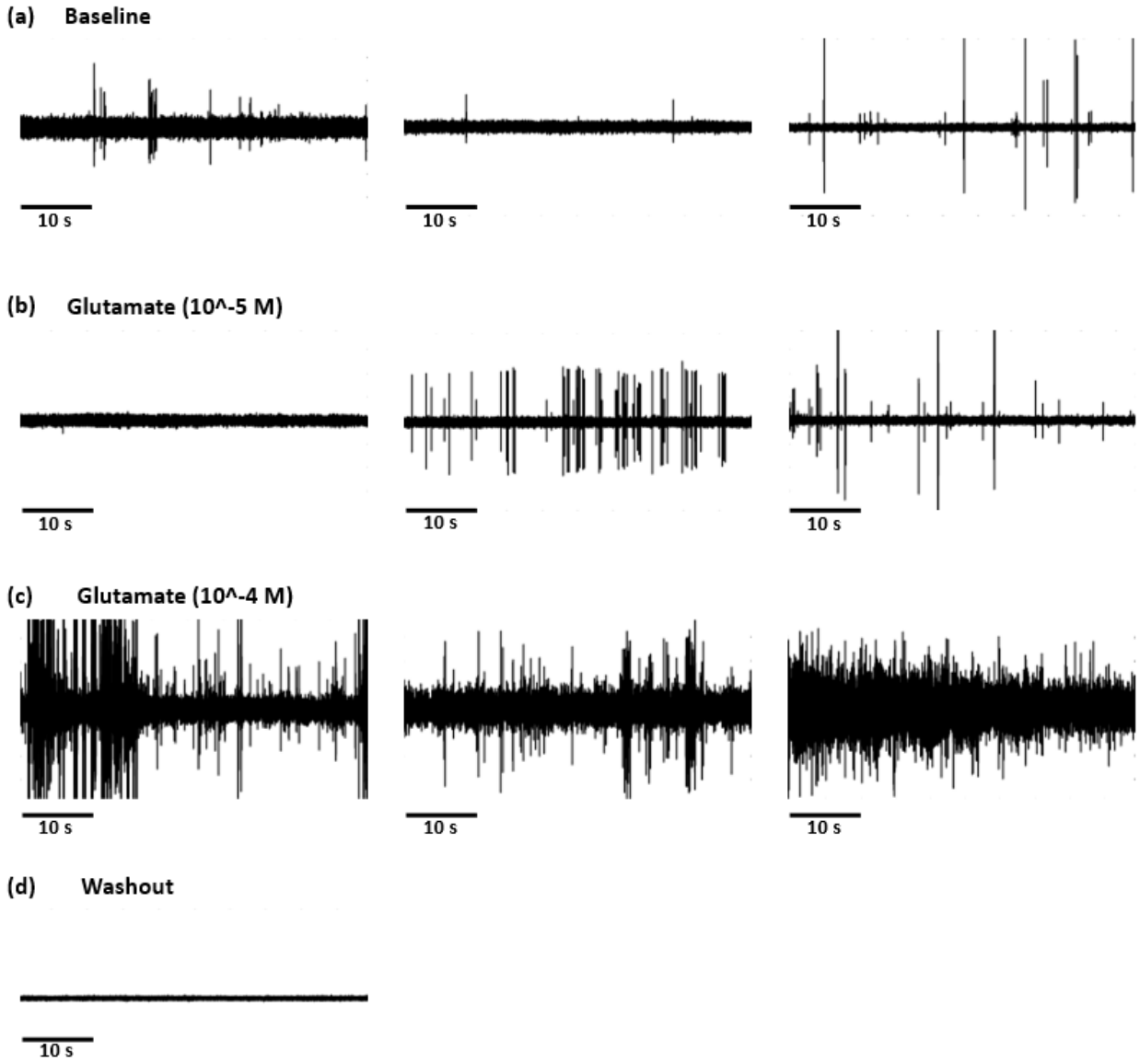

Figure 2.5. Recordings from lumbar spinal cords cultured for one week demonstrate infrequent spontaneous activity and a slightly reduced sensitivity to glutamate stimulation compared to acute conditions. **(a)** Spinal cord activity at baseline occurs in small random bursts with large potentials found occasionally. **(b)** One dose of glutamate (10 µM) increases the firing rate of the spinal cord. The firing of both large and small units can be detected. **(c)** A high dose of glutamate (final concentration 100 µM) elicits robust, sustained action potentials. **(d)** After washing out the glutamate (5 full replacement washes), activity dissipates almost completely. Voltages are relative values, and therefore not displayed.

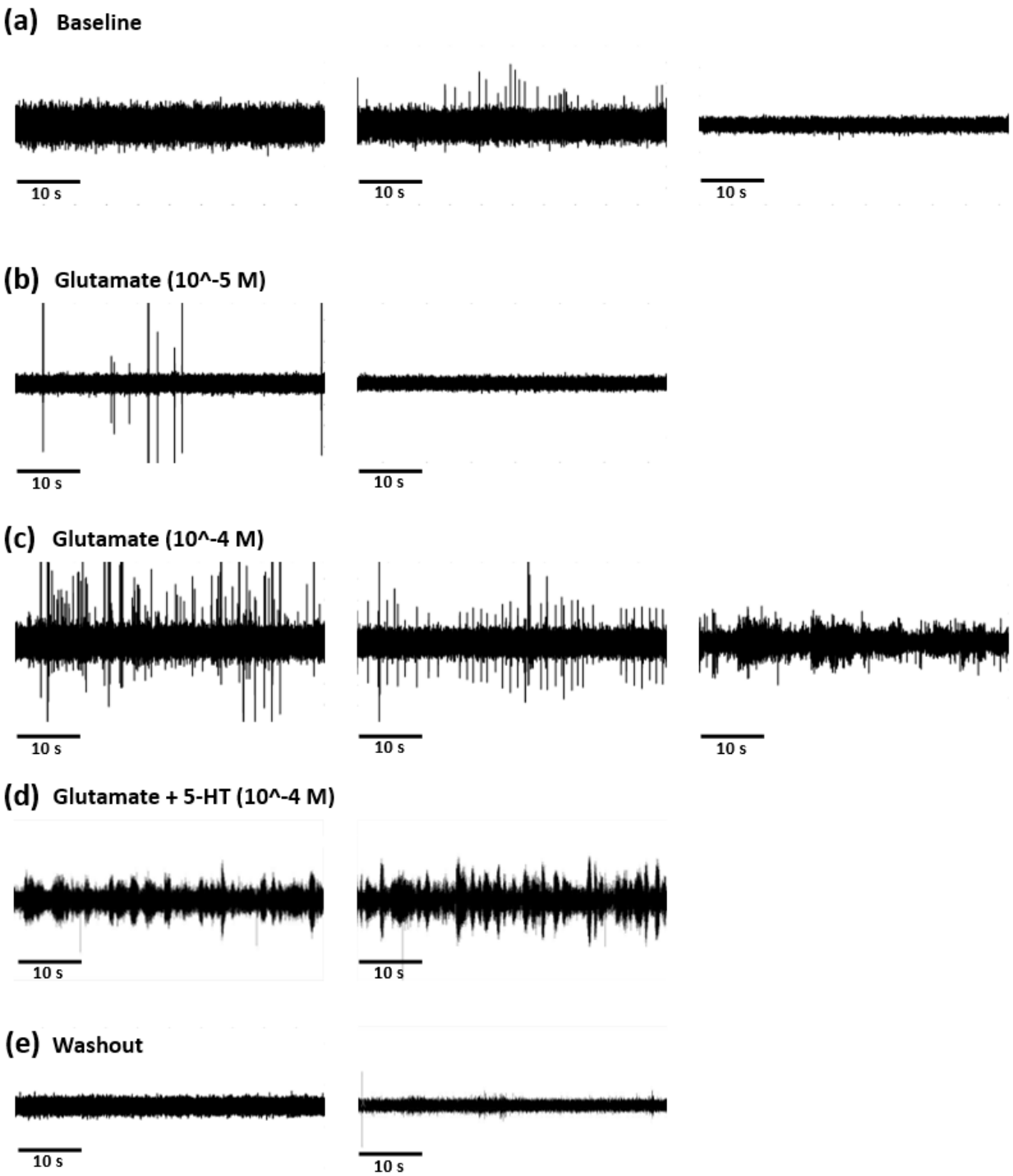

Figure 2.6. Recordings from lumbar spinal cords cultured for two weeks exhibit very little spontaneous activity and only respond to a high dose of glutamate. **(a)** There is very little spontaneous electrical activity at baseline, though small unit firings occur sporadically. **(b)** Spinal cords that have been cultured for two weeks do not always respond to a low dose of glutamate (10 µM), but they can demonstrate weak activity greater than what is observed at baseline. **(c)** A

Fig. 2.6 (cont.). high dose of glutamate (final concentration 100 µM) elicits robust, sustained action potentials. Some spinal cords begin firing in patterned bursts in response to a bolus of 100 µM glutamate. **(d)** Burst firing pattern is observed in response to a 5-HT + glutamate (100 µM each) neurotransmitter cocktail. **(e)** After washing out the glutamate (5 full replacement washes), no activity is recorded. Voltages are relative values, and therefore not displayed.

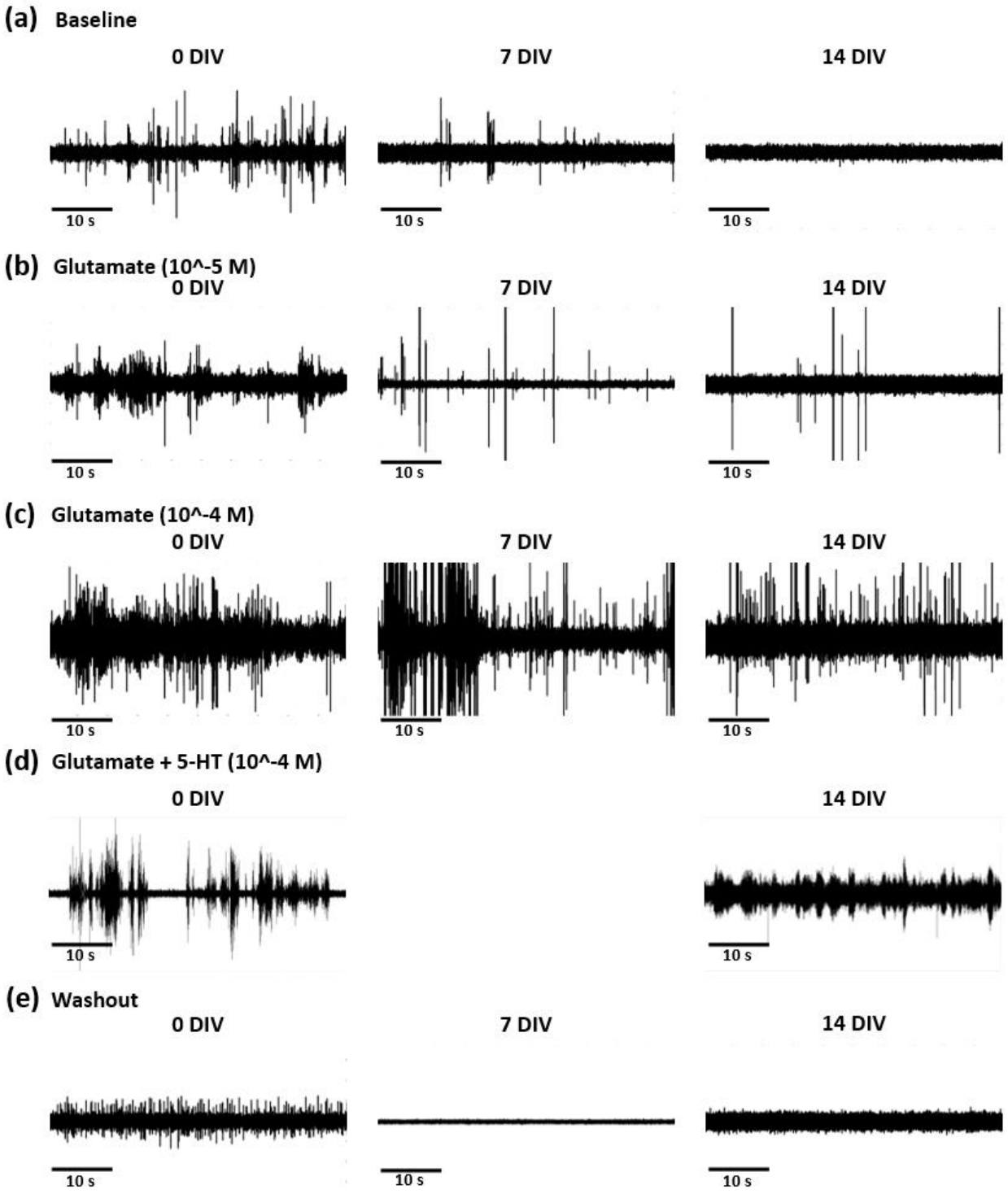

Figure 2.7. Spinal cord responds to high doses of glutamate in monoculture out to 14 DIV. **(a)** At 0 DIV, the spinal cord is highly active at baseline. The addition of glutamate reduces the overall firing rate at both 10 µM and 100 µM doses. **(b)** By 7 DIV, the spontaneous firing at baseline is greatly reduced. Both low and high doses of glutamate cause the spinal cord to become highly

Fig. 2.7 (cont.). electrically active. **(c)** At 14 DIV, spinal cords do not exhibit spontaneous firing at baseline or respond to a low dose of glutamate. However, a high dose of glutamate initiates robust electrical activity with a clear bursting pattern indicative of a pattern generating circuit. **(d)** Dual application of glutamate and 5-HT elicits burst firing in both acute and 14 DIV spinal cords. **(e)** Post-wash activity is reduced below baseline in the acute spinal cords and disappears completely in both the 7 DIV and 14 DIV conditions. Voltages are relative values, and therefore not displayed.

2.6 References

1. Brown, T. G. (1911). The intrinsic factors in the act of progression in the mammal. *Proceedings of the Royal Society of London. Series B, containing papers of a biological character*, *84*(572), 308-319.
2. Grillner, S. in Handbook of Physiology (ed. Brooks, V.) 1179–1236 (American Physiological Society, 1981)
3. Cazalets, J. R., Borde, M., & Clarac, F. (1995). Localization and organization of the central pattern generator for hindlimb locomotion in newborn rat. *Journal of Neuroscience*, *15*(7), 4943-4951.
4. Grillner, S., & Wallen, P. (1985). Central pattern generators for locomotion, with special reference to vertebrates. *Annual review of neuroscience*, *8*(1), 233-261.
5. Grillner, S. (1986). Interaction between sensory signals and the central networks controlling locomotion in lamprey, dogfish and cat. In *Neurobiology of vertebrate* Anderson and Grillner 1983
6. Pearson, K. G., & Rossignol, S. (1991). Fictive motor patterns in chronic spinal cats. *Journal of neurophysiology*, *66*(6), 1874-1887.
7. Kiehn, O. (2006). Locomotor circuits in the mammalian spinal cord. *Annu. Rev. Neurosci.*, *29*, 279-306.
8. Grillner, S. (1975). Locomotion in vertebrates: central mechanisms and reflex interaction. *Physiological reviews*, *55*(2), 247-304.
9. Poon, M. L. (1980). Induction of swimming in lamprey by L-DOPA and amino acids. *Journal of comparative physiology*, *136*(4), 337-344.
10. Grillner, S., & Wallen, P. (1985). Central pattern generators for locomotion, with special reference to vertebrates. *Annual review of neuroscience*, *8*(1), 233-261.
11. Cohen, A. H., & Wallén, P. (1978). Rhythmic locomotor activity induced in an *in vitro* preparation of the lamprey spinal cord. *Neurosci Letters [Suppl]*, *1*, S92.
12. Cohen, A. H., & Wallén, P. (1980). The neuronal correlate of locomotion in fish. *Experimental brain research*, *41*(1), 11-18.
13. Skinner, F. K., Kopell, N., & Mulloney, B. (1997). How does the crayfish swimmeret system work? Insights from nearest-neighbor coupled oscillator models. *Journal of computational neuroscience*, *4*(2), 151-160.
14. Yu, X., Nguyen, B., & Friesen, W. O. (1999). Sensory feedback can coordinate the swimming activity of the leech. *Journal of Neuroscience*, *19*(11), 4634-4643.
15. Büschges, A., Schmitz, J., & Bässler, Ulrich (1995). Rhythmic patterns in the thoracic nerve cord of the stick insect induced by pilocarpine. *Journal of Experimental Biology*, *198*(2), 435-456.
16. Kahn, J. A., & Roberts, A. (1982). Experiments on the central pattern generator for swimming in amphibian embryos. *Philosophical Transactions of the Royal Society of London. B, Biological Sciences*, *296*(1081), 229-243.
17. Cohen I, Rimer M, Lomo T, McMahan UJ. 1997. Agrin-induced postsynaptic-like apparatus in skeletal muscle fibers *in vivo*. *Mol. Cell. Neurosci.* 9: 237–53
18. Grillner, S., & Matsushima, T. (1991). The neural network underlying locomotion in lamprey-synaptic and cellular mechanisms. *Neuron*, *7*(1), 1-15.

19. Tunstall, M. J., & Sillar, K. T. (1993, February). Physiological and developmental aspects of intersegmental coordination in Xenopus embryos and tadpoles. In *Seminars in Neuroscience* (Vol. 5, No. 1, pp. 29-40). Academic Press.
20. Duysens, J., & Van de Crommert, H. W. (1998). Neural control of locomotion; Part 1: The central pattern generator from cats to humans. *Gait & posture*, *7*(2), 131-141.
21. Cruse and Warnecke Cruse, H., & Warnecke, H. (1992). Coordination of the legs of a slow-walking cat. *Experimental brain research*, *89*(1), 147-156.
22. Grillner, S., & Zangger, P. (1979). On the central generation of locomotion in the low spinal cat. *Experimental Brain Research*, *34*(2), 241-261.
23. Naito, A., Shimizu, Y., & Handa, Y. (1990). Analyses of airstepping movement in adult spinal dogs. *The Tohoku journal of experimental medicine*, *162*(1), 41-48.
24. Kristan, W. B., & Calabrese, R. L. (1976). Rhythmic swimming activity in neurones of the isolated nerve cord of the leech. *Journal of Experimental Biology*, *65*(3), 643-668.
25. Sillar, K. T., & Skorupski, P. E. T. E. R. (1986). Central input to primary afferent neurons in crayfish, Pacifastacus leniusculus, is correlated with rhythmic motor output of thoracic ganglia. *Journal of Neurophysiology*, *55*(4), 678-688.
26. Chrachri, A., & Clarac, F. (1990). Fictive locomotion in the fourth thoracic ganglion of the crayfish, Procambarus clarkii. *Journal of Neuroscience*, *10*(3), 707-719.
27. Roberts, A. L. A. N., Soffe, S. R., Clarke, J. D., & Dale, N. (1983, January). Initiation and control of swimming in amphibian embryos. In *Symposia of the society for experimental biology* (Vol. 37, pp. 261-284).
28. Kudo, N. O. R. I. O., & Yamada, T. O. S. H. I. Y. A. (1987). Morphological and physiological studies of development of the monosynaptic reflex pathway in the rat lumbar spinal cord. *The Journal of physiology*, *389*(1), 441-459.
29. Smith, J. C., Feldman, J. L., & Schmidt, B. J. (1988). Neural mechanisms generating locomotion studied in mammalian brain stem-spinal cord in vitro. *The FASEB journal*, *2*(7), 2283-2288.
30. Cazalets, J. R., Nagy, F., & Moulins, M. (1990). Suppressive control of the crustacean pyloric network by a pair of identified interneurons. II. Modulation of neuronal properties. *Journal of Neuroscience*, *10*(2), 458-468.
31. Cazalets, J. R., Grillner, P., Menard, I., Cremieux, J., & Clarac, F. (1990). Two types of motor rhythm induced by NMDA and amines in an in vitro spinal cord preparation of neonatal rat. *Neuroscience letters*, *111*(1-2), 116-121.
32. Cazalets, J. R., Sqalli-Houssaini, Y., & Clarac, F. (1992). Activation of the central pattern generators for locomotion by serotonin and excitatory amino acids in neonatal rat. *The Journal of physiology*, *455*(1), 187-204.
33. Lanuza, G. M., Gosgnach, S., Pierani, A., Jessell, T. M., & Goulding, M. (2004). Genetic identification of spinal interneurons that coordinate left-right locomotor activity necessary for walking movements. *Neuron*, *42*(3), 375-386.
34. Pierani, A., Moran-Rivard, L., Sunshine, M. J., Littman, D. R., Goulding, M., & Jessell, T. M. (2001). Control of interneuron fate in the developing spinal cord by the progenitor homeodomain protein Dbx1. *Neuron*, *29*(2), 367-384.
35. Kiehn, O. (2016). Decoding the organization of spinal circuits that control locomotion. *Nature Reviews Neuroscience*, *17*(4), 224-238.

36. Talpalar, A. E., Bouvier, J., Borgius, L., Fortin, G., Pierani, A., & Kiehn, O. (2013). Dual-mode operation of neuronal networks involved in left-right alternation. *Nature*, *500*(7460), 85-88.
37. Borowska, J., Jones, C. T., Zhang, H., Blacklaws, J., Goulding, M., & Zhang, Y. (2013). Functional subpopulations of V3 interneurons in the mature mouse spinal cord. *Journal of Neuroscience*, *33*(47), 18553-18565.
38. Zhang, Y., Narayan, S., Geiman, E., Lanuza, G. M., Velasquez, T., Shanks, B., ... & Fan, C. M. (2008). V3 spinal neurons establish a robust and balanced locomotor rhythm during walking. *Neuron*, *60*(1), 84-96.
39. Grillner, S., & Jessell, T. M. (2009). Measured motion: searching for simplicity in spinal locomotor networks. *Current opinion in neurobiology*, *19*(6), 572-586.
40. Roberts, A., Li, W. C., Soffe, S. R., & Wolf, E. (2008). Origin of excitatory drive to a spinal locomotor network. *Brain research reviews*, *57*(1), 22-28.
41. Goulding, M. (2009). Circuits controlling vertebrate locomotion: moving in a new direction. *Nature Reviews Neuroscience*, *10*(7), 507-518.
42. Hägglund, M., Borgius, L., Dougherty, K. J., & Kiehn, O. (2010). Activation of groups of excitatory neurons in the mammalian spinal cord or hindbrain evokes locomotion. *Nature neuroscience*, *13*(2), 246-252.
43. Hägglund, M., Dougherty, K. J., Borgius, L., Itohara, S., Iwasato, T., & Kiehn, O. (2013). Optogenetic dissection reveals multiple rhythmogenic modules underlying locomotion. *Proceedings of the National Academy of Sciences*, *110*(28), 11589-11594.
44. Stuart, D. G., & Hultborn, H. (2008). Thomas Graham Brown (1882–1965), Anders Lundberg (1920–), and the neural control of stepping. *Brain research reviews*, *59*(1), 74-95.
45. Deliagina, T. G., Feldman, A. G., Gelfand, I. M., & Orlovsky, G. N. (1975). On the role of central program and afferent inflow in the control of scratching movements in the cat. *Brain research*, *100*(2), 297-313.
46. Busetto, G., Buffelli, M., Tognana, E., Bellico, F., & Cangiano, A. (2000). Hebbian mechanisms revealed by electrical stimulation at developing rat neuromuscular junctions. *Journal of Neuroscience*, *20*(2), 685-695.
47. Pearson, K. G. (1995). Proprioceptive regulation of locomotion. *Current opinion in neurobiology*, *5*(6), 786-791.
48. Brownstone, R. M., & Wilson, J. M. (2008). Strategies for delineating spinal locomotor rhythm-generating networks and the possible role of Hb9 interneurones in rhythmogenesis. *Brain research reviews*, *57*(1), 64-76.
49. Rybak, I. A., Dougherty, K. J., & Shevtsova, N. A. (2015). Organization of the mammalian locomotor CPG: review of computational model and circuit architectures based on genetically identified spinal interneurons. *ENeuro*, *2*(5).
50. Muller, D., Buchs, P. A., & Stoppini, L. (1993). Time course of synaptic development in hippocampal organotypic cultures. *Developmental Brain Research*, *71*(1), 93-100.
51. Uesaka, N., Hirai, S., Maruyama, T., Ruthazer, E. S., & Yamamoto, N. (2005). Activity dependence of cortical axon branch formation: a morphological and electrophysiological study using organotypic slice cultures. *Journal of Neuroscience*, *25*(1), 1-9.

52. Rohrbacher, J., Ichinohe, N., & Kitai, S. T. (2000). Electrophysiological characteristics of substantia nigra neurons in organotypic cultures: spontaneous and evoked activities. *Neuroscience*, *97*(4), 703-714.
53. Millet, L. J., Stewart, M. E., Sweedler, J. V., Nuzzo, R. G., & Gillette, M. U. (2007). Microfluidic devices for culturing primary mammalian neurons at low densities. *Lab on a Chip*, *7*(8), 987-994.
54. Volterra, A., Magistretti, P. J., & Haydon, P. G. (2002). *The tripartite synapse: glia in synaptic transmission* (No. LNDC-BOOK-2010-002). Oxford University Press.
55. Rosenthal JL, Taraskevich PS. 1977. Reduction of multiaxonal innervation at the neuromuscular junction of the rat during development. *J. Physiol*. 270: 299–310
56. Couteaux R. 1973. Motor endplate structure. In *Structure and Function of Muscle*, Vol. 2, ed. GH Bourne, p. 483–530. New York
57. Prosser, R. A., & Gillette, M. U. (1989). The mammalian circadian clock in the suprachiasmatic nuclei is reset in vitro by cAMP. *Journal of Neuroscience*, *9*(3), 1073-1081.
58. Gillette, M. U., & Tischkau, S. A. (1999). Suprachiasmatic nucleus: the brain's circadian clock. *Recent progress in hormone research*, *54*(1), 33-58.
59. Odawara, A., Saitoh, Y., Alhebshi, A. H., Gotoh, M., & Suzuki, I. (2014). Long-term electrophysiological activity and pharmacological response of a human induced pluripotent stem cell-derived neuron and astrocyte co-culture. *Biochemical and biophysical research communications*, *443*(4), 1176-1181.
60. Balice-Gordon RJ, Lichtman JW. 1993. *In vivo* observations of pre-and postsynaptic changes during the transition from multiple to single innervation at developing neuromuscular junctions*. J. Neurosci.* 13: 834–55
61. Bennett MR, Pettigrew AG. 1976. The formation of neuromuscular synapses. *Cold Spring Harbor Symp. Quant. Biol.* 40: 409–24
62. Ghosh, M., & Pearse, D. D. (2015). The role of the serotonergic system in locomotor recovery after spinal cord injury. *Frontiers in neural circuits*, *8*, 151.
63. Courtine, G., Gerasimenko, Y., Van Den Brand, R., Yew, A., Musienko, P., Zhong, H., ... & Roy, R. R. (2009). Transformation of nonfunctional spinal circuits into functional states after the loss of brain input. *Nature neuroscience*, *12*(10), 1333.
64. Guertin, P. A., & Steuer, I. (2005). Ionotropic 5-HT3 receptor agonist-induced motor responses in the hindlimbs of paraplegic mice. *Journal of neurophysiology*, *94*(5), 3397-3405.
65. Liu, J., Akay, T., Hedlund, P. B., Pearson, K. G., & Jordan, L. M. (2009). Spinal 5-HT7 receptors are critical for alternating activity during locomotion: *in vitro* neonatal and *in vivo* adult studies using 5-HT7 receptor knockout mice. *Journal of neurophysiology*, *102*(1), 337-348.
66. Jacobs, B. L., & Fornal, C. A. (1993). 5-HT and motor control: a hypothesis. *Trends in neurosciences*, *16*(9), 346-352.
67. Harvey, P. J., Li, X., Li, Y., & Bennett, D. J. (2006). 5-HT2 receptor activation facilitates a persistent sodium current and repetitive firing in spinal motoneurons of rats with and without chronic spinal cord injury. *Journal of neurophysiology*, *96*(3), 1158-1170.

68. Li, X., Murray, K., Harvey, P. J., Ballou, E. W., & Bennett, D. J. (2007). Serotonin facilitates a persistent calcium current in motoneurons of rats with and without chronic spinal cord injury. *Journal of neurophysiology*, *97*(2), 1236-1246.
69. Perrier, J. F., Rasmussen, H. B., Christensen, R. K., & Petersen, A. V. (2013). Modulation of the intrinsic properties of motoneurons by serotonin. *Current pharmaceutical design*, *19*(24), 4371-4384.
70. Gackière, F., & Vinay, L. (2014). Serotonergic modulation of post-synaptic inhibition and locomotor alternating pattern in the spinal cord. *Frontiers in neural circuits*, *8*, 102.
71. Saber, I., Milewski, A., Reitz, A. B., Rawls, S. M., & Walker, E. A. (2019). Effects of dopaminergic and serotonergic compounds in rats trained to discriminate a high and a low training dose of the synthetic cathinone mephedrone. *Psychopharmacology*, 1-15.
72. Edgerton, V. R., Tillakaratne, N. J., Bigbee, A. J., de Leon, R. D., & Roy, R. R. (2004). Plasticity of the spinal neural circuitry after injury. *Annu. Rev. Neurosci.*, *27*, 145-167.
73. Rossignol, J. F., Hidalgo, H., Feregrino, M., Higuera, F., Gomez, W. H., Romero, J. L., ... & Ayers, M. S. (1998). A double-'blind'placebo-controlled study of nitazoxanide in the treatment of cryptosporidial diarrhoea in AIDS patients in Mexico. *Transactions of the Royal Society of Tropical Medicine and Hygiene*, *92*(6), 663-666.
74. McDonald, J. W., Becker, D., Sadowsky, C. L., Jane, J. A., Conturo, T. E., & Schultz, L. M. (2002). Late recovery following spinal cord injury: case report and review of the literature. *Journal of Neurosurgery: Spine*, *97*(2), 252-265.
75. Rossiter J, Walters P, Stoimenov B. Printing 3D dielectric elastomer actuators for soft robotics. In: Bar-Cohen Y, Wallmersperger T (eds). *Electroactive Polymer Actuators and Devices (EAPAD) 2009*. SPIE, 2009 doi:10.1117/12.815746.
76. Alblalaihid K, Overton J, Lawes S, Kinnell P. A 3D-printed polymer micro-gripper with self-defined electrical tracks and thermal actuator. *J Micromechanics Microengineering* 2017; 27: 45019.
77. Park YL, Santos J, Galloway KG, Goldfield EC, Wood RJ. A soft wearable robotic device for active knee motions using flat pneumatic artificial muscles. In: *2014 IEEE International Conference on Robotics & Automation* (*ICRA*). IEEE, Hong Kong, 2014, pp. 4805–4810.

CHAPTER 3. CULTURE PARADIGM OF SKELETAL MUSCLE INFLUENCES MUSCLE SUB-TYPE DIFFERENTIATION

3.1 Introduction

The advent of new technologies has allowed for cells and tissues to be studied in ways never before possible. By reaching across the disciplines of developmental biology, tissue engineering, and personalized medicine, scientists are now able to answer deeper questions about even the most well-studied systems. Researchers have understood for years that cell lines and 2D cell culture paradigms had stark differences to what has frequently been observed *in vivo*, and recent advances in cell sourcing and cell biology have provided ways to help bridge that gap. These new techniques have renewed the study and characterization of systems like developing muscle to investigate muscular dystrophies, the design of better bioactuators, and the production of lab-grown meats.

Previous work on skeletal muscle has commonly used C2C12-derived myoblasts to study muscle differentiation, force production, and neuromuscular interactions (Kislinger *et al*, 2005; Bajaj *et al*, 2011; Al-Rekabi and Pelling, 2013; Fu *et al*, 2001; Benveniste *et al*, 2005). Since their use was first documented, C2C12 cells have been available from commercial suppliers and commonly used to study muscle *in vitro* (Yaffe and Saxel, 1977). C2C12 were initially obtained by serially passaging myoblasts isolated from the quadriceps muscle of C3H mice with the homozygous recessive *dy* gene that had undergone crush injury. The *dy* gene primarily dysregulates the M-laminin component of the basement membrane produced by muscle cells, resulting in a phenotype similar to early-onset human muscular dystrophy. However, the *dy* mutation does not dysregulate dystrophin (Xu *et al*, 1994), the key cytoplasmic protein mutated in Duchenne's muscular dystrophy. Healthy dystrophin connects the cytoskeleton to the extracellular matrix (Monaco *et al*, 1986; Zubrzycka-Gaarn *et al*, 1988). It is not commonly known among muscle researchers that C2C12 are from a dystrophic mutant, in part because none of the biggest vendors – Sigma Aldrich, Thermo Fisher, ATCC, or AbCam – include on their protocols or information sheets that the cells come from a *dy*-mutant or that they were multiply passaged from crush-injury mouse models before immortalization. When engineering a 3D muscle tissue,

it is important to contrast C2C12 to their primary cell counterparts to determine which cell source is most useful for a specific study.

For over a century, researchers have used 2D cell cultures as models to study cellular and molecular behaviors. Although these approaches are well-accepted and have significantly advanced our understanding of cell behavior, a growing body of evidence shows that culturing cells in 2D systems can result in irregular biophysical and biochemical responses. Specific behaviors of cancer cells, muscle fibers, and hepatocytes have all been more closely aligned with *in vivo* knowledge when cultured in 3D rather than 2D (Choi *et al*, 2010; Mudera *et al*, 2010; Gieseck III *et al*, 2014). Recent advances in 3D culture such as sandwich culture, micropatterning, porous hydrogels, and 3D printing (Bi *et al*, 2006; Chaubey *et al*, 2008; Lee *et al*, 2015; Cvetkovic *et al*, 2014) have contributed to the rapid rise of publications studying cell populations in 3D, aiming to improve upon older, 2D data. The production of mature muscle fibers in 2D cultures has always been difficult due to the intrinsic spontaneous twitching of healthy myotubes during development (Capers, 1960). On a stiff substrate, such as the traditional hard glass or plastic of a petri dish or cell culture flask, spontaneous contractions will often cause the myotubes to pull themselves off the substrate. This results in cultures that have been biased for fibers that either contract weakly or not at all. There is also strong evidence that muscle cells in 3D culture systems reach later stages of development, and do so more quickly (Langelaan *et al*, 2010; Grabowska *et al*, 2011).

Skeletal muscle fibers are broadly classified into two different fiber types, Type I (slow-twitch) and Type II (fast-twitch) fibers. Fiber type can have a profound impact on muscle dysregulation due to genetic muscular dystrophies or aging-induced muscle atrophy (Talbot and Maves, 2016). Muscle fiber types are generally defined by the myosin heavy chain isoforms that they express, but many other components contribute to a fiber's physiological characteristics as well. Most vertebrate muscles contain a mix of Type I and Type II fibers, though the ratio of each is tailored to the needs of that specific muscle. Slow-twitch muscle fibers are more efficient over long periods of time and are frequently used for controlling posture (e.g. abdomen), holding up the head (neck), or endurance exercise like running or walking long distances (*e.g.*

gastrocnemius). Type II fibers have larger diameters, contract with greater force, and tire much more quickly (e.g. biceps, quadriceps and trapezius muscles). This variation is at least partly due to the metabolic differences between the fiber types. Type I muscle has more mitochondria than Type II and generally relies more on aerobic respiration to generate energy. Because of this increased metabolic workload, Type I-dominant muscles are more vascularized and visually appear to be red rather than white like Type II-dominant muscles. Slow- and fast-twitch muscle fibers display different contractile profiles which will influence the force production, behavior, and stimulus-response coupling of any engineered muscle tissue. Muscle fiber subtype can be determined based on which myosin heavy chain (MHC) isoforms they express. Some muscles contain only a single isoform of MHC, but others are composed of isoforms. 'Pure' skeletal muscles contain exactly one of Type I (MHC-Iβ), Type IIA (MHC-IIa), Type IIB (MHC-IIb), or Type IID (MHC-IId) fibers (Pette and Staron, 1990; Schiaffino and Reggiani, 1994, 1996). Hybrid skeletal muscle tissues co-express specific pairs of fiber subtypes, including I/IIA, IIAD, and IIBD (Pette and Staron, 1990; Schiaffino and Reggiani, 1994, 1996, 2000 Microscopy Research and Technique). There are other muscle fiber types associated with specific muscles throughout the body. For example, MHC-Iα fibers are found in extraocular and laryngeal muscles (Pette and Staron, 1997) and MHC-IIc has been implicated in the growth of neuronal processes (Wylie and Chantler, 2008 Molecular Biology of the Cell).

Here, we aim to compare C2C12 to primary skeletal muscle and investigate how cell source, culture paradigm, and the presence of neurogenic signals can influence muscle cell development *in vitro*. First, we developed a modified protocol for the 2D culture of primary skeletal muscle from rat hindlimb (gastrocnemius and soleus). We determined that primary cultures have larger myotube diameters, the average AChR cluster has a greater surface area, and observed more consistent spontaneous contractions than their C2C12-derived counterparts. Then, we designed a new platform for multiple 3D muscle strips created from isolated primary muscle cells. Iterative optimization revealed that allowing the muscle cells to proliferate before seeding them on rounded pillars and being treated with a protease inhibitor greatly increased the yield of intact muscle strips. These muscle cells exhibited spontaneous contractions and were capable of matching electric stimulus frequencies at 1, 2, and 4 Hz with a variable force of

contraction. Western blots revealed that although the extracted primary tissue was a mix of Type I and Type II fibers, this identity was not retained by the dissociated satellite cells when cultured on Matrigel-coated glass in 2D. When cultured in spinal cord-conditioned media, primary skeletal muscle cells regained a mixed Type I/Type II fiber type identity. Cell source, 2D culture, and neuronal releasates are all important factors that influence skeletal muscle development *in vitro*.

3.2 Materials and Methods

3.2.1 Animal Welfare

Animal procedures were developed in accordance with Public Health Service Policy on Humane Care and Use of Laboratory Animals and reviewed and approved by the University of Illinois at Urbana-Champaign Institutional Animal Care and Use Committee. Cultures of primary skeletal muscle were from postnatal day 8-10 Long-Evans BluGill rats from an inbred colony maintained by our laboratory, according to previously established protocols (Millet *et al*, 2007).

3.2.2 Cell Culture Media

Primary Proliferation Medium (PPM) consists of 68% DMEM (Corning, Corning, NY), 20% Fetal Bovine Serum (FBS, ThermoFisher), 10% Horse Serum (HS, Thermofisher), 1% chicken embryo extract (CEE, US Biological Life Sciences, Swampscott, Massachusetts), and 1% penicillin-streptomycin (Cellgro Mediatech, Inc., Herndon, VA). Full media replacement occurred every 2-4 days, determined by phenol red pH indicator present in DMEM.

Primary Differentiation Medium (PDM) consists of 97% DMEM (Corning), 2% Horse Serum (HS, ThermoFisher) and 1% penicillin-streptomycin (Cellgro Mediatech, Inc., Herndon, VA). Full media replacement occurred every 2-4 days, determined by phenol red pH indicator present in DMEM.

C2C12 Proliferation Medium (CPM) consists of 88% DMEM, 10% FBS, 1% L-glutamine, and 1% penicillin-streptomycin. C2C12 Differentiation Medium (CDM) consists of 88% DMEM, 10% HS, 1% L-glutamine, and 1% penicillin-streptomycin. Full media replacement occurred every 2-4 days, determined by phenol red pH indicator present in DMEM.

3.2.3 Primary Skeletal Muscle Dissection, Dissociation, and Seeding for 2D Culture

A T-75 cell culture flask with (ThermoFisher Scientific, Waltham, MA) was coated for a minimum of 1 h at room temperature in 1% growth factor-reduced (GFR) Matrigel (BD Biosciences, San Jose, CA) for pre-plating cells. Additional T-25 cell culture flasks with (ThermoFisher Scientific) were coated for a minimum of 3 h at room temperature in 10% growth factor-reduced (GFR) Matrigel (BD Biosciences) for culturing cells. In both cases, the Matrigel was rinsed 1-2 times with sterile DMEM and flasks were kept wet until just before seeding. For each culture, 3 BluGill rat pups between postnatal day 8-10 (P8-P10) were decapitated. The gastrocnemius and soleus muscles were rapidly dissected from each leg of the pup and placed into ice-cold DMEM.

The muscles were moved into a laminar flow hood where they were minced into small (~1 mm^2) pieces using a pair of micro-scissors. They were then rinsed with fresh DMEM and transferred to a second petri dish with room temperature DMEM using a pipette with the tip cut to increase the distal diameter and reduce shear on the tissue. The tissue was then transferred in the same way to a conical tube with 1% v/v Pronase (EMD Millipore) in a water bath at 37° C for 1 h. The tissue gently shaken every 15 mins (alternatively, one can use a low-speed agitator placed inside the water bath). After 1 h, the suspension was spun down by low-speed centrifugation at 400 x g for 5 mins. The supernatant was carefully aspirated without disturbing the loose tissue pellet and stored in a separate 15 mL conical tube. The pellet was resuspended in 5 mL of 10% horse serum (HS, ThermoFisher) in DMEM (Corning) and mechanically triturated with a 10 mL serological pipette until the tissue pieces pass easily through the tip of the pipette. After allowing the suspension to settle, we collected the supernatant and added it to the original supernatant vial. The tissue was then resuspended in mL of 10% HS in DMEM and underwent a second round of mechanical dissociation using a fire-polished Pasteur pipette. After the tissue settled, the supernatant was again collected and added to the other supernatants. The pooled supernatants were strained through a 40 µm cell-strainer and centrifuged at 1000 x g for 10 mins. The supernatant was carefully aspirated (and discarded) and the pellet was resuspended in 8 mL of PPM. The entire 8 mL volume was then seeded in the 1% Matrigel-coated T-25 cell culture flask

and allowed to sit for 90-120 mins in the incubator. After the pre-plate, the cells were counted on a hemocytometer and resuspended at an ideal dilution. In this experiment, each T25 flask was seeded with ~100,000 cells and placed back in the incubator for 45 mins to allow the cells to settle before adding 5 mL of PM. The first media change was performed 24 h after seeding, followed by half media replacement every 2-4 days to maintain the presence of secreted extracellular cues while still providing a fresh source of nutrients. When the cells reached 75-80% confluence, the PPM was aspirated and the cells were rinsed 1-2 times with warm DMEM. The cells were then switched to PDM and underwent half media replacement every 2-4 days. All cells were maintained at 37° C and 5% CO2.

3.2.4 2D C2C12 Culture and Passaging

A T-75 cell culture flask with (ThermoFisher Scientific, Waltham, MA) was coated for a minimum of 1 h at room temperature in 1% growth factor-reduced (GFR) Matrigel (BD Biosciences, San Joses, CA). The C2C12 cells were gently thawed at 37° C and seeded in the coated T-75 cell culture flask in CPM. When they reached 80% confluency, they were either differentiated or passaged. Differentiation was performed by aspirating the CPM, rinsing the cells 1-2 times with warm DMEM, and switching them to CDM. The cells were passaged by aspirating the entire volume of media and replacing it with 5 mL TryplE (ThermoFisher) to release the cells from the substrate. The flasks with TryplE were placed in the incubator for 1 min. Once the cells were released, they were aspirated and mixed with 10 mL of 10% HS in DMEM before being centrifuged at 800 x g for 5 mins. The supernatant was aspirated and was replaced by 1 mL CPM. A cell count was performed on a hemocytometer and the cells were diluted according to the specific experiment before being re-seeded.

3.2.5 Spinal Cord Culture and Conditioned Medium

Spinal cords were extracted and cultured as previous described in Chapter 2, Section 2.2.3. We performed an initial full media replacement at 1 DIV and additional half media replacements at 3 and 5 DIV. The media was then conditioned for 48 h between 5 and 7 DIV before being collected. The spinal cord conditioned medium (SCCM) was then strained through

a 40 µm cell strainer, aliquoted, and stored at -20° C. Once a sufficient volume of SCCM was collected, skeletal muscle cultures were incubated in 60% PDM/40% SCCM and underwent half media replacements every 2-4 days.

3.2.6 Design and Fabrication of Multiple Muscle Array

PDMS platforms were fabricated using microfabricated silicon molds and manual post-processing. Silicon wafers were patterned by photolithography, etched using the Bosch process, and coated with polytetrafluoroethylene to facilitate removal of PDMS from the mold. PDMS (Sylgard 184) base and cross-linker were mixed at 10:1 ratio by weight, poured onto the silicon molds, and degassed using a vacuum desiccator. Samples were cured at 60° C for 12hr and peeled off the silicon mold. To achieve the T-shape of the pillars that is necessary to anchor muscle strips, caps were manually attached to the pillars. Approximately 200 x 200 µm square pieces were cut from 50 µm thick spin-coated PDMS films using a razor blade. These caps were then manually glued onto the pillars using uncured PDMS. Prior to tissue seeding, platforms were cleaned by sonicating in ethanol for 20 mins and then autoclaving at 121° C for 45 min while immersed in DI water. Platforms were then blow dried and sterilized by autoclaving at 121° C for another 45 min with 30 min drying time.

3.2.7 Formation of 3D Primary Skeletal Muscle Strip

For all tissue seeding procedures, extracellular matrix (ECM) solution was prepared on ice by first neutralizing Type I collagen from rat tail (Corning, Corning, NY) with 1N sodium hydroxide, 10X phosphate buffered saline (PBS), and molecular biology grade water, and then mixing pH-neutralized collagen thoroughly with growth factor reduced Matrigel (Corning). Collagen and Matrigel were used at final concentrations of 2mg/ml each. To form muscle strips, primary skeletal muscle cells were suspended in the ECM solution at a density of $2x10^6$ cells/mL. The cell-ECM mixture was pipetted into each well and polymerized at room temperature for 20 mins. During this time, samples were inverted every 2-4 mins. After this, samples were incubated at 37° C for 15 mins to complete the ECM polymerization. Samples were then flooded with PPM and incubated for 1 day while the myoblasts compacted the ECM gel and formed a strip. Full media

replacement was performed after 1 day. After 3 DIV, PPM was switched to PDM to facilitate myotube formation. All cells underwent full media changes every 2 days while being maintained at 37° C and 5% CO2.

3.2.8 Immunofluorescence and Histology

Tissues were rinsed in PBS and fixed in 4% (vol/vol) paraformaldehyde. Prior to immunostaining, tissues were permeabilized with 0.3% (vol/vol) Triton X-100 (EMD Millipore) and blocked with 5% Normal Goat Serum (NGS, Abcam, Cambridge, UK) for 30 mins. Tissues were incubated with alpha-actinin (1:2000, Abcam) and conjugated alpha bungarotoxin (1:1000 EMD Millipore) for 48 h at 4° C and washed with PBS. Tissues were incubated with Alexa Fluor 568 goat anti-mouse IgG in PBS for 2 h at room temperature in the dark.

3.2.9 Western Blot Protein Assay

Muscle samples were freeze dried by dry ice and stored at -80 °C until assay. Frozen tissue samples were mixed with 30 µL Tissue Protein Extraction Reagent (T-PER, Pierce, Rockford, IL), plus 0.2% SDS, 1 mM EDTA, and 1x complete protease inhibitor cocktail (CalBioChem, Darmstadt, DE) on ice, and homogenized. After 2-min incubation on ice, the samples were centrifuged at 14000 rpm for 2 mins, and the supernatant was transferred to a clean tube. Protein content of each sample was determined by BCA protein assay (Pierce, Rockford, IL). Total protein (25 µg/sample) was resolved in 8% SDS-PAGE and transferred to a 2-20% gradient gel membrane (Bio-Rad, Hercules, CA). Membranes were probed with 1:2000 dilution of mouse anti-biotin-myosin heavy chain type I and the same dilution of rabbit anti-biotin-myosin heavy chain type II antibody (Cellsignaling, Danvers, MA) overnight, and developed with SuperSignal West Femto Maximum Sensitivity Substrate (Pierce, Rockford, IL).

3.2.10 Statistical Analysis

Statistical differences were determined by ANOVA followed by the Tukey's post-hoc test for the change in outgrowth length and for amplitude of muscle contraction, and by Student's t-

test for acetylcholine cluster surface area. In all cases, significance is indicated by $p < 0.05$. Sample size is indicated within corresponding figure legends.

3.3 Results

3.3.1 Two-dimensional monocultures of primary skeletal muscle produce myotubes with larger fiber diameters and clusters of AChRs than C2C12

To develop a bioactuator that is capable of producing a biologically relevant amount of force and of mimicking natural *in vivo* development, we needed to determine an ideal cell source. We isolated and cultured primary skeletal muscle satellite cells from a combined sample of the gastrocnemius and soleus muscles from young (P8-P11) rats for comparison with myoblasts from the C2C12 murine cell line. Figures 3.1a,d show two representative images of C2C12 and primary skeletal muscle (1^o SkM) cultures on 10% Matrigel-coated glass at 10 DIV. The primary myotubes have a mean diameter 46.41 μm, more than 2-fold greater than the mean diameter of C2C12 myotubes (22.75 μm, Fig 1g). Fluorescently labeled α-bungarotoxin (α-BTX, green) was used to label nicotinic AChR. α-BTX appears more diffuse on C2C12 myotubes (Fig. 3.1b), as opposed to the brighter, more concentrated staining on primary muscle cells (Fig. 3.1e). The number of AChR clusters per myotube is not different between the primary and cell-line derived cultures (Fig. 3.1i), however the clusters on the primary myotubes have significantly larger surface areas than the C2C12-derived myotubes (Fig. 3.1h). Myosin heavy chains drive contraction by pulling against nearby actin molecules but cannot do this without being anchored by titin to the z-disk at the other end. Figures 3.1c,f show more organized z-disks (α-actinin, red) in primary muscle cells than C2C12, demonstrating a more complete and organized contractile apparatus. Additionally, a greater percentage of primary skeletal muscle cultures exhibited spontaneous contractions than C2C12 at 4, 7, and 10 DIV (Fig. 3.1j). However, by 14 DIV the percentage of dishes with spontaneously contracting fibers significantly decreased in both conditions. Primary skeletal muscle cultures on glass have greater diameters, larger AChR clusters, more clearly organized z-disks, and exhibit more spontaneous contractions than their C2C12 counterparts.

3.3.2 Design, fabrication, and optimization of an array for seeding multiple engineered, three-dimensional muscle tissues

Based on measurements from Figure 2.2d, we know that with no additional stimuli, cultured spinal cords can extend neuronal processes up to 1.66 mm from the spinal cord and that the diameter of a rat spinal cord is approximately 1.2 mm (Fig. 2.1a). The platform was designed such that the distance from the longitudinal midpoint of the platform to the longitudinal midpoint of the muscle strip is 1.5 mm. This was designed such that the distance from the lateral edge of the spinal cord to the lateral edge of the muscle strip is 0.7 mm. The pillars in the wells serve as anchoring points, much like tendons within the musculoskeletal system, for the muscle to adhere to during its compaction and development. The original design was 3D-printed using a poly (ethylene glycol) diacrylate (PEGDA) hydrogel. However, after one iteration on this design where I failed to account for the resolution of the laser, the stereolithographic apparatus (SLA) experienced severe technical problems and needed to be replaced. Searching for alternatives, I began a collaboration with Onur Aydin in the Saif Lab where he agreed to help re-design the devices for microfabrication. In the second design, we made the muscle strips smaller and increased the number of muscle strips on each side to two sets of pillars. By designing smaller strips, we believed it would increase innervation ratio and contraction force without greatly affecting the surface area available to the spinal cord for innervation. Figure 3.2a shows an early iteration of this device with the smaller wells and rectangular pillars with square caps. Seeding the satellite cells directly on the original design resulted in 53.6% of wells containing a full muscle strip (connecting both pillars), 25% of wells had broken, or 'half' strips where the tissue had collapsed around one pillar, and the remaining 21.4% of wells were completely empty by 4 DIV (Fig. 3.2d). By 8 DIV, only 7.1% of wells contained full strips while there were more than 2 times as many half strips at 8 DIV (64.3%) as there were at 4 DIV (25%) (Fig. 3.2d,e). Based on other experiments being done in both the Bashir and Saif labs with muscle cell culture, we decided to culture the primary satellite cells to 80% confluence before passaging them and seeding the devices (MT). This resulted in a greater ratio of intact strips at both 4 (10.7% more) and 8 (14.3% more) DIV (Fig. 3.2d,e), though the majority were still rupturing by 8 DIV. We hypothesized that this breakage may be occurring due to the sharp edges of the rectangular pillars (Fig. 3.2b)

rupturing the muscle strip as it contracted and switched to a rounded pillar (Fig. 3.2c) design for the next iteration of devices. This did not have a significant effect on the ratio of intact muscle strips through 8 DIV. Previous work has shown that the addition of a protease inhibitor, such as the broad-spectrum cathepsin inhibitor E-64, prolonged the lifespan of 3D muscle tissue cultures (Cvetkovic *et al*, 2017). The presence of the protease inhibitor E-64 in the primary skeletal muscle differentiation media resulted in 68.8% of wells containing full strips at 8 DIV, significantly greater than any other condition.

3.3.3 Engineered, three-dimensional muscle strips in multiple muscle array contract spontaneously and synchronize with patterned electrical stimulation

The functionality of the multi-muscle array was tested at baseline and with electrical stimulation and contractions were recorded by video (Fig. 3.3a). While more spontaneous twitching was observed in 2D cultures by 4 DIV, the trend is reversed and a greater percentage of dishes exhibited spontaneous muscle contractions by 8 DIV in the 3D cultures (Fig. 3.3b). Initially, the platform is submerged in differentiation media and provided no additional cues during baseline recording, where we observed a mean pillar displacement of 10.47 μm due to spontaneous muscle contractions (Fig. 3.3c). Stimulation was applied via a 10 V electric field at 1, 2, and 4 Hz which caused the muscle strips to alter both the frequency and amplitude of their contractions (Fig. 3.3d). To analyze the videos of muscle contraction, a region of interest (ROI) around one of the hydrogel pillars was isolated (shown as dotted rectangles in Fig. 3.3a) and its displacement plotted over time (Fig. 3.3c-d). The amplitude of contraction, or the displacement of the pillar within the ROI decreases from 9.78 μm at 1 Hz to 7.81 μm at 2 Hz to 4.28 μm at 4 Hz (Fig. 3.3e). The elicited contractions from the 1 Hz, 2 Hz, and 4 Hz stimuli were 0.944 Hz, 2.00 Hz, and 4.16 Hz respectively (Fig. 3.3f). Interestingly, the spontaneous contractions occurred at 2.32 Hz, but the spontaneous amplitude did not correlate to the trend observed during electrical stimulation. One possible explanation is the presence of predominantly Type II (fast-twitch) muscle fibers which would produce smaller forces is response to higher frequency stimulations, unlike Type I (slow-twitch) fibers.

3.3.4 Primary skeletal muscle fibers lose their source identity when cultured, but can recover a mixed fiber type identity in the presence of released spinal cord factors

To track the differentiation of muscle cells into different fiber subtypes, we compared the original whole muscle cocktail (WM, left and right gastrocnemius and soleus muscles), 2D dissociated satellite cell monocultures (2D), and 2D dissociated satellite cell monocultures in spinal cord-conditioned medium (SC CM). Muscle subtype was determined by performing Western blots for myosin heavy chain (MHC) isoforms commonly found in Type I (slow-twitch, MHC-S) or Type II (fast-twitch, MHC-F) muscle. Figures 3.4a,b are representative Western blots for all conditions and both muscle fiber isoforms. Both Type I and Type II muscle were present in the WM samples (Fig. 3.4a,b), as expected from previous characterization of rat gastrocnemius and soleus muscles (Kanda *et al*, 1986). The 2D cultures were flash frozen and analyzed after observing two consecutive days of spontaneous contractions between 4-7 DIV. The complete lack of labeled protein in the 2D cultures was highly unexpected due to the observed contractions before the sample was prepared for blotting. However, the 2D samples were run on the same gel as the WM and biotinylated ladder, a Ponceau stain revealed protein in those lanes after transfer (Fig. 3.4c), the staining procedure was performed at the same time under the same conditions for WM and 2D, and multiple repeats (three biological repeats and two technical repeats of each biological sample) were performed. When satellite cells were grown and differentiated in SCCM, the resultant fibers stained positively for both mature Type I and Type II isoforms of myosin heavy chain (Fig. 3.2a,b). This is consistent with previous work has demonstrated that fiber type differentiation is affected by the presence (or absence) of motor neurons during maturation (Pette and Staron, 1997).

3.4 Discussion

This chapter demonstrates the development of a novel platform for forming multiple, 3D muscle strips with primary skeletal muscle and makes a compelling case for the use of primary cells over the most common alternative, the C2C12 immortalized cell line. Primary muscle cells exhibit greater similarity to *in vivo* tissues, making them a better model for studying development, disease, and dystrophy. The multiple muscle array demonstrated here allows

researchers to not only study gross muscle properties such as alignment, force generation, and neuronal innervation, but also to investigate deeper histological and functional questions in 3D. This enables future experiments involving either contralateral (left-right pairing) or ipsilateral (flexor-extensor) coordination of multiple muscles. Additionally, by using an open-faced, modular platform, scientists can replace the healthy muscle tissue with diseased or dystrophic tissue and use conventional microscopy techniques to answer basic research questions or to test pharmacological interventions.

Previous work has demonstrated a lack of sarcomeric structure in C2C12 which was confirmed in our study (Langelaan *et al*, 2010; Fig. 3.1c,f). It has also been established that there is a strong correlation between the cross-sectional area of a myotube and its force output (Kayani *et al*, 2010). Another predictive metric of force production *in vivo* is innervation ratio (Totosy de Zepetnek *et al*, 1992). A greater number of innervated fibers will lead to a larger summed contraction, in part because neuronal excitation is an important step of myotube maturation (Engel and Karpati, 1968; Eftimie *et al*, 1991). Having larger, more defined AChR clusters on the primary muscle fibers is expected to aid with neuronal innervation and, subsequently, contractile force (Steinbach, 1981). Here, we demonstrated that primary cultures have larger myotube diameters, the AChR clusters had greater surface areas, and we observed more stronger, more consistent spontaneous contractions in primary cells than in C2C12. Due to these findings, we believe researchers should use primary skeletal muscle to best mimic natural, healthy physiology when possible.

We also used Western blots to assess mature myosin heavy chain isoforms linked with Type I (slow-twitch) and Type II (fast-twitch) muscle fibers. This revealed that 2D primary muscle cultures lose their fiber-type identity, despite performing spontaneous contractions on at least two consecutive days. The lack of protein present in the Western blots from the 2D cultures was unexpected. Spontaneous contractions were observed before the samples were processed for blotting. The total amount of protein (25 µg/well) was consistent across both the whole muscle (WM) and 2D conditions, the Ponceau stain for total protein showed significant protein on the blotting paper indicating the transfer was successful, and the staining protocols were identical

and performed simultaneously in both conditions. This experiment was repeated with 2 technical repeats for each of 3 biological repeats. Previous studies have shown that muscle fibers mature more slowly in 2D and that there are additional, immature forms of myosin heavy chain (e.g., MHC-8) (Langelaan *et al*, 2010; Grabowska *et al*, 2011; Schiaffino and Reggiani, 2011). We hypothesize that the spontaneous contractions observed in the 2D muscle cultures express this immature isoform of myosin heavy chain rather than the mature Type I and Type II MHC epitopes that our antibodies recognize. Motor neuron signaling also plays an integral role in muscle maturation and fiber type identity (Goubel and Marini, 1987; Burnham et al, 1997), which is supported by our findings with skeletal muscle cultures exposed to spinal cord conditioned media (Fig. 3.4).

Future experiments could demonstrate the effects of 2D monoculture *vs.* 3D monoculture *vs.* 3D co-culture with spinal neurons on muscle development. Based on previous literature we hypothesize that the 3D cultures will express mature Type I epitopes, even though the 2D cultures did not. The conditioned medium 2D skeletal muscle cultures expressed a mixed Type I/Type II identity which means they likely have the ability to mature into more pure Type I or Type II muscle based on stimulation type (Goubel and Marini, 1987; Burnham et al, 1997). Previous work also demonstrates that 3D muscle cultures mature more quickly than cultures performed in two dimensions, which informs our hypothesis that 3D muscle monocultures would be more likely to gain a fiber type identity than their 2D counterparts (Langelaan *et al*, 2010; Grabowska *et al*, 2011). This data takes a key step towards building better tissue engineering platforms because it is important to understand not only how the cells interact with each other, but also to what degree the platform affects how the cells develop.

The negative correlation of electric field-stimulus frequency and muscle-contraction amplitude (Fig. 3.3) in the 3D muscle strips can be at least partially explained by knowing the fiber type composition of the muscles themselves. Generally, fast twitch fibers generate high force for brief periods of time and reach exhaustion quickly while slow twitch fibers generate less force but can maintain it for longer periods of time without tiring. The pattern we observed in Figure 3.3c,d is puzzling because we see short duration contractions with moderate force output and no

evidence of rapid exhaustion. Even more strangely, the spontaneous contractions do not fit the pattern of the stimulated contractions (Fig. 3.3). While the spontaneous contractions were 2.32 Hz with a magnitude of 10.47 μm, the stimulated data would have predicted contractions at that frequency of ~8 μm instead. One possible explanation of the decreased force production for higher frequency electrical stimulation is that the muscles are approaching a tetanic state where they were not allowed to fully relax in between contractions. However, tetanus is usually induced at ≥ 50 Hz, while in this experiment we were more than 10X below that threshold (Verburg *et al*, 2001). Further information on the fiber type makeup of the muscle strips may reveal additional explanations for this behavior.

A platform with modular, functional 3D skeletal muscle strips could serve a variety of uses across disciplines. It would be an excellent tool for studying the pathology of muscular diseases and dystrophies and as a platform for studying the efficacy and modes of action of novel drugs for treatment. We could also visualize this muscle array as a model for Duchenne's muscular dystrophy, Steinart's disease, or age-related atrophy. Engineering functional 3D muscle tissues can also be useful in the production of edible lab-grown meat. Other variations on engineered, 3D muscles have been grown on spider silk, hydrogels, or on grooved substrates but suffer from small diameter muscle fibers, low myofiber density, and excessive extracellular matrix (Yao *et al*, 2016; Ostrovidov *et al*, 2014; Ko *et al*, 2019; Powell *et al*, 2002). Future generations of multi-muscle platforms can interface with neural tissues such as the spinal cord to become capable of autonomous or multi-limbed motor behaviors, goal-directed behaviors, or other higher tasks.

3.5 Figures

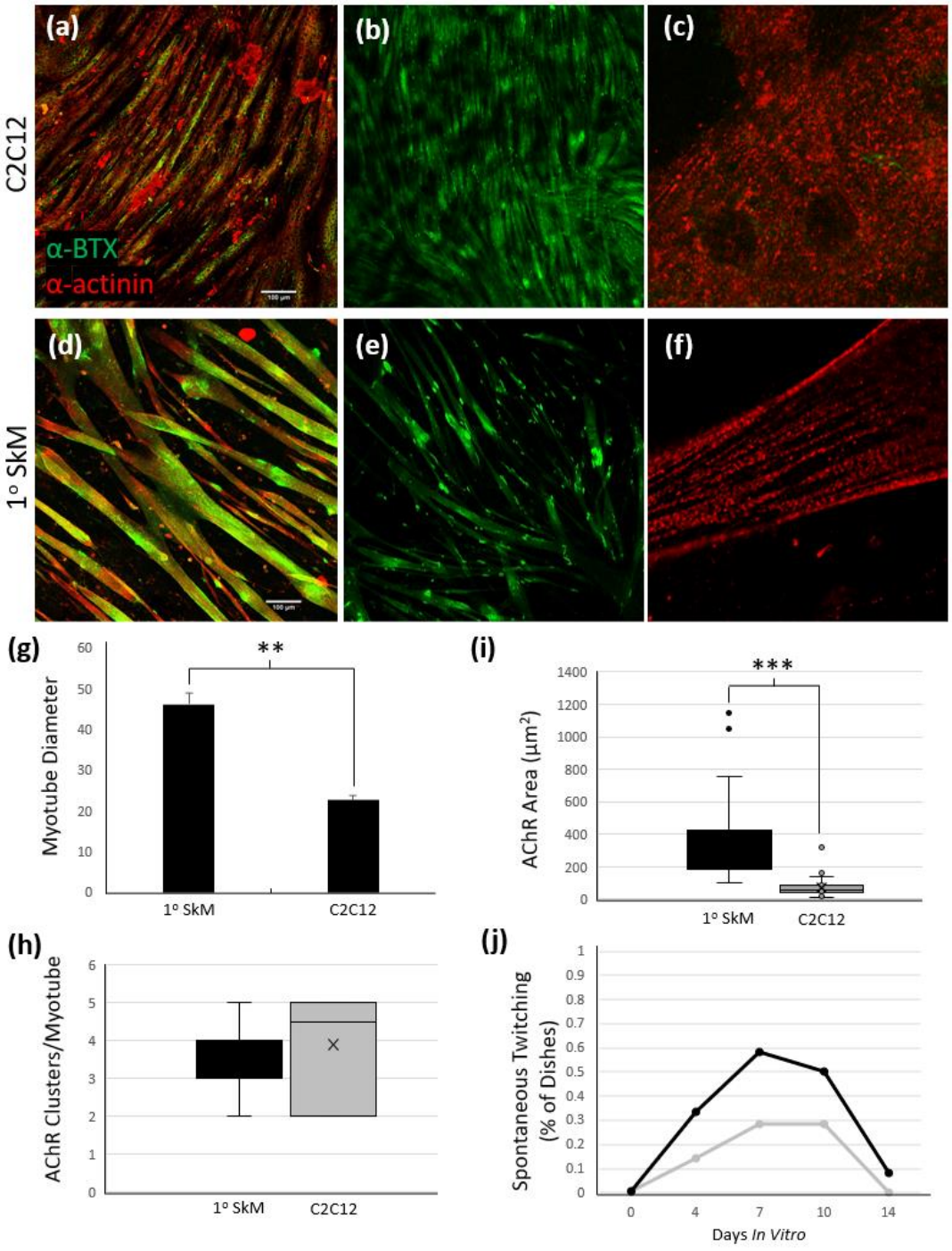

Figure 3.1. Primary skeletal muscle exhibits greater functionality than C2C12 in 2D culture. **(a)-(c)** 2D culture of C2C12 early myotubes at 5 DIV. **(a)** Muscle fibers (red, α-actinin) align with each other and have thin diameters. **(b)** Small clusters of acetylcholine receptors (green, α-bungarotoxin) are spread diffusely along the fibers. **(c)** Banding is not seen even at high

Fig. 3.1 (cont.). magnification. **(d)-(f)** 2D culture of primary skeletal muscle at 5 DIV. **(d)** Muscle fibers (red, α-actinin) have large diameters, well defined domains, and are well-aligned. **(e)** Large, bright clusters of acetylcholine receptors (green, α-bungarotoxin) are tightly grouped on the muscle fibers. **(f)** Clear striations due to well-formed z-disks are evident. **(g)** Primary skeletal muscle fibers are more than 2-fold greater than the diameters of age- and density-matched C2C12 cultures. **(h)** The number of AChR clusters per myotube is not significantly different between primary and C2C12-derived cultures, but **(i)** the AChR clusters on primary muscle are larger than those found on C2C12. **(j)** More dishes with primary skeletal muscle cultures exhibit spontaneous contractions than C2C12 cultures, but both peak around 7-10 DIV that decreases by 14 DIV.

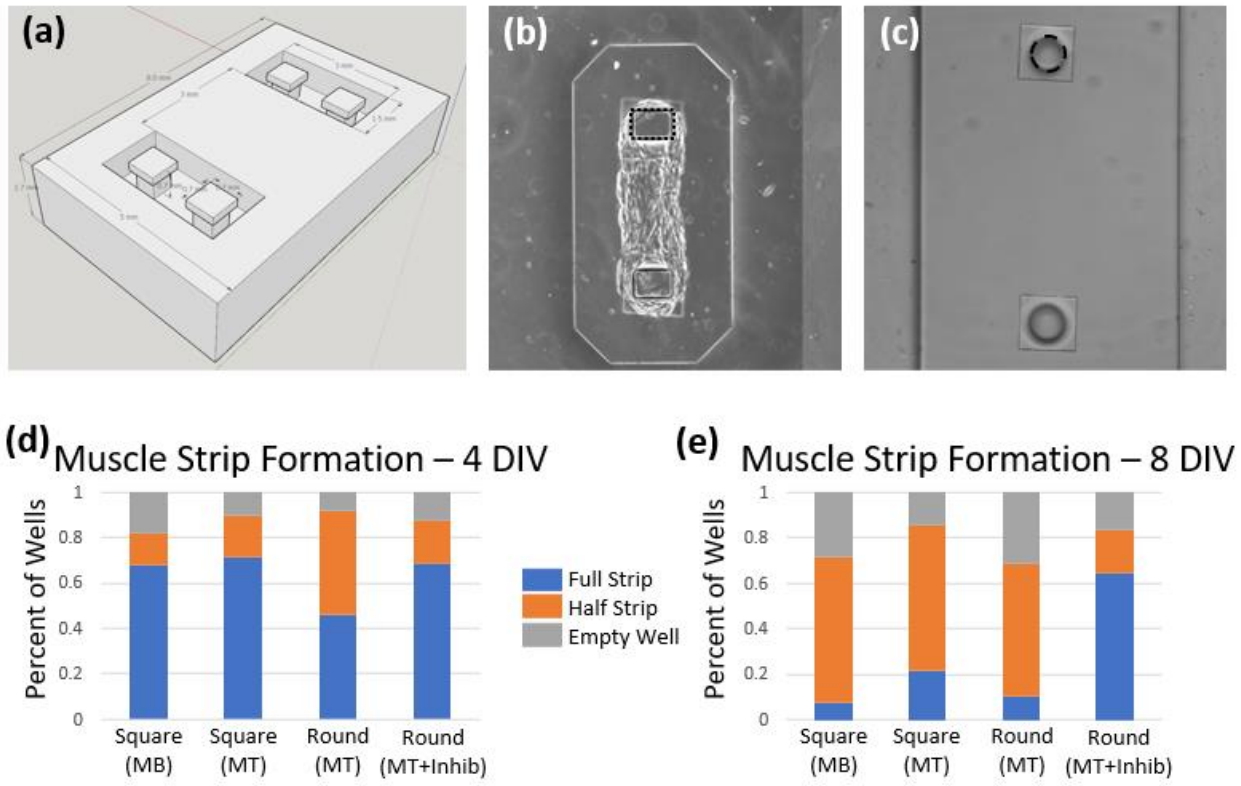

Figure 3.2. Design of a platform for the innervation of multiple muscle strips from a cultured spinal cord. **(a**) CAD for the first iteration of microfabricated device. **(b)** Example of a successful primary muscle strip that was seeded on square pillars (indicated by dotted box). **(c)** Example of the rounded pillars (indicated by dotted box) that were designed to reduce shearing of the muscle on the sharp corners in (b). **(d)-(e)** The percent of wells that contained a full strip wrapped around both pillars, a half strip where the muscle had collapsed around a single pillar, or that were completely empty in each iteration of the device at **(d)** 4 DIV and **(e)** 8 DIV. First, we mixed primary myoblast precursors with the collagen-Matrigel ECM and seeded them directly on the platform. To improve our strip yield, we delayed seeding until we expanded the primary culture and passaged it one time. Still seeing strip breakages, we rounded the anchoring pillars expecting that to improve strip yield. The most effective improvement made was adding the broad-spectrum cathepsin inhibitor, E-64 which resulted in a majority of intact muscle strips by 8 DIV.

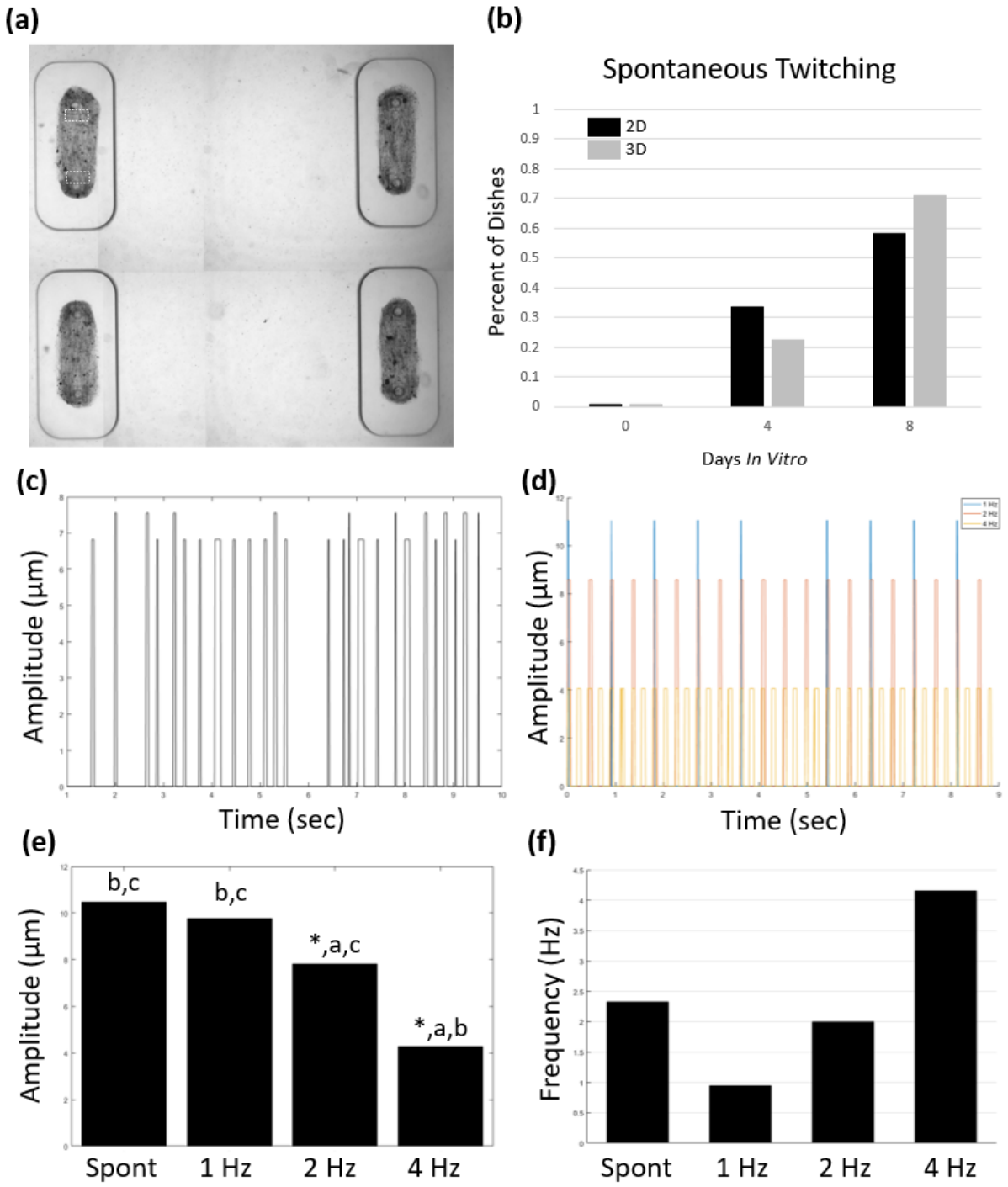

Figure 3.3. 3D muscle cultures perform both spontaneous and elicited contractions in the novel device. **(a)** Two pairs of two parallel primary skeletal muscle strips are seeded in the microfabricated device. White rectangles indicate the region of interest (ROI) where we measured deflection of the pillars. **(b)** No significant differences were observed in the number of dishes that exhibit spontaneous contraction at 4 or 8 DIV between 2D and 3D culture.

Fig. 3.3 (cont.). (c) Raw spontaneous contraction data of a single muscle strip over 10 s. **(d)** Raw contractile data of a muscle strip while being stimulated by an electrical field at 1 Hz, 2 Hz, and 4 Hz. **(e)** Spontaneous contractions caused greater pillar deflection than was observed at 2 and 4 Hz but was not different from the 1 Hz stimulated amplitudes. The magnitudes of muscle contraction at 1 Hz were greater than those at 2 Hz and 4 Hz and the contractions under 2 Hz stimulation were larger than those at 4 Hz. * denotes significant difference from spontaneous contractions, 'a' denotes significant differences from 1 Hz contractions, 'b' denotes significant differences from 2 Hz contractions, and 'c' denotes significant differences from 4 Hz contractions **(f)** Muscle contractions occur spontaneously at 2.32 Hz and synchronize perfectly to 1 Hz stimulation (0.944 Hz), 2 Hz stimulation (2.00 Hz), and 4 Hz stimulation (4.16 Hz).

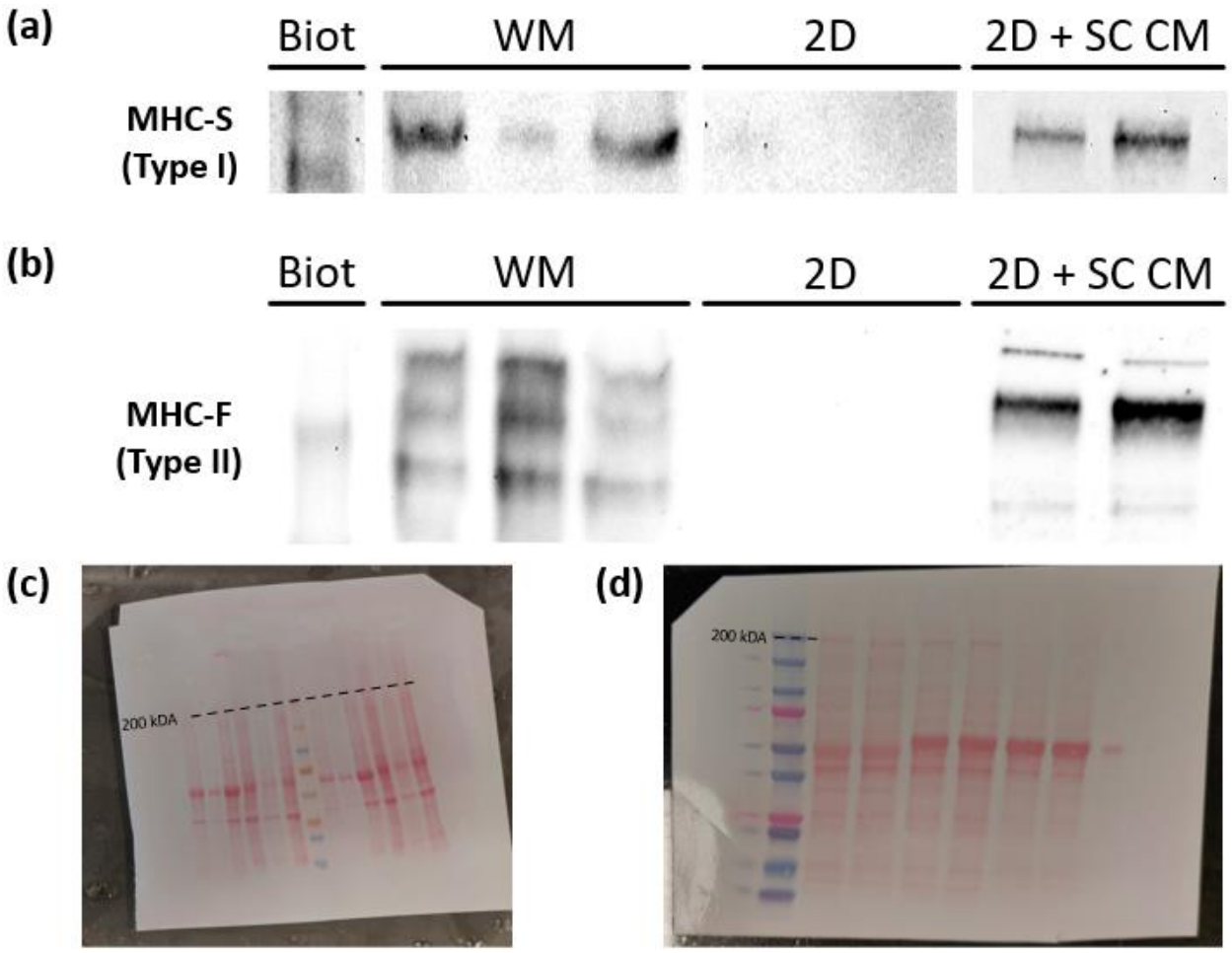

Figure 3.4. Determination of muscle fiber type identity across different culture conditions **(a)** Western blot for myosin heavy chain for slow twitch muscle (MHC-S) shows strong bands at ~200 kDa in the whole muscle (WM, rat gastrocnemius and soleus) samples. There is no discernable signal in the 2D skeletal muscle cultures (P8-P11 rats, 3 DIV Differentiation Media, 3 DIV Proliferation Media). The 200 kDa MHC-S band returns when 2D skeletal muscle cultures are incubated in conditioned spinal cord media (SC CM). **(b)** Western blot for myosin heavy chain for fast twitch muscle (MHC-F) shows multiple strong bands above ~200 kDa, including one at ~223 kDa in the whole muscle tissue (WM) samples. There is no discernable signal in the 2D SkM cultures. When grown in SC CM, 2D SkM cultures once again express multiple bands around 223 kDa for MHC-F. The multiple bands are likely from the different isoforms of MHC-F (Type IIa-c fibers). **(c)** A ponceau stain shows that protein was transferred onto the membrane for two samples each of WM (left of the ladder) and 2D conditions (right of the ladder). **(d)** A ponceau stain for the conditioned medium blots shows robust protein transfer across all 6 experimental lanes

3.6 References

1. Kislinger, T., Gramolini, A. O., Pan, Y., Rahman, K., MacLennan, D. H., & Emili, A. (2005). Proteome dynamics during C2C12 myoblast differentiation. *Molecular & Cellular Proteomics*, *4*(7), 887-901.
2. Bajaj, P., Marchwiany, D., Duarte, C., & Bashir, R. (2013). Patterned Three-Dimensional Encapsulation of Embryonic Stem Cells using Dielectrophoresis and Stereolithography. *Advanced healthcare materials*, *2*(3), 450-458.
3. Al-Rekabi, Z., & Pelling, A. E. (2013). Cross talk between matrix elasticity and mechanical force regulates myoblast traction dynamics. *Physical biology*, *10*(6), 066003.
4. Fu, A. K., Fu, W. Y., Cheung, J., Tsim, K. W., Ip, F. C., Wang, J. H., & Ip, N. Y. (2001). Cdk5 is involved in neuregulin-induced AChR expression at the neuromuscular junction. *Nature neuroscience*, *4*(4), 374.
5. Benveniste, O., Jacobson, L., Farrugia, M. E., Clover, L., & Vincent, A. (2005). MuSK antibody positive myasthenia gravis plasma modifies MURF-1 expression in C2C12 cultures and mouse muscle *in vivo*. *Journal of neuroimmunology*, *170*(1-2), 41-48.
6. Yaffe, D., & Saxel, O. R. A. (1977). Serial passaging and differentiation of myogenic cells isolated from dystrophic mouse muscle. *Nature*, *270*(5639), 725.
7. Xu, H., Christmas, P., Wu, X. R., Wewer, U. M., & Engvall, E. (1994). Defective muscle basement membrane and lack of M-laminin in the dystrophic dy/dy mouse. *Proceedings of the National Academy of Sciences*, *91*(12), 5572-5576.
8. Monaco, A. P., Neve, R. L., Colletti-Feener, C., Bertelson, C. J., Kurnit, D. M., & Kunkel, L. M. (1986). Isolation of candidate cDNAs for portions of the Duchenne muscular dystrophy gene. *Nature*, *323*(6089), 646.
9. Zubrzycka-Gaarn, E. E., Bulman, D. E., Karpati, G., Burghes, A. H., Belfall, B., Klamut, H. J., ... & Worton, R. G. (1988). The Duchenne muscular dystrophy gene product is localized in sarcolemma of human skeletal muscle. *Nature*, *333*(6172), 466.
10. Choi, S. W., Yeh, Y. C., Zhang, Y., Sung, H. W., & Xia, Y. (2010). Uniform beads with controllable pore sizes for biomedical applications. *Small*, *6*(14), 1492-1498.
11. Mudera, V., Smith, A. S. T., Brady, M. A., & Lewis, M. P. (2010). The effect of cell density on the maturation and contractile ability of muscle derived cells in a 3D tissue-engineered skeletal muscle model and determination of the cellular and mechanical stimuli required for the synthesis of a postural phenotype. *Journal of cellular physiology*, *225*(3), 646-653.
12. Gieseck III, R. L., Hannan, N. R., Bort, R., Hanley, N. A., Drake, R. A., Cameron, G. W., ... & Vallier, L. (2014). Maturation of induced pluripotent stem cell derived hepatocytes by 3D-culture. *PloS one*, *9*(1), e86372.
13. Bi, Y. A., Kazolias, D., & Duignan, D. B. (2006). Use of cryopreserved human hepatocytes in sandwich culture to measure hepatobiliary transport. *Drug Metabolism and Disposition*, *34*(9), 1658-1665.
14. Chaubey, A., Ross, K. J., Leadbetter, R. M., & Burg, K. J. (2008). Surface patterning: tool to modulate stem cell differentiation in an adipose system. *Journal of Biomedical Materials Research Part B: Applied Biomaterials*, *84*(1), 70-78.
15. Lee, M. K., Rich, M. H., Baek, K., Lee, J., & Kong, H. (2015). Bioinspired tuning of hydrogel permeability-rigidity dependency for 3D cell culture. *Scientific reports*, *5*, 8948.

16. Cvetkovic, C., Raman, R., Chan, V., Williams, B. J., Tolish, M., Bajaj, P., ... & Bashir, R. (2014). Three-dimensionally printed biological machines powered by skeletal muscle. *Proceedings of the National Academy of Sciences*, *111*(28), 10125-10130.
17. Capers, C. R. (1960). Multinucleation of skeletal muscle *in vitro*. *The Journal of Cell Biology*, *7*(3), 559-565.
18. Langelaan, M. L., Boonen, K. J., Rosaria-Chak, K. Y., van der Schaft, D. W., Post, M. J., & Baaijens, F. P. (2011). Advanced maturation by electrical stimulation: Differences in response between C2C12 and primary muscle progenitor cells. *Journal of tissue engineering and regenerative medicine*, *5*(7), 529-539.
19. Grabowska, I., Szeliga, A., Moraczewski, J., Czaplicka, I., & Brzóska, E. (2011). Comparison of satellite cell-derived myoblasts and C2C12 differentiation in two-and three-dimensional cultures: changes in adhesion protein expression. *Cell biology international*, *35*(2), 125-133.
20. Talbot, J., & Maves, L. (2016). Skeletal muscle fiber type: using insights from muscle developmental biology to dissect targets for susceptibility and resistance to muscle disease. *Wiley Interdisciplinary Reviews: Developmental Biology*, *5*(4), 518-534.
21. Pette, D., & Staron, R. S. (1990). Cellular and molecular diversities of mammalian skeletal muscle fibers. *Reviews of Physiology, Biochemistry and Pharmacology, Volume 116*, 1-76.
22. Schiaffino, S. T. E. F. A. N. O., & Reggiani, C. A. R. L. O. (1994). Myosin isoforms in mammalian skeletal muscle. *Journal of applied physiology*, *77*(2), 493-501.
23. Schiaffino, S., & Reggiani, C. (1996). Molecular diversity of myofibrillar proteins: gene regulation and functional significance. *Physiological reviews*, *76*(2), 371-423.
24. Pette, D., & Staron, R. S. (2000). Myosin isoforms, muscle fiber types, and transitions. *Microscopy research and technique*, *50*(6), 500-509.
25. Pette, D., & Staron, R. S. (1997). Mammalian skeletal muscle fiber type transitions. *International review of cytology*, *170*, 143-223.
26. Millet, L. J., Stewart, M. E., Sweedler, J. V., Nuzzo, R. G., & Gillette, M. U. (2007). Microfluidic devices for culturing primary mammalian neurons at low densities. *Lab on a Chip*, *7*(8), 987-994.
27. Cvetkovic, C., Ferrall-Fairbanks, M. C., Ko, E., Grant, L., Kong, H., Platt, M. O., & Bashir, R. (2017). Investigating the life expectancy and proteolytic degradation of engineered skeletal muscle biological machines. *Scientific reports*, *7*(1), 3775.
28. Kanda, K., Hashizume, K., Nomoto, E., & Asaki, S. (1986). The effects of aging on physiological properties of fast and slow twitch motor units in the rat gastrocnemius. *Neuroscience research*, *3*(3), 242-246.
29. Kayani, A. C., Close, G. L., Dillmann, W. H., Mestril, R., Jackson, M. J., & McArdle, A. (2010). Overexpression of HSP10 in skeletal muscle of transgenic mice prevents the age-related fall in maximum tetanic force generation and muscle Cross-Sectional Area. *American Journal of Physiology-Regulatory, Integrative and Comparative Physiology*, *299*(1), R268-R276.
30. Totosy de Zepetnek, J. E., Zung, H. V., Erdebil, S. E. R. A. P., & Gordon, T. E. S. S. A. (1992). Innervation ratio is an important determinant of force in normal and reinnervated rat tibialis anterior muscles. *Journal of neurophysiology*, *67*(5), 1385-1403.

31. Engel, W. K., & Karpati, G. (1968). Impaired skeletal muscle maturation following neonatal neurectomy. *Developmental biology*, *17*(6), 713-723.
32. Eftimie, R., Brenner, H. R., & Buonanno, A. (1991). Myogenin and MyoD join a family of skeletal muscle genes regulated by electrical activity. *Proceedings of the National Academy of Sciences*, *88*(4), 1349-1353.
33. Steinbach, J. H. (1981). Developmental changes in acetylcholine receptor aggregates at rat skeletal neuromuscular junctions. *Developmental biology*, *84*(2), 267-276.
34. Schiaffino, S., & Reggiani, C. (2011). Fiber types in mammalian skeletal muscles. *Physiological reviews*, *91*(4), 1447-1531.
35. Goubel, F., & Marini, J. F. (1987). Fibre type transition and stiffness modification of soleus muscle of trained rats. *Pflügers Archiv*, *410*(3), 321-325.
36. Burnham, R., Martin, T., Stein, R., Bell, G., MacLean, I., & Steadward, R. (1997). Skeletal muscle fibre type transformation following spinal cord injury. *Spinal cord*, *35*(2), 86-91.
37. Baldwin, K. M., & Tipton, C. M. (1972). Work and metabolic patterns of fast and slow twitch skeletal muscle contractingin situ. *Pflügers Arch*
38. Verburg, E., Thorud, H. M. S., Eriksen, M., Vøllestad, N. K., & Sejersted, O. M. (2001). Muscle contractile properties during intermittent nontetanic stimulation in rat skeletal muscle. *American Journal of Physiology-Regulatory, Integrative and Comparative Physiology*, *281*(6), R1952-R1965.
39. Yao, D., Liu, H., & Fan, Y. (2016). Silk scaffolds for musculoskeletal tissue engineering. *Experimental Biology and Medicine*, *241*(3), 238-245.
40. Ostrovidov, S., Hosseini, V., Ahadian, S., Fujie, T., Parthiban, S. P., Ramalingam, M., ... & Khademhosseini, A. (2014). Skeletal muscle tissue engineering: methods to form skeletal myotubes and their applications. *Tissue Engineering Part B: Reviews*, *20*(5), 403-436.
41. Ko, E., Yu, S. J., Pagan-Diaz, G. J., Mahmassani, Z., Boppart, M. D., Im, S. G., ... & Kong, H. (2019). Matrix topography regulates synaptic transmission at the neuromuscular junction. *Advanced Science*, *6*(6), 1801521.
42. Powell, C. A., Smiley, B. L., Mills, J., & Vandenburgh, H. H. (2002). Mechanical stimulation improves tissue-engineered human skeletal muscle. *American Journal of Physiology-Cell Physiology*, *283*(5), C1557-C1565.

CHAPTER 4. EMERGENCE OF FUNCTIONAL NEUROMUSCULAR JUNCTIONS IN AN ENGINEERED, MULTICELLULAR SPINAL CORD-MUSCLE BIOACTUATOR

This chapter heavily utilizes the following publication. According to APL Bioengineering, ResearchGate, and Google Scholar, this publication has been cited 3 times and has over 4700 full-text downloads in the ~1 year since it was published.

[1]Kaufman, C. D., Liu, S. C., Cvetkovic, C., Lee, C. A., Naseri Kouzehgarani, G., Gillette, R., Bashir, R., & Gillette, M. U. (2020). Emergence of functional neuromuscular junctions in an engineered, multicellular spinal cord-muscle bioactuator. *APL bioengineering*, *4*(2), 026104.

4.1 Introduction

Biological robotics is a growing field which derives inspiration from biological systems for real world applications. Challenges that have historically plagued more traditional, rigid robotics include interacting with biological tissue, self-repair, and collapsing into biodegradable parts after completion of a task (Cvetkovic *et al*, 2018). Biology has already solved many of these problems faced by rigid robots in creative ways. By abstracting and recapitulating these solutions we will be able to replicate increasingly natural, complex motor behaviors with novel engineering approaches to biorobotics (Majidi, 2013).

Mimicking how organisms actuate is one approach that has already led to bio-inspired devices and machines (Vincent *et al*, 2006; Han *et al*, 2017; Gul *et al*, 2016; Full, 2001; Ricotti and Menciassi, 2012). Recent work on biological soft robots has already produced 'biobots' that recapitulate a variety of locomotive behaviors; *e.g.* crawling, swimming, walking, jumping (Gul *et al*, 2016; Park *et al*, 2016; Wen *et al*, 2013; Low, 2007; Herr and Dennis, 2004; Cvetkovic *et al*, 2014; Pagan-Diaz *et al*, 2018; Kovač, 2013; Bartlett *et al*, 2015). These locomotive biohybrid

[1] Contributions: C.D.K. designed and performed experiments, conducted analysis, and wrote the manuscript. S.C.L. designed and performed experiments. C.C. designed materials, performed SEM imaging, and performed experiments. C.L. designed and performed experiments. G.N.K. performed experiments and ran statistical models. R.B. analyzed data. R.G. analyzed data. M.U.G. designed experiments and analyzed data. All authors edited the manuscript.

actuators are produced primarily with either cardiac or skeletal muscle, and may also use flexible materials such as aluminum, shape metal alloys, hydrogels (Park *et al*, 2016; Low, 2007), and soft plastics (Mosadegh *et al*, 2014; Majidi, 2013; Full, 2001; Wirekoh and Park, 2017; Nawroth *et al*, 2012). Cardiac muscle provides rhythmic contractions without requiring external input, but the intrinsic frequency of those cells is not easily modified, thereby limiting the scope of potential behaviors. Skeletal muscle allows for a wider array of potential behaviors but requires extrinsic control mechanisms such as electric fields, optogenetics, and chemical stimulation (Vincent *et al*, 2006; Park *et al*, 2016; Webster *et al*, 2016; Vincent *et al*, 2006; Webster *et al*, 2016; Cvetkovic *et al*, 2017; Uzel *et al*, 2016; Frank and Fischbach, 1979; Kiehn, 2006).

Previous work on skeletal muscle has commonly used C2C12-derived myoblasts to study muscle differentiation, force production, and neuromuscular interactions *in vitro* (Kislinger *et al*, 2005; Bajaj *et al*, 2011; Al-Rekabi and Pelling, 2013; Fu *et al*, 2001; Benveniste *et al*, 2005). C2C12 is also the most common cell line used when developing biohybrid machines (Osaki *et al*, 2018; Pagan-Diaz *et al*, 2018; Umbach *et al*, 2012; Smith *et al*, 2016; Li *et al*, 2019; Raman *et al*, 2016; Cvetkovic *et al*, 2014). Research has demonstrated that engineered C2C12 muscle tissues maintain a consistent degree of contraction for over 250 days after seeding (Cvetkovic et al, 2017). Actuation independent from experimenter influence requires a wireless, onboard control unit. Vertebrates have solved this through neural control of muscle tissues. Some previous work has bypassed motor neuron input to the muscle entirely through extrinsic control mechanisms, such as applied electric fields (Han, 2017), optogenetics (Park, 2016; Uzel, 2016; Raman, 2016), and chemical stimulation (Han, 2017; Webster, 2016; Cvetkovic, 2017). However, neurons and muscles exhibit different phenotypes and behaviors when in monoculture or when cultured together (Fischbach, 1979). Therefore, to create an *in vitro* model of the NMJ, it is important to co-culture these cells to allow for emergent organization and multicellular interactions to occur *in vitro*.

In vertebrates, complex locomotor tasks are primarily controlled by spinal cord and brainstem networks. While these networks are heavily modulated by the brainstem, most of the pattern and rhythm generation involved with locomotion are housed within the spinal cord. An intact rat spinal cord has three distinct anatomical regions from rostral to caudal: cervical,

thoracic, and lumbar (Cazalet *et al*, 1995). The lumbar enlargement is a widened area of the caudal spinal cord that serves as the attachment site for nerves of the lower limbs. CPGs are complex, oscillatory networks within the spinal cord which govern a range of rhythmic actions from locomotion to breathing (Frank and Fischbach, 1979). Quadrupedal locomotion requires the coordination of flexor-extensor muscle pairing simultaneously within a limb, and between ipsi- and contralateral pairs of limbs. This is performed by spinal circuits known as central pattern generators (CPGs). CPGs are roughly symmetrical circuits that generally consist of lateral excitatory interneurons, medial inhibitory interneurons, and output information to ventrolateral cholinergic motor neurons. The function of a CPG is to produce patterned output from non-patterned input. Previous work has identified the first and second lumbar vertebrae (L1-L2) as the location of the hind-limb locomotor CPG in rats (Cazalets *et al*, 1995).

Embryonic stem cell (ESC)-derived neuron-like cells can interact with skeletal muscle to cause small contractions (Cvetkovic *et al*, 2017; Uzel *et al*, 2016). However, stem cell-derived neurons share only a subset of known characteristics with rodent motor neurons and contain cell types in varying ratios that are not fully identified (Quadrato *et al*, 2017; Spangler *et al*, 2018). Human induced pluripotent stem cells (hIPSCs) have been used to form 3D NMJs that contain many of the sub-cellular components of *in situ* NMJs (Osaki *et al*, 2018; Maffioletti *et al*, 2018; Bakooshli *et al*, 2019). While the activity of stochastically formed neuronal networks can demonstrate synchronous activity (Van Pelt *et al*, 2004), functional *in situ* neuronal circuits are highly organized for specific purposes. The processes of natural embryonic development that shape the spinal cord are more robust than current stem cell differentiation protocols and the resulting circuits are more consistent and well-characterized. The rat spinal cord contains approximately 36 million cells, of which over 10 million are neurons (Bjugn & Gundersen, 1993). It is beyond current capabilities to reproduce such a complex, multicellular system using embryoid bodies, organoids, or other stem cell-derived neural tissues.

Here we use a mixture of top-down and bottom-up design principles to take advantage of the intrinsic locomotor circuitry of the spinal cord and generate patterned contractions of a self-assembled, three-dimensional (3D) muscle tissue by chemical stimulation of an isolated, intact locomotor CPG. Bottom-up design of the muscle allows us to develop a tissue that is an

appropriate size to interface with a rat spinal cord while also minimizing necrosis (Pagan-Diaz *et al*, 2018). Utilizing top-down design principles, we interface an intact locomotor CPG to drive muscle contraction with the engineered muscle tissue to produce a multi-cellular system capable of spinally-driven muscle contraction. We confirmed the presence of pre- and post-synaptic structural components of a motor unit on the 3D striated muscle. We also showed that while the muscle contracts spontaneously, the contractile frequency is controllable through the application and subsequent blockade of neurotransmitter applied to the spinal cord. Neurochemical stimulation of the spinal cord generated patterned contractions of the muscle, indicating the functionality of the CPG. This 'spinobot' is a novel biohybrid robot with multicellular architecture that demonstrates CPG-driven muscle contractions.

4.2 Materials and Methods

4.2.1 Animal Welfare

Animal procedures were developed in accordance with Public Health Service Policy on Humane Care and Use of Laboratory Animals and reviewed and approved by the University of Illinois at Urbana-Champaign Institutional Animal Care and Use Committee. Cultures of primary hippocampal neurons were from postnatal day 1-2 Long-Evans BluGill rats from an inbred colony maintained by our laboratory, according to previously established protocols (Millet *et al*, 2007).

4.2.2 Spinal Cord Extraction and Seeding for 2.5-D Culture

A 35 mm Petri dish with a 14 mm glass coverslip bottom (MatTek Corporation, Ashland, MA) was coated for a minimum of 1 h in 0.1% gelatin (EMD Millipore, Burlington, MA). The gelatin was rinsed 3-5 times with sterile PBS, followed by the addition of 100 µL of 1% Matrigel onto each glass coverslip. The Petri dishes were then placed in the incubator for 60-90 mins to allow for Matrigel polymerization. For each dish, a single BluGill rat pup between postnatal day 1-5 (P1-P5) was decapitated. The vertebral column was rapidly dissected from the pup and cleaned to expose the vertebrae. A small section of the spinal column from the T13 to L2 vertebrae was isolated using a pair of small scissors. Then, making two diagonal cuts at ± 45 degrees from the ventral midline, the ventral bone was removed thereby exposing the spinal cord. The spinal cord was then rapidly and gently dissected with a pair of fine-tipped tweezers.

The spinal cord was placed on ice in 5 mL HibernateA (Life Technologies, Gaithersburg, MD) where the dorsal root ganglia were removed. The spinal cord was moved to a laminar flow hood where it was rinsed in fresh HibernateA. Using forceps, the spinal cord was seeded with the ventral side facing down directly onto the polymerized Matrigel. The spinal cords were placed back in the incubator for 45 mins to allow the spinal cord to settle before adding 5 mL Spinal Cord Growth Medium (SCGM) consisting of 96.825% NeurobasalA (Life Technologies) without L-glutamine or phenol red (Life Technologies), 2% GS21 (MTI-GlobalStem, Gaithersburg, MD), 1% penicillin-streptomycin (Cellgro Mediatech, Inc., Herndon, VA), 0.125% Glutamax (Life Technologies), 0.025% Brain Derived Neurotrophic Factor (10 ng/mL, EMD Millipore) , and 0.025% Nerve Growth Factor (1 ng/mL, EMD Millipore). All cells were maintained at 37° C and 5% CO2, with half media replacement every 2-4 days. Half media changes were implemented to maintain the presence of secreted extracellular cues while still providing a fresh source of nutrients.

4.2.3 Design and Fabrication of Parts

A commercial stereolithography apparatus (SLA, 250/50, 3D Systems) was modified for polymerization as previously described (Cvetkovic, *et al*., 2014). Parts generated using computer-aided design software were exported to 3D Lightyear software (v1.4, 3D Systems), which sliced the part into layers. Prepolymer solutions for biobots and holders are described previously (Cvetkovic, *et al*., 2014). For fabrication of biobots, an 18 × 18-mm-square cover glass was secured to the center of a 35-mm culture dish before fabrication. For biobot holders, cover glass slides were first treated with 2% (vol/vol) 3-(trimethoxysilyl)propyl methacrylate (EMD Millipore) in 200-proof ethanol (100% EtOH) for 5 min and then washed in 100% EtOH for 3 min, dried, and secured to the center of a 35-mm dish. Following fabrication, each structure was rinsed in PBS, sterilized in 70% EtOH for 1 h, and allowed to re-swell in PBS for at least 1 h. This protocol has been previously published with additional detail (Cvetkovic, *et al*., 2014).

4.2.4 Formation of Muscle Strip

C2C12 murine myoblasts were maintained in muscle growth medium (CPM) consisting of Dulbecco's Modified Eagle Medium with L-glutamine and sodium pyruvate (DMEM, Corning

Cellgro), supplemented with 10% FBS (Lonza, Alpharetta, GA), 1% penicillin-streptomycin, and 1% L-glutamine (both Cellgro Mediatech, Inc., Herndon, VA) or muscle differentiation medium (CDM) which consisted of DMEM supplemented with 10% horse serum (HS, Lonza, Alpharetta, GA), 1% penicillin-streptomycin, and 1% L-glutamine. During cell seeding, C2C12 cells suspended in CPM were mixed with an ice-cold liquid solution of Matrigel (30% of total cell–matrix volume, BD Biosciences), fibrinogen (4 mg/ml, EMD Millipore), thrombin from bovine plasma (0.5 U/(mg fibrinogen), EMD Millipore). C2C12 cells were suspended in CPM at a concentration of 5 × 106 cells/ml and added to each holder in a total volume of 120 µL unless otherwise specified. After 1 h, 4 mL of CPM was added. After 24 h, biobots were released from holders and switched to CDM with anti-fibrinolytic 6-ACA (EMD Millipore) and human IGF-1 (EMD Millipore) as noted. All cells and biobots were maintained at 37° C and 5% CO2, with full media replacement every 1-2 days. This protocol has been previously published with additional detail (Cvetkovic *et al*, 2014; Raman *et al*, 2017).

4.2.5 Spinal Cord Extraction and Seeding on Biobot

For each biobot, a single neonatal spinal cord was extracted as described above. C2C12-seeded biobots at 7 DIV were also brought into the hood at this time. The media was aspirated from the biobot Petri dishes and the spinal cord was carefully seeded onto the muscle strip. The multicellular biobot was placed in a standard incubator at 37° C and 5% CO_2 for 90 mins before adding 5 mL of co-culture medium (CCM) consisting of 50% NeurobasalA without L-glutamine or phenol red, 50% Dulbecco's Modified Eagle Medium with L-glutamine and sodium pyruvate, 10% FBS, 2% GS21, 1% penicillin-streptomycin, 0.125% Glutamax, 0.025% Brain Derived Neurotrophic Factor, and 0.025% Nerve Growth Factor. All cells and biobots were maintained at 37 °C and 5% CO2, with full media replacement every 1-2 days.

4.2.6 Chemical Stimulation and Recording

The spinal cord was excised and placed in the recording chamber where it was submerged in 2 mL CCM such that the dorsal side was just covered in media. Glutamate (stock, 10 mM) was prepared in 300 µM aliquots in DMEM, frozen, and stored at -20^{o} C. APV and DNQX aliquots were also pre-prepared, frozen, and stored at -20^{o} C with stock concentrations of 50 µM and 20 µM in

dH_20, respectively. The construct was allowed to rest in un supplemented CCM for 5 min (Baseline). 20 µL glutamate was added to the CCM bath for 5 min (Stimulation). The CCM-glutamate mixture was washed out three times with pure CCM and followed by CCM supplemented with 20 µM APV and DNQX. After 1 min, 20 µL glutamate was added and recording continued for 5 min (Inhibition). At this point, three full media replacements were performed to wash out all chemicals from the chamber. The construct was once again recorded in unsupplemented CCM for 5 min (Washout). Finally, a 20 µL bolus of glutamate was applied for 5 min. During each 5 min phase, a video camera was used to record all motions from time t=0-60 sec, and t=240-300 sec.

4.4.7 Immunofluorescence and Histology

Tissues were rinsed in PBS and fixed in 4% (vol/vol) paraformaldehyde. Prior to immunostaining, tissues were permeabilized with 0.3% (vol/vol) Triton X-100 (EMD Millipore) and blocked with 3% Normal Goat Serum (NGS, Abcam, Cambridge, UK) for 30 min. Tissues were incubated with alpha-actinin (1:2000, Abcam), Beta-III Tubulin (1:2000, Abcam), conjugated alpha bungarotoxin (1:1000 EMD Millipore), and glial fibrillary acidic protein (1:20000, Abcam) antibodies for 48 h at 4^{o} C and washed with PBS. Biobots were incubated with Alexa Fluor 488 goat anti-mouse IgG, Alexa Fluor 568 goat anti-chicken IgG, and Alexa Fluor 647 goat anti-rabbit IgG secondary antibodies (1:1000, Invitrogen, Walktam, MA) in PBS for 2 h at room temperature in the dark.

4.2.8 Spinal Cord Electrophysiology

For each biobot, a single neonatal spinal cord was extracted as described above. The isolated spinal cord was submerged in physiological saline (composition in mM: NaCl, 129; KCl, 4; $CaCl_2$, 2.5; $MgCl_2$, 1.14; NaH_2PO_4, 0.5; $NaHCO_3$, 25, glucose, 10, adjusted to pH = 7.4 with HCl) that had been superfused with oxygen (95% O_2/5% CO_2) before recording. The bath temperature was kept constant at 24° C. Locomotor-like activity was induced by bath applying glutamate (10 mM stock, frozen, and stored at -20^{o} C). Neurons in the ventral horns were recorded with inspect pin electrodes connected to a differential A/C amplifier (Model1700, A-M Systems, Sequim, WA)

and a data acquisition system (PowerLab 8/30, ADInstruments, Dunedin, New Zealand). Records were digitized and recorded in LabChart 7.3 (ADInstruments) at a sampling rate of 20kHz.

4.2.9 Statistical analysis

Statistical differences were determined by ANOVA followed by the Tukey's post-hoc test for the magnitude and number of contractions, the Mann-Whitney U test for the frequency of contraction, and Hartley's Fmax for analyzing the variance of frequency, all with significance indicated by $p < 0.05$. Sample size is indicated within corresponding figure legends. All data are presented as a mean ± standard error. Each study was repeated three times.

4.3 Results

4.3.1 Fabrication of spinobot skeleton and seeding of C2C12 and spinal cord components to form a spinobot

First, we 3D-printed a poly (ethylene glycol) diacrylate (PEGDA) hydrogel skeleton composed of two pillars connected by a flexible beam (Fig. 4.1a,b). The pillars serve as attachment points much like tendons within the musculoskeletal system. A gel composed of myoblasts and extracellular matrix (ECM) proteins (Matrigel, thrombin, and fibrinogen) is seeded around the pillars to form a solid muscle strip (Fig. 4.1a,b). As the myocell-ECM gel solidifies and the muscle cells differentiate, they cause the pillars to be pulled closer together due to passive tension (Fig 1a,b). An L1-L2 spinal cord segment was placed along the longitudinal axis of the muscle strip when the muscle reached 10 DIV and cultured for an additional 7 DIV together (Fig. 4.1a,b). When cultured on glass, C2C12 myotubes roughly align with each other and express acetylcholine receptors (AChRs) distributed along their total length (Fig. 4.1c).

4.3.2 3-dimensional co-culture of spinal cord and engineered muscle tissue form structural motor units

High resolution, high magnification scanning electron microscopy (SEM) images of the spinobot revealed that neurites extended from the spinal cord and probed the muscle tissue (Fig. 4.2a, left panel). The neurites were not only investigating the surface of the tissue but were also found to seek deeper muscle fibers (Fig. 4.2a, middle and right panels). AChRs were found to be

clustered at specific locations along the myotubes, and these locations overlapped with the presence of cholinergic neurons (Fig. 4.2b, middle panel). In areas where no ChAT-positive cells were found, there was also a notable lack of receptors (Fig. 4.2b, left panel). This suggests the possibility of bi-directional neuron-muscle communication *in vitro* that mimics what happens *in vivo* (Fitzsimonds and Poo, 1998). Furthermore, the structure of the AChR clusters revealed the usual pretzel-like shape of an NMJ (Fig. 4.2b, right panel) (Takahashi *et al*, 1987). The degree of complexity noted at this motor end plate matches previous literature for a motor end plate approximately 7 days after first contact between neuron and muscle *in vivo*. The close apposition of neuron and muscle fibers, the co-localization of cholinergic neurons with their receptors on the muscle, and the presence of pretzel-shaped AChR clusters suggests the presence of neuromuscular junctions within the 3D multicellular system.

4.3.3 Muscle contractions are driven by spinal cord stimulation and can be blocked by inhibiting excitatory neuronal firing

The functionality of the spinal cord-muscle system was tested at baseline, stimulated, and inhibited conditions (Fig. 4.3a, Movies M1-M3) and recorded by video. Initially, the spinobot was placed in co-culture medium (CCM) and provided no additional modulatory cues during the baseline recording, where we observed spontaneous muscle contractions that generated 10-40 µN of active tension across the beam (Fig. 4.3b). The addition of 300 µM glutamate to the solution caused a distinct change in the pattern of muscle contraction, with glutamate-induced contractions occurring with more consistent magnitudes and in a more patterned manner (Fig. 4.3c). The addition of glutamate receptor antagonists (20 µM DNQX to block AMPA receptors and 50 µM APV to block NMDA receptors (Traynelis *et al*, 2010) resulted in a near complete cessation of muscle contraction, even with additional glutamate application (Fig. 4.3d). The observation that the twitching did not completely cease under glutamate inhibition is expected as muscles have some degree of spontaneous contraction *both in vivo* and *in vitro* (Xie and Poo, 1986; Dennis *et al*, 2001). DNQX/APV application caused inhibition beyond baseline levels, indicating that the spinal cord was driving the majority of the observed spontaneous contractions.

4.3.4 Neuromodulatory effects of glutamate and glutamate antagonists on neuron-muscle co-culture.

To analyze the videos of muscle contraction, a region of interest (ROI) around one of the hydrogel pillars was isolated (Fig. 4.3a) and its displacement plotted over time (Fig. 4.3b-d). The overall number of contractions in a given time period was not significantly different between the baseline (BL; 52 ± 12) and glutamate (GLUT; 70 ± 4) conditions (Fig. 4.4a). However, DNQX/APV application resulted in 78-fold and 105-fold reductions in the number of contractions at baseline or with glutamate, respectively. Upon wash out of glutamate and glutamate antagonists, another post-washout baseline was recorded. Significantly more contractions were observed (WASH; 74 ± 30) than at inhibition (INHIB; 1.3 ± 1.8) but without any significant change from baseline (Fig. 4.4a). Pillar displacements from within the ROI were translated into force using Hooke's Law. Contraction force was also not different between baseline (26 ± 2 μN) and glutamate (26 ± 2 μN) conditions (Fig. 4.4b). The post-washout contraction magnitudes were slightly larger (30 ± 2 μN) than those that occurred during the original baseline and glutamate conditions (Fig. 4.4b).

Though application of glutamate did not result in a change in number or magnitude of contractions, it did significantly alter the frequency and the variance of that frequency. The contractile frequency was measured as the inverse of the peak-to-peak inter-contraction interval. The frequency of contraction decreased by 20%, from 2.11 Hz at baseline to 1.59 Hz with glutamate application (Fig. 4.4a), both of which are within the known range of contractile frequencies observed *in vivo* (0.5 – 2 Hz) (Person and Kudina, 1972). This decrease in frequency occurred without a concomitant increase in contractile magnitude (Fig. 4.4b) or a change in the number of contractions (Fig. 4.4a). The primary driver of this difference in contractile frequency was a change in the patterning of neural stimulation. The variance of glutamate-stimulated contractions was decreased to only 10.67% of the baseline variance, indicating that spinal cord neurons produced a rhythmic firing pattern that generated the patterned muscle contractions. Electrophysiological recordings confirm that cultured spinal cord segments can produce rhythmic firing patterns out to 16 DIV (Fig. 2.6,7). This rhythmicity indicates that there is a glutamate-sensitive pattern generating circuit within the spinal cord segment.

4.4 Discussion

Our study demonstrates the engineering of a first fully functional 3D neuromuscular junction using a physiologically intact spinal cord CPG to drive patterned muscle contraction. The co-culturing of an intact spinal cord CPG with a 3D muscle tissue resulted in a skeletomuscular system under neuronal control that not only responds to glutamate signaling, but is also capable of patterned muscle contractions, a key component for any locomotor task. The sustained, patterned muscle contractions observed in response to tonic glutamate stimulation of the spinal cord demonstrate that the L1-L2 segment isolated forms functional NMJs with the muscle and that the internal spinal cord circuitry of the CPG remains electrically active throughout the co-culture. This enables a future design space involving the coordination of multiple muscles into flexor-extensor pairings, turning capabilities, or the ability to incorporate the sensory dorsal root ganglion as inputs for the spinobot.

When cultured, spinal cords project a complex arbor of motor neurons and glia which co-localize with nicotinic AChRs when paired with engineered muscle tissue. The neurotransmitter glutamate mimics excitation from upper motor neurons of the brainstem which control and coordinate lower motor neuron firing. The engineered spinal cord-skeletal muscle construct contracts in response to glutamatergic neuronal stimulation, which is nearly completely suppressed by the addition of glutamate receptor antagonists DNQX and APV. This confirms that the observed baseline contractions were driven by spontaneous spinal cord activity and that the spinobot itself exhibits a low level of spontaneous muscle twitching. The lack of spontaneous muscle twitching under glutamatergic inhibition is another hallmark of muscle innervation. Non-innervated muscle monocultures will twitch frequently and spontaneously, while innervated muscle demonstrates very few muscle-initiated spontaneous contractions (Lewis, 1915). Finally, we show that muscle contractions exhibit more rhythmic patterning when spinal neurons are chemically excited than at baseline.

During normal embryonic development, motor neurons reach the muscle just as the myoblasts are fusing into multinucleated muscle cells and early myotubes, a timeline we approximated experimentally. In our experiments, the spinal cord was introduced to the

engineered muscle tissue 10 days post-seeding (7 days after the muscle was switched to differentiation medium) after the muscle had finished compacting and the muscle fibers had begun to fuse. The developing NMJ forms as a result of bi-directional signaling between motor neurons and skeletal muscle fibers (Dai and Peng, 1996; Fitzsimonds and Poo, 1998). Within minutes of initial contact, presynaptic motor neurons begin firing and release ACh into the synaptic cleft (Gan and Lichtman, 1998; Xie and Poo, 1986; Chow and Poo, 1985). This causes the postsynaptic muscle to begin producing retrograde signaling molecules, e.g. neuregulin, as well as synthesizing and reorganizing AChRs into pretzel-like clusters (Meier *et al*, 1998; Jones *et al*, 1996; Gan and Lichtman, 1998; Kelly and Zacks, 1969; Takahashi *et al*, 1987). Over about a week, synaptic vesicle production increases, cytoskeletal reorganization occurs on both sides of the synapse, and AChR clustering begins, along with many other changes (Lupa and Hall, 1989; Dhawan *et al*, 2007; Hood, 2001; Kelly and Zacks, 1969). Our results confirm the structural development of motor end plates in our 3D neuromuscular system closely matches the *in vivo* developmental program, which we hypothesize would not be possible without both retro- and anterograde signaling (McComas *et al*, 1984).

A C2C12-derived skeletal muscle bioactuator approximates mammalian muscle contraction by mimicking the articulation of bones across flexible joints (Cvetkovic *et al*, 2014). To induce a locomotion-driving contraction of the muscle strip, the biobot was positioned inside of an electric field and subjected to pulsed stimulations, which resulted in large-scale contractions. Pulsed 1 Hz stimulation generated contractions with forces between ~75 - 200 µN. A second iteration of this biobot used C2C12-derived cells that were genetically modified to express Channel rhodopsin (ChR2) (Raman *et a.*, 2016). These optogenetic muscle bioactuators produced significantly smaller contractile forces, between 25 - 45 µN in response to 1 Hz stimulation. The authors posit that one reason for the reduced force may be that the penetration depth of the 470-nm light was only ~600 µm, about half of the maximum thickness of the muscle strip (~1200 µm). This rendered the optical stimulus unable to excite the entire muscle strip simultaneously. More recently, a novel “figure eight”-style design of a bioactuator powered by a C2C12-derived muscle was able to generate forces up to 1.1 mN via electric-field stimulation (Pagan-Diaz *et al*, 2018).

In situ, neuronally-innervated skeletal muscle contractions produce more force than the spontaneous contractions of an isolated muscle (Dhawan *et al*, 2007). However, early attempts at innervating C2C12-derived muscle strips with stem cell-derived motor neurons have not achieved this force. Previous research utilized mouse embryonic stem cell (mESC)-derived embryoid bodies (EBs) that undergo a motor neuron differentiation program to innervate 3D C2C12-derived muscle tissues. One method is to implant the EBs directly onto the muscle strip as it compacts, permitting them to co-differentiate. When stimulated with 200 µM or 400 µM glutamate, which excites the motor neurons, small muscle contractions of ~6 µN and ~10 µN, respectively, were observed (Cvetkovic *et al*, 2017). Muscle contractions also have been measured in a microfluidic device that enables 3D co-culture of C2C12-derived muscle and optogenetic mESC-derived embryoid bodies (Uzel *et al*, 2016). When mESC-derived embryoid bodies were optically stimulated, the downstream muscle exhibited maximal contractile forces of ~0.5 µN. By co-culturing motor neurons derived from human induced pluripotent stem cells with C2C12 myoblasts, stimulating the neurons with 0.1 mM glutamate generated contractile forces in the differentiated muscle tissue of ~1 µN (Osaki *et al,* 2018). Here we demonstrate spinal cord-driven contractions with a maximum force of ~41 µN, with the mean contractile force of ~25 µN. This notably larger force is likely due to the robust innervation of the muscle by the profusion of outgrowths from the spinal cord (Fig. 4.1)."

All derived muscle tissues contract less than native fetal muscle in rat which can exhibit forces up to 16 N (Schmoll *et al*, 2017). Previous data has shown that C2C12 skeletal muscle contracts less than primary skeletal muscle *in vitro* (Dennis *et al*, 2001) which likely accounts for some of the difference between engineered and native muscle. However, it has also been demonstrated that innervated skeletal muscle contracts with more force than muscle alone (Dhawan *et al*, 2007). We hypothesize that the large discrepancy between neurally-mediated contractions and direct stimulation of the muscle via electric fields or optogenetics is also due to the number of muscle fibers being recruited by the stimulation (Zajac and Faden, 1985). In the neural stimulation paradigms, the innervation does not reach as many fibers as when the whole tissue is stimulated simultaneously by an electric field. However, we note that the spinal neurons produce stronger contractions than their stem cell-derived counterparts. This is likely due to

increased motor neuronal innervation of the muscle tissue. Another explanation is that neuromuscular junction development occurs over approximately 3 weeks *in vivo* while the platforms described here and elsewhere generally provide only 7-10 days of co-culture. As the NMJs approach full maturity, it is expected that the amount of spontaneous neural firing will decrease, more myotubes will become singly innervated and stimulated muscle contractions will generate more force (Lupa and Hall, 1989; Takahashi *et al*, 1987; Xie and Poo, 1986).

A 3D spinal cord-skeletal muscle platform with functional and controllable neuromuscular junctions could serve a variety of uses across disciplines. It would be an excellent tool for studying the pathology of neuromuscular diseases and as a platform for studying the efficacy and modes of action of novel drugs for treatment. We could also visualize this spinobot as a model for ALS, spinal muscular atrophy, Duchenne's muscular dystrophy, and peripheral neuropathies such as those secondary to diabetes mellitus. Some researchers have already begun adapting *in vitro* NMJ platforms for the study of these diseases (Osaki *et al*, 2018). The modularity of the 'spinobot' demonstrated here, innervation from a living spinal cord, and the use of an easily transfectable cell line are unique strengths of this platform. Early biohybrid robots and actuators are also expected to one day appear in surgical training tools, the study and repair of biological systems in dangerous environments, and at the interface for human-computer devices (Rossiter *et al*, 2009; Albalaihid *et al*, 2017; Park *et al*, 2014). Other variations on 3D microphysiological systems have been developed with microfluidic chambers, neural stem cells, and/or photolithography control. However, these platforms all lack the ability to generate the patterned contractions we produce by stimulating the spinal cord CPG. Notably, the contraction forces generated by spinal cord-controlled C2C12 were greater than skeletal muscle under mouse ESC control. The use of the spinal cord also enables a future design space involving the coordination of multiple muscles from a single neuronal source or the ability to incorporate the sensory dorsal root ganglion as inputs for the spinobot allowing it to respond to environmental cues.

4.5 Figures

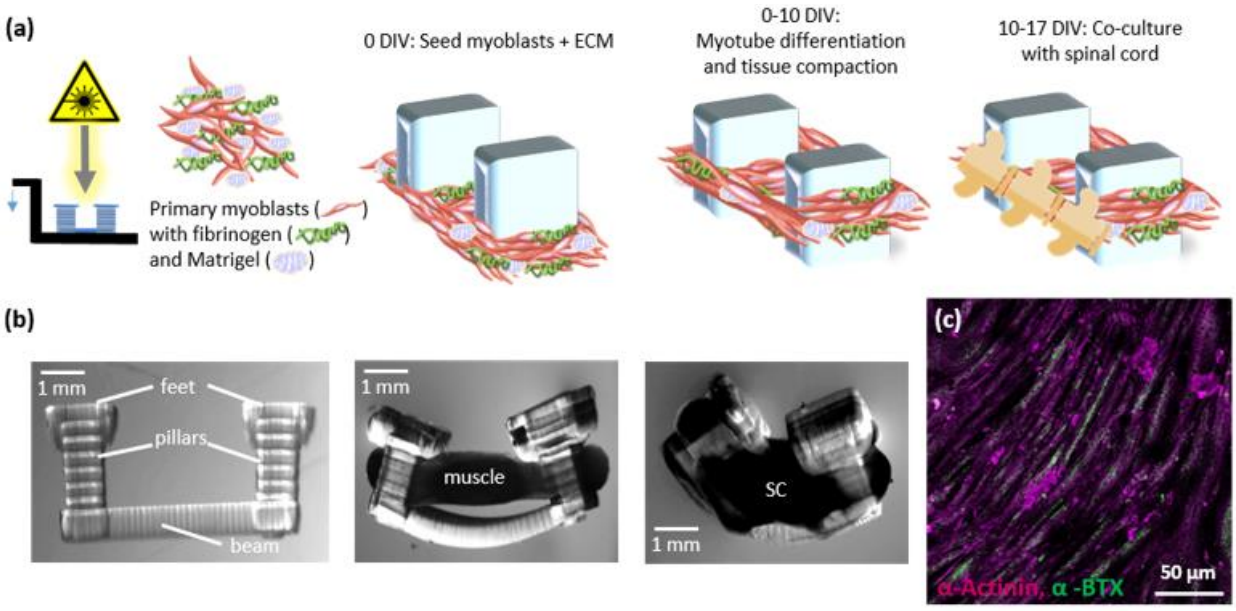

Figure 4.1. Methodology of spinal cord-skeletal muscle biohybrid machine development. **(a)** From left to right: A stereolithography apparatus (SLA) was used to polymerize hydrogel structures in an additive process. Made a cell-ECM mixture of C2C12 myoblasts, thrombin, fibrinogen, and Matrigel and seeded it onto the 3D-printed skeleton. Over 10 DIV, myotubes compact the ECM and begin to differentiate. At 10 DIV, a segment of lumbar spinal cord is seeded onto the spinal cord and co-cultured for an additional 7 days. **(b)** Lateral step-by-step view of the multicellular spinobot construction. *Left:* A hydrogel skeleton is 3D printed using a stereolithography apparatus (SLA). *Middle:* Muscle attached to the hydrogel skeleton causes bending by generating passive tension. *Right:* Co-culture of spinal cord (SC) and muscle strip over beam of hydrogel skeleton. **(c)** 2D culture of C2C12 myoblasts form aligned myotubes over 10 days on untreated glass. Alpha-actinin marks the skeletal muscle (magenta) and nicotinic AChR clusters (alpha-bungarotoxin, green) can be visualized along the whole length.

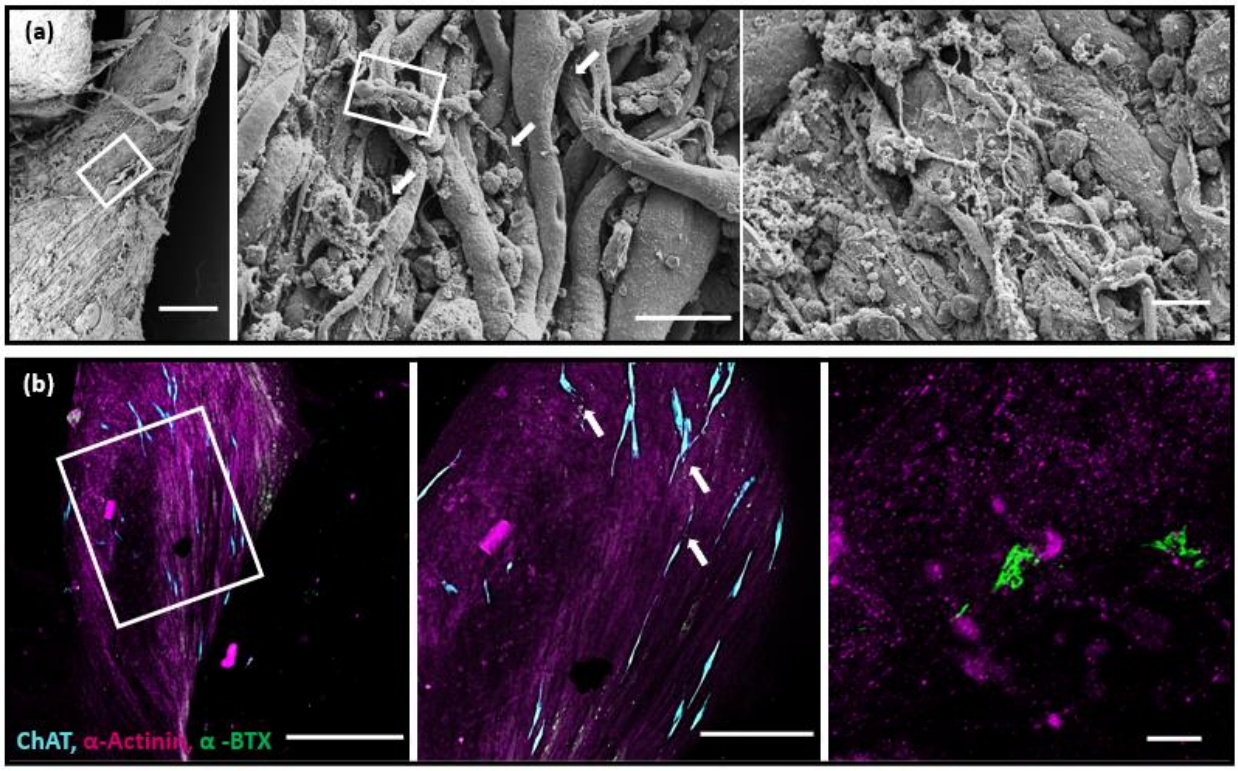

Figure 4.2. Structural evidence of abutting cholinergic neurons and postsynaptic acetylcholine receptors. **(a)** SEM images of inferior side of spinobot at increasing magnification from left to right: Scale bars are 200 µm, 25 µm, and 20 µm, respectively. Myotubes appear aligned and neuronal processes lie in close apposition to muscle fibers. Neuronal processes probe beyond the surface layer of myotubes into deeper muscle tissue where indicated by the arrows. **(b)** Photomicrographs of immunohistochemically stained spinobot at increasing magnification from left to right: Scale bars are 500 µm, 250 µm, and 10 µm respectively. *Left:* Muscle fibers (α-actinin, magenta) align along the longitudinal axis of the spinobot. AChR clusters (α-bungarotoxin, green) are present, but largely clustered around the cholinergic neurons (ChAT, cyan). *Middle:* Acetylcholine receptors and ChAT-positive neurons are found localized close together, as indicated by arrows. *Right:* Development of typical pretzel-like motor end plate structures on the postsynaptic muscle indicates the formation of structural neuromuscular junctions.

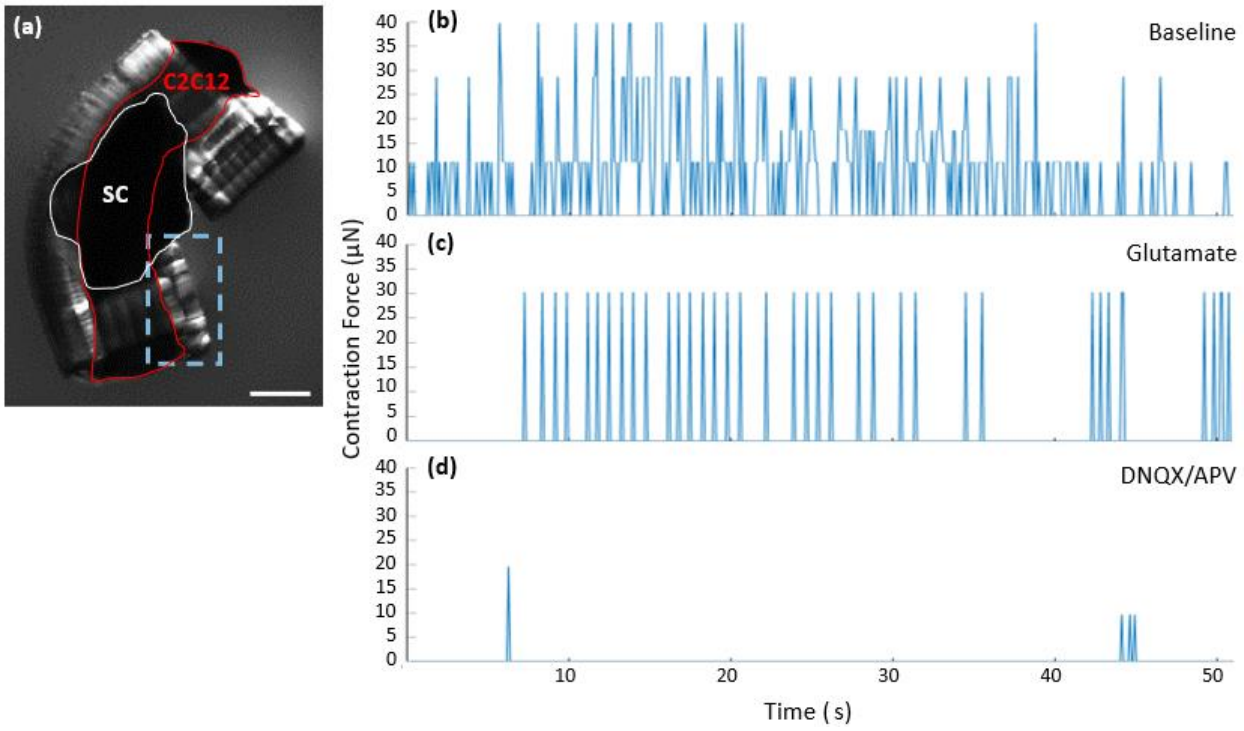

Figure 4.3. Spontaneous contractions of the spinobot can be controlled by neurochemical modulation. **(a)** Lateral image of a spinobot. Red outline shows the muscle, white outline indicates the spinal cord placement, and dashed blue box indicates region of interest for video capture of pillar displacement. Scale bar is 1 mm. **(b)-(d)** Representative traces of contraction force under baseline **(b**), stimulation **(c)**, and inhibition **(d)** conditions. As shown in (b), muscle contracts spontaneously with variable frequency and magnitude at baseline. When glutamate is added to the media (c), contractions become more consistent in strength and frequency. **(d)** After washing out the glutamate-treated media, the addition of inhibitors plus additional glutamate results in a drastic reduction in both the number and frequency of contractions.

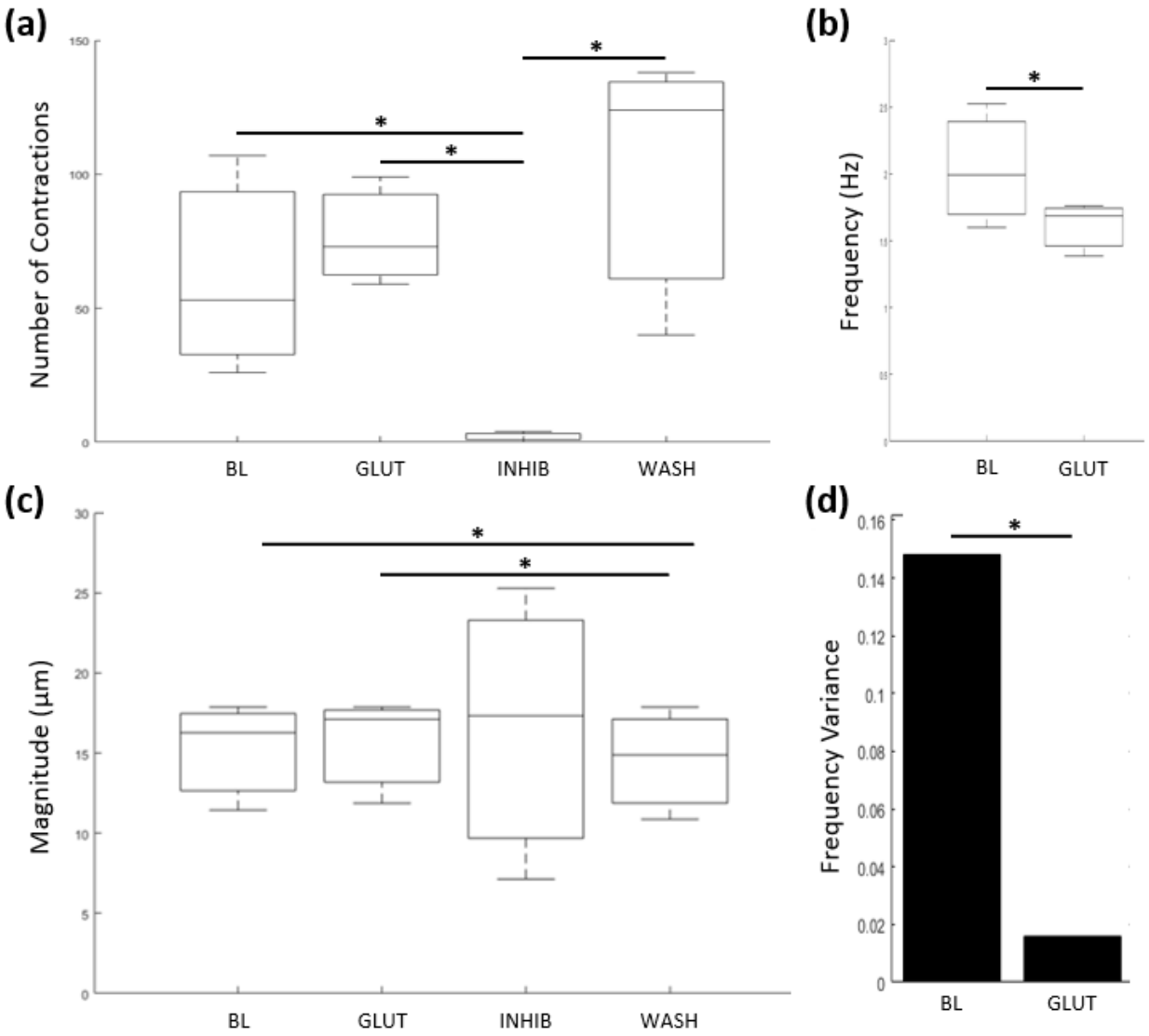

Figure 4.4. Glutamate signaling within the spinal cord mediates patterned muscle contraction. **(a)** The overall number of muscle contractions did not increase when glutamate was added, however inhibition of glutamatergic signaling reduced the number of contractions to nearly zero. Contractile behavior was recovered by washing out the inhibitors. **(b**) Glutamate application did not significantly change the force of muscle contraction from baseline. Due to the very low number of contractions under inhibition, the force of those contractions is not significantly reduced. The contraction force was fully recovered by washing out the inhibitors. One-way ANOVA, Dunnett's test. **(c)** Spontaneous spinal cord firing at baseline caused the muscle to contract at 2 Hz, and the addition of glutamate reduced the contractile frequency to 1.5 Hz. Mann-Whitney Test, *$p < 0.05$ ($n = 3$). **(d)** Glutamate-initiated contraction demonstrated significantly less variable frequencies of contraction, indicating a consistent, patterned output from the spinal cord. Hartley's Fmax test, ($n = 3$ for all conditions). *$p < 0.05$. Graphs (a)-(c) are mean + SEM.

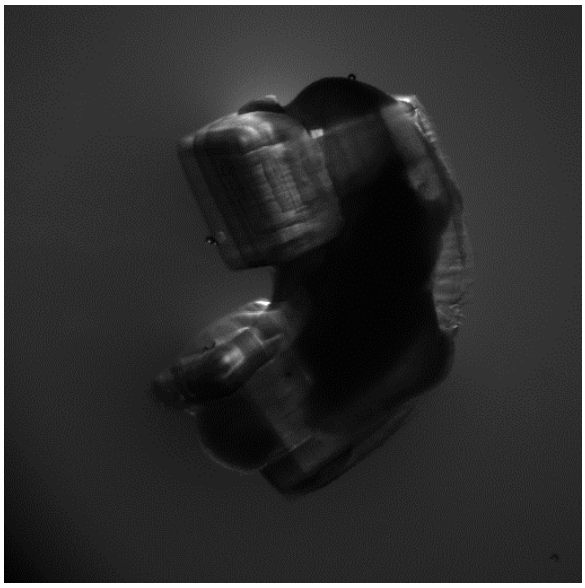

Movie M1. Movie of spontaneous spinobot contractions in basal media over 60 seconds, shown at 3X speed.

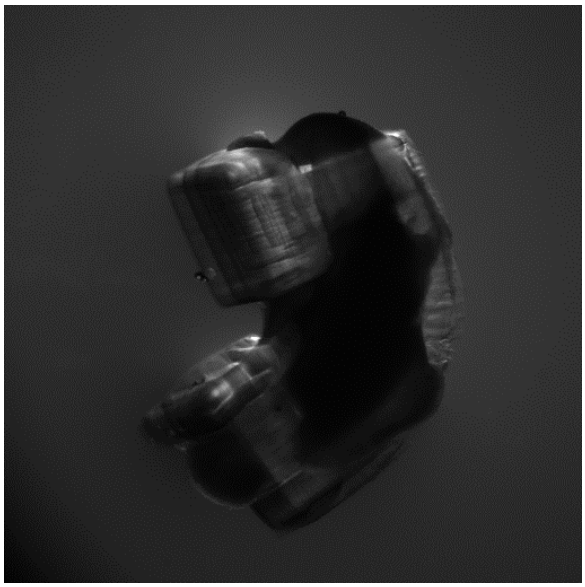

Movie M2. Movie of spinobot contractions in response to glutamate over 60 seconds, shown at 3X speed.

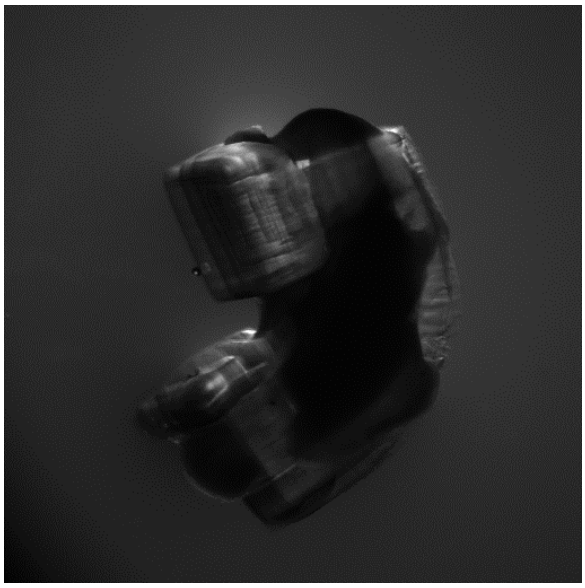

Movie M3. Movie of spinobot contractions after washing out the media + glutamate, the addition of media + inhibitors + glutamate, shown at 3X speed.

4.6 References

1. Cvetkovic, C., Ko, E., Kaufman, C., Grant, L., Gillette, M., Kong, H., & Bashir, R. (2018). Rapid prototyping of soft bioactuators. *3D Bioprinting in Regenerative Engineering: Principles and Applications*.
2. Majidi C. Soft robotics: A perspective—current trends and prospects for the future. *Soft Robot* 2013; 1: 5–11.
3. Vincent JFV, Bogatyreva OA, Bogatyrev NR, Bowyer A, Pahl A-K. Biomimetics: Its practice and theory. *J R Soc Interface* 2006; 3: 471–482.
4. Han, D., Gu, H., Kim, J. W., & Yokota, S. (2017). A bio-inspired 3D-printed hybrid finger with integrated ECF (electro-conjugate fluid) micropumps. *Sensors and Actuators A: Physical*, *257*, 47-57.
5. Gul JZ, Yang B-S, Yang YJ, Chang DEE, Choi KH, Gul JZ *et al*. In situ UV curable 3D printing of multi-material tri-legged soft bot with spider mimicked multi- step forward dynamic gait. *Smart Mater Struct* 2016; 25: 1–12.
6. Full RJ. Using biological inspiration to build artificial life that locomotes. *EvoWorkshops* 2001; 2217: 110–120.
7. Ricotti L, Menciassi A. Bio-hybrid muscle cell-based actuators. *Biomed Microdevices* 2012; 14: 987–998.
8. Park, S. J., Gazzola, M., Park, K. S., Park, S., Di Santo, V., Blevins, E. L., Lind, J. U., Campbell, P. H., Dauth, S., Capuli, A. K., Pasqualini, F. S., Ahn, S., Cho, A., Yuan, H., Maoz, B. M., Vijaykumar, R., Choi, J-W., Deisseroth, K., Lauder, G. V., Mahadevan, L., Parker, K. K. (2016). Phototactic guidance of a tissue-engineered soft-robotic ray. *Science*, *353*(6295), 158-162.
9. Wen L, Wang T, Wu G, Liang J. Quantitative thrust efficiency of a self-propulsive robotic fish: Experimental method and hydrodynamic investigation. *IEEE/ASME Trans Mechatronics* 2013; 18: 1027–1038.
10. Low KH. Design, development and locomotion control of bio-fish robot with undulating anal fins. *Int J Robot Autom* 2007; 22: 88–99.
11. Herr H, Dennis RG. A swimming robot actuated by living muscle tissue. *J Neuroeng Rehabil* 2004; 1: 1–9.
12. Cvetkovic C, Raman R, Chan V, Williams BJ, Tolish M, Bajaj P *et al*. Three dimensionally printed biological machines powered by skeletal muscle. *Proc Natl Acad Sci USA* 2014; 111: 10125–10130.
13. Pagan-Diaz, G. J., Zhang, X., Grant, L., Kim, Y., Aydin, O., Cvetkovic, C., Ko, E., Solomon, E., Hollis, J., Kong, H., Saif, T., Gazzola, M., Bashir, R. (2018). Simulation and fabrication of stronger, larger, and faster walking biohybrid machines. *Advanced Functional Materials*, *28*(23), 1801145.
14. Kovač M. The bioinspiration design paradigm: A perspective for soft robotics. *Soft Robot* 2013; 1: 28–37.
15. Bartlett NW, Tolley MT, Overvelde JTB, Weaver JC, Mosadegh B, Bertoldi K *et al*. A 3D-printed, functionally graded soft robot powered by combustion. *Science* 2015; 349: 161–165.

16. Mosadegh B, Polygerinos P, Keplinger C, Wennstedt S, Shepherd RF, Gupta U *et al.* Pneumatic networks for soft robotics that actuate rapidly. *Adv Funct Mater* 2014; 24: 2163–2170
17. Wirekoh H, Park Y-L. Design of flat pneumatic artificial muscles. *Smart Mater Struct* 2017; 26: 1–10.
18. Nawroth JC, Lee H, Feinberg AW, Ripplinger CM, McCain ML, Grosberg A *et al*. A tissue-engineered jellyfish with biomimetic propulsion. *Nat Biotechnol* 2012; 30: 792–797.
19. Raman, R., Cvetkovic, C., Uzel, S. G., Platt, R. J., Sengupta, P., Kamm, R. D., & Bashir, R. (2016). Optogenetic skeletal muscle-powered adaptive biological machines. *Proceedings of the National Academy of Sciences*, *113*(13), 3497-3502.
20. Webster, V. A., Chapin, K. J., Hawley, E. L., Patel, J. M., Akkus, O., Chiel, H. J., & Quinn, R. D. (2016, July). Aplysia californica as a novel source of material for biohybrid robots and organic machines. In *Conference on Biomimetic and Biohybrid Systems* (pp. 365-374).
21. Cvetkovic, C., Rich, M. H., Raman, R., Kong, H., & Bashir, R. (2017). A 3D-printed platform for modular neuromuscular motor units. *Microsystems & Nanoengineering*, *3*, 17015.
22. Uzel, S. G., Platt, R. J., Subramanian, V., Pearl, T. M., Rowlands, C. J., Chan, V., Boyer, L. A., So, P. T. C., Kamm, R. D. (2016). Microfluidic device for the formation of optically excitable, three-dimensional, compartmentalized motor units. *Science advances*, *2*(8), e1501429.
23. Frank E, Fischbach GD. 1979. Early events in neuromuscular junction formation *in vitro*: induction of acetylcholine receptor clusters in the postsynaptic membrane and morphology of newly formed synapses. *J. Cell Biol.* 83: 143–58
24. Kiehn, O. (2006). Locomotor circuits in the mammalian spinal cord. *Annu. Rev. Neurosci.*, *29*, 279-306.
25. Kislinger, T., Gramolini, A. O., Pan, Y., Rahman, K., MacLennan, D. H., & Emili, A. (2005). Proteome dynamics during C2C12 myoblast differentiation. *Molecular & Cellular Proteomics*, *4*(7), 887-901.
26. Bajaj, P., Reddy Jr, B., Millet, L., Wei, C., Zorlutuna, P., Bao, G., & Bashir, R. (2011). Patterning the differentiation of C2C12 skeletal myoblasts. *Integrative Biology*, *3*(9), 897-909.
27. Al-Rekabi, Z., & Pelling, A. E. (2013). Cross talk between matrix elasticity and mechanical force regulates myoblast traction dynamics. *Physical biology*, *10*(6), 066003.
28. Fu, A. K., Fu, W. Y., Cheung, J., Tsim, K. W., Ip, F. C., Wang, J. H., & Ip, N. Y. (2001). Cdk5 is involved in neuregulin-induced AChR expression at the neuromuscular junction. *Nature neuroscience*, *4*(4), 374-381.
29. Benveniste, O., Jacobson, L., Farrugia, M. E., Clover, L., & Vincent, A. (2005). MuSK antibody positive myasthenia gravis plasma modifies MURF-1 expression in C2C12 cultures and mouse muscle in vivo. *Journal of neuroimmunology*, *170*(1-2), 41-48.
30. Osaki, T., Sivathanu, V., & Kamm, R. D. (2018). Vascularized microfluidic organ-chips for drug screening, disease models and tissue engineering. *Current opinion in biotechnology*, *52*, 116-123.
31. Umbach, J. A., Adams, K. L., Gundersen, C. B., & Novitch, B. G. (2012). Functional neuromuscular junctions formed by embryonic stem cell-derived motor neurons. *PloS one*, *7*(5).

32. Smith, A. S., Passey, S. L., Martin, N. R., Player, D. J., Mudera, V., Greensmith, L., & Lewis, M. P. (2016). Creating interactions between tissue-engineered skeletal muscle and the peripheral nervous system. *Cells Tissues Organs*, *202*(3-4), 143-158.
33. Li, Z., Seo, Y., Aydin, O., Elhebeary, M., Kamm, R. D., Kong, H., & Saif, M. T. A. (2019). Biohybrid valveless pump-bot powered by engineered skeletal muscle. *Proceedings of the National Academy of Sciences*, *116*(5), 1543-1548.
34. Cvetkovic, C., Ferrall-Fairbanks, M. C., Ko, E., Grant, L., Kong, H., Platt, M. O., & Bashir, R. (2017). Investigating the life expectancy and proteolytic degradation of engineered skeletal muscle biological machines. *Scientific reports*, *7*(1), 1-13.
35. Cazalets, J. R., Borde, M., & Clarac, F. (1995). Localization and organization of the central pattern generator for hindlimb locomotion in newborn rat. *Journal of Neuroscience*, *15*(7), 4943-4951.
36. Quadrato, G., Nguyen, T., Macosko, E. Z., Sherwood, J. L., Yang, S. M., Berger, D. R., Maria, N., Scholvin, J., Goldman, M., Kinney, J. P., Boyden, E. S., Lichtman, J. W., Williams, Z. M., McCarroll, S. A., Arlotta, P. (2017). Cell diversity and network dynamics in photosensitive human brain organoids. *Nature*, *545*(7652), 48.
37. Spangler, A., Su, E. Y., Craft, A. M., & Cahan, P. (2018). A single cell transcriptional portrait of embryoid body differentiation and comparison to progenitors of the developing embryo. *Stem cell research*, *31*, 201-215.
38. Maffioletti, S. M., Sarcar, S., Henderson, A. B., Mannhardt, I., Pinton, L., Moyle, L. A., Steele-Stallard, H., Cappelari, O., Wells, K. E., Ferrari, G., Mitchell, J. S., Tyzack, G.E., Kotiadis, V. N., Khedr, M., Ragazzi, M., Wang, W., Duchen, M.R., Patani, R., Zammit,. P. S., Wells, D. J., Eschenhagen,, T., Saverio Tedesco, F. (2018). Three-dimensional human iPSC-derived artificial skeletal muscles model muscular dystrophies and enable multilineage tissue engineering. *Cell reports*, *23*(3), 899-908.
39. Bakooshli, M. A., Lippmann, E. S., Mulcahy, B., Iyer, N., Nguyen, C. T., Tung, K., Stewart, B. A., van den Dorpel, H., Fuehrmann, T., Shoichet, M., Bigot, A., Pegoraro, E., Ahn,, H., Ginsberg, H., Zhen, M., Scott Ashton, R., Gilbert, P. M. (2019). A 3D culture model of innervated human skeletal muscle enables studies of the adult neuromuscular junction. *Elife*, *8*, e44530.
40. Van Pelt, J., Corner, M. A., Wolters, P. S., Rutten, W. L. C., & Ramakers, G. J. A. (2004). Longterm stability and developmental changes in spontaneous network burst firing patterns in dissociated rat cerebral cortex cell cultures on multielectrode arrays. *Neuroscience letters*, *361*(1-3), 86-89.
41. Bjugn, R., & Gundersen, H. J. G. (1993). Estimate of the total number of neurons and glial and endothelial cells in the rat spinal cord by means of the optical disector. *Journal of Comparative Neurology*, *328*(3), 406-414.
42. Samuel, M. A., Valdez, G., Tapia, J. C., Lichtman, J. W., & Sanes, J. R. (2012). Agrin and synaptic laminin are required to maintain adult neuromuscular junctions. *PLoS One*, *7*(10), e46663.
43. Yohn DC, Miles GB, Rafuse VF, Brownstone RM (2008) Transplanted mouse embryonic stem-cell-derived motoneurons form functional motor units and reduce muscle atrophy. *J Neurosci 28: 12409–12418.*

44. Volterra, A., Magistretti, P. J., & Haydon, P. G. (2002). *The tripartite synapse: glia in synaptic transmission* (No. LNDC-BOOK-2010-002). Oxford University Press.
45. Traynelis, S. F., Wollmuth, L. P., McBain, C. J., Menniti, F. S., Vance, K. M., Ogden, K. K., Hansen, K. B., Yuan, H., Myers, S. J., Dingledine, R. (2010). Glutamate receptor ion channels: structure, regulation, and function. *Pharmacological reviews*, *62*(3), 405-496.
46. Schmoll, M., Unger, E., Sutherland, H., Haller, M., Bijak, M., Lanmüller, H., & Jarvis, J. C. (2017). In-situ measurements of tensile forces in the tibialis anterior tendon of the rat in concentric, isometric, and resisted co-contractions. *Physiological reports*, *5*(8), e13245.
47. Dennis, R. G., Kosnik, P. E., Gilbert, M. E., & Faulkner, J. A. (2001). Excitability and contractility of skeletal muscle engineered from primary cultures and cell lines. *American Journal of Physiology-Cell Physiology*, *280*(2), C288-C295.
48. Person, R. S., & Kudina, L. P. (1972). Discharge frequency and discharge pattern of human motor units during voluntary contraction of muscle. *Electroencephalography and clinical neurophysiology*, *32*(5), 471-483.
49. Lewis, M. R. (1915). Rhythmical contraction of the skeletal muscle tissue observed in tissue cultures. *American Journal of Physiology-Legacy Content*, *38*(1), 153-161.
50. McComas, A. J., Kereshi, S., & Manzano, G. (1984). Multiple innervation of human muscle fibers. *Journal of the neurological sciences*, *64*(1), 55-64.
51. Xie ZP, Poo MM. 1986. Initial events in the formation of neuromuscular synapse: rapid induction of acetylcholine release from embryonic neuron. *Proc. Natl. Acad. Sci.* USA 83:7069–73
52. Riley DA. 1981. Ultrastructural evidence for axon retraction during the spontaneous elimination of polyneuronal innervation of the rat soleus muscle. *J. Neurocytol.* 10: 425–40
53. Chow I, Poo MM. 1985. Release of acetylcholine from embryonic neurons upon contact with muscle cell. *J. Neurosci.* 5:1076–82
54. Dai Z, Peng HB. 1996. From neurite to nerve terminal: induction of presynaptic differentiation by target-derived signals. *Semin. Neurosci.* 8:97–106
55. Fitzsimonds RM, Poo MM. 1998. Retrograde signaling in the development and modification of synapses. *Physiol. Rev.* 78: 143–70
56. Meier T, Masciulli F, Moore C, Schoumacher F, Eppenberger U, *et al*. 1998. Agrin can mediate acetylcholine receptor gene expression in muscle by aggregation of muscle-derived neuregulins. *J. Cell Biol.* 141: 715–26
57. Jones G, Herczeg A, Ruegg MA, Lichsteiner M, Kroger S, Brenner HR. 1996. Substrate-bound agrin induces expression of acetylcholine receptor ε-subunit gene in cultured mammalian muscle cells. *Proc. Natl. Acad. Sci.*
58. Gan W-B, Lichtman JW. 1998. Synaptic segregation at the developing neuromuscular junction. *Science.*
59. Kelly AM, Zacks SI. 1969. The fine structure of motor endplate morphogenesis. *J. Cell Biol.* 42:154–69
60. Takahashi T, Nakajimi Y, Hirosawa K, Nakajimi S, Onodera K. 1987. Structure and physiology of developing neuromuscular synapses in culture. *J. Neurosci.* 7:473–81
61. Lupa MT, Hall ZW. 1989. Progressive restriction of synaptic vesicle protein to the nerve terminal during development of the neuro- muscular junction. *J. Neurosci.* 9:3937–45

62. Dhawan, V., Lytle, I. F., Dow, D. E., Huang, Y. C., & Brown, D. L. (2007). Neurotization improves contractile forces of tissue-engineered skeletal muscle. *Tissue engineering*, *13*(11), 2813-2821.
63. Zajac FE, Faden JS (1985). Relationship among recruitment order, axonal conduction velocity and muscle-unit properties of type-identified motor units in cat plantaris muscle*. J Neurophysiol* 53:1303–1322
64. Hood, D. A. (2001). Invited Review: contractile activity-induced mitochondrial biogenesis in skeletal muscle. *Journal of applied physiology*, *90*(3), 1137-1157.
65. Rossiter J, Walters P, Stoimenov B. Printing 3D dielectric elastomer actuators for soft robotics. In: Bar-Cohen Y, Wallmersperger T (Eds.). *Electroactive Polymer Actuators and Devices* (*EAPAD*) *2009*. SPIE, 2009. doi:10.1117/12.815746.
66. Alblalaihid K, Overton J, Lawes S, Kinnell P. A 3D-printed polymer micro-gripper with self-defined electrical tracks and thermal actuator. *J Micromechanics Microengineering* 2017; 27: 45019.
67. Park YL, Santos J, Galloway KG, Goldfield EC, Wood RJ. A soft wearable robotic device for active knee motions using flat pneumatic artificial muscles. In: *2014 IEEE International Conference on Robotics & Automation* (*ICRA*). IEEE, Hong Kong, 2014, pp. 4805–4810.
68. Millet, Larry J., *et al*. "Microfluidic devices for culturing primary mammalian neurons at low densities." *Lab on a Chip* 7.8 (2007): 987-994.
69. Raman, R., Cvetkovic, C., & Bashir, R. (2017). A modular approach to the design, fabrication, and characterization of muscle-powered biological machines. *Nature protocols*, *12*(3), 519.

CHAPTER 5: GENERAL DISCUSSION AND FUTURE DIRECTIONS

5.1 General Discussion

Biological robotics is a growing field which derives inspiration from biological systems for real world applications. More traditional, rigid robotics have historically struggled to interact with biological tissue, undergo self-repair, and are rarely biodegradable (Cvetkovic *et al*, 2018). Biology has already solved many of these problems faced by rigid robots. By abstracting and recapitulating similar solutions, we will be able to replicate increasingly natural, complex biological robots through the application of novel engineering approaches (Majidi, 2013). Researchers are already using biological materials, including DNA, motor proteins, myosin-actin complexes, bacteria, algae, single cells or clusters, and natural or engineered tissues, to develop bioactuators (Chan *et al*, 2014; Feinberg, 2015). These actuators are often small and can emulate locomotive behaviors, such as climbing (Unver *et al*, 2006), crawling, walking, jumping, or swimming (Umedachi *et al*, 2016; Cvetkovic *et al*, 2014; Kovac, 2013; Bartlett *et al*, 2015; Feinberg *et al*, 2007; Wen *et al*, 2013; Low, 2007; Herr and Dennis, 2004; Nawroth *et al*, 2012). They can also mimic other functions such as the peristaltic pumping action of the intestines (Li et al, 2019). Small biological robots at the millimeter scale also offer several advantages over larger robots. Their small size allows them to be used in environments where large robots would be impractical or impossible, such as inside the body, and their small size also allows for more uniform transport of nutrients throughout the tissue.

Both living and nonliving bioactuators must be designed such that the form matches the intended function (Uzel *et al*, 2014; Feinberg, 2015; Kim *et al*, 2014). Most tissues and organs are not composed of a monolith of identical cells and cell types; many different cell types perform important roles in the maintenance of the local environment, tissue function, and homeostatic equilibrium of the overall organism. The production of a multicellular tissue can allow for a collective output that is greater than the sum of its parts. Moreover, complexity and functionality both increase when progressing from single cells to multicellular tissues and systems (Carlsen and Sitti, 2014; Kamm and Bashir, 2013). This is due not only to the increased complexity of cell-cell interactions, but these engineered systems are also more likely to be 3D than classical 2D cell

culture techniques. When cultured in 3D rather than 2D, the specific behaviors of cancer cells, muscle fibers, and hepatocytes have all been more closely aligned with the reality of *in-vivo* systems (Choi *et al*, 2010; Mudera *et al*, 2010; Gieseck III *et al*, 2014). The best way to engineer a multicellular engineered system capable of rhythmic, coordinated, and/or patterned behaviors is to combine our knowledge of these behaviors in evolved biological systems with the cutting edge of fabrication and cell culture techniques available to researchers today.

In vertebrates, locomotion is primarily controlled by spinal cord and brainstem networks. While these networks are heavily modulated by the brainstem, most of the pattern and rhythm generation involved with locomotion are housed within the spinal cord. Quadrupedal locomotion requires the coordination of flexor-extensor muscle pairing simultaneously within a limb, and between ipsi- and contralateral pairs of limbs. This is performed by spinal circuits known as central pattern generators (CPGs). The best way to study intact circuits *in vitro* is through organotypic culture (Prosser and Gillette, 1989), yet there are no prior studies that have assessed the cellular makeup or electrical activity of organotypic 2.5-D cultures of intact spinal cords. In order to use a spinal cord as an on-board computer for controlling muscular contraction in a biological robot, we first needed to demonstrate how a spinal cord behaved under organotypic culture conditions for several weeks. Immunohistochemistry of cleared whole spinal cords and of lumbar cross-sections revealed the presence of interneurons, motor neurons, astrocytes, and Schwann cells which are known to exist as part of a CPG and its motor outputs. When cultured on Matrigel-coated glass, spinal cords produce a complex arbor of motor neurons and astrocytes that extends over a 1 mm away from the spinal cord. These outgrowths do not exhibit electrical activity immediately, but electrical activity is detectable as the processes mature by 7 DIV.

These processes contain not only structural and cell type-specific proteins indicating a dominant population of motor neurons, but are also highly electrically active. Acute lumbar spinal cord recordings with pin electrodes demonstrate both spontaneous and stimulated activity in response to glutamate. Additional recordings from lumbar spinal cords cultured for one week demonstrate infrequent spontaneous activity and a slightly reduced sensitivity to glutamate stimulation compared to acute conditions. Recordings from lumbar spinal cords cultured for two weeks exhibit very little spontaneous activity and respond to a higher dose of glutamate. By 14

DIV, spinal cords do not exhibit spontaneous firing at baseline or respond to a low dose of glutamate. However, a high dose of glutamate initiates robust electrical activity with a clear bursting pattern indicative of a pattern generating circuit. This time-dependent decrease in spontaneous activity is consistent with previous work on dissociated hippocampal cultures which have demonstrated reduced levels of spontaneous activity as well as reduced sensitivity to stimulation when cultured for up to 5 weeks (Odawara *et al*, 2014; Fig. 2.7). However, previous work with organotypic CNS cultures has shown minimal differences between *in-situ* electrophysiology and the organotypic brain-slice cultures (Muller *et al*, 1993; Uesaka *et al*, 2005; Rohrbacher *et al*, 2000; Gillette and Tischkau, 1999). It has also been reported that neuronal activity is heavily modulated by the presence of other cells (e.g., skeletal muscle), and we hypothesize that passive spinal cord activity would be modulated by being co-cultured with muscle (Odawara *et al*, 2014; Balice-Gordon and Lichtman, 1993; Rosenthal and Taraskevich, 1977; Bennett and Pettigrew, 1976). Future studies can investigate the effect of muscle-conditioned medi on spinal cord rhythms and more direct comparisons to age-matched *in-vivo* tissues. Overall, these data are the first to demonstrate that spinal cords extend a complex, multicellular arbor of motor neurons and glia and that they retain the ability to generate robust electrical potentials for up to two weeks *in vitro*. This indicates that spinal cord locomotor circuits can be extracted and harnessed to build a multicellular, muscular bioactuator controlled by a locomotor CPG.

The co-culturing of an intact spinal cord CPG with a 3D muscle tissue resulted in a skeletomuscular system under neuronal control that not only responds to glutamate signaling, but is also capable of patterned muscle contractions, a key component of many forms of locomotion. In our experiments, the spinal cord was introduced to the engineered muscle tissue 10 days post-seeding (7 days after the muscle was switched to differentiation medium) after the muscle had finished compacting and the muscle fibers had begun to fuse. As shown in Figure 2.5 the spinal cord is still spontaneously active and responsive to glutamate stimulation at this stage. It has been shown that the developing NMJ forms as a result of bi-directional signaling between motor neurons and skeletal muscle fibers (Dai and Peng, 1996; Fitzsimonds and Poo, 1998). Within minutes of initial contact, presynaptic motor neurons begin firing and release ACh into

the synaptic cleft (Gan and Lichtman, 1998; Xie and Poo, 1986; Chow and Poo, 1985). This causes the postsynaptic muscle to begin producing retrograde signaling molecules and synthesizing and reorganizing AChRs into pretzel-like clusters (Meier *et al*, 1998; Jones *et al*, 1996; Gan and Lichtman, 1998; Kelly and Zacks, 1969; Takahashi *et al*, 1987). Over about a week, synaptic vesicle production increases, cytoskeletal reorganization occurs on both sides of the synapse, and AChR clustering begins, along with many other changes (Lupa and Hall, 1989; Dhawan *et al*, 2007; Hood, 2001; Kelly and Zacks, 1969). We observe a formation of the iconic, pretzel-like shape of the motor endplate at 7 DIV (Figure 4.2) as well as a close apposition of motor neurons and muscle-bound acetylcholine receptor (AChR) clusters (Figure 4.2). Our results confirm the structural development of motor end plates in our 3D neuromuscular system closely matches the developmental program *in vivo* (Figure 1.5; Figure 2.4; McComas *et al*, 1984).

Our studies also demonstrate the functionality of these NMJs on the spinobot platform. Sustained, patterned muscle contractions are observed in response to tonic glutamate stimulation of the spinal cord, demonstrating that the L1-L2 segment forms functional NMJs with the muscle and that neurons within the spinal cord maintain the ability for neurotransmitter-based control. When supplied with a bolus of glutamate, the muscle contractions are more rhythmic and patterned than the spontaneous, baseline contractions. When glutamate signaling is inhibited through the application of an NMDA/APV cocktail, there is a complete cessation of muscle twitching. This is consistent with our findings in both 2D and 3D skeletal muscle cultures and fundamental muscle research which discovered that non-innervated muscle monocultures will twitch frequently and spontaneously, while innervated muscle demonstrates very few muscle-initiated spontaneous contractions (Figure 3.1; Lewis, 1915). Our study demonstrates the engineering of a first fully functional 3D neuromuscular junction using a physiologically intact spinal cord CPG to drive patterned muscle contraction.

However, we observed contractile forces far below what is observed in native fetal rat tissues. Fetal muscle in rat can exhibit forces up to 16 N, which is greater than what has been reported in all derived muscle tissues (Schmoll *et al*, 2017; Osaki *et al*, 2018; Maffioletti *et al*, 2018; Bakooshli *et al*, 2019; Cvektovic *et al*, 2014). During normal embryonic development, motor neurons reach the muscle just as the myoblasts are fusing into multinucleated muscle cells and

early myotubes. We approximated this timeline experimentally by quantifying the rate and distance that spinal cord outgrowths propagate *in vitro* (Figure 2.2) and introducing the spinal cord to the skeletal muscle construct at the same time the muscle cells began differentiating. However, the spinal cord is taken from a neo-natal animal rather than an embryonic one when those contacts are made *in situ*. Therefore, future experiments that introduce the two tissue at different time points may enhance the maturation rate and success of the co-culture system. Another likely hypothesis for the difference in force production between engineered and native muscle tissues is that that C2C12 cells lack the sarcomeric structure of primary muscle (Langelaan *et al*, 2010; Fig. 3.1c,f). We investigated some differences between C2C12-derived muscle and primary skeletal muscle from the rat hindlimb (gastrocnemius and soleus) and found that primary cultures have larger myotube diameters, the average AChR cluster has a greater surface area, and spontaneous contractions in primary muscle are more consistent than their C2C12-derived counterparts. Western blots revealed that though the extracted primary tissue was a mix of Type I and Type II fibers, this identity was not retained by the dissociated satellite cells when cultured on Matrigel-coated glass in 2D. It has also been demonstrated that innervated skeletal muscle contracts with more force than muscle alone (Dhawan *et al*, 2007). When cultured in spinal cord-conditioned media, we found that primary skeletal muscle cells regained a mixed Type I/Type II fiber type identity. This is consistent with previous literature which has determined that motor neurons release factors such as agrin, which plays an integral role in forming the post-synaptic structures of the NMJ as well as muscular maturation (Frank and Fischbach, 1979; Bezakova and Ruegg, 2003; Sarrazin *et al*, 2011; Ebrahimi et al, 2018; Tissue Engineering and Regenerative Medicine). Future work could begin to test the hypothesis about the presence and concentration of agrin. Further characterization of the factors present in the spinal cord conditioned media would shed light on the exact process that drives this re-determination of myosin heavy chain isotyping. Cell source, 2D culture, and neuronal releasates are all important factors that influence skeletal muscle development *in vitro*.

However, we note that the spinal neurons produce stronger contractions than their stem cell-derived counterparts. This is likely due to increased motor neuronal innervation of the muscle tissue. Spinal cords contain orders of magnitude more cells than most neuronal stem cell

models and appear to produce larger neuronal arbors. Another explanation is that neuromuscular junction development occurs over approximately 3 weeks *in vivo* while the platforms described here and elsewhere generally provide only 7-10 days of co-culture. As the NMJs approach full maturity, it is expected that the amount of spontaneous neural firing will decrease, more myotubes will become singly innervated and stimulated muscle contractions will generate more force (Lupa and Hall, 1989; Takahashi *et al*, 1987; Xie and Poo, 1986).

5.2 Future Directions

The next step for this work would combine our data about organotypic spinal cord electrophysiology, 3D engineered muscle tissues with primary skeletal muscle, and controllable muscle contractions through spinal cord signaling and begin progressing towards multi-limbed locomotive behaviors. In Figure 3.2 we demonstrated the development of a novel platform for forming multiple, 3D muscle strips with primary skeletal muscle. Through an iterative optimization process, we learned that allowing the muscle cells to proliferate before seeding them on rounded pillars and being treated with a protease inhibitor greatly increased the yield of intact muscle strips (Figure 3.2). These muscle cells exhibited spontaneous contractions and were capable of matching electric stimulus frequencies at 1, 2, and 4 Hz with a variable force of contraction. Seeding a spinal cord in the middle of this array would cause the spinal cord outgrowths to extend laterally and innervate each of up to four individual muscle strips, forming a 'PNS-on-a-chip.'

By stimulating the pattern generating circuitry within the rat spinal cord, we hypothesize that it will drive simultaneous, coordinated, antiphase contractions of multiple engineered 3-D skeletal muscle tissues. This platform has several advantages over other existing devices. By switching to primary skeletal muscle and allowing the NMJs to reach a later stage of maturity, we hypothesize that the contractions will be greater than we showed before, though they will not reach the level of the autotypic muscle tissue or of *in-situ* muscles. The muscle strips are also only 1 mm in length and contain orders of magnitude fewer cells than the muscle strip demonstrated in Chapter 4. By providing the same number of motor neuron outgrowths and drastically fewer muscle fibers to innervate, we hypothesize that the innervation ratio of each muscle strip would

be significantly higher than has been previously achieved. No researchers to this point have engineered muscle tissues that contract as much as native fetal muscle in rats (~1000 µm; Dennis and Kosnik, 2000). We believe our results are more likely to follow that trend than previously established paradigms by using a more robust cell source, attaining a higher innervation ratio, and enhancing the degree of NMJ maturity. The multiple muscle array demonstrated here allows researchers to not only study gross muscle properties such as alignment, force generation, and neuronal innervation, but also to investigate deeper histological and functional questions in 3D. This would enable future experiments involving either contralateral (left-right pairing) or ipsilateral (flexor-extensor) coordination of multiple muscles. Additionally, by using an open-faced, modular platform, scientists can replace the healthy muscle tissue with diseased or dystrophic tissue and use conventional microscopy techniques to answer basic research questions or to test pharmacological interventions. More mature NMJs exhibit reduced amounts of spontaneous neuromuscular firing (Takahashi et al, 1987). Demonstrating the functionality and responsiveness of this *in-vitro* PNS will be an important step forward for the study of neuromuscular development and biorobotics.

Exercise is a key factor in both embryonic and adult muscle growth. Skeletal muscle is a highly dynamic, flexible tissue capable of remarkable changes to its behavior and morphology based on environmental conditions. For example, the rat soleus muscle increases in weight by 40% within six days after the tendon of its synergistic muscle, the gastrocnemius, is severed with no rehabilitation program beyond normal use (Goldberg et al, 1975). Previous work by Raman et al. improved force production of optogenetically transfected C2C12 cells by forcing the engineered, 3D tissues to undergo an “exercise regimen” of daily optical stimulation throughout muscle differentiation (Raman et al, 2016). Exercise was shown to improve myotube formation, leading to increased tension and locomotive speed. Providing electrical stimulation to the muscle strips in our platform during differentiation should lead to increased muscle force and more rapid maturation, in line with previous work. We hypothesize that these changes will also affect the formation of NMJs and lead to stronger muscle contractions overall.

Neural stimulation is another important factor for NMJ maturation. The initial polyneuronal innervation that occurs at immature NMJs is thought to be eliminated based on

activity-dependent release of chemicals from both neurons and muscles. Inhibition of synaptic release causes a drastic reduction in the rate of synaptic elimination while overstimulation expedites the process (Thompson, 1985). Additionally, if a particular neuron is more active than its neighbors, it is less likely to be eliminated (Balice-Gordon and Lichtman, 1994). Foundational neuroscience principles, such as Hebbian plasticity at the neuron-neuron synapse, have also been confirmed at the neuromuscular junction (Busetto et al, 2000). We hypothesize that stimulating both the spinal cord and skeletal muscle components of our platform simultaneously will result in the first engineered, *in-vitro* PNS that is capably able to mimic *in vivo* development and behavior in a modular, easily imaged system.

A 3D spinal cord-skeletal muscle platform with functional and controllable neuromuscular junctions could serve a variety of uses across disciplines. It would be an excellent tool for studying the pathology of neuromuscular diseases and as a platform for studying the efficacy and modes of action of novel drugs for treatment. We could also visualize this spinobot as a model for ALS, spinal muscular atrophy, Duchenne's muscular dystrophy, and peripheral neuropathies such as those secondary to diabetes mellitus. Some researchers have already begun adapting *in vitro* NMJ platforms for the study of these diseases (Osaki *et al*, 2018). The modularity of the 'spinobot' demonstrated here, innervation from a living spinal cord, and the use of an easily transfectable cell line are unique strengths of this platform. Early biohybrid robots and actuators are also expected to one day appear in surgical training tools, the study and repair of biological systems in dangerous environments, and at the interface for human-computer devices (Rossiter *et al*, 2009; Albalaihid *et al*, 2017; Park *et al*, 2014). It is expected that custom-printed 3D soft robots and actuator structures will start to appear in areas as diverse as medical implants, devices for human-computer interaction, and even children's toys (Rossiter *et al*, 2009). Other variations on 3D microphysiological systems have been developed with microfluidic chambers, neural stem cells, and/or photolithography control, significantly extending design possibilities.

Humanoid robots could assist human beings in numerous ways, from military applications and firefighting to entertainment, socially assistive devices, medical studies, and education. Soft actuators lay the groundwork for the development of these humanoid robots for cognitive

studies or for training medical professionals. In addition, facially expressive robots are demonstrating encouraging results as therapeutic tools for children with Autism Spectrum Disorder (Tadesse *et al*, 2016). The use of the spinal cord also enables a future design space involving the coordination of multiple muscles from a single neuronal source or the ability to incorporate the sensory dorsal root ganglion as inputs for the spinobot allowing it to respond to environmental cues. Soft robotics has almost unlimited potential to universally impact human life.

5.3 References

1. Cvetkovic, C., Ko, E., Kaufman, C., Grant, L., Gillette, M., Kong, H., & Bashir, R. (2018). Rapid prototyping of soft bioactuators. *3D Bioprinting in Regenerative Engineering: Principles and Applications*.
2. Majidi C. Soft robotics: A perspective—current trends and prospects for the future. *Soft Robot* 2013; 1: 5–11.
3. Chan V, Asada HH, Bashir R. Utilization and control of bioactuators across multiple length scales. *Lab Chip* 2014; **14**: 653–70.
4. Feinberg AW. Biological Soft Robotics. *Annu Rev Biomed Eng* 2015; **17**: 243–65.
5. Unver, O., Uneri, A., Aydemir, A., & Sitti, M. (2006, May). Geckobot: a gecko inspired climbing robot using elastomer adhesives. In *Proceedings 2006 IEEE International Conference on Robotics and Automation, 2006. ICRA 2006.* (pp. 2329-2335). IEEE.
6. Umedachi T, Vikas V, Trimmer BA. Softworms: the design and control of non-pneumatic, 3D-printed, deformable robots. *Bioinspir Biomim* 2016; **11**. doi:10.1088/1748-3190/11/2/025001.
7. Cvetkovic, C., Raman, R., Chan, V., Williams, B. J., Tolish, M., Bajaj, P., ... & Bashir, R. (2014). Three-dimensionally printed biological machines powered by skeletal muscle. *Proceedings of the National Academy of Sciences*, *111*(28), 10125-10130.
8. Bartlett, N. W., Tolley, M. T., Overvelde, J. T., Weaver, J. C., Mosadegh, B., Bertoldi, K., ... & Wood, R. J. (2015). A 3D-printed, functionally graded soft robot powered by combustion. *Science*, *349*(6244), 161-165.
9. Feinberg, A. W., Feigel, A., Shevkoplyas, S. S., Sheehy, S., Whitesides, G. M., & Parker, K. K. (2007). Muscular thin films for building actuators and powering devices. *Science*, *317*(5843), 1366-1370.
10. Wen, L., Wang, T., Wu, G., & Liang, J. (2012). Quantitative thrust efficiency of a self-propulsive robotic fish: Experimental method and hydrodynamic investigation. *IEEE/ASME Transactions on Mechatronics*, *18*(3), 1027-1038.
11. Low, K. H. (2007). Design, development and locomotion control of bio-fish robot with undulating anal fins. *International Journal of Robotics & Automation*, *22*(1), 88.
12. Herr, H., & Dennis, R. G. (2004). A swimming robot actuated by living muscle tissue. *Journal of neuroengineering and rehabilitation*, *1*(1), 6.
13. Nawroth, J. C., Lee, H., Feinberg, A. W., Ripplinger, C. M., McCain, M. L., Grosberg, A., ... & Parker, K. K. (2012). A tissue-engineered jellyfish with biomimetic propulsion. *Nature biotechnology*, *30*(8), 792.
14. Li, Z., Seo, Y., Aydin, O., Elhebeary, M., Kamm, R. D., Kong, H., & Saif, M. T. A. (2019). Biohybrid valveless pump-bot powered by engineered skeletal muscle. *Proceedings of the National Academy of Sciences*, *116*(5), 1543-1548.
15. Uzel SGM, Pavesi A, Kamm RD. Microfabrication and microfluidics for muscle tissue models. *Prog Biophys Mol Biol* 2014; **115**: 279–293.
16. Feinberg AW. Biological Soft Robotics. *Annu Rev Biomed Eng* 2015; **17**: 243–65.
17. Kim J, Kim HN, Lang Y, Pandit A. Biologically Inspired Micro- and Nanoengineering Systems for Functional and Complex Tissues. *Tissue Eng Part A* 2014; **19**: 1–4.

18. Carlsen, R. W., & Sitti, M. (2014). Bio-hybrid cell-based actuators for microsystems. *Small*, *10*(19), 3831-3851.
19. Kamm, R. D., & Bashir, R. (2014). Creating living cellular machines. *Annals of biomedical engineering*, *42*(2), 445-459.
20. Choi, S. W., Yeh, Y. C., Zhang, Y., Sung, H. W., & Xia, Y. (2010). Uniform beads with controllable pore sizes for biomedical applications. *Small*, *6*(14), 1492-1498.
21. Mudera, V., Smith, A. S. T., Brady, M. A., & Lewis, M. P. (2010). The effect of cell density on the maturation and contractile ability of muscle derived cells in a 3D tissue-engineered skeletal muscle model and determination of the cellular and mechanical stimuli required for the synthesis of a postural phenotype. *Journal of cellular physiology*, *225*(3), 646-653.
22. Gieseck III, R. L., Hannan, N. R., Bort, R., Hanley, N. A., Drake, R. A., Cameron, G. W., ... & Vallier, L. (2014). Maturation of induced pluripotent stem cell derived hepatocytes by 3D-culture. *PloS one*, *9*(1), e86372.
23. Prosser, R. A., & Gillette, M. U. (1989). The mammalian circadian clock in the suprachiasmatic nuclei is reset in vitro by cAMP. *Journal of Neuroscience*, *9*(3), 1073-1081.
24. Odawara, A., Saitoh, Y., Alhebshi, A. H., Gotoh, M., & Suzuki, I. (2014). Long-term electrophysiological activity and pharmacological response of a human induced pluripotent stem cell-derived neuron and astrocyte co-culture. *Biochemical and biophysical research communications*, *443*(4), 1176-1181.
25. Muller, D., Buchs, P. A., & Stoppini, L. (1993). Time course of synaptic development in hippocampal organotypic cultures. *Developmental Brain Research*, *71*(1), 93-100.
26. Uesaka, N., Hirai, S., Maruyama, T., Ruthazer, E. S., & Yamamoto, N. (2005). Activity dependence of cortical axon branch formation: a morphological and electrophysiological study using organotypic slice cultures. *Journal of Neuroscience*, *25*(1), 1-9.
27. Rohrbacher, J., Ichinohe, N., & Kitai, S. T. (2000). Electrophysiological characteristics of substantia nigra neurons in organotypic cultures: spontaneous and evoked activities. *Neuroscience*, *97*(4), 703-714.
28. Gillette, M. U., & Tischkau, S. A. (1999). Suprachiasmatic nucleus: the brain's circadian clock. *Recent progress in hormone research*, *54*(1), 33-58.
29. Balice-Gordon RJ, Lichtman JW. 1993. *In vivo* observations of pre-and postsynaptic changes during the transition from multiple to single innervation at developing neuromuscular junctions*. J. Neurosci.* 13: 834–55
30. Rosenthal JL, Taraskevich PS. 1977. Reduction of multiaxonal innervation at the neuromuscular junction of the rat during development. *J. Physiol*. 270: 299–310
31. Bennett MR, Pettigrew AG. 1976. The formation of neuromuscular synapses. *Cold Spring Harbor Symp. Quant. Biol.* 40: 409–24
32. Dai Z, Peng HB. 1996. From neurite to nerve terminal: induction of presynaptic differentiation by target-derived signals. *Semin. Neurosci.* 8:97–106
33. Fitzsimonds RM, Poo MM. 1998. Retrograde signaling in the development and modification of synapses. *Physiol. Rev.* 78: 143–70
34. Gan W-B, Lichtman JW. 1998. Synaptic segregation at the developing neuromuscular junction. *Science.*

35. Xie ZP, Poo MM. 1986. Initial events in the formation of neuromuscular synapse: rapid induction of acetylcholine release from embryonic neuron. *Proc. Natl. Acad. Sci.* USA 83:7069–73
36. Chow I, Poo MM. 1985. Release of acetyl- choline from embryonic neurons upon con- tact with muscle cell. *J. Neurosci.* 5:1076–82
37. Meier T, Masciulli F, Moore C, Schoumacher F, Eppenberger U, *et al*. 1998. Agrin can mediate acetylcholine receptor gene expression in muscle by aggregation of muscle-derived neuregulins. *J. Cell Biol.* 141: 715–26
38. Jones G, Herczeg A, Ruegg MA, Lichsteiner M, Kroger S, Brenner HR. 1996. Substrate-bound agrin induces expression of acetylcholine receptor ε-subunit gene in cultured mammalian muscle cells. *Proc. Natl. Acad. Sci.*
39. Kelly AM, Zacks SI. 1969. The fine structure of motor endplate morphogenesis. *J. Cell Biol.* 42:154–69
40. Takahashi T, Nakajimi Y, Hirosawa K, Nakajimi S, Onodera K. 1987. Structure and physiology of developing neuromuscular synapses in culture. *J. Neurosci.* 7:473–81
41. Lupa MT, Hall ZW. 1989. Progressive restriction of synaptic vesicle protein to the nerve terminal during development of the neuro- muscular junction. *J. Neurosci.* 9:3937–45
42. Dhawan, V., Lytle, I. F., Dow, D. E., Huang, Y. C., & Brown, D. L. (2007). Neurotization improves contractile forces of tissue-engineered skeletal muscle. *Tissue engineering*, *13*(11), 2813-2821.
43. Hood, D. A. (2001). Invited Review: contractile activity-induced mitochondrial biogenesis in skeletal muscle. *Journal of applied physiology*, *90*(3), 1137-1157.
44. McComas, A. J., Kereshi, S., & Manzano, G. (1984). Multiple innervation of human muscle fibers. *Journal of the neurological sciences*, *64*(1), 55-64.
45. Lewis, M. R. (1915). Rhythmical contraction of the skeletal muscle tissue observed in tissue cultures. *American Journal of Physiology-Legacy Content*, *38*(1), 153-161.
46. Schmoll, M., Unger, E., Sutherland, H., Haller, M., Bijak, M., Lanmüller, H., & Jarvis, J. C. (2017). In-situ measurements of tensile forces in the tibialis anterior tendon of the rat in concentric, isometric, and resisted co-contractions. *Physiological reports*, *5*(8), e13245.
47. Osaki, T., Sivathanu, V., & Kamm, R. D. (2018). Vascularized microfluidic organ-chips for drug screening, disease models and tissue engineering. *Current opinion in biotechnology*, *52*, 116-123.
48. Maffioletti, S. M., Sarcar, S., Henderson, A. B., Mannhardt, I., Pinton, L., Moyle, L. A., Steele-Stallard, H., Cappelari, O., Wells, K. E., Ferrari, G., Mitchell, J. S., Tyzack, G.E., Kotiadis, V. N., Khedr, M., Ragazzi, M., Wang, W., Duchen, M.R., Patani, R., Zammit,. P. S., Wells, D. J., Eschenhagen,, T., Saverio Tedesco, F. (2018). Three-dimensional human iPSC-derived artificial skeletal muscles model muscular dystrophies and enable multilineage tissue engineering. *Cell reports*, *23*(3), 899-908.
49. Bakooshli, M. A., Lippmann, E. S., Mulcahy, B., Iyer, N., Nguyen, C. T., Tung, K., Stewart, B. A., van den Dorpel, H., Fuehrmann, T., Shoichet, M., Bigot, A., Pegoraro, E., Ahn,, H., Ginsberg, H., Zhen, M., Scott Ashton, R., Gilbert, P. M. (2019). A 3D culture model of innervated human skeletal muscle enables studies of the adult neuromuscular junction. *Elife*, *8*, e44530.

50. Cvetkovic C, Rich MH, Raman R, Kong H, Bashir R. A 3D-printed platform for modular neuromuscular motor units. *Microsystems Nanoeng* 2017; **3**. doi:10.1038/micronano.2017.15.
51. Langelaan, M. L., Boonen, K. J., Rosaria-Chak, K. Y., van der Schaft, D. W., Post, M. J., & Baaijens, F. P. (2011). Advanced maturation by electrical stimulation: Differences in response between C2C12 and primary muscle progenitor cells. *Journal of tissue engineering and regenerative medicine*, *5*(7), 529-539.
52. Frank E, Fischbach GD. 1979. Early events in neuromuscular junction formation *in vitro*: induction of acetylcholine receptor clusters in the postsynaptic membrane and morphology of newly formed synapses. *J. Cell Biol.* 83: 143–58
53. Bezakova G, Ruegg MA. 2003. New insights into the roles of agrin. *Nat. Rev. Mol. Cell Biol.* 4: 295-308
54. Sarrazin S, Lamanna WC, Esko JD. 2011. Heparan sulfate proteoglycans. *Cold Spring Harb Perspect Biol.* 3:
55. Ebrahimi, M., Ostrovidov, S., Salehi, S., Kim, S. B., Bae, H., & Khademhosseini, A. (2018). Enhanced skeletal muscle formation on microfluidic spun gelatin methacryloyl (GelMA) fibres using surface patterning and agrin treatment. *Journal of tissue engineering and regenerative medicine*, *12*(11), 2151-2163.
56. Dennis RG, Kosnik PE. Excitability and isometric contractile properties of mammalian skeletal muscle constructs engineered *in vitro*. *Vitr Cell Dev Biol - Anim* 2000; **36**: 327–335.
57. Goldberger, M. E. (1977). Locomotor recovery after unilateral hindlimb deafferentation in cats. *Brain research*, *123*(1), 59-74.
58. Raman R, Cvetkovic C, Uzel SGM, Platt RJ, Sengupta P, Kamm RD. Optogenetic skeletal muscle-powered adaptive biological machines. *Proc Natl Acad Sci* 2016. doi:10.1073/pnas.1516139113.
59. Thompson WJ. 1985. Activity and synapse elimination at the neuromuscular junction. *Cell. Mol. Neurobiol*. 5: 167–82
60. Balice-Gordon RJ, Lichtman JW. 1994. Long-term synapse loss induced by focal blockade of postsynaptic receptors. *Nature.* 372: 519– 24
61. Busetto, G., Buffelli, M., Tognana, E., Bellico, F., & Cangiano, A. (2000). Hebbian mechanisms revealed by electrical stimulation at developing rat neuromuscular junctions. *Journal of Neuroscience*, *20*(2), 685-695.
62. Osaki, T., Sivathanu, V., & Kamm, R. D. (2018). Vascularized microfluidic organ-chips for drug screening, disease models and tissue engineering. *Current opinion in biotechnology*, *52*, 116-123.
63. Rossiter J, Walters P, Stoimenov B. Printing 3D dielectric elastomer actuators for soft robotics. In: Bar-Cohen Y, Wallmersperger T (Eds.). *Electroactive Polymer Actuators and Devices* (*EAPAD*) *2009*. SPIE, 2009. doi:10.1117/12.815746.
64. Alblalaihid K, Overton J, Lawes S, Kinnell P. A 3D-printed polymer micro-gripper with self-defined electrical tracks and thermal actuator. *J Micromechanics Microengineering* 2017; 27: 45019.
65. Park YL, Santos J, Galloway KG, Goldfield EC, Wood RJ. A soft wearable robotic device for active knee motions using flat pneumatic artificial muscles. In: *2014 IEEE International Conference on Robotics & Automation* (*ICRA*). IEEE, Hong Kong, 2014, pp. 4805–4810.

66. Tadesse, Y., Wu, L., & Saharan, L. K. (2016). Musculoskeletal system for bio-inspired robotic systems. *Mechanical Engineering Magazine Select Articles*, *138*(03), S11-S16.

APPENDIX A1. RAPID PROTOTYPING OF SOFT BIOACTUATORS

This chapter heavily utilizes the following publication.

[2]Cvetkovic, C., Ko, E., Kaufman, C., Grant, L., Gillette, M., Kong, H., & Bashir, R. (2018). Rapid prototyping of soft bioactuators. *3D Bioprinting in Regenerative Engineering: Principles and Applications*.

A1.1 Abstract

The driving principle behind most robots is force actuation leading to a form of directed movement. Natural or organic systems can inspire the design of biological robots that replicate or enhance many basic locomotive strategies with novel solutions, facilitating engineering approaches to challenges historically plaguing traditional robotics. Stiff skeletons and electromagnetic actuators can result in rigid bioactuators that exhibit few degrees of freedom (DOF) and lack multi-functionality or adaptability. Conversely, effective soft bioactuators generally have more DOF, higher power-to-weight ratios, and are more compliant than their rigid counterparts. Typically composed of flexible polymers and fluids (sometimes with biological materials), they are often capable of untethered and directional locomotion, elastic deformation, efficient energy storage, and robust motion control. These lightweight materials have lower stiffness that corresponds to properties of biological matter with which they might interact. Rapid prototyping (RP) refers to a group of techniques that collect digital information to fabricate physical 3D structures in an additive fashion, allowing for complex structures and geometries, high spatial control, and a range of properties. In this chapter, we discuss the use of RP technologies to achieve the development of soft bioactuators.

[2] All authors wrote and edited the manuscript. All authors have given approval to the final version of the manuscript.

A1.2 Background: Bio-inspiration in Tissue Engineering and Robotic Actuators

The driving principle behind man-made robots is force actuation leading to a form of directed movement or locomotion. Natural systems can motivate the design and development of robots that replicate or enhance many basic locomotive strategies – such as climbing, crawling[1], walking[2], jumping[3,4] or swimming[5–9] – with novel solutions. Biological soft robotics derives inspiration and design principles from organic systems to facilitate engineering approaches to challenges that have historically plagued conventional robotic actuators. Traditional hard skeletons (made of high stiffness metals or plastics) and electromagnetic actuators can result in rigid bioactuators that exhibit few degrees of freedom (DOF), low complexity, difficulty in grasping actions, and aggressive collisions with living tissues. Moreover, they rarely present multi-functionality, versatility, or adaptability[10].

Conversely, soft bioactuators (typically composed of gels, polymers, and fluids, sometimes with the addition of biological materials) must not only be functional in a research laboratory, but also effective in situations where they may be called upon to move over unstable terrain while carrying heavy loads of sensors, imagers, or samplers. These devices would also ideally be capable of untethered as well as directional locomotion, elastic deformation or stiffness modulation, efficient energy storage, and robust motion control, in order to be both effective and useful. Finally, these continuum robots must be environmentally safe and sufficiently low-cost such that they can be abandoned if damaged or polluted[11]. Soft bio-robotic manipulators with high power-to-weight ratios generally have more DOF and are more compliant than their rigid counterparts, and can manipulate fragile and unknown objects via a simple control algorithm. The lightweight and flexible polymers, hydrogels, and elastomers used to form soft robots have lower stiffness (moduli of 10^4 – 10^9 Pa) that corresponds to properties of biological matter with which they might interact (Figure A1.1a). Due to recent manufacturing advancements, they can be rapidly produced with high spatial control and a range of properties in three dimensions (3D)[3,12–15].

Beyond structures, soft bio-robotic systems require an actuating source and fuel supply. It therefore follows that living biological materials (or relevant mimics thereof) would inspire and

comprise a large portion of demonstrated bioactuators[15,16]. Beyond simple bio-mimicry, the field of "bio-design" incorporates living organisms into artificial or manmade systems[17]. The addition of living biological actuator sources (e.g., muscle tissues) can increase the efficiency and responsiveness of soft actuators, as many of these living components have evolved with efficient standard processes for force production, energy consumption, or net movement[18–21]. The world of biology is full of intricate systems designed to solve extremely complex locomotive and manipulative tasks with high efficiency at a wide variety of scales. Depending on the ecosystem, there are numerous methods of potential locomotion among diverse structures and species, including both plants and animals[22]. Considering the breadth of methods of propulsion, it is perhaps unsurprising that there are also many ways for these robots to generate a range of locomotive forces, from molecular (e.g., motor proteins; 10^{-9} m) to cellular (e.g., individual microorganisms or cells; 10^{-6} m) to tissue (e.g., muscles or cell clusters; 10^{-3} m) length scales[21]. In addition to locomotors, there are also bio-robots that imitate peristalsis to act as pumps or valves, transport cargo, actuate a joint, sense a signal, or perform as micro-grippers, rotors, mixers, or manipulators to achieve other tasks[23–26]. It is apparent that the development of soft bioactuators necessitates the intersection and integration of advancements in diverse fields such as nanotechnology, tissue engineering, and developmental biology[27]. In this chapter, we discuss the use of rapid prototyping technologies to achieve that end.

A1.3 Rapid Prototyping Techniques and Applications

The malleable nature, micro- to macro- scale, and potential for intricate composition and structure of bioactuators suggests that researchers will require a different manufacturing approach than can generally be employed for rigid robots. Rapid prototyping (RP) refers to a group of techniques that collect digital information to robotically fabricate physical 3D polymers, metals, and ceramic solids[28–30]. These 3D structures are dictated by a computer-assisted design (CAD) model of the desired part, which can be built from scratch or derived from medical images in order to print patient-specific structures. Although various techniques exist (Figure A1.1b-g), all methods of RP adapt a similar fundamental approach: a CAD model is converted into a standard tessellated language (STL) file; a computer program then receives the information and

slices the 3D model; and finally, these cross sections are sequentially layered using additive manufacturing technologies that employ extrusion, melting, jetting, or photo-polymerization to create a final structure. All RP techniques have short fabrication times, low costs, minimal post-processing and waste, and variable material choices and properties, with resolutions that extend from micron to centimeter scale[18,31–33].

CAD not only serves as the input for an important method by which soft robotic actuators or patient specific scaffolds can be fabricated, but also provides a substrate for virtual testing and development. Due to both the increasing ubiquity of (and immense improvements in) computational power, simulation tools can now be used to calculate kinematic, dynamic, and finite element analysis-based responses of a prototype and visualize the results in an interactive, 3D virtual environment. The ability to model prototypes realistically and accurately while validating preliminary prototype results has become integral in nearly all facets of engineering design, including bio-inspired robotics[34]. Finally, CAD libraries can also be utilized for input on material selection and design optimization[35].

RP allows for the fabrication of complex and multi-layered 3D structures and geometries that cannot be achieved using conventional multi-step processes such as mask-based soft lithography, and was therefore introduced to tissue engineering to overcome limitations of conventional fabrication techniques[24,36,37]. For example, some RP techniques could allow for printing of spatially-controlled growth factors, or the use of multiple nozzles loaded with different biomaterials to create more advanced tissue structures composed of diverse matrix components[38–40]. Importantly, stereolithography (SL) enables the construction of micro- or meso-scale tissue structures with desired shapes and physical properties[41], and provides the user with a wide range of synthetic and natural material options (e.g., hydrogels that can encapsulate living cells[42,43]) that offer greater versatility and compatibility than PDMS or metallic structures. Furthermore, through the specification of light intensity, irradiation time, and chemical makeup of the liquid resin, the mechanical properties of a printed part can be precisely regulated. The ability to fine-tune these features, including strength and porosity, can have implications for cells that are sensitive to the stiffness, topography, and geometry of their micro-environment[42,44–47].

Moreover, CAD allows for the production of advanced designs that closely resemble the physical morphology, orientation, or finer details of native tissue; interconnected pores, complex surface topography, and internal structures can be easily reconstructed into rapidly manufactured scaffolds[48–50].

Due to increasing automation speeds as well as high throughput and iterative capabilities that allow for design optimization, rapid prototyping technologies are especially useful for the production of soft bioactuators in an inexpensive and mass-producible manner[10,30,51]. These techniques can be utilized to construct temporary or sacrificial shape-specific molds, or to print the bodies of flexible bioactuating devices themselves[19]. In the case of the latter, high-yield RP allows for manufacturing of complex structures in a single step process, with the possibility of shape variations or heterogeneous properties[18].

Each RP technique requires different materials in a specific form. The selected material thus needs to be compatible with the fabrication method as well as the intended application. In addition, the specific architecture of the scaffold depends on the type of RP technique. For example, selective laser sintering (SLS) of powders is not suitable for building porous structures or smooth surfaces; on the other hand, extrusion-based fused deposition modeling (FDM) produces thermoplastic parts with smooth surfaces that need further modification to ensure cell adhesion. Soft actuators necessitate a flexible bio-degradable or bio-compatible polymer[18,40,51]. Therefore, it is important to consider material properties and the design of the scaffold, whether the user desires to successfully regenerate a tissue or build a functional bioactuator. The user's choice of RP fabrication technique, materials, and biological actuating source (if applicable), should be entirely context- and application-dependent.

A1.4 Non-Living Bioactuators

In many cases, synthetic RP devices have been developed to mimic the agonist-antagonist style of actuation that characterizes living tissues (Figure A1.2a-d). While they do exhibit many favorable characteristics (such as greater DOF and flexibility) compared to rigid actuators and are not subject to the sensitivity or strict environmental conditions necessitated by metabolically

active cells, non-living soft bioactuators can be at a loss when compared to the volumetric efficiency of native muscle, or the controllability of rigid actuators. Moreover, these systems often require an external power source, which adds extraneous weight that further increases energy requirements. This additional hardware, however, can contribute to significantly improved power density for synthetic actuators. The movement of non-living soft devices can be controlled with fluidic elastomer actuators (FEAs, which utilize pneumatic or hydraulic pressure), variable length tendons (such as tension cables or shape-memory materials), or electroactive polymers (EAPs, which can be ionic or electronic)[18,52]. Considering the advantages, it is not surprising that RP fabrication methods also permit low production costs and printing times for soft bioactuators[19,53]. 3D printed soft actuator materials, utilized stimuli, speeds, and pros and cons are reviewed in Refs[1,51,52].

A1.4.1 Fluidic Elastomer Actuators

FEAs are a frequently utilized actuation method that relies on pressurized fluid or compressed air for controlled structural deformation. Design or geometric asymmetry can allow for net movement upon fluid inflation. Pneumatic systems (such as McKibben actuators[54] or artificial muscles) generally consist of both extensible as well as inextensible but flexible layers, broken up into a series of internal chambers or channels. Upon pressurization, the more inflexible shell constrains the material to increase its diameter, shorten, and exhibit greater rigidity or stiffness – i.e., to contract like muscle[52,55]. These versatile soft robots can be modeled after worms[56], octopuses[57], flat muscle[58], and novel multi-limbed organisms[59]. Recent advances have resulted in the development of soft, miniaturized pneumatic hardware that allows the robots to behave somewhat autonomously, such as crawling through tightly confined spaces – which would be impossible to navigate with rigid or tethered robots[60,61]. Pneumatic actuators are lightweight, robust, and easily controlled; moreover, they can operate in wider temperature ranges than muscle *in vivo*[62]. However, some pneumatic systems still lack robustness, reliability, and overall control[63].

Yang *et al* created a variable stiffness robotic finger that exhibited a change in elastic modulus of the 3D printed shape memory polymer (see 6.3.2) skeleton with temperature. Heating of

selective regions within the pneumatic actuator caused bending of the substrate, and could be modified to achieve gripping or grasping[64]. Bartlett *et al* 3D printed a multi-material robot that exhibited a wide stiffness gradient within its body. The jumping robot was powered by both a combustion reaction within the body's chamber as well as inflation of its pneumatic legs[4]. Recently, Wang *et al* directly 3D printed an air-driven soft robot, with integrated curvature sensors, capable of gripping. It has been hypothesized that the use of soft grippers could increase safety and decrease scar formation in surgical applications[55,65].

Some work has moved away from the use of air as its medium and instead incorporates denser fluids in the creation of hydraulic-powered soft robots[66]. MacCurdy *et al* used a 5-head printer to fabricate a bellows actuator of solid polymers and liquid material simultaneously. The legs were actuated by pumping fluid throughout the bellows of the hexapod robot's body[67]. Using propulsion principles seen in the octopus, Fischer *et al* created a hydraulic underwater actuator by using FDM to fabricate a flexible thermoplastic material[68]. Hydraulic power increases the ceiling frequency of actuation and provides higher forces and durations of actuation than pneumatic pressure. However, pneumatic actuation is more environmentally benign and exhibits less weight[19,69].

A1.4.2 Variable Length Tendon Actuators and "Smart" Materials

Variable-length tendon actuators that conform or morph their properties can take the form of shape memory alloy (SMA) actuators, lightweight metals with highly tunable mechanical properties depending on the specific alloy used, or tension cables, which require an external conventional motor. Advantages of SMAs include minimal weight and bidirectional scaling. As shown in tentacular soft robots[60], application of a thermoelectric stimulus to composite SMAs can result in directed movement with high force and large DOF during a temperature-induced phase transformation. However, the phase transition is relatively slow and lacking in high precision, and researchers lack a targeted method for heating the wires[55,70].

The materials used in soft robotics must contain an additional level of complexity that allows them to be stable along a wide range of environmental conditions, but undergo drastic

conformational changes upon variation of this environmental stimulus around a given critical point[71]. A common category of bioactuator utilizes rapidly prototyped or printed "smart" materials that can physically react to dynamic stimuli. Though response time and control mechanisms vary by stimulus, these materials can controllably and reversibly respond to changes in pH, light, pressure, moisture, temperature, ionic gradient, and electric or magnetic fields by altering one or more physical properties, such as contraction or expansion of shape – much like an organism might do when subjected to varying ecological conditions[71–75].

Combining smart materials with rapid prototyping can have interesting outcomes for soft bio-robotics. For example, a composite biomimetic actuating system could contain SMAs embedded in soft 3D printed materials for greater control. These smart materials can provide actuation power as well as structural support, lending soft bioactuators increased flexibility and dexterity. Walters *et al* prototyped a tentacle-like elastomer fabricated by 3D printing and actuated by inserted SMAs[76]. Gui *et al* manufactured a tri-pedal soft robot modeled after a spider. Forward locomotion was powered by an SMA "muscle" (a metal fiber) directly printed into a soft 3D photopolymer adhesive structure[11]. Drawing inspiration from the deformation of crawling and climbing insects, Umedachi *et al* designed electrically powered, SMA- or electric tendon-actuated "softworms." These multi-limbed actuators contained a rubber body fabricated from multi-material 3D printing. SMAs provided structural support as well as actuation; variable friction control allowed for net forward crawling, as well as control of speed and steering[1,77,78]. The combination of 3D fabrication with controllable spatiotemporal properties is sometimes referred to as "four dimensional (4D) printing"[70,72].

Shape memory polymers (SMPs) can recover their original conformation from a temporary stimulus-induced change in shape. Compared to SMAs, these softer materials are cheaper and have a larger range of tunable properties (mechanical, thermal, or optical), and are more similar to native muscle[72,79,80]. Importantly, they do not require the extensive current supply or activation heat of SMAs[18]. Bodaghi *et al* printed SMPs into various arrangements of flexible beams in planar and tubular arrangements. A stress anisotropy resulted in expansion and shrinking of the polymer bioactuator upon thermo-mechanical stimulus[81]. Mao *et al* designed a

3D printed arrangement of two different materials. Two-way actuation was achieved as the system could reversibly switch between twofold stable configurations in response to temperature (SMPs) or water absorption (hydrogel) stimuli[82]. Wu *et al* controlled the bending, folding, and opening of 2D substrates by adjusting the SMP fiber volume fraction within a 3D printed composite to mimic insect, helix, and hook designs[83].

Hydrogels are capable of swelling upon water absorption and can be considered "smart" materials for 4D printing. Bakarich *et al* developed a thermally stimulated actuator with large strain by printing an ionic covalent entanglement hydrogel (PNIPAAm) with high toughness. The transition of the material at a critical temperature caused a decrease in water content and change in volume[74]. Sydney Gladman *et al* printed a patterned hydrogel composite out of a soft polyacrylamide matrix with embedded stiff cellulose fibrils. The multi-material system mimicked a plant cell wall composition and produced a controlled curvature due to anisotropic swelling when immersed in water[72]. Zolfagharian *et al* demonstrated a photo-thermal-responsive bioactuator, additively manufactured from an extrusion-based chitosan hydrogel, with remote control over folding[84]. Zhu *et al* developed an optical 3D printing technology to fabricate an artificial PEG-hydrogel microfish with magnetic guidance[85].

A1.4.3 Electroactive Polymer Actuators

When subjected to an electric field stimulus, EAPs are capable of changes in overall shape, resulting in strain and therefore actuation. These materials have been utilized for a range of applications, including the development of electrically active soft bioactuators[55,86]. Asaka *et al* presented a thorough review of EAP materials and biomedical applications in Ref[87]. Dielectric elastomer actuators (DEAs) are capable of thickness contraction and area expansion under high voltage. They can demonstrate high strain (200%), elasticity, efficiency, and energy density. Rossiter *et al* fabricated a DEA using a combination of 3D printing techniques with soft and rigid materials. A simple antagonistic structure composed of two membranes was proposed as a prototype for soft robotics[88]. Recently, Cai *et al* developed an acrylic DEA to robotically mimic native facial muscles using both FDM for the frame and a multi-material 3D printer for the

dielectric film[89], and Nguyen *et al* fabricated a scalable DEA hexapod robot with controllable directional locomotion, rotation, and turning[90].

Ionic polymer-metal composites (IPMCs) require low actuating voltages to change shape or bend and are therefore promising for soft robotics. They must operate in wet conditions (amenable to swimming bioactuators), and thus require some protection in air[14,19,52,76]. While these compliant materials have been developed as intelligent artificial muscles, only a few groups have constructed soft EAP bioactuators with rapid prototyping technologies[86]. Carrico *et al* demonstrated a novel method for printing soft IMPC structures using fused filament additive manufacturing. A polymer was printed in a layer-by-layer fashion and rendered electroactive via subsequent chemical functionalization[91].

A1.4.4 3D Printed Molds for Fabrication of Soft Bioactuators

In addition to the printing of entire bioactuators themselves, RP has been used to manufacture both sacrifical and permanent molds[60,63,92] in which to shape bioactuators from rubber, PDMS, or other soft materials (sometimes dubbed "semi-printing"). For example, Ahn *et al* created a smart material actuator, capable of bending and twisting, embedded in a soft matrix that was cast with a 3D printed mold[93]. Low *et al* formed silicone-based soft pneumatic grippers[55], and Martinez *et al* demonstrated a micro-pneumatic tentacle that could grasp and manipulate complex objects[57], by casting soft materials into custom-printed 3D molds. An IMPC-embedded tube (cast into a 3D printed mold) with multi-DOF capability was developed by Liu *et al* to aid in minimally invasive surgical procedures[94].

Regarding actuators whose entire structures can achieve net locomotion, Jin *et al* fabricated a soft robot capable of swimming, gripping, and crawling, whose body was integrated with SMA wires and molded using 3D printed parts[70]. Lin *et al* used 3D printed plastic molds to create a soft, rolling, coiled SMA-actuated "GoQBot"[95]. Mosadegh *et al* molded a "pneu-net" (pneumatic network) soft robot whose body was actuated by air inflation[56]. Most recently, Yuk *et al* published a hydraulic, polyacrylamide-alginate hydrogel actuator molded from 3D printed solids[96], and

Wehner *et al* cured an elastomer containing an embedded controller in a 3D printed mold to fabricate a multi-material pneumatic soft "octobot" with eight arms[97].

However, it should be noted that elastomeric bioactuators printed in whole, as compared to those cast in a 3D printed mold, can boast easier and shorter fabrication without a subsequent need for post-processing or assembly[76]. Morrow *et al* modified a FDM printer to directly fabricate a silicone pneumatic actuator; comparison to an identical structure made from a molding process demonstrated no tradeoff in force[98].

A1.5 Living Bioactuators

The use of biological materials (including DNA, motor proteins, myosin-actin complexes, bacteria, algae, single cells or clusters, and natural or engineered tissues – either independently or collectively) as the primary actuators of locomotive force is still an extremely young field, but has resulted in some interesting possibilities (see Refs[21,99] for a review). The basic requirements of an ideal living biological actuation source include the ability to generate a controllable or repeatable force, operate under a range of environments, and be easily maintained[24]. Evolution has produced optimal living actuators that can operate long-term at physiological conditions (favorable for bio-medical applications), wirelessly convert chemical energy (from glucose or fats, for example, which can boast energy densities up to 100 times that of a battery[10]) to mechanical work more efficiently than non-living power sources, produce nontoxic and biodegradable byproducts from fuel conversion, and be stimulated electro- or pharmaco-mechanically – thus eliminating the need for an external energy source. Additionally, they are proficient at self-assembly and replication, protein synthesis, rapid adaptation (responses as short as tens of milliseconds), and high sensitivity to environmental conditions. Understandably, they are also biodegradable and biocompatible, and can dynamically interact with other living or non-living components[15,53,99].

In general, when exploiting the innate contractility of cells or tissue to power a bioactuator, it is critical to consider the stimuli (mechanical, electrical, and biochemical) necessary for differentiation, development, or maintenance[46,53]. RP techniques can assist in providing a

suitable scaffold or environment in which appropriate cues can be tuned or added (Figure A1.2e-g). For example, a stereolithography apparatus (SLA) can print hydrogels with tissue-like stiffness values that are mechanically similar to cells' extracellular environment *in vivo*. The elastic modulus of the extracellular matrix (ECM) not only affects viability and proliferation, but also dictates the differentiation bias of cultured stem cells[100]; for this reason, stereolithography has been used to fabricate a variety of matrices that can realistically simulate cellular microenvironments and aid in engineered tissue development[42].

Though engineered molecular[21,24,73] and bacterial[101] bioactuators are capable of cargo transport and fluidic pumping and can thrive in a range of environmental temperatures or pH, few have been incorporated with RP techniques[99]. The combination of many cells can allow for a collective output that is greater than the sum of its parts. Moreover, complexity (and thus functionality) increases when progressing from single cells to cell clusters (2D sheets or 3D arrangements) to tissues and systems[24,27]. Therefore, in this section we will focus only on living eukaryotic bioactuators at the multi-cellular and tissue scale, comprised of a synthetic mechanical scaffold and one or more actuating biological components.

Scalable molecular motors and contraction machinery that comprise muscular sarcomeres in particular can generate active contraction in multiple forms and size scales, be hierarchically combined in series or in parallel, and has evolved over millions of years with extremely high plasticity and volumetric efficiency[21,24,35]. Functional bioactuators have been devised using whole explanted tissues[8,102,103], cells differentiated within a scaffold or gel[104], or self-organized engineered tissue[105]. It is worth noting that although smooth muscle[106] is capable of force production, its relatively slow contraction has prohibited its employment in bio-robots that require rapid actuation[99].

A1.5.1 Cardiac Muscle

Cardiomyocytes (cardiac muscle cells) provide an excellent source for bioactuation due to their intrinsic, synchronous contraction; thus, external stimulation is unnecessary. The cells can form a syncytium through gap junctions and cell-cell adhesions, and produce spontaneous

contractions[21,27]. The original developments in cardiac-based bioactuators included locomotive machines such as walking micro-robots[5,107,108], on-chip pumps[109], and swimming robots[110] and "jellyfish"[9]. However, most were constructed on silicon or PDMS substrates that did not mimic the native cellular microenvironment nor allow for dynamic adaptation; few have been coupled to substrates fabricated from RP methods.

To demonstrate the ability of cardiac cells to induce the locomotion of a material with an elastic modulus similar to that of the native myocardium, Chan *et al* developed a biological robot (dubbed "bio-bot") from poly(ethylene glycol) (PEG) hydrogel[41,111]. A modified SLA was utilized to fabricate a micro-cantilever, the surface of which was functionalized with collagen in order to adhere a culture of primary neonatal rat cardiomyocytes. To transform this hybrid structure into a bioactuator capable of directional locomotion, a net asymmetry of actuation was introduced in the cantilever design. Furthermore, the thickness of the cantilever was optimized to control the curvature of the actuating leg and maximize the locomotive speed. The occurrence of a "power stroke" induced by rhythmic spontaneous cardiac sheet contraction drove the actuating leg to bend downward, increasing the friction and causing the bio-bot to propel forward. With a maximum velocity of 236 μm/sec, the cardiac bio-hybrid actuator demonstrated efficient mechanisms of autonomous locomotion as well as a novel approach to spatially control biochemical and physical cues during fabrication.

A1.5.2 Skeletal Muscle

The behavioral complexity and degree of external control that can be imposed on cardiac muscle is limited by its intrinsic spontaneous contractility. The ability to regulate an actuator through the modulation of an applied stimulus not only allows for precise control over its motion, but also opens up avenues for greater functionality. Skeletal muscle is the primary generator of animal locomotion, with a dense structure comprising a modular hierarchy with an arrangement of motor units that can be recruited individually or in summation. It exhibits a greater force-to-weight ratio in comparison to many rigid mechanical actuators[21,24,27,99]. A high degree of spatial and temporary control over actuation, even of single fibers, is possible via external sources such as electrical[2], optical[112,113], or neural[114,115] stimulation.

A skeletal muscle-powered bio-bot developed by Cvetkovic *et al* mimicked the mammalian musculoskeletal system, wherein muscle contraction drives the articulation of bones across flexible joints[2,116]. A 3D printed skeleton (comprised of a flexible beam connected to two stiff pillars) was fabricated using a SLA and subsequently anchored to an engineered muscle strip containing differentiating C2C12 myoblasts. The 3D muscle strip contained natural ECM hydrogels (fibrin and Matrigel™) that supported the densely embedded cells. To induce the locomotion-driving contraction of the muscle strip, the bio-bot was positioned within an electric field and subjected to a pulse stimulation of 1-4 Hz, resulting in a global response of the excitable cells. The introduction of deliberate asymmetry in the pillars (achievable with a slight modification in the rapid prototyping technique) allowed the bio-bot to move in a unidirectional trajectory along a surface in a fluid with a maximum locomotion of ~150 µm/s.

Although the muscle strip successfully induced net locomotion, the muscle was permanently tethered to the skeleton, preventing the adaptation of the muscle to other skeleton structures[2]. A second iteration by Raman *et al* was devised with a muscle ring structure, formed in a separate 3D printed mold before being transferred to the skeleton[113]. Muscle rings exhibited higher myofiber alignment as well as increased viability[116]. The C2C12s were also genetically modified to express Channel rhodopsin (ChR2), a membrane protein which causes muscle contraction under the presence of blue light[117]. This allowed for the control of locomotion through an optical stimulus, which could be positioned on localized regions of the bio-bot, thus enabling the development of a symmetrical yet bi-directional bioactuator whose direction of locomotion was determined by which ring the light stimulated. Similarly, a single device could also be forced to rotate by stimulating only one half of a single muscle ring. To maximize force production, the bio-bots underwent an "exercise regimen" of daily optical stimulation throughout muscle differentiation. Exercise was shown to improve myotube formation, leading to increased tension and locomotive speed up to 310 µm/s.

A1.5.3 Control Mechanisms for Living Bioactuators

Cell- and tissue-based bioactuators can be controlled in a variety of manners, both internally regulated and externally applied. Internal, cell-based control utilizes intrinsic sensory pathways

or mechanisms within the biological material. External, non cell-based control involves remote operation or local environmental stimuli – whether chemical, magnetic, electrical, optical, or a combination thereof[24]. Cardiomyocytes, for example, can be controlled with temperature variance, and skeletal muscle cells can be activated via electrical fields, optogenetics, or a neuronal network (requiring acetylcholine release from an innervating motor neuron). Optical control is negligibly invasive, irreversible, and can provide precise spatiotemporal control. It can also be used as an on/off toggle switch to quickly modulate contraction, pacing, or net actuation[21,118,119].

The ability to non-invasively control living bioactuators with such specificity sets the stage for the development of future biological machines for a variety of applications. However, care must be taken to ensure that stimuli are applied within ranges that are acceptable or minimally invasive for living biological material, especially when dealing with exposure to ultraviolet (UV) light or electromagnetic fields, changes in pH and temperature, media electrolysis, and toxic waste byproducts[24].

A1.6 Applications

Rapid prototyping technologies, which continue to advance in efficiency, resolution, and bio-compatible material selection[72,120], provide a controlled, economical, and potentially high-throughput solution to the production of responsive bioactuators for myriad applications. The extreme diversity of fabrication approaches, material composition, and functionalities suggests that soft bioactuators can be used in a variety of manners and systems. They boast many useful capabilities, including shape deformation, conformation and sensitivity to their surroundings, movement in unstructured environments, and manipulation of delicate objects[57]. Their scalability also enables operation in environments where movement of their larger counterparts would be impractical or impossible. Furthermore, these devices are lighter, undergo more continuous and natural deformation with simple control inputs, and are more easily mass produced than their motor-driven counterparts[121].

It is expected that custom printed 3D robots and actuator structures will appear in application areas as diverse as devices for human-computer interaction, chemical and environmental remediation, or surgical tools for training[88]. For example, Alblalaihid *et al* used a projection micro-stereolithography system to 3D print polymer components on top of which thin metals could be coated to create a micro-scale gripper. The gripper was thermo-electrically activated and could be used for surgical manipulation[122]. Also, applications are being explored with fluid-powered actuators demonstrating human potential in macro-scale self-healing medical implants or wearable orthotics[18,123]. Park *et al* designed an artificial soft bio-robotic pneumatic muscle actuator attached to a 3D printed leg model that could be worn over the knee[124], and Doncieux *et al* developed a bio-inspired "Gummi Arm" fabricated of 3D printed plastic structures connected by agonist-antagonist joints that mimicked soft tendons[125].

Bioactuators with or without cells might be designed for drug screening or delivery[126], bio-reactors or lab-on-a-chip devices, vascular pumps and monitors, or adaptive prosthetics[24,27,53]. Some aspects of this technology have been proposed for use as part of drug delivery systems where a drug could detect body-site specific temperatures during local infection or low pH tumor environments, and intelligently self-locate and self-release pharmaceuticals[71]. Independently or in large numbers, these actuators might also be programmed to form mobile and robust sensor and communication networks, allowing them to work in rubble fields, utility conduits, or the ocean floor to assist work in multiple industries[127,128]. Terrestrial actuators that could navigate dense environments and change shape, color, or surface temperature for camouflage would fit in well with outdoor research or military operations[70].

Both living and non-living bioactuators must be to designed such that the form matches the intended function[46,99,129]. When building with muscle, for example, the devices might need to closely match the performance of their *in vivo* equivalents, especially if their intended use is to mimic a native tissue for a drug testing or regenerative application, or to provide a novel platform for understanding fundamental biological phenomena. However, when physiological relevance is less important to the end objective, replication of natural performance might be overlooked in favor of maximal efficiency, contractility, or power output. For example, primary cardiomyocytes

might be overlooked in favor of a skeletal muscle cell line if extensive scaling up or wider contractile ranges were necessary to the functionality of the bioactuator, but favored in certain temperatures or situations requiring cellular synchrony.

A1.7 Limitations and Future Directions

Though much progress has been made, significant fundamental challenges still remain. Soft bioactuators must be manufactured in a manner that preserves the mechanical integrity of their structure and allows for shock absorption, deformation, flexibility, and minimal damage. A major challenge is attempting to increase force output from elastic or synthetic systems without compromising the bio-mimetic properties that promote integration with living materials or the complexity of design and function which characterizes the natural world[15,18,19,40,120]. When integrating living biomaterials, researchers must consider scenarios which might enhance or hinder force production – for example, cellular viability, (self-)adhesion, organization, alignment, directionality, and overall struture, which all contribute significantly to function. Moreover, cells must be maintained in cell culture media at highly regulated conditions ensuring nutrient and oxygen delivery, with the application of appropriate external cues for guidance of tissue development and mechanical performance. They are subject to a variety of failure modes, including mechanical (within the tissue or at the interface), metabolic, fatigue, damage or injury, and necrosis[24,53]. Finally, it can also be difficult to model the active and passive response of a cellular or living system in uncertain environmental conditions. Researchers still lack a deep understanding of how fundamental processes of cells (such as local interactions) function globally across length scales[27].

Thus far, 3D printed actuators have been assembled mostly with singular modalities. However, just as traditional robots contain multiple systems for various modalities (actuation, perception, computation, power, etc.), future designs of soft bioactuators should integrate multiple components and functionalities – including sensing[121,130] and processing of information – as well as multiple cell types or materials to achieve more complex, precise, and useful actuation[52,99]. In the future, it will be necessary to implement feedback systems and control mechanisms that help to extend the lifetime, precision, repeatability, and outputs of bioactuators, while also enhancing

their operation outside of encapsulated or restricted environmental conditions[24,35,131,132]. With living bioactuators, co-culture systems can provide a synergistic support system to enhance overall performance. In order to meet metabolic demands of living cells on larger size (> 0.5 mm) or time scales, a vascular component will be necessary for consistent nutrient delivery. Indeed, the lack of perfusive blood vessels within regenerated tissues has historically plagued developments in the tissue engineering field. Guo, Miller, and Kolesky all have demonstrated various 3D bio-printing methods that could be used in microvascular network formation[133–135]. Additionally, innervation of muscle fibers with motor neurons can aid in the preservation of skeletal muscle phenotype, while allowing for better control, directed motion, or more complex functional outputs[46,53].

With regards to fabrication, some limitations exist within the realm of technological advancements that might permit the construction of specific structures applicable to bioactuators. In the future, researchers will need to consider how to develop materials and scaffolds that can support cell and tissue outputs with maximal efficiency or power. This may include specific nano- or micro-scale geometries, shorter print times for large structures, higher resolution, greater range of material properties, improvement of surface adhesion techniques, and attachment of ECM[29,35]. Moreover, there exists a demand for multi-material rapid prototyping advancements that could combine properties of multiple materials in one product[11,36,51]. Soft bioactuators might integrate new techniques in 3D printing of layered fabrics[136,137], SMPs for flexible electronics[80], and direct printing of electronic fluidic components[138] for on-board automation. From any perspective, these advancements represent a rapidly growing field with the potential to significantly benefit human life.

A1.8 Figures

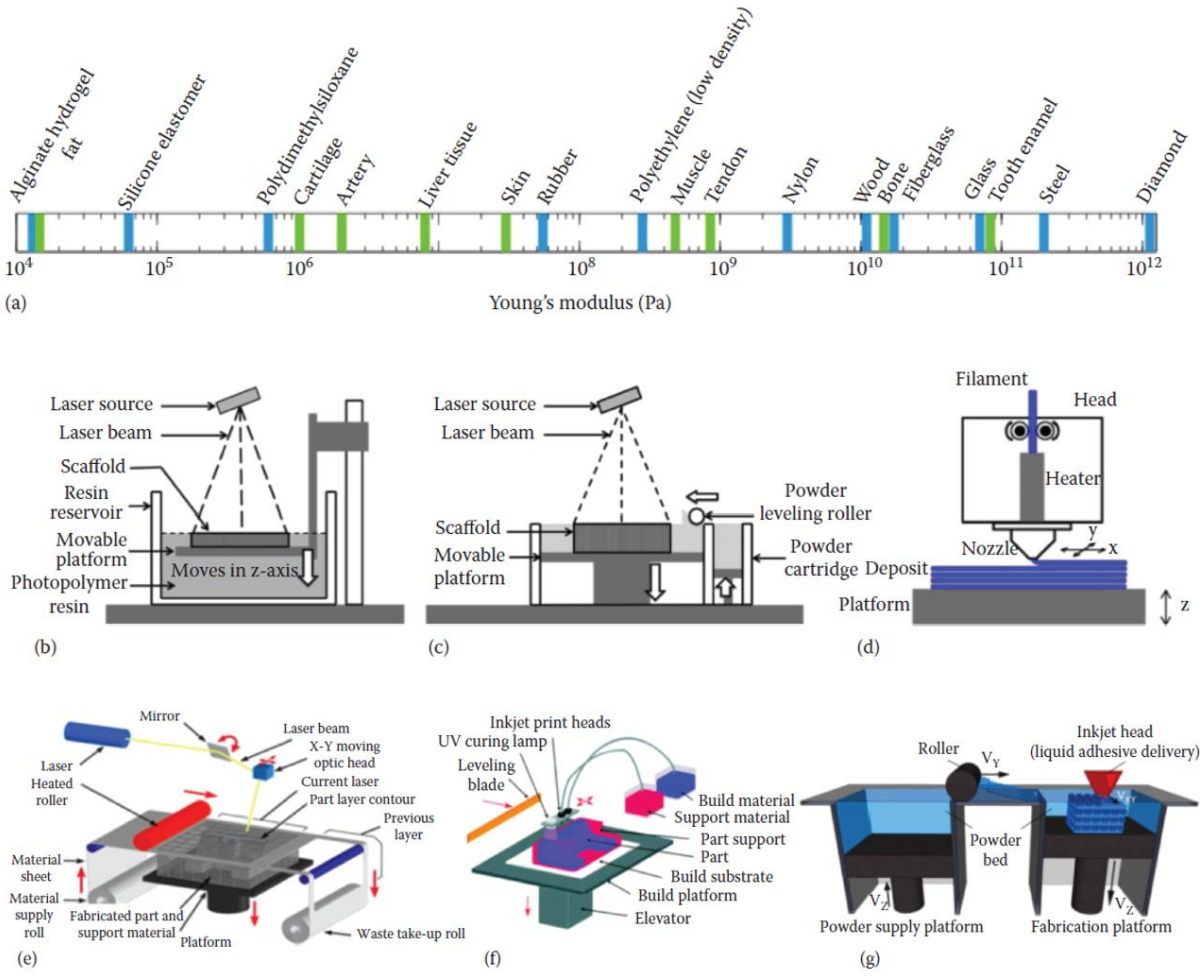

Figure A1.1: Rapid Prototyping Methods. **(a)** Range of tensile elastic moduli of biological and synthetic materials. Soft bioactuators mimic the material properties of biological tissues. (Reprinted from Rus 2015 with permission from Nature Publishing Group[52].) **(b)** Stereolithography (SL) is a maskless solid freeform method that requires a photosensitive resin and a UV light source. The apparatus (SLA) contains a platform that moves vertically. This technique traced the laser or projected image to photopolymerize a liquid resin in a layer-by-layer fashion. (Reprinted from Wu 2015[139].) **(c)** Selective laser sintering (SLS) is the laser-based fusing of thermoplastics or metal powders to create a desired 3D structure. When a laser hits the first layer of powder on the stage, the particles fuse. A new powdered layer is deposited on the first layer and exposed to the laser again. After the fabrication is complete, the unsintered powder is removed. (Reprinted from Wu 2015[139].) **(d)** Fused deposition modeling (FDM) is a solids-based system that utilizes extrusion. The nozzles (which can dispense different materials) extrude a filament-shaped material on the stage to pattern the first layer; then, the platform

lowers, and the next layer subsequently forms on the first. Since the nozzle dispenses the material at high temperature, all the layers bind well without additional treatment. (Reprinted from Ahn 2009 with permission from Elsevier[140].) **(e)** With laminated object manufacturing (LOM), a single layered material, such as paper, plastic, or metal, is adhered to the platform. Then, a laser beam sketches the outline by cutting and removing the excessive material. The platform moves down by thickness of a single layer and another sheet of material is adhered on the first layer. The process is repeated until the final layer is patterned. LOM is economical and fast, but not effective for fabricating geometrically complex designs. (Reprinted from Ahn 2012 with permission from Elsevier[141].) **(f)** Multi Jet Modeling (MJM) combines different RP techniques. A base thermoplastic polymer material is dispensed from an array of nozzles moving in the X-Y plane. The array draws the desired shape with the polymer on the platform, which then lowers relative to the array before the next layer is formed. (Reprinted from Bhattacharjee 2016 with permission from the Royal Society of Chemistry[142].) **(g)** Three-dimensional printing (3DP) can employ an inkjet type processing method. There are two adjacent chambers in this system. A feed roller on top of the material chamber spreads a powdered plaster material evenly on a platform moving vertically in the build chamber. A cartilage hanging above the build chamber moves over the surface to dispense a binding material. The build chamber moves down by one layer thickness, the process is repeated, and excess material is removed. Compared to other RP technologies, 3DP is fast and starting material is inexpensive. (Reprinted from Billiet 2012 with permission from Elsevier[143].)

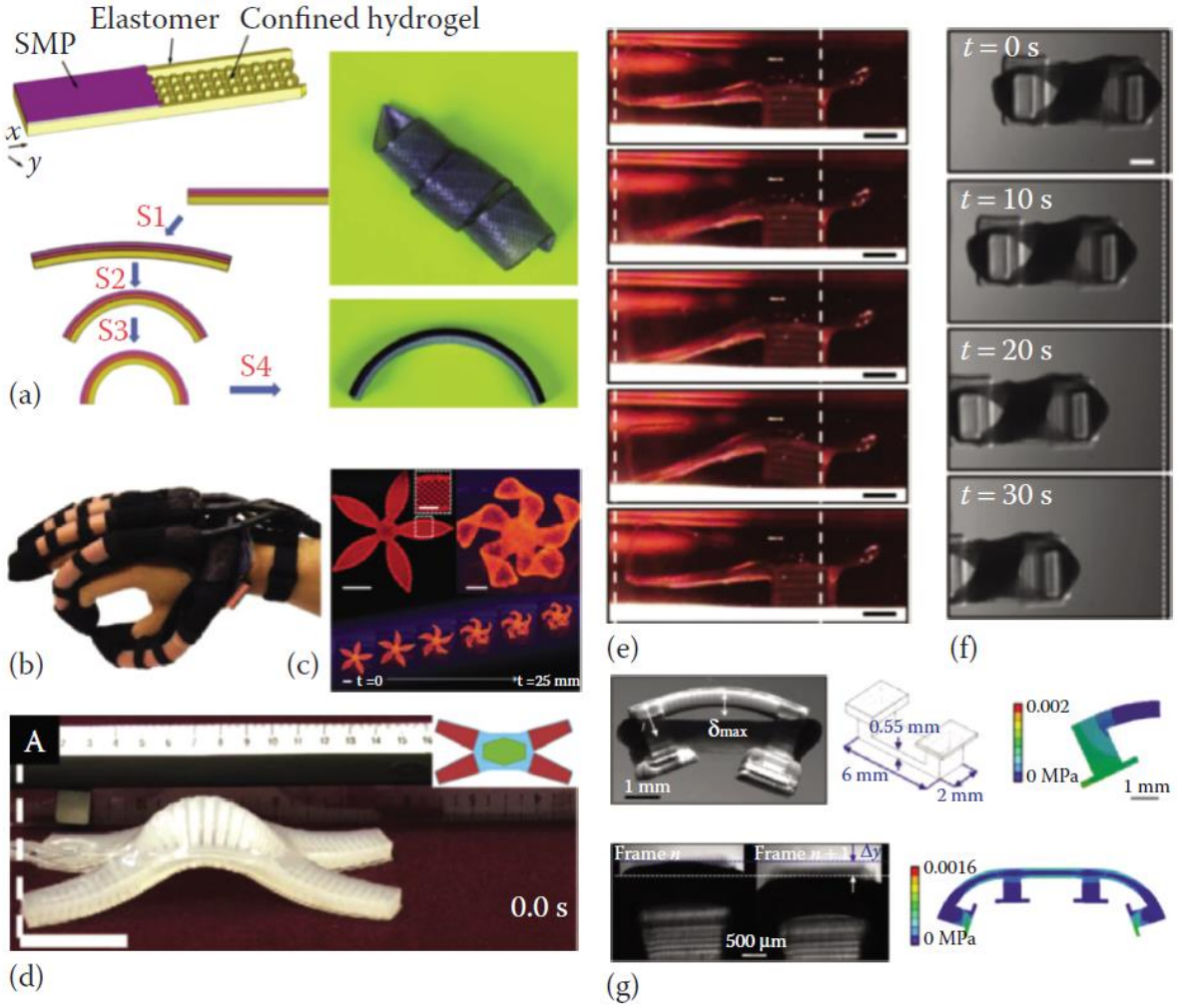

Figure A1.2: Soft Bioactuators. Examples of soft bioactuators fabricated with rapid prototyping methods are demonstrated in both non-living (a-d) and living (e-g) systems. **(a)** The combination of hydrogels and SMPs allowed for a two-way actuator that could reversibly bend or coil. (Adapted from Mao 2016[82].) **(b)** A hydraulic-powered soft robotic globe fabricated from a 3D printed mold was able to demonstrate precise grasping. (Reprinted from Polygerinos 2015 with permission from Elsevier[66].) **(c)** The complex morphological transformation of a flower structure was made possible with 4D bio-printing. (Reprinted from Sydney Gladman 2016 with permission from Nature Publishing Group[72].) **(d)** An elastomeric crawling soft robot was powered by pneumatic pressure. (Reprinted from Shepherd 2011[59].) **(e)** A 3D printed bio-hybrid cantilever was powered by the spontaneous contraction of cardiac muscle cells. (Reprinted from Chan 2012 with permission from Nature Publishing Group[111].) **(f)** An electrically powered bio-bot was fabricated from a hydrogel skeleton made with a stereolithographic 3D printer and a combination of skeletal muscle cells and ECM proteins. (Reprinted from Cvetkovic 2014[2].) **(g)** An optically

powered and exercised skeletal muscle bio-bot demonstrated directionality and control. (Reprinted from Raman 2017[116].)

References

1 Umedachi T, Vikas V, Trimmer BA. Softworms: the design and control of non-pneumatic, 3D-printed, deformable robots. *Bioinspir Biomim* 2016; **11**. doi:10.1088/1748-3190/11/2/025001.

2 Cvetkovic C, Raman R, Chan V, Williams BJ, Tolish M, Bajaj P *et al.* Three-dimensionally printed biological machines powered by skeletal muscle. *Proc Natl Acad Sci USA* 2014; **111**: 10125–10130.

3 Kovač M. The Bioinspiration Design Paradigm: A Perspective for Soft Robotics. *Soft Robot* 2013; **1**: 28–37.

4 Bartlett NW, Tolley MT, Overvelde JTB, Weaver JC, Mosadegh B, Bertoldi K *et al.* A 3D-printed, functionally graded soft robot powered by combustion. *Science (80-)* 2015; **349**: 161–165.

5 Feinberg AW, Feigel A, Shevkoplyas SS, Sheehy S, Whitesides GM, Parker KK. Muscular thin films for building actuators and powering devices. *Science (80-)* 2007; **317**: 1366–1370.

6 Wen L, Wang T, Wu G, Liang J. Quantitative thrust efficiency of a self-propulsive robotic fish: Experimental method and hydrodynamic investigation. *IEEE/ASME Trans Mechatronics* 2013; **18**: 1027–1038.

7 Low KH. Design, development and locomotion control of bio-fish robot with undulating anal fins. *Int J Robot Autom* 2007; **22**: 88–99.

8 Herr H, Dennis RG. A swimming robot actuated by living muscle tissue. *J Neuroeng Rehabil* 2004; **1**: 1–9.

9 Nawroth JC, Lee H, Feinberg AW, Ripplinger CM, McCain ML, Grosberg A *et al.* A tissue-engineered jellyfish with biomimetic propulsion. *Nat Biotechnol* 2012; **30**: 792–797.

10 Majidi C. Soft Robotics: A Perspective—Current Trends and Prospects for the Future. *Soft Robot* 2013; **1**: 5–11.

11 Gui JZ, Yang B-S, Yang YJ, Chang DEE, Choi KH, Gul JZ *et al.* In situ UV curable 3D printing of multi-material tri-legged soft bot with spider mimicked multi- step forward dynamic gait. *Smart Mater Struct* 2016; **25**: 1–12.

12 Vincent JF V, Bogatyreva OA, Bogatyrev NR, Bowyer A, Pahl A-K. Biomimetics: its practice and theory. *J R Soc Interface* 2006; **3**: 471–82.

13 Full RJ. Using Biological Inspiration to Build Artificial Life That Locomotes. *EvoWorkshops* 2001; **2217**: 110–120.

14 Ricotti L, Menciassi A. Bio-hybrid muscle cell-based actuators. *Biomed Microdevices* 2012; **14**: 987–998.

15 Kim S, Laschi C, Trimmer B. Soft robotics: a bioinspired evolution in robotics. *Trends Biotechnol* 2013; : 1–8.

16 Tadesse Y, Wu L, Saharan LK. Musculoskeletal System for Bio-Inspired Robotic Systems. *Focus Dyn Syst Control* 2016; : 11–17.

17 Bernabei R, Power J. On Three Categories of Conscious Machines. In: Lepora NF, Mura A, Mangan M, Verschure PFMJ, Desmulliez M, Prescott TJ (eds). *Biomimetic and Biohybrid Systems: Proceedings of the 5th International Conference, Living Machines 2016, Edinburgh, UK*. Springer International Publishing, 2016, pp 40–47.

18 Zolfagharian A, Kouzani AZ, Khoo SY, Gibson I, Kaynak A. 3D Printed Hydrogel Soft Actuators. In: *IEEE Region 10 Conference (TENCON)*. 2016, pp 2274–2279.
19 Lee C, Kim M, Kim YJ, Hong N, Ryu S, Kim HJ *et al.* Soft Robot Review. *Int J Control Autom Syst* 2017; **15**: 3–15.
20 Inoue D, Kabir AR, Sada K, Gong JP. Tissue Engineering Approach to Making Soft Actuators. 2014; : 475–487.
21 Chan V, Asada HH, Bashir R. Utilization and control of bioactuators across multiple length scales. *Lab Chip* 2014; **14**: 653–70.
22 Burgert I, Fratzl P. Actuation systems in plants as prototypes for bioinspired devices. *Philos Trans A Math Phys Eng Sci* 2009; **367**: 1541–57.
23 Kabumoto K, Hoshino T, Akiyama Y, Morishima K. Voluntary Movement Controlled by the Surface EMG Signal for Tissue-engineered Skeletal Muscle on a Gripping Tool Department of Bio-Application and Systems Engineering , Tokyo University of Agriculture. ; : 1–25.
24 Carlsen RW, Sitti M. Bio-hybrid cell-based actuators for microsystems. *Small* 2014; **10**: 3831–51.
25 Bowers AE, Rossiter JM, Walters PJ, Ieropoulos IA. Dielectric elastomer pump for artificial organisms. *Proc SPIE* 2011; **7976**: 797629-797629–7.
26 Cho K-J, Wood R. Biomimetic Robots. In: *Springer Handbook of Robotics*. 2016, pp 543–574.
27 Kamm RD, Bashir R. Creating Living Cellular Machines. *Ann Biomed Eng* 2013; **42**: 445–59.
28 Prinz F, Atwood C, Aubin R, Beaman J, Brown R, Fussel P *et al.* JTEC/WTEC Panel Report on Rapid prototyping in Europe and Japan. 1997.
29 Hinton TJ, Lee A, Feinberg AW. 3D Bioprinting from the Micrometer to Millimeter Length Scales: Size Does Matter. *Curr Opin Biomed Eng* 2017. doi:http://dx.doi.org/10.1016/j.cobme.2017.02.004.
30 Lantada AD, Morgado PL. Rapid prototyping for biomedical engineering: current capabilities and challenges. *Annu Rev Biomed Eng* 2012; **14**: 73–96.
31 Peltola S, Melchels FPW, Grijpma DW, Kellomäki M. A Review of Rapid Prototyping Techniques for Tissue Engineering Purposes. *Ann Med* 2008; **40**: 268–280.
32 Stanek M, Manas D, Manas M, Navratil J, Kyas K, Senkerik V *et al.* Comparison of different rapid prototyping methods. *Int J Math Comput Simul* 2012; **6**: 550–557.
33 Upcraft S, Fletcher R. The rapid prototyping technologies. *Assem Autom* 2003; **23**: 318–330.
34 Bhatt R, Tang CP, Lee L-F, Krovi V. Web-Based Self-Paced Virtual Prototyping Tutorials. *Proc DETC* 2003; : 1–7.
35 Lantada AD. Cell-Based Sensors and Cell-Based Actuators. In: Díaz Lantada A (ed). *Microsystems for Enhanced Control of Cell Behavior*. Springer International Publishing: Cham, 2016, pp 373–386.
36 Keating SJ, Gariboldi MI, Patrick WG, Sharma S, Kong DS, Oxman N. 3D printed multimaterial microfluidic valve. *PLoS One* 2016; **11**: 1–13.
37 Munaz A, Vadivelu RK, St J, Barton M, Kamble H, Nguyen N. Three-dimensional printing of biological matters. *J Sci Adv Mater Devices* 2016; **1**: 1–17.

38 Khademhosseini A, Langer R. A decade of progress in tissue engineering. *Nat Protoc* 2016; **11**: 1775–1781.
39 Yeong W-Y, Yeong WY, Chua C-K, Chua CK, Leong K-F, Leong KF *et al.* Rapid prototyping in tissue engineering: challenges and potential. *Trends Biotechnol* 2004; **22**: 643–652.
40 Zhu W, Castro NJ, Zhang LG. Nanotechnology and 3D bioprinting for neural tissue regeneration. In: *3D Bioprinting and Nanotechnology in Tissue Engineering and Regenerative Medicine*. Elsevier Inc., 2015, pp 307–331.
41 Chan V, Jeong JH, Bajaj P, Collens MB, Saif T, Kong H *et al.* Multi-material bio-fabrication of hydrogel cantilevers and actuators with stereolithography. *Lab Chip* 2012; **12**: 88–98.
42 Arcaute K, Mann BK, Wicker RB. Practical Use of Hydrogels in Stereolithography for Tissue Engineering Applications. In: Bártolo PJ (ed). *Stereolithography: Materials, Processes and Applications*. Springer US: Boston, MA, 2011, pp 299–331.
43 Zorlutuna P, Jeong JH, Kong H, Bashir R. Stereolithography-Based Hydrogel Microenvironments to Examine Cellular Interactions. *Adv Funct Mater* 2011; **21**: 3642–3651.
44 Bajaj P, Chan V, Jeong JH, Zorlutuna P, Kong H, Bashir R. 3-D biofabrication using stereolithography for biology and medicine. In: *Engineering in Medicine and Biology Society (EMBC), 2012 Annual International Conference of the IEEE*. 2012, pp 6805–8.
45 Melchels FPW, Feijen J, Grijpma DW. A review on stereolithography and its applications in biomedical engineering. *Biomaterials* 2010; **31**: 6121–6130.
46 Uzel SGM, Pavesi A, Kamm RD. Microfabrication and microfluidics for muscle tissue models. *Prog Biophys Mol Biol* 2014; **115**: 279–293.
47 Bajaj P, Schweller RM, Khademhosseini A, West JL, Bashir R. 3D Biofabrication Strategies for Tissue Engineering and Regenerative Medicine. *Annu Rev Biomed Eng* 2014; **16**: 247–76.
48 Burg T, Cass C a P, Groff R, Pepper M, Burg KJL. Building off-the-shelf tissue-engineered composites. *Philos Trans A Math Phys Eng Sci* 2010; **368**: 1839–62.
49 Ahn SH, Lee J, Park SA, Kim WD. Three-dimensional bio-printing equipment technologies for tissue engineering and regenerative medicine. *Tissue Eng Regen Med* 2016; **13**: 663–676.
50 Pfister A, Landers R, Laib A, Hübner U, Schmelzeisen R, Mülhaupt R. Biofunctional Rapid Prototyping for Tissue-Engineering Applications: 3D Bioplotting versus 3D Printing. *J Polym Sci Part A Polym Chem* 2004; **42**: 624–638.
51 Zolfagharian A, Kouzani AZ, Khoo SY, Moghadam AAA, Gibson I, Kaynak A. Evolution of 3D printed soft actuators. *Sensors Actuators, A Phys* 2016; **250**: 258–272.
52 Rus D, Tolley MT. Design, fabrication and control of soft robots. *Nature* 2015; **521**: 467–475.
53 Dennis RG, Herr H. Engineered muscle actuators: cells and tissues. In: Bar-Cohen Y (ed). *Biomimetics: Biologically Inspired Technologies*. CRC Press, 2005, pp 243–266.
54 Schulte HF. The Characteristics of the McKibben Artificial Muscle. In: *The Application of External Power in Prosthetics and Orthotics*. National Acadamey of Sciences-National Research Council: Washington DC, 1961, pp 94–102.
55 Low J-H, Yeow C-H. Rod-based Fabrication of Customizable Soft Robotic Pneumatic Gripper Devices for Delicate Tissue Manipulation. *J Vis Exp* 2016; **114**: e54175.

56 Mosadegh B, Polygerinos P, Keplinger C, Wennstedt S, Shepherd RF, Gupta U *et al.* Pneumatic networks for soft robotics that actuate rapidly. *Adv Funct Mater* 2014; **24**: 2163–2170.
57 Martinez R V., Branch JL, Fish CR, Jin L, Shepherd RF, Nunes RMD *et al.* Robotic tentacles with three-dimensional mobility based on flexible elastomers. *Adv Mater* 2013; **25**: 205–212.
58 Daerden F, Lefeber D. Pneumatic artificial muscles: actuators for robotics and automation. *Eur J Mech Environ Eng* 2002; **47**: 11–21.
59 Shepherd RF, Ilievski F, Choi W, Morin SA, Stokes AA, Mazzeo AD *et al.* Multigait soft robot. *Proc Natl Acad Sci U S A* 2011; **108**: 20400–20403.
60 Ilievski F, Mazzeo AD, Shepherd RF, Chen X, Whitesides GM. Soft robotics for chemists. *Angew Chemie - Int Ed* 2011; **50**: 1890–1895.
61 Suzumori K, Iikura S, Tanaka H. Applying a Flexible Microactuator to Robotic Mechanisms. *IEEE Control Syst* 1992; **February**: 21–27.
62 Caldwell DG, Tsagarakis N, Medrano-Cerda GA. Bio-mimetic actuators: polymeric Pseudo Muscular Actuators and pneumatic Muscle Actuators for biological emulation. *Mechatronics* 2000; **10**: 499–530.
63 Robertson MA, Sadeghi H, Florez JM, Paik J. Soft Pneumatic Actuator Fascicles for High Force and Reliability. *Soft Robot* 2016; **4**: soro.2016.0029.
64 Yang Y, Chen Y. Novel design and 3D printing of variable stiffness robotic fingers based on shape memory polymer. In: *6th IEEE RAS/EMBS International Conference on Biomedical Robotics and Biomechatronics (BioRob) June 26-29, 2016*. Singapore, 2016, pp 195–200.
65 Wang Z, Hirai S. A 3D Printed Soft Gripper Integrated with Curvature Sensor for Studying Soft Grasping. In: *Proceedings of the 2016 IEEE/SICE International Symposium on System Integration*. IEEE: Sapporo, Japan, 2016, pp 629–633.
66 Polygerinos P, Wang Z, Galloway KC, Wood RJ, Walsh CJ. Soft robotic glove for combined assistance and at-home rehabilitation. *Rob Auton Syst* 2015; **73**: 135–143.
67 MacCurdy R, Katzschmann R, Kim Y, Rus D. Printable Hydraulics: A Method for Fabricating Robots by 3D Co-Printing Solids and Liquids. In: *2016 IEEE International Conference on Robotics and Automation (ICRA)*. 2016.
68 Underwater propulsion from a 3D printer. Phys.Org. 2013.
69 Katzschmann RK, Marchese AD, Rus D. Hydraulic Autonomous Soft Robotic Fish for 3D Swimming. In: Kumar V, Khatib O, Hsieh MA (eds). *Experimental Robotics*. Springer Tracts in Advanced Robotics, 2000, pp 149–163.
70 Jin H, Dong E, Xu M, Liu C, Alici G, Jie Y. Soft and smart modular structures actuated by shape memory alloy (SMA) wires as tentacles of soft robots. *Smart Mater Struct* 2016; **25**: 85026.
71 Mano JF. Stimuli-responsive polymeric systems for biomedical applications. *Adv Eng Mater* 2008; **10**: 515–527.
72 Sydney Gladman A, Matsumoto EA, Nuzzo RG, Mahadevan L, Lewis JA. Biomimetic 4D printing. *Nat Mater* 2016; **15**: 413–8.
73 Knoblauch M, Peters WS. Biomimetic actuators: Where technology and cell biology merge. *Cell Mol Life Sci* 2004; **61**: 2497–2509.

74 Bakarich SE, Gorkin R, Panhuis M In Het, Spinks GM. 4D printing with mechanically robust, thermally actuating hydrogels. *Macromol Rapid Commun* 2015; **36**: 1211–1217.
75 Ge Q, Qi HJ, Dunn ML. Active materials by four-dimension printing. *Appl Phys Lett* 2013; **103**. doi:10.1063/1.4819837.
76 Walters P, McGoran D. Digital fabrication of 'smart' structures and mechanisms-creative applications in art and design. In: *International Conference on Digital Printing Technologies and Digital Fabrication 2011*. Minneapolis, 2011, pp 185–188.
77 Umedachi T, Trimmer BA. Design of a 3D-printed soft robot with posture and steering control. In: *2014 IEEE International Conference on Robotics & Automation (ICRA)*. Hong Kong, 2014, pp 2874–2879.
78 Umedachi T, Vikas V, Trimmer BA. Highly deformable 3-D printed soft robot generating inching and crawling locomotions with variable friction legs. In: *2013 IEEE/RSJ International Conference on Intelligent Robots and Systems (IROS)*. Tokyo, 2013, pp 4590–4595.
79 Mao Y, Yu K, Isakov MS, Wu J, Dunn ML, Jerry Qi H. Sequential Self-Folding Structures by 3D Printed Digital Shape Memory Polymers. *Sci Rep* 2015; **5**: 13616.
80 Zarek M, Layani M, Cooperstein I, Sachyani E, Cohn D, Magdassi S. 3D Printing of Shape Memory Polymers for Flexible Electronic Devices. *Adv Mater* 2016; **28**: 4449–4454.
81 Bodaghi M, Damanpack AR, Liao WH. Self-expanding / shrinking structures by 4D printing. *Smart Mater Struct* 2016; **25**.
82 Mao Y, Ding Z, Yuan C, Ai S, Isakov M, Wu J *et al.* 3D Printed Reversible Shape Changing Components with Stimuli Responsive Materials. *Sci Rep* 2016; **6**: 24761.
83 Wu J, Yuan C, Ding Z, Isakov M, Mao Y, Wang T *et al.* Multi-shape active composites by 3D printing of digital shape memory polymers. *Sci Rep* 2016; **6**. doi:10.1038/srep24224.
84 Zolfagharian A, Z. Kouzani A, Nasri-Nasrabadi B, Adams S, Yang Khoo S, Norton M *et al.* 3D Printing of a Photo-thermal Self-folding Actuator. In: *DesTech Conference Proceedings: The International Conference on Design and Technology*. KEG, 2017, pp 15–22.
85 Zhu W, Li J, Leong YJ, Rozen I, Qu X, Dong R *et al.* 3D-Printed Artificial Microfish. *Adv Mater* 2015; **27**: 4411–4417.
86 Bar-Cohen Y. Biologically Inspired Intelligent Robots using Artificial Muscles. *Strain* 2005; **41**: 19–24.
87 Asaka K, Nakamura K. Current Status of Applications and Markets of Soft Actuators. In: K. Asaka HO (ed). *Soft Actuators*. Springer Japan, 2014, pp 19–30.
88 Rossiter J, Walters P, Stoimenov B. Printing 3D dielectric elastomer actuators for soft robotics. In: Bar-Cohen Y, Wallmersperger T (eds). *Electroactive Polymer Actuators and Devices (EAPAD) 2009*. SPIE, 2009 doi:10.1117/12.815746.
89 Cai J, Vanhorn A, Mullikin C, Stabach J, Alderman Z. 4D Printing of Soft Robotic Facial Muscles. In: *International Solid Freeform Fabrication (SFF) Symposium – An Additive Manufacturing Conference*. Austin, 2015, pp 1537–1553.
90 Nguyen CT, Phung H, Jung H, Kim U, Nguyen TD, Park J *et al.* Printable monolithic hexapod robot driven by soft actuator. *2015 IEEE Int Conf Robot Autom* 2015; : 4484–4489.

91 Carrico JD, Traeden NW, Aureli M, Leang KK. Fused filament 3D printing of ionic polymer-metal composites (IPMCs). *Smart Mater Struct* 2015; **24**: 125021.
92 Wei T, Stokes A, Webb B. A Soft Pneumatic Maggot Robot. *Living Mach* 2016; **1**: 375–386.
93 Ahn S, Lee K, Kim H, Wu R, Kim J, Song S. Smart Soft Composite : An Integrated 3D Soft Morphing Structure Using Bend – Twist Coupling of Anisotropic Materials. *Int J Precis Eng Manuf* 2012; **13**: 631–634.
94 Liu J, Wang Y, Zhao D, Zhang C, Chen H, Li D. Design and fabrication of an IPMC-embedded tube for minimally invasive surgery applications. In: Bar-Cohen Y (ed). *Electroactive Polymer Actuators and Devices (EAPAD)*. 2014, p 90563K.
95 Lin H-T, Leisk GG, Trimmer B. GoQBot: a caterpillar-inspired soft-bodied rolling robot. *Bioinspir Biomim* 2011; **6**. doi:10.1088/1748-3182/6/2/026007.
96 Yuk H, Lin S, Ma C, Takaffoli M, Fang NX, Zhao X *et al.* Hydraulic hydrogel actuators and robots optically and sonically camouflaged in water. *Nat Commun* 2017; **8**: 14230.
97 Wehner M, Truby RL, Fitzgerald DJ, Mosadegh B, Whitesides GM, Lewis JA *et al.* An integrated design and fabrication strategy for entirely soft, autonomous robots. *Nature* 2016; **536**: 451–455.
98 Morrow J, Hemleben S, Menguc Y. Directly Fabricating Soft Robotic Actuators With an Open-Source 3-D Printer. *IEEE Robot Autom Lett* 2016; **2**: 277–281.
99 Feinberg AW. Biological Soft Robotics. *Annu Rev Biomed Eng* 2015; **17**: 243–65.
100 Engler AJ, Griffin M a, Sen S, Bönnemann CG, Sweeney HL, Discher DE. Myotubes differentiate optimally on substrates with tissue-like stiffness: pathological implications for soft or stiff microenvironments. *J Cell Biol* 2004; **166**: 877–87.
101 Stanton MM, Park B-W, Miguel-López A, Ma X, Sitti M, Sánchez S. Biohybrid Microtube Swimmers Driven by Single Captured Bacteria. *Small* 2017; : 1603679.
102 Akiyama Y, Hoshino T, Iwabuchi K, Morishima K. Room temperature operable autonomously moving bio-microrobot powered by insect dorsal vessel tissue. *PLoS One* 2012; **7**: e38274.
103 Goebel R, Wahlster W. Aplysia Californica as a Novel Source of Material for Biohybrid Robots and Organic Machines. 2015; **1**: 268–279.
104 Hinds S, Bian W, Dennis RG, Bursac N. The role of extracellular matrix composition in structure and function of bioengineered skeletal muscle. *Biomaterials* 2011; **32**: 3575–3583.
105 Dennis RG, Kosnik PE. Excitability and isometric contractile properties of mammalian skeletal muscle constructs engineered in vitro. *Vitr Cell Dev Biol - Anim* 2000; **36**: 327–335.
106 Duan B, Hockaday LA, Kang KH, Butcher JT. 3D Bioprinting of heterogeneous aortic valve conduits with alginate / gelatin hydrogels. *J Biomed Mater Res Part A* 2012; : 1–10.
107 Park J, Ryu J, Choi SK, Seo E, Cha JM, Ryu S *et al.* Real-time measurement of the contractile forces of self-organized cardiomyocytes on hybrid biopolymer microcantilevers. *Anal Chem* 2005; **77**: 6571–6580.
108 Kim J, Park J, Yang S, Baek J, Kim B, Lee SH *et al.* Establishment of a fabrication method for a long-term actuated hybrid cell robot. *Lab Chip* 2007; **7**: 1504–1508.

109 Tanaka Y, Morishima K, Shimizu T, Kikuchi A, Yamato M, Okano T *et al.* An actuated pump on-chip powered by cultured cardiomyocytes. *Lab Chip* 2006; **6**: 362–8.
110 Williams BJ, Anand S V, Rajagopalan J, Saif MTA. A self-propelled biohybrid swimmer at low Reynolds number. *Nat Commun* 2014; **5**: 3081.
111 Chan V, Park K, Collens MB, Kong H, Saif TA, Bashir R. Development of miniaturized walking biological machines. *Sci Rep* 2012; **2**: 1–8.
112 Park S, Gazzola M, Park KS, Park S, Dauth S, Capulli AK *et al.* Phototactic guidance of a tissue-engineered soft-robotic ray. *Science (80-)* 2016; **353**: 158–162.
113 Raman R, Cvetkovic C, Uzel SGM, Platt RJ, Sengupta P, Kamm RD. Optogenetic skeletal muscle-powered adaptive biological machines. *Proc Natl Acad Sci* 2016. doi:10.1073/pnas.1516139113.
114 Uzel SGM, Platt RJ, Subramanian V, Pearl TM, Rowlands CJ, Chan V *et al.* Microfluidic device for the formation of optically excitable, three-dimensional, compartmentalized motor units. *Sci Adv* 2016; **2**: e1501429.
115 Cvetkovic C, Rich MH, Raman R, Kong H, Bashir R. A 3D-printed platform for modular neuromuscular motor units. *Microsystems Nanoeng* 2017; **3**. doi:10.1038/micronano.2017.15.
116 Raman R, Cvetkovic C, Bashir R. A modular approach to the design, fabrication, and characterization of muscle-powered biological machines. *Nat Protoc* 2017; **12**: 519–533.
117 Sakar MS, Neal D, Boudou T, Borochin MA, Li Y, Weiss R *et al.* Formation and optogenetic control of engineered 3D skeletal muscle bioactuators. *Lab Chip* 2012; **12**: 4976–4985.
118 Uzel SGM, Platt RJ, Subramanian V, Pearl TM, Rowlands CJ, Chan V *et al.* Microfluidic device for the formation of optically motor units. 2016.
119 Chan V, Neal DM, Uzel SGM, Kim H, Bashir R, Asada HH. Fabrication and Characterization of Optogenetic, Multi-Strip Cardiac Muscles. *Lab Chip* 2015. doi:10.1039/C5LC00222B.
120 Kapsali V, Toomey A, Oliver R, Tandler L. Biomimetic Spatial and Temporal (4D) Design and Fabrication. In: Lepora NF, Mura A, Krapp HG, Verschure PFMJ, Prescott TJ (eds). *Biomimetic and Biohybrid Systems: Second International Conference, Living Machines 2013, London, UK, July 29 -- August 2, 2013, Proceedings*. Springer, 2013, pp 387–389.
121 Zhao H, O'Brien K, Li S, Shepherd RF, O 'brien K, Li S *et al.* Optoelectronically innervated soft prosthetic hand via stretchable optical waveguides. *Sci Robot* 2016; **7529**: eaai7529.
122 Alblalaihid K, Overton J, Lawes S, Kinnell P. A 3D-printed polymer micro-gripper with self-defined electrical tracks and thermal actuator. *J Micromechanics Microengineering* 2017; **27**: 45019.
123 Wirekoh H, Park Y-L. Design of flat pneumatic artificial muscles. *Smart Mater Struct* 2017; **26**: 1–10.
124 Park YL, Santos J, Galloway KG, Goldfield EC, Wood RJ. A soft wearable robotic device for active knee motions using flat pneumatic artificial muscles. In: *2014 IEEE International Conference on Robotics & Automation (ICRA)*. IEEE: Hong Kong, 2014, pp 4805–4810.
125 Doncieux S, Girard B, Guillot A, Hallam J, Meyer J-A, Mouret J-B. Co-exploring Actuator Antagonism and Bio-inspired Control in a Printable Robot Arm. *11th Int Conf Simul Adapt Behav SAB 2010, Paris - Clos Lucé, Fr August 25-28, 2010 Proc* 2010; **1**: 662.
126 Vandenburgh H. High-content drug screening with engineered musculoskeletal tissues. *Tissue Eng Part B Rev* 2010; **16**: 55–64.

127 Jung Y, Bae J. A Six-Legged Walking Robot Bio-Inspired Walking Pattern : Kinematic Analysis. 2013; : 257–264.
128 Schuldt DW, Rife J, Trimmer BA, Saunders F, Trimmer BA, Rife J *et al.* Softworms: the design and control of non-pneumatic, 3D-printed, deformable robots. *Bioinspir Biomim* 2016; **11**: 1–16.
129 Kim J, Kim HN, Lang Y, Pandit A. Biologically Inspired Micro- and Nanoengineering Systems for Functional and Complex Tissues. *Tissue Eng Part A* 2014; **19**: 1–4.
130 Katz E. Biomolecular logic systems: applications to biosensors and bioactuators. In: Cullum BM, McLamore ES (eds). *Smart Biomedical and Physiological Sensor Technology XI*. SPIE, 2014 doi:10.1117/12.2049959.
131 Baryshyan AL, Domigan LJ, Hunt B, Trimmer BA, Kaplan DL. Self-assembled insect muscle bioactuators with long term function under a range of environmental conditions. *RSC Adv* 2014; **4**: 39962–68.
132 Akiyama Y, Sakuma T, Funakoshi K, Hoshino T, Iwabuchi K, Morishima K. Atmospheric-operable bioactuator powered by insect muscle packaged with medium. *Lab Chip* 2013; **13**: 4870–4880.
133 Guo SZ, Gosselin F, Guerin N, Lanouette AM, Heuzey MC, Therriault D. Solvent-cast three-dimensional printing of multifunctional microsystems. *Small* 2013; **9**: 4118–4122.
134 Miller JS, Stevens KR, Yang MT, Baker BM, Nguyen D-HT, Cohen DM *et al.* Rapid casting of patterned vascular networks for perfusable engineered three-dimensional tissues. *Nat Mater* 2012; **11**: 768–774.
135 Kolesky DB, Truby RL, Gladman AS, Busbee TA, Homan KA, Lewis JA. 3D bioprinting of vascularized, heterogeneous cell-laden tissue constructs. *Adv Mater* 2014; **26**: 3124–3130.
136 Peng H, Mankoff J, Hudson SE, McCann J. A Layered Fabric 3D Printer for Soft Interactive Objects. In: *Proceedings of the ACM CHI'15 Conference on Human Factors in Computing Systems: Design and 3D Object Fabrication*. Seoul, Korea, 2015, pp 1789–1798.
137 Pei E, Shen J, Watling J. Direct 3D printing of polymers onto textiles: experimental studies and applications. *Rapid Prototyp J* 2015; **21**: 556–571.
138 Sochol RD, Sweet E, Glick CC, Venkatesh S, Avetisyan A, Ekman KF *et al.* 3D printed microfluidic circuitry via multijet-based additive manufacturing. *Lab Chip* 2016; **16**: 668–678.
139 Wu GH, Hsu SH. Review: Polymeric-based 3D printing for tissue engineering. *J Med Biol Eng* 2015; **35**: 285–292.
140 Ahn D, Kweon JH, Kwon S, Song J, Lee S. Representation of surface roughness in fused deposition modeling. *J Mater Process Technol* 2009; **209**: 5593–5600.
141 Ahn D, Kweon JH, Choi J, Lee S. Quantification of surface roughness of parts processed by laminated object manufacturing. *J Mater Process Technol* 2012; **212**: 339–346.
142 Bhattacharjee N, Urrios A, Kang S, Folch A. The upcoming 3D-printing revolution in microfluidics. *Lab Chip* 2016; **16**: 1720–1742.
143 Billiet T, Vandenhaute M, Schelfhout J, Van Vlierberghe S, Dubruel P. A review of trends and limitations in hydrogel-rapid prototyping for tissue engineering. *Biomaterials* 2012; **33**: 6020–41.

APPENDIX A2. GRAPHENE OXIDE SUBSTRATES WITH N-CADHERIN STIMULATES NEURONAL GROWTH AND INTRACELLULAR TRANSPORT

This chapter heavily utilizes the following publication.

[3]Qin, E. C., Kandel, M. E., Liamas, E., Shah, T. B., Kim, C., Kaufman, C.D., Zhang, Z.J., Popescu, G., Gillette, M.U., Leckband, D.E., & Kong, H.J (2019). Graphene oxide substrates with N-cadherin stimulates neuronal growth and intracellular transport. *Acta biomaterialia*, *90*, 412-423.

A2.1 Abstract

Intracellular transport is fundamental for neuronal function and development and is dependent on the formation of stable actin filaments. N-cadherin, a cell–cell adhesion protein, is actively involved in neuronal growth and actin cytoskeleton organization. Various groups have explored how neurons behaved on substrates engineered to present N-cadherin; however, few efforts have been made to examine how these surfaces modulate neuronal intracellular transport. To address this issue, we assembled a substrate to which recombinant N-cadherin molecules are physiosorbed using graphene oxide (GO) or reduced graphene oxide (rGO). N-cadherin physiosorbed on GO and rGO led to a substantial enhancement of intracellular mass transport along neurites relative to N-cadherin on glass, due to increased neuronal adhesion, neurite extensions, dendritic arborization and glial cell adhesion. This study will be broadly useful for recreating active neural tissues in vitro and for improving our understanding of the development, homeostasis, and physiology of neurons.

A2.2 Statement of Significance

Intracellular transport of proteins and chemical cues is extremely important for culturing neurons in vitro, as they replenish materials within and facilitate communication between neurons. Various studies have shown that intracellular transport is dependent on the formation of stable

[3] E.C.Q. and H.J.K. developed the concept and designed experiments. E.C.Q., M.E.K., and E.L. performed the experiments. E.C.Q., M.E.K., and C.K. analyzed the data. T.B.S. and C.D.K. prepared dissociated neurons. E.C.Q., D.E.L., and H.J.K. wrote the manuscript. E.C.Q., M.E.K., C.D.K., P.G., G.L.M., D.E.L., and H.J.K. edited the manuscript.

actin filaments. However, the extent to which cadherin-mediated cell–cell adhesion modulates intracellular transport is not heavily explored. In this study, N-cadherin was adsorbed onto graphene oxide-based substrates to understand the role of cadherin at a molecular level and the intracellular transport within cells was examined using spatial light interference microscopy. As such, the results of this study will serve to better understand and harness the role of cell–cell adhesion in neuron development and regeneration.

A2.3 Introduction

The intracellular transport of synaptic vesicle precursors, neurotransmitter and neurotrophic factors, proteins and mRNA is fundamental for the function, survival, and morphogenesis of neurons. Motor proteins bidirectionally transport cargoes containing various membrane organelles and protein complexes along the axons and dendrites. The transport of molecules and organelles from the cell body to the synapses or cell membrane is referred to as anterograde transport, whereas the opposite is referred to as retro-grade transport. For instance, a variety of newly synthesized proteins such as actin and neurofilaments are produced in the cell body and transported along the cytoskeleton filaments to the neuronal membrane to form and maintain axons that are involved in communication with neighboring and distant cells [1]. On the other hand, neurotrophic factors which are crucial to neuronal survival, such as nerve growth factor (NGF), bind to the membrane-associated receptors, are internalized, and actively transported to the cell body [2].

Impairment of intracellular transport has often been linked to neurodegenerative diseases. Genetic mutations in Alzheimer's dis-ease, for example, alters the roles of several proteins involved in trafficking cargo inside nerve cells, and the disruption of intracellular transport due to the protein defects results in cell death [3,4]. Similar impairments in intracellular transport have also been linked to Parkinson's disease, amyotrophic lateral sclerosis (ALS), and hereditary spastic paraplegia [5]. Defective transport can arise from various mechanisms, including the destabilization of micro-tubules, impairment of motor protein attachment to the micro-tubules, and/or altered kinase activities [6]. As a result, the formation of stable actin

filaments, which form tracks for motor proteins to transport cargos, is extremely important for proper intracellular transport [7].

Various extracellular matrix and cell–cell adhesion proteins are involved in the formation of the actin cytoskeleton. Cadherins, in particular, are cell–cell adhesion proteins which associate with catenin and interact with the actin cytoskeleton [8–10]. N-cadherin is essential for the functional organization of adult neural tissue and the development of neural networks by mediating axon guidance [11], neurite outgrowth [12–14], dendritic arborizations [9], and synaptogenesis [15,16], all of which require actin polymerization at the growth cones [17]. In addition, studies demonstrate that the function of N-cadherin can be recapitulated in vitro [18]. For example, recombinant N-cadherin protein coated onto various surfaces has been shown to mediate neurite outgrowth of neurons [14,19]. Approaches to improve the function of N-cadherin exploit either the use of an adhesive peptide motif for N-cadherin [20–22] or the use of engineered epitopes to bind and orient cadherin extracellular domains on different substrates [23–25]. Until now, current studies have primarily focused on understanding how neurons interact with N-cadherin coated surfaces in terms of neurite outgrowth; [14,23,24,26]; however, to our knowledge, no studies have examined how N-cadherin mediated interactions between neurons and N-cadherin coated surfaces affects intracellular trans-port thus far. In addition, the exact nature of neuronal interactions on N-cadherin coated GO compared to rGO is still unknown.

In recent years, a quantitative phase imaging technique called spatial light interference microscopy (SLIM) has been developed for non-invasive and label-free imaging of the intracellular mass transport within cells [27–31]. Using SLIM, the optical path length differences in the neuronal cell body and neurites due to intracellular mass transport can be observed and quantified [28,32]. SLIM is an improvement from the conventional phase contrast imaging, in which the halo artifact from phase contrast imaging overestimates the neuronal cell size and prevents quantitative information about the intracellular mass transport [33]. Moreover, SLIM offers an opportunity to monitor the intracellular transport non-invasively over multiple days. Using SLIM, it has been demonstrated that inhibitors and neuronal densities strongly affect intra-cellular transport in neurons [28,31]. For this study, SLIM allows the ability to examine how N-

cadherin mediated interactions between neurons and N-cadherin coated surfaces affects intracellular transport.

Recently, graphene oxide (GO) and reduced graphene oxide (rGO) have been shown to promote protein adhesion and support neuronal function [34–36]. For instance, graphene functionalized with poly-lysine has been shown to significantly enhance neurite numbers and lengths in hippocampal neurons [35]. Graphene functionalized with laminin also enhances the differentiation of neural stem cells to neurons [37]. Gonzalez-Mayorga et al. recently demonstrated poly-lysine and N-cadherin can be coated onto microfibers made of rGO through non-covalent interactions and chemical means using carbodiimide chemistry. The resulting microfiber has been shown to improve neural growth in injured central neural tissue [26]. In addition, Lee et al. showed that insulin interacts with graphene differently than GO. The resulting changes in protein conformation is attributed to varying degrees of non-covalent interactions. In turn, insulin when bound to graphene or GO affects stem cell growth and differentiation differently [38]. This study demonstrated the importance of investigating the effects of both GO and rGO on protein adsorption and cellular interactions.

To regulate the cytoskeleton formation and subsequent intra-cellular transport, we hypothesized that adsorbing N-cadherin onto graphene-based substrates will enhance the growth and intracellular transport of hippocampal neurons. We tested this hypothesis by adsorbing recombinant N-cadherin extracellular domains onto uncoated glass or onto glass coated with either GO or rGO flakes. The adhesivity of N-cadherin layers on GO or rGO coated glass and the number of N-cadherin bound to the different substrates was evaluated by atomic force microscopy (AFM) and enzyme-linked immunosorbent assay (ELISA), respectively. In parallel, the secondary structure of adsorbed N-cadherin on GO or rGO flakes was examined using circular dichroism spectroscopy. Primary rat hippocampal neurons were seeded on the N-cadherin ecto domain coupled to uncoated and coated glass substrates, and the attachment of neuron and glial cells, neurite extension, and dendritic arborizations were examined. We further monitored the intracellular mass transport of vesicles within the cell bodies of the neurons and through the neurites using a form of quantitative phase imaging called spatial light interference

microscopy (SLIM). These results will be broadly useful to improve efforts to understand the developmental and physiological processes of neural tissues for the treatment of neural injuries and disorders.

A2.4 Experimental method

A2.4.1 Production and purification of recombinant, soluble N-cadherin extracellular domains

Soluble, recombinant N-cadherin ectodomains with C-terminal Fc tags (N-cadherin-Fc) were stably expressed in human embryonic kidney cells (HEK293, American Type Culture Collection), as previously described [39,40]. Cells were cultured in Dulbecco's Modified Eagle Medium (DMEM) containing 10% (v/v) fetal bovine serum (FBS) and 0.4 mg/mL G418 (Sigma Aldrich) as a selection marker. The cell culture supernatant containing the recombinant N-cadherin protein was collected every two to three days. The supernatant was later filtered and purified using a protein-A affinity column (Bio-Rad) and gel filtration chromatography 16/60 Sephacryl S-200 HR, Sigma-Aldrich) using the AKTA pure protein purification system. Protein purity was assessed using sodium dodecyl sulfate polyacrylamide gel electrophoresis (SDS-PAGE).

A2.4.2. Preparation of graphene oxide (GO) and reduced graphene oxide (rGO) suspension

Dry graphene oxide platelets (GO), with a diameter of 0.2–2 mm and a thickness of 1.1 ± 0.2 nm, was purchased from the manufacturer (Graphene Supermarket, Product Number: SKU-GO-005). Reduced graphene oxide (rGO), prepared by thermal exfoliation and hydrogen reduction of graphene oxide with a diameter of0.4–0.5mm and a thickness between 0.6 and 1.2 nm, was purchased from the manufacturer (ACS Materials, Product Number:GN1P0005). GO was suspended in 70% ethanol and rGO was sus-pended in 70% ethanol and 0.5% sodium dodecyl sulfate to a final concentration of 1 mg/mL and sonicated for 1 h before use to ensure the GO and rGO are in single layers and separated from each other.

A2.4.3. Surface modification of glass with GO/rGO and N-cadherin

Glass coverslips were plasma treated with air for 1 min to ren-der the surface hydrophilic. Then, 15mL of either GO or rGO flakes in suspension at a concentration of 1.0 mg/mL were spin

coated onto the glass. The coated glass substrates were then incubated at 55°C for 10 min, to evaporate the ethanol and water from the glass substrate, and to facilitate the uniform distribution of GO and rGO onto the glass surface. As the drying temperature was lower than the temperature used to reduce GO, the drying process did not result in significant reduction of GO and rGO (Fig. A1.1) [41]. The resulting coated glass substrates were incubated with 50mg/mL N-cadherin-Fc in phosphate-buffered saline with calcium (cPBS) for 1 h at room temperature. Six conditions were tested as shown in Table 1.

A2.4.4. FTIR and XPS characterization of GO/rGO flakes

The compositions of GO and rGO were determined using Fourier transform infrared (FT-IR) and X-ray photoelectron spectroscopy (XPS). For FT-IR, samples were prepared by pressing1 wt% GO/rGO flakes that were thermally treated with the conditions described in Section 2.3together with potassium bromide (KBr, Sigma Aldrich) to form a transparent pellet. The spectra of the pel-lets were recorded using a Thermo-Nicolet Nexus 670 at a spectral range between 1000 and 4000 cm^{-1}. The resulting spectra was the result of 64 scans obtained at a resolution of 4 cm^{-1}, and the baseline for the spectra was corrected in Origin using the 2nd derivative method and connected using the spline interpolation method. The Asymmetric Least Squares Smoothing Baseline Method was used to smooth the spectra. For XPS, the samples were prepared by depositing a thick layer of GO/rGO onto a glass via repeated drop drying, and thermal treatment with the conditions described in Section 2.3. XPS measurements were acquired using a Kratos AxisULTRA with a monochromated Al-KaX-ray source (hm= 1486.61 eV). The atomic ratios of carbon to oxygen were calculated from the survey spectra by considering the integrated areas of their respective peak positions (294.5 and 533.0 eV). The deconvolution of the carbon spectra was performed using the CasaXPS software.

A2.4.5. Spatial distribution and characterization of GO/rGO spin-coated onto glass using Raman spectroscopy

The Raman spectra of the glass substrates coated with GO/rGO were acquired in air at ambient conditions with a NanophotonRaman-11 Laser Microscope. The spectra were recorded

with a 532-nm laser between 1000 and 3000 cm^{-1}. For Raman XY mapping, a surface area of 140x140 μm^2 was recorded using a 20X objective lens (numerical aperture NA = 0.45). The laser beam was focused on each point for a 0.01 s exposure time and averaged two times per point, and the samples were measured at 35x35 pixels with a resolution of 4.1 mm. The data was further processed using a Raman image processing software (Raman Viewer; Nanophoton Corporation, Japan) to generate the average Raman spectra with baseline correction and normalization and to plot the surface maps of GO/rGO. The Raman maps show the total intensity of D-band (1320 – 1370 cm^{-1}) and G-band (1550 – 1610 $cm^{-1)}$ to the intensity of the second-order optical phonon peak (850 – 1050 cm^{-1}) of the glass substrate in the Raman spectrum.

A2.4.6. Surface energy of glass modified with GO/rGO

The contact angles of water and methylene iodide (SigmaAldrich) were recorded using the sessile drop method with a Rame-Hart Contact Angel Goniometer. The DROP image standard software was used to calculate the surface energy of the various substrates. The surface energy was based on a two component model for solid surface energy developed by Owens and Wendt, as described in the equation below (1): [42] rLðcoshþ1Þ2ðrLDÞ1=2¼ðrSPÞ1=2rLPrLD1=2þðrSDÞ1=2ð1Þ where :rL= overall surface tension of the liquid, rLD= dispersive component of the surface tension of the liquid, rLP= polar component of the surface tension of the liquid, rS= overall surface energy of the solid, rSD= dispersive component of the surface energy of the solid, rSP= polar component of the surface energy of the solid, rSL= the interfacial tension between the solid and the liquid, and h= the contact angle between the liquid and the solid. For water, rL= 72.8 erg/cm^2, rLD= 21.8 erg/cm2, and rLP= 51.0 erg/cm^2. Formethylene iodide, rL= 50.8 erg/$cm^{2,}$ rLD= 48.5 erg/cm^2, and rLP= 1.3 erg/cm^2. The total surface energy of the surface is the sum of the slope, (rsP)1/2, and the intercept, (rsD)1/2.

A2.4.7. Circular dichroism analysis of N-cadherin secondary structure

To prepare the samples, 0.28mg/mL recombinant N-cadherin-Fc solution was mixed with 0.20 mg/mL GO or rGO suspension for one hour at room temperature. All samples were prepared in cPBS. Circular dichroism (CD) measurements of unbound N-cadherin and N-cadherin associated with GO and rGO flakes were conducted using the Jasco 715 spectropolarimeter. A quartz cell with an optical pathlength of 1 mm was used. The scanning speed was set at 50 nm/min, and a wavelength range was examined between 200 and250 nm.

A2.4.8. Enzyme-linked immunosorbent assay (ELISA) to determine amount of adsorbed N-cadherin

A mass balance approach was used to quantify the amount of N-cadherin immobilized on the coated and uncoated glass substrate. After incubation with the glass substrates, the unbound N-cadherin was collected and added to a polystyrene 96-well plate. After incubation for 1 h at 37°C, the plate was washed and then incubated with 2% bovine serum albumin (BSA) in cPBS for 1 h at 37°Ctoblock nonspecific interactions. Then, the wells were incubated with N-cadherin rabbit polyclonal antibody (1:600, ProteinTech) over-night at 4°C. Horse radish peroxidase (HRP)-conjugated anti-rabbit IgG (1:10,000, Sigma Aldrich) was added to each well and incubated at room temperature for one hour. Between each step, the wells were washed extensively with cPBS. A 3,30,5,50-tetramethylbenzidine (TMB) ELISA substrate kit (ThermoFisher) was used as a chromogenic substrate for HRP. After incubation for 20 min with the TMB and peroxide solution from the kit, the absorbance of each well was measured at 370 nm with a microplate reader (Tecan Infinite 200 PRO). A calibration curve was conducted with known amounts of N-cadherin and their corresponding absorbance to determine the surface density of N-cadherin immobilized on the substrate.

A2.4.9. Atomic force microscopy imaging and adhesion force measurement

Topographic images and force–displacement curves were acquired using a Multimode Nanoscope III atomic force microscope (AFM) equipped with Nanoscope III controller (Veeco, CA). Silicon nitride AFM cantilevers, with a nominal spring constant of 0.27 N/m, (nominal spring constant 0.27 N/m) were purchased from BudgetSensors (Sofia, Bulgaria). AFM was operated in

intermittent contact mode for imaging on substrates with and without N-cadherin. One hundred force curves were collected with unmodified AFM tips over a 10x10 μm^2 region on either GO or RGO cluster with or without N-cadherin, using the aid of the system integrated optical microscope. This process was repeated over three different locations on the substrates, in order to acquire a total of 300 force curves for each sample examined. The applied load and tip retraction velocity were kept at 4 nN and 2mm/s respectively for the force measurements. Surface adhesion values were quantified by registering the force required to separate the AFM tip from surface and analyzed using Matlab scripts (developed by Carpick's group at the University of Pennsylvania). All experiments were performed in cPBS at room temperature.

A2.4.10. Primary hippocampal neuron culture

All experimental procedures were performed with protocols approved by the Institutional Animal Care and Use Committee, University of Illinois at Urbana-Champaign, and in compliance with the principles and procedures outlined in the National Institutes of Health Guide for the Care and Use of Laboratory Animals. Hippocampal neurons were obtained from neonatal (P1-P2) Long-Evans BluGill rat brains, as previously described. After isolation, the hippocampi were placed in Hibernate-A (Brain Bits, Springfield, IL) on ice, and then treated with 18 U/mL papain (Sigma Aldrich) in Hibernate-A for 30 min at 37°C. Following enzymatic digestion, the hippocampi were rinsed with Hibernate-A, and mechanically dissociated through trituration using a fire-polished Pasteur pipette. The dissociated cells were centrifuged and re-suspended in standard maintenance media containing Neurobasal media (Gibco), supplemented with 0.5 mM GlutaMAX (Gibco), serum-free neural media supplement (GS21, Sigma Aldrich), 100 U/mL penicillin and 0.1 mg/mL streptomycin. Prior to cell culture, the coated and uncoated glass substrates were incubated with complete culture medium for 15 min at37°C. Primary hippocampal neurons were seeded onto the different glass substrates prepared as summarized in Table 1. For low-density cell experiments, the cells were seeded at a density of150,000 cells/cm2, and cultured at 37°C in the presence of 5%CO2. For high density, long-term cell experiments, the cells were seeded at a density of 375,000 cells/cm2, and the osmolality of the medium was adjusted to 275 mOsm with

sodium chloride. For the low and high cell density experiments, half of the medium was removed and replaced with fresh maintenance medium every three days.

A2.4.11. Immunofluorescence imaging and neuronal analysis

After 4 and 10 days of culture, the cells on the coated and uncoated glass substrates were fixed with acetone:methanol (1:1) for 20 min at -20°C and then were blocked with 2% BSA for 30 min. The cultures were then incubated with rabbit poly-clonal anti-microtubule associated protein 2 (MAP2) (1:500, Abcam) and mouse anti-glial fibrillary acid protein (GFAP) (1:250, BD Biosciences) overnight at 4°C. Afterwards, the cells were incubated with fluorescently labeled goat anti-rabbit (H + L)cross-adsorbed secondary antibody Alexa Fluor 488 (1:25, Thermo-Fisher) and goat anti-mouse IgG (H + L) Alexa Fluor 555 (1:250, CellSignaling Technology) for 60 min at room temperature. Finally, the cell nuclei were stained with DAPI (10mg/mL, Invitrogen) for 8 min at room temperature. Between steps, the coated and uncoated glass substrates were rinsed with PBS. The immunofluorescence imaging was obtained using a confocal microscope (Zeiss LSM700). Afterwards, ImageJ was used to quantify the total number of cells stained for GFAP and MAP2, the number of primary and terminal neurites, and the length of the neurites. Due to clustering of cells present on the glass substrate, several assumptions are made to quantify the neuronal behavior on the glass substrate for the higher density cultures. First, to estimate the number of dendrites, the width of the dendrites was divided by the average width of the individual dendrites, measured from the dendrites on neurons cultured on the N-cadherin coated GO and rGO substrates. Second, to estimate the number of cells, only cells that had direct contact with the substrate was counted. Third, morphological conditions were used to classify neurons from glial cells.

A2.4.12. Label-free intracellular transport with quantitative phase imaging

Spatial Light Interference Microscopy (SLIM), a technique that measures the optical path length shifts in the phase contrast geometry, was used to examine the intracellular mass transport in the neuronal cell body and neurites. Images were acquired with a SLIM system (CellVista SLIM Pro, Phi optics, Inc.) attached to a Zeiss Z1microscope, as described previously

[33]. The cells were seeded at 250,000 cells cells/cm2in maintenance medium. After 22 h in culture, the neurons were continuously monitored (in ‘‘bursts”) for 12 min at each field-of-view with a separation of 5.5-hour time intervals between bursts for a total of approximately 40 h. During imaging, the cells were kept at 37°C and in a 5% CO2atmospherewith an incubator and heated stage insert (Zeiss). To characterize mass transport phenomena, the mean spread of advection velocities was examined using dispersion-relation phase spectroscopy (DPS), a method that uses time-resolved quantitative phase imaging to analyze intracellular transport [27,30]. The phase map time-sequence was manually annotated into neurites and bodies using ImageJ to yield a single advection spread coefficient [32].

A2.4.13. Statistical analysis

All in vitro experiments were conducted with at least two independent cell experiments and with at least four different samples per group. All results represented mean ± standard error of mean, unless otherwise noted. For in vitro experiments, a one-analysis of variance (ANOVA) followed by Tukey-HSD post-hoc tests were performed on all data sets. For SLIM experiments, a Wilcoxon rank-sum test was used to compare between groups, and the data was reported as a box-and-whisker plot, where the whiskers show the minimum and maximum, and the box shows the 25th, 50th, and 75th percentiles.

A2.5. Results

A2.5.1. Characterization of GO and rGO flakes

Fourier-transform infrared (FT-IR) spectra of the functional groups of GO and rGO flakes are shown in Fig. A2.1a. GO flakes have peaks at 3400, 1730, 1412, 1225, and 1047 cm^{-1}, which correspond to the OAH, C@O, C@C, CAOAC, and CAO groups, respectively. In contrast, rGO flakes only exhibit some of the oxygen containing functional groups (C@O, C@C, and CAOAC). This result was re-confirmed with X-ray photoelectron spectroscopy (XPS). XPS elemental analysis shows that the carbon to oxygen atom ratio of GO is 0.46, while that of rGO is 2.14, due to the reduction of the epoxides and hydroxyl groups (Fig. A2.1b). Both GO and rGO have peaks at 284.6 eV, which corresponds to the emission from thesp2-hybridized carbons. However, GO has

another higher binding energy peak at 286.7 eV, which is assigned to the hydroxyl group, as well as an additional peak at 289.4 eV, which corresponds to the carboxylic acid group (Fig. A2.1c). rGO showed smaller peaks corresponding to hydroxyl and carboxylic acid groups than GO (Fig. A2.1d).

A2.5.2. Characterization of glass substrates coated with GO and rGO flakes

GO and rGO flakes were spin-coated onto plasma-treated glass substrates. Raman spectroscopy of glass coated with GO or with rGO flakes revealed two broad peaks: a D-band at 1,360 cm^{-1} and a G-band 1,600 cm^{-1}. The D-band represents the out-of-plane vibrations of sp2carbon due to the presence of structural defects, and the G-band represents the in-plane vibrations of sp2carbon from a 532-nm excitation laser. The additional oxygen-containing functional groups on GO disrupted the in-plane sp2con-figuration and resulted in a higher relative peak intensity ratio of the D- to the G-band (1.06) than rGO flakes (0.72). The ratio of the G-band at1,360 cm^{-1} to the 2D band at 1,600 cm^{-1} was 0.21 for glass coated with GO and 0.17 for glass coated with rGO. This result states that the GO and rGO are single-layered [43]. Raman spectroscopy mapping and confocal images of the total intensity of D-band (1320–1370 cm^{-1}) and G-band (1550–1610 cm^{-1}) confirmed that GO and rGO flakes were evenly dis-tributed across the surface (Fig. A2.2b). Confocal images showed that the surface coverage of GO and rGO to the glass substrates were around40%. There was no significant difference between the surface coverage of GO and rGO. Water contact angle measurements showed that glass substrates coated with GO and rGO flakes were more hydrophobic than uncoated glass substrates, as noted by the increased advancing water contact angles (Fig. A2.2c). As expected, the glass substrate coated with rGO flakes was slightly more hydrophobic than the glass substrate coated with GO flakes. The contact angle of water was 31 ± 3° for GO, and 38 ± 3° for rGO. For glass, the contact angle of water was only 19 ± 2°. The total surface energy of glass substrates coated with GO or rGO flakes was calculated based on the two-component model developed by Owens and Wendt to be around 65 ± 2 and 68 ± 2 mN/m, respectively [42]. This value was around 10 mN/m lower than that of the uncoated glass substrate (Fig. A2.2d).

A2.5.3. Physisorption of N-cadherin onto GO/rGO-coated glass substrates

Recombinant N-cadherin molecules were physiosorbed onto the surface of un-, GO-, or rGO-coated glass by exposing the substrates to a solution of 50mg/mL N-cadherin-Fc (Fig. A2.3a). AFM images acquired in PBS containing calcium showed that N-cadherin adhered to all three substrates (Fig. A2.3b, Fig. A2), and the adsorbed protein was approximately 2–3 nm in height with an average diameter of 15 nm (Fig. A3). In comparison with prior electron microscopy images of N-cadherin on mica [44], the images presented here suggest that N-cadherin adsorbs as aggregates or as 'collapsed' globules. AFM-based force spectroscopy was used to quantify the surface adhesion between an uncoated AFM tip and the N-cadherin layer on the uncoated, GO, and rGO-coated glass. The adhesion is defined as the force required to separate the AFM tip from the solid surface, with or without the N-cadherin (Fig. A4). It was found that the GO-and rGO-coated glass substrates had greater mean adhesion strength of N-cadherin than uncoated glass substrates. The surface adhesion of uncoated glass is approximately 0.57 ± 0.04 nN, as measured by AFM. In contrast, the mean adhesion strength of N-cadherin to the GO- or rGO-coated glass substrates was approximately ten times higher than the uncoated glass substrate (Fig. A2.3c). While the mean values do not demonstrate a significant difference in adhesion strength, the force histogram distribution were much broader for the N-cadherin layer on GO- and rGO-coated glass. In addition, the maximum adhesion, determined by the peak of the histogram, appeared to shift to higher values on the rGO-coated glass. rGO (3.5 nN) had a maximum surface adhesion between the N-cadherin and AFM tip, compared to uncoated glass (1 nN) and GO (2 nN). Control studies of the adhesion between AFM and the uncoated, GO-, and rGO-coated glass with-out N-cadherin revealed a significantly lower adhesion over all samples (Fig. A5). This result confirmed that the adhesion force was dependent on the interaction between the N-cadherin layer and AFM tip, which was influenced by the underlying substrate. Importantly, these measurements did not quantify the strengths of individual cadherin bonds [25,45], but rather semi-quantitatively compared the relative adhesion of the AFM tip to the different substrates. This was apparent from the high values of the reported adhesion (nN) relative to the piconewton forces to rupture individual cadherin bonds [25]. The force-extension curves also indicated multiple unbinding events over retraction distances of more than 150 nm. We separately examined whether GO and rGO also increased the total number of N-cadherin physiosorbed to

the various substrates using an enzyme-linked immunosorbent assay (ELISA) (Fig. A2.3d). Interestingly, GO and rGO did not increase the total density of N-cadherin bound to the glass substrate, compared to the N-cadherin adhered to the uncoated glass. GO and rGO-coated glass resulted in slightly higher amounts of physiosorbed N-cadherin (0.36 ± 0.06 and 0.37 ± 0.08 pmol/cm2, respectively) than uncoated glass (0.34 ± 0.02 pmol/cm2). In addition, circular dichroism spectroscopy confirmed that N-cadherin mixed with the GO or rGOflakes in solution retained its original beta-sheet confirmation, with a negative band at 212 nm (Fig. A2.3e).

A2.5.4. Enhanced N-cadherin adhesive function on GO/rGO-coated glass substrates promotes neuronal cell adhesion and dendritic arborization

Primary rat hippocampal neurons were cultured on the differ-ent substrates, and the morphologies of neurons seeded on the different substrates were evaluated by staining neurons and glial cells with microtubule associated protein 2 (MAP2) and glial fibrillary acidic protein (GFAP), respectively, after four days in vitro. To investigate the neuronal morphologies, the cells were seeded at an initial low density of 150,000 cells/cm2. N-cadherin adsorbed on GO-coated glass substrates (N-cadherin-GO-glass) or N-cadherin adsorbed on rGO-coated glass substrates (N-cadherin-rGO-glass) increased the percentage of MAP2-positive neurons relative to neurons on glass. In contrast, N-cadherin adsorbed on the uncoated glass (N-cadherin-glass) did not increase the number ofMAP2-positive neurons, compared to cells on the uncoated glass substrate (Fig. A2.4a&b; Fig. A6). All conditions resulted in minimal adhesion of glial cells (1–4%), stained with GFAP. Treatment with N-cadherin function-blocking antibody prevented cell attachment to the glass substrates with physiosorbed recombinant N-cadherin (Fig. A7), which confirmed the binding specificity of the adhesive N-cadherin ligand. In addition, N-cadherin-GO-glass and N-cadherin-rGO-glass increased the number of primary dendrites per cell by 2.5 and 4-fold, respectively, compared to GO- and rGO-coated glass substrates without N-cadherin (Fig. A2.4a&c, Fig. A8). Furthermore, on N-cadherin-rGO-glass, the mean lengths of the neurites and the number of primary dendrites extended from the neuron were greater than on the uncoated glass (Fig. A2.4a&d). In the absence of N-cadherin, the neurite length was only slightly higher on GO-or rGO-coated glass compared with cells on the uncoated glass. Interestingly, none of the

coatings affected dendritic arborization. The effects of N-cadherin and GO/rGO flakes on neurons were further observed when neurons were plated at sub-confluent densities for long-term culture. As it was difficult to maintain cultures of primary neurons at low cell densities due to the lack of trophic support from adjacent neurons and glia [46], the neurons were seeded at a higher density of 375,000 cells/cm2. After 3 days in vitro on N-cadherin-glass, the neurons self-aggregated to form clusters (Fig. A9). The clusters showed limited dendritic arborization by 9 days in vitro (Fig. A2.5a; Fig. A9). In contrast, neurons cultured on the N-cadherin-GO-glass or on N-cadherin-rGO-glass did not form clusters. Instead, the neurons were homogenously distributed across the substrates, and formed extensively interconnected neural networks. Uncoated and coated glass substrates without physiosorbed N-cadherin did not support long-term cultures past 4 days in vitro (Fig. A10). Because the neurons clustered on N-cadherin-glass, it was difficult to determine the total number of cells adhered to the surface, the cell types, and the number of dendritic extensions per neuron. For instance, the cluster prevented proper labeling of neuron and glial cells within the clusters. In addition, multiple neurites were grouped together, which made discerning the source of the neu-rites from individual neuronal cell bodies impossible. By contrast, valuable information could be perceived from the neurons that were evenly distributed over the substrates. The density of neurons that adhered to the N-cadherin-GO-glass was higher than then number of neurons adhered on N-cadherin-rGO-glass glass (Fig. A2.5b, Fig. A11). N-cadherin-GO-glass facilitated the adhesion of glial cells marked with GFAP compared to the two other conditions, which resulted in a higher neuron to glia ratio on the N-cadherin-rGO-glass than on the N-cadherin-GO-glass (Fig. A2.5a&c, Fig. A12). In addition, neurons cultured on the N-cadherin-rGO-glass displayed greater primary and terminal arborization than those grown on N-cadherin-GO-glass (Fig. A2.5a, d&e, Fig. A8). The arborization of primary dendrites originating from the cell body of the neurons was 3 ± 1 primary dendrites per cell on N-cadherin-GO-glass and 5 ± 2 primary dendrites per cell on N-cadherin-rGO-glass. The total number of terminal neurites was also two times higher on N-cadherin-rGO-glass (6 ± 3 terminal dendrites per cell) than that on N-cadherin-GO-glass (11 ± 6 terminal dendrites per cell).

A2.5.5. N-cadherin modulates intracellular mass transport through interconnected neurons

To determine how the different substrates affected neuronal functions, we quantified the intracellular vesicular mass transport throughout the neurites and cell body using a non-invasive and label-free quantitative phase imaging modality called spatial light interference microscopy (SLIM) [33].Within the neuronal cell bodies, the intracellular mass transport was more active on substrates physiosorbed with N-cadherin than glass substrates without N-cadherin, as demonstrated by the higher mean advection velocity (Fig. A2.6a&b; Movies A1–A6).The mean advection velocities for neurons cultured on uncoated, GO- and rGO-glass were 1.6 ± 0.3, 1.8 ± 0.6, and 1.6 ± 0.4lm/min, respectively. On the other hand, the mean velocities of N-cadherin-glass, N-cadherin-GO-glass, and N-cadherin-rGO-glass, were 2.0 ± 0.4, 2.0 ± 0.4, and 2.0 ± 0.4lm/min, respectively. GO and rGO flakes alone did not significantly affect the advection velocity in the cell body, regardless of the presence of N-cadherin (Fig. A2.6b). Within the neurites, there was increased intracellular mass transport in neurons grown on N-cadherin-GO-glass and N-cadherin-rGO-glass compared to N-cadherin-glass. Interestingly, in neurons cultured on N-cadherin-GO-glass or on N-cadherin-rGO-glass, the mean advection velocity in the neurites increased (0.2 ± 0.2 and 0.3 + 0.2lm/min, respectively), in comparison to transport in cells on N-cadherin-glass (0.1 ± 0.1lm/min) (Fig. A2.6c&d; Movies A7–A9). Representative images of the time required for intracellular vesicular transport from one end to the other end of the frame are shown in Fig. A2.6c. Compared to the mean advection velocity in the cell body, the mean advection velocity in the neurites was 5–10 times slower. Neurons grown on glass without N-cadherin did not extend sufficient neurites for analyses of mass transport, due to shortened lengths and decreased dendritic arborizations. As a result, intracellular mass transport was only assessed in neurites on N-cadherin-glass

A2.6. Discussion

Results presented in this study show that soluble, recombinant N-cadherin extracellular domains retain greater adhesive function when physiosorbed to GO or rGO coated glass, relative to N-cadherin directly adsorbed to uncoated glass. This resulted in greater neuron adhesion, arborization, and intracellular vesicle transport on N-cadherin-GO or N-cadherin-rGO-glass, relative to cells on N-cadherin-glass. Furthermore, AFM adhesion measurements confirmed

greater N-cadherin-dependent tip-substrate adhesion to N-cadherin-GO or N-cadherin-rGO compared to N-cadherin-glass, at similar physiosorbed protein densities.

We found that GO-glass and rGO-glass supported increased neuron adhesion and prevented cell clustering on N-cadherin modified substrates. Compared to cells adhered to N-cadherin-glass, N-cadherin-GO-glass and N-cadherin-rGO-glass resulted in increased neurite extension lengths and dendritic arborization. Also, hippocampal neurons adhered to the N-cadherin modified glass better than to glass without N-cadherin. This result indicates that neurons recognize and adhere to the recombinant N-cadherin molecules immobilized on the glass. More interestingly, neurons adhered to the N-cadherin-GO-glass or the N-cadherin-rGO-glass exhibited more active neurite extension and dendritic arborization than cells adhered to the N-cadherin-glass. This active neurite extension and dendritic arborization would allow for increased chances for synapse formation and communication between neighboring cells. In addition, despite the discontinuous, uncoated glass areas on N-cadherin-GO-glass and N-cadherin-rGO-glass, improvements in neuronal adhesion, neurite extension, and dendritic arborization can be observed. As the key difference between N-cadherin-glass and N-cadherin GO-glass or N-cadherin-rGO-glass is the presence of GO and rGO, respectively, the results suggest that these improvements are primarily due to GO and rGO.

In addition, we also found that GO-glass and rGO-glass sup-ported glial cell adhesion, particularly with high initial seeding densities (375,000 cells/cm^2). Two-way communication between neurons and glial cells are extremely important for neuronal function. Glial cells, for instance, release neurotransmitters and other extracellular signaling molecules that affect synapse formation, synaptic transmission, and synaptic strength [47,48]. In this regard, glial cells are required for normal functioning of the nervous system. Previous studies have also shown that glial cells, which also express N-cadherin, binds preferentially to N-cadherin [49]. With lower density cultures (150,000 cells/cm^2), where glial cells were not present, we observed early neuronal death after four days of culture. By 10 days of culture, a majority of the neurons have died (95%). In the presence of glial cells, the neurons interacted with the glial cells and the

substrate. The neurons continued to grow and exhibit neurite arborizations after ten days of culture.

Numerous studies have shown that N-cadherin promotes neu-rite extensions [13,14]. It has been proposed that N-cadherin stimulates the neurite outgrowth through a ‘‘molecular clutch” mechanism, which involves a direct mechanical linkage between the N-cadherin/catenin complexes at the membrane and intracellular actin [8]. These results suggest that a critical density of functional N-cadherin bonds is required to stabilize adhesions and resist actin flow. The strength of single N-cadherin bonds is 50 pN [45,50]. At the single molecule level, these individual weak bonds may not be sufficient to stabilize neuronal adhesion and support neurite extensions, but clusters of N-cadherin on beads used in optical trapping studies were capable of resisting actin flow, and N-cadherin adhesion to the cell surface stimulated neu-rite outgrowth [8]. Thus, increasing the population of active, physiosorbed N-cadherin on the GO and rGO coated glass substrates, as suggested by AFM results presented here, would similarly increase the density of neuron-substrate bonds to a level sufficient to stabilize N-cadherin adhesions and support both neurite out-growth and increased arborization. These results demonstrate increased dendritic outgrowth and arborization, neuronal adhesion, and intracellular transport on conditions with N-cadherin compared to the control (without N-cadherin). Therefore, we believe that there is a significant advantage to using N-cadherin for neuronal cultures, as without N-cadherin, we would not see the aforementioned effects. N-cadherin has been shown to promote neuronal outgrowth more rapidly compared to non-adhesive polymers such as polylysine [14]; however, another paper reports that both N-cadherin and polylysine results high interconnected neuronal cultures [26]. As the exact mechanism for this behavior is complex, it is difficult to cross-compare the effects of N-cadherin to synthetic polymers.

Although the exact physical and chemical basis for the greater specific adhesion and amount of protein bound on the substrates is unclear, the results suggest that GO- and rGO-flakes bind Fc-tagged N-cadherin in a manner that both exposes the binding site and preserves the physiosorbed protein function. For instance, glass surfaces are negatively charged, so that the difference in retained N-cadherin activity could be due to the different effects of electrostatic

versus van der Waals and non-polar interactions on the N-cadherin structure and activity. In contrast, the minimal difference in the adhesive function of N-cadherin-GO- and N-cadherin-rGO-glass implies that differences in local hydrogen bonding and electrostatic interactions between the GO/rGO flakes did not significantly alter the N-cadherin function. Our results indicated that the N-cadherin protein retains its original beta-sheet conformation when bound to both GO and rGO, unlike proteins such as insulin, which change conformation when bound to graphene derivatives [38].

Using SLIM, a highly sensitive form of quantitative phase imaging, we found that the presence of N-cadherin molecules on these substrates supported increased advection mass velocity in neu-rites, particularly when the protein was adsorbed onto the GO or rGO-coated glass. The ability of neurons to actively transport macromolecules and organelles is extremely important for forming physiologically functional neural networks. Proteins, soluble growth factors, and hormones are produced in the cell body, loaded in vesicles, and transported across the neurites [51]. As neurons grow and interact with neighboring proteins, neurons release intracellular molecules through exocytosis at the synaptic junction between cells. Defective transport due to protein aggregation or accumulation can lead to numerous neurodevelopmental and neurodegenerative disorders [5].

Our findings demonstrate that neuronal adhesion to N-cadherin extracellular domains physiosorbed to the GO- or rGO-coated glass resulted in increased advection velocity of the intracellular mass in neurites relative to cells adhered to less adhesive, uncoated glass. The increased intracellular transport is possibly due to the increased regulation of the microtubule and actin cytoskeleton through cadherin-mediated adhesion. Cadherins are actin regulatory proteins and they also link to microtubules through the micro-tubule binding proteins PLEKHA7 and Nezha [52]. The latter interaction increases microtubule density and impacts the micro-tubule network [53]. Relevant to this study, the longer neurites, which were formed on N-cadherin-GO-glass and on N-cadherin-rGO-glass are indicative of stable microtubules. While receptors other than N-cadherin are also associated with microtubule formation [54], our studies suggest that surfaces coated with N-cadherin formed stable microtubules, which preferentially

bind to kinesin and dynein motors [55]. In addition, increased glial cell adhesion may increase intracellular transport, possibly through the release of neurotransmitters and other extracellular signaling molecules [47].

A2.7. Conclusion

Overall, this study demonstrated that physiosorbed Fc-tagged, N-cadherin extracellular domains on GO and rGO flakes coated on glass exhibited greater average adhesive function than N-cadherin adsorbed directly to glass substrates. The increased N-cadherin-based adhesion resulted in dispersed neurons on substrates with improved intracellular mass transport along neurites. This result is attributed to concomitant increases in neurite extensions, dendritic arborization, neural network formation, and improved intracellular mass transport throughout the neural networks. These substrates thus enhance physiologically relevant neural functions in vitro and will facilitate future studies aimed at better understanding the development, homeostasis, and pathology of neural networks. In addition, the ability of N-cadherin-GO- and rGO-coated substrates to support single-layer neuronal cultures may facilitate drug and gene delivery studies, due to the homogeneity of the neurons in exposure to delivered drugs and genes. Furthermore, the strong coupling of cadherins between neurons with N-cadherin coated GO and rGO would thus allow for stabilization of the growth cones involved in neural path-finding and extensions.

A2.8 Figures

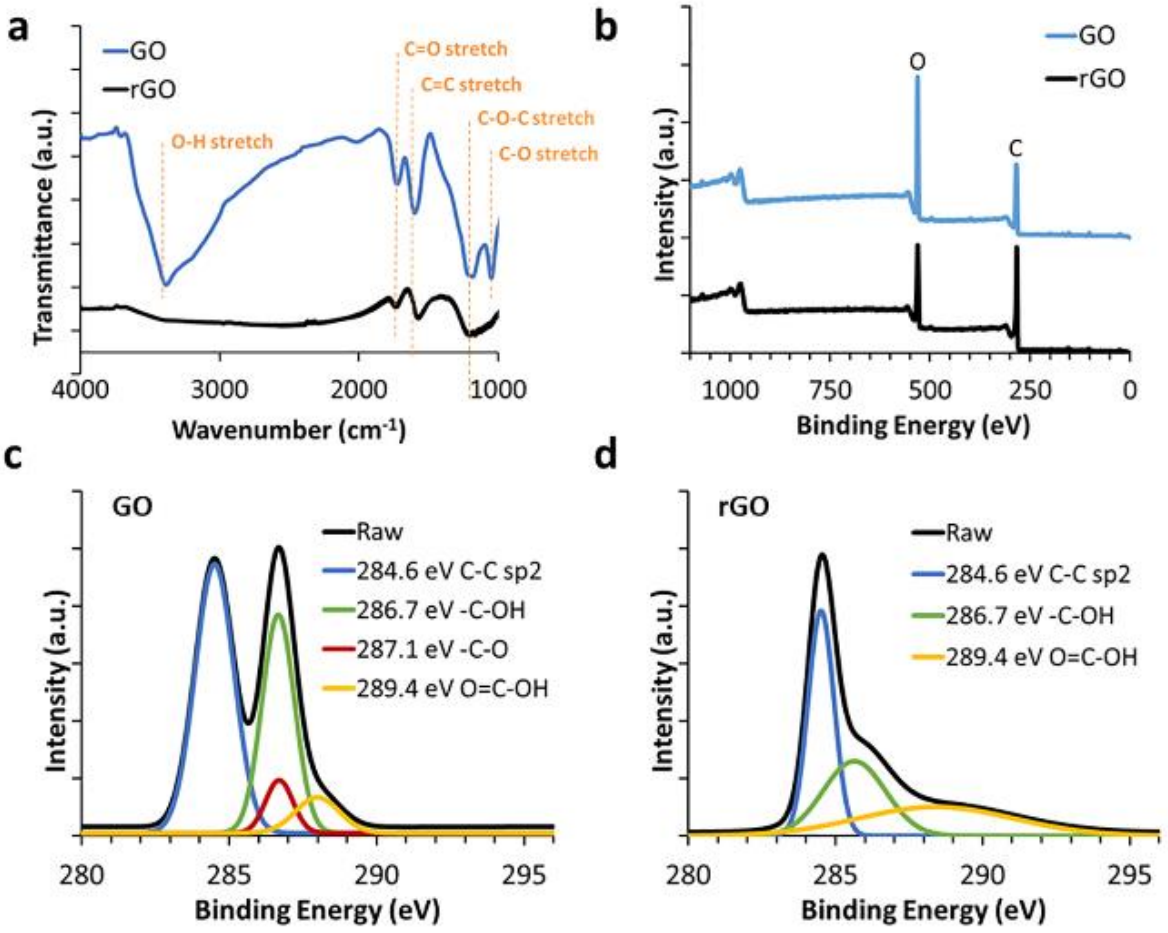

Figure A2.1. Characterization of GO/rGO flakes. **(a)** FT-IR spectra of GO/rGO flakes. **(b)** XPS elemental analysis. Deconvolution of the C1s XPS spectra of **(c)** GO and **(d)** rGO.

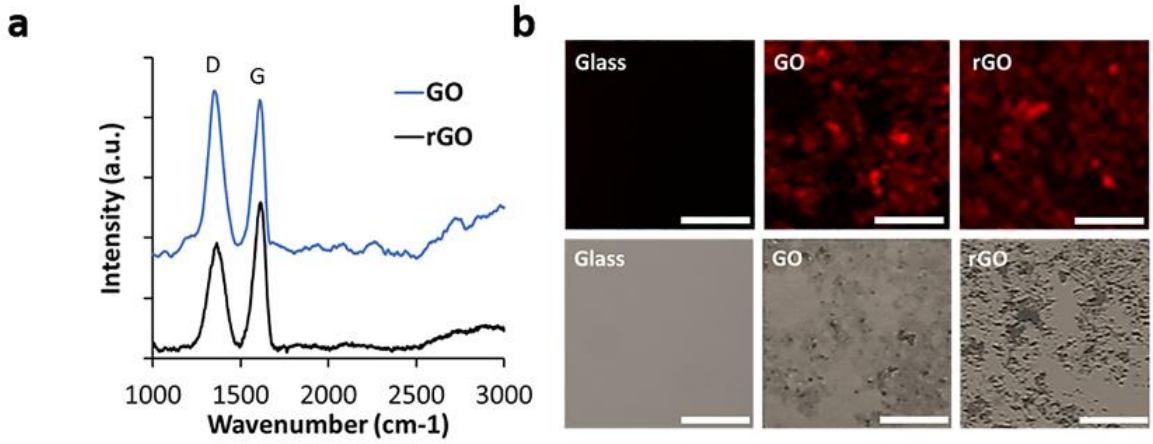

d

Sample	Contact Angle of Water (°)	Polar Surface Energy (mN/m)	Dispersive Surface Energy (mN/m)	Total Surface Energy (mN/m)
Glass	19 ± 2	34 ± 1	40 ± 1	74 ± 1
GO coated glass	31 ± 3	34 ± 1	32 ± 1	65 ± 2
rGO coated glass	38 ± 3	22 ± 2	45 ± 2	68 ± 2

Figure A2.2. Surface analysis of GO/rGO coated substrates. **(a)** Raman spectroscopy of GO and rGO. **(b)** 1st row: Representative intensity mapping of the total intensity of the D-(1320–1370 cm^{-1}) and G-band (1550–1610 cm^{-1}). 2nd row: Corresponding phase contrast confocal images of substrates. Scale bar represents 50 µm. **(c)** Images of water droplets on uncoated, GO and rGO-coated glass. **(d)** Table of the contact angle and surface energy of the substrates. The values represent the mean ± the standard error of the mean (n = 4)

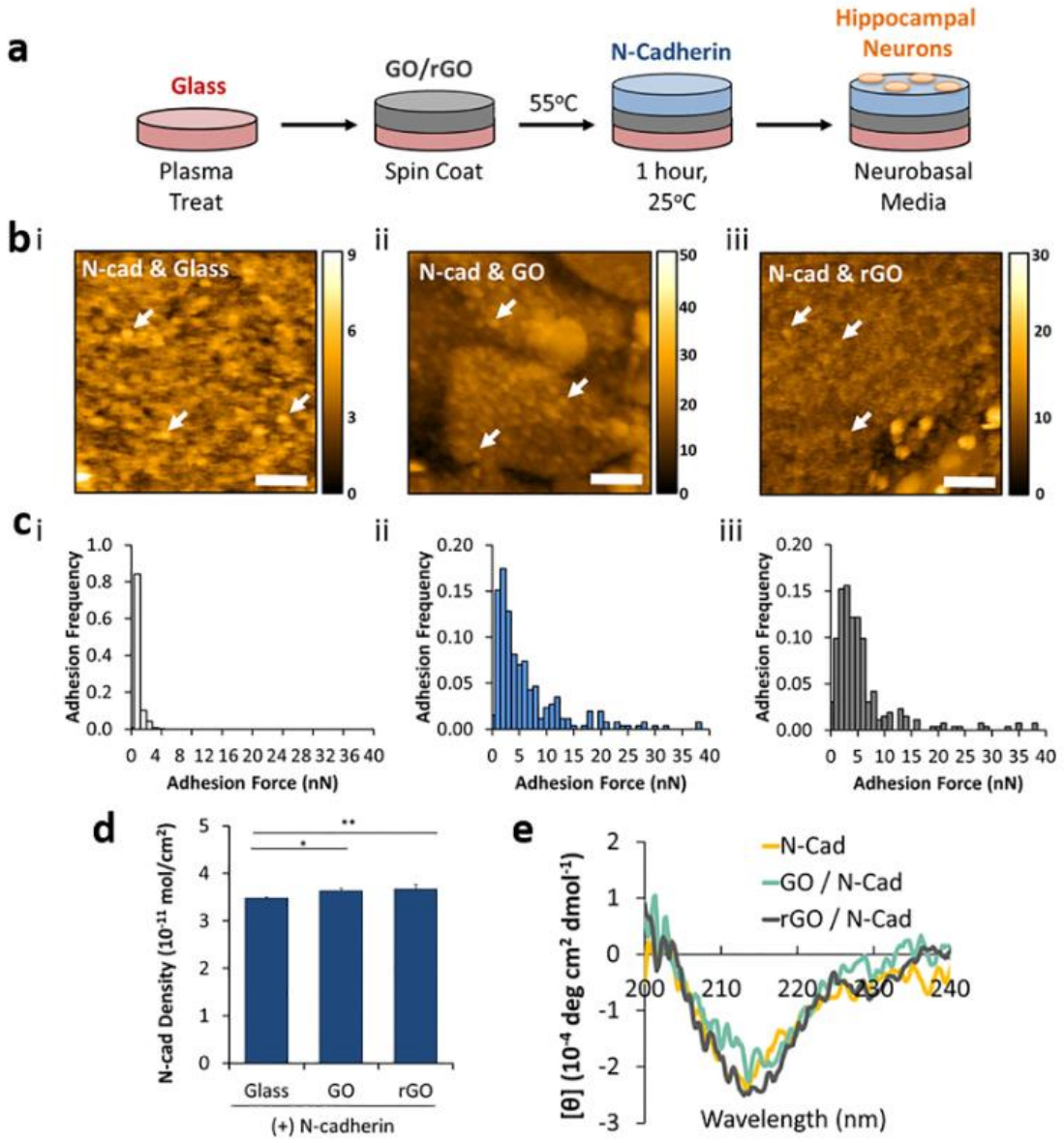

Figure A2.3. Immobilization of N-cadherin onto GO/rGO-coated glass surfaces. **(a)** Scheme that depicts the procedure to immobilize N-cadherin on the GO/rGO-coated substrates. **(b)** AFM images N-cadherin adhered onto (i) uncoated glass, (ii) GO-coated glass, and (iii) rGO-coated glass. AFM experiments were performed in liquid, and the arrows represent areas where N-cadherin molecules are bound. The scale bar represents 100 nm. **(c)** Adhesion force histograms obtained by force-distance curves for N-cadherin adhered on (i) the uncoated glass, (ii) GO-coated glass, and (iii) rGO-coated glass. **(d)** Average density of adsorbed N-cadherin on the various substrates (n = 3). *represents ap-value < 0.05 and **represents a p value < 0.01 by a one-way ANOVA. **(e)** Circular dichroism spectra of either soluble N-cadherin or N-cadherin physiosorbed to GO or rGO flakes.

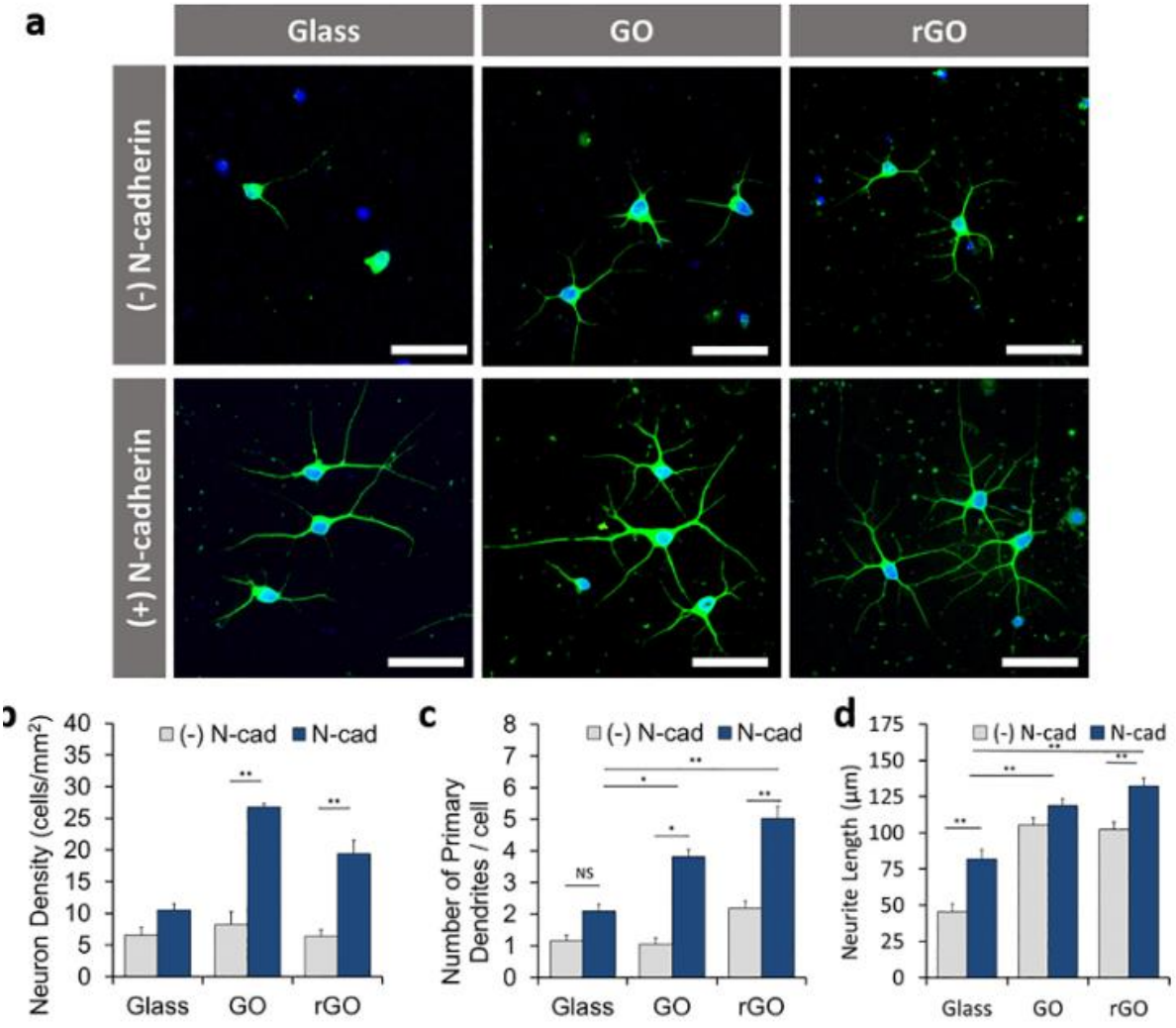

Figure A2.4. Hippocampal neurons cultured on substrates modified with physiosorbed N-cadherin on GO- or rGO-coated glass. Cells were seeded at a density of 150,000 cells/cm2and imaged at 4 days in vitro. **(a)** Representative confocal images of hippocampal neurons on uncoated, GO-, and rGO-coated substrates immobilized with and without N-cadherin. Scale bar represents 50 µm. Green represents MAP2 and blue represents DAPI. Quantification of **(b)** density of neurons stained for MAP2 (n = 4 per group), **(c)** number of primary dendrites per cell, (n > 30 cells per group) and **(d)** average neurite length (n > 50 neurites per group). In all figures, *represents a p value < 0.05 and **represents a p-value < 0.01 as determined by a one-way ANOVA with Tukey's post-hoc. The bars represent the mean values ± the standard error of mean. (For interpretation of the references to color in this figure legend, the reader is referred to the web version of this article.)

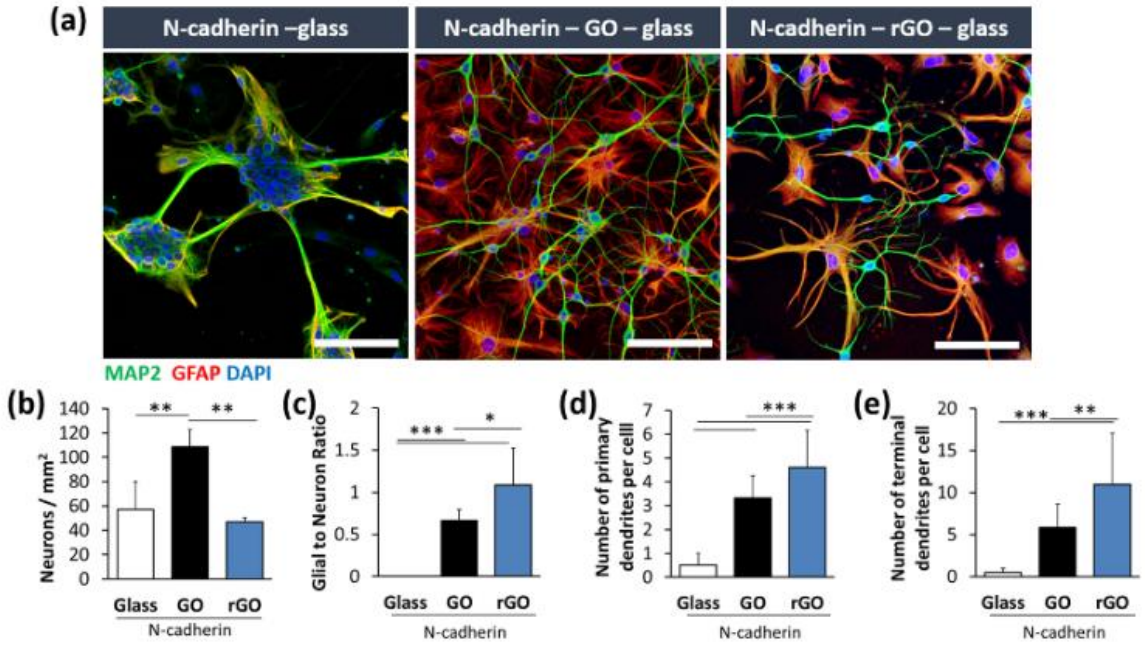

Figure A2.5. High density neuronal cultures on substrates coated with GO/rGO and immobilized with N-cadherin. Cells were seeded at a density of 375,000 cells/cm2and imaged at 10 days in vitro. **(a)** Representative confocal images of hippocampal neurons on uncoated, GO-, and rGO-coated substrates immobilized with and without N-cadherin. Scalebars represent 100 µm. The green color represents, the red color represents GFAP, and the blue color represents DAPI. Quantification of the **(b)** neuronal density (n = 4 per group), **(c)** neuron to glial ratio (n = 4 per group), **(d)** number of primary dendrites per cell (n > 30 cells per group), and **(e)** the total number of terminal dendrites per cell (n > 30 cells per group). In all figures, *represents a p-value < 0.05, **represents a p-value < 0.01, and ***represents a p-value < 0.001 as determined by a one-way ANOVA with Tukey's post-hoc. The bars represent the mean values ± the standard error of mean. (For interpretation of the references to color in this figure legend, the reader is referred to the web version of this article.)

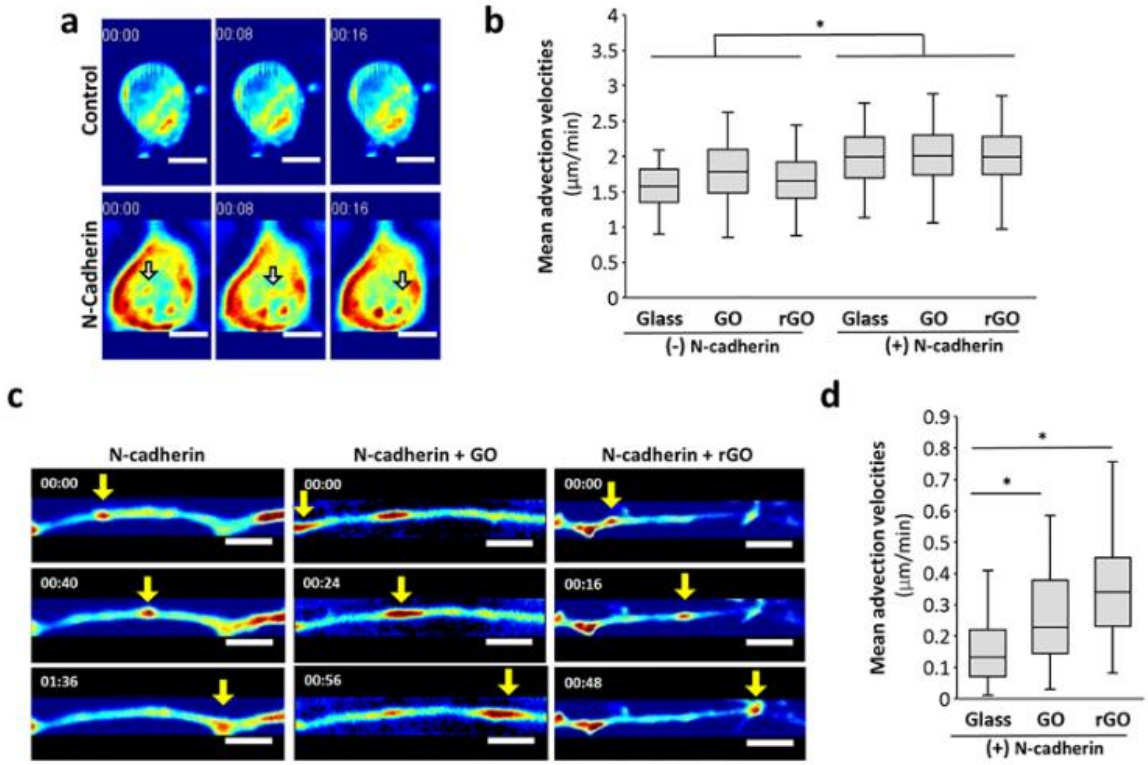

Figure A2.6. SLIM-based quantitative imaging of mass transport of hippocampal neurons. **(a)** Representative images from SLIM of cell bodies on uncoated substrates immobilized with and without N cadherin. The times are in minutes: seconds. Scale bar represents 5 μm. **(b)** Comparison of mean advection velocities of neuronal cell bodies (n > 30 cells per group). **(c)** Representative images from SLIM of neurites on uncoated and rGO-coated substrates immobilized with N-cadherin. The times are in minutes: seconds. Scalebar represents 5 μm. **(d)** Comparison of mean advection velocities in neurites (n > 45 neurites per group). The box plots show the 25th, 50th, and 75th percentiles, and the whiskers show the minimum and maximum. *represents a p-value < 0.05 as determined by the Wilcoxon rank-sum test.

A2.9 References

1. O.I. Wagner, The interaction of neurofilaments with the microtubule motor cytoplasmic dynein, Mol. Biol. Cell. 15 (2004) 5092–5100.
2. H. Ye, R. Kuruvilla, L.S. Zweifel, D.D. Ginty, Evidence in support of signaling endosome-based retrograde survival of sympathetic neurons, Neuron 39(2003) 57–68.
3. Kamal, A. Almenar-Queralt, J.F. LeBlanc, E.A. Roberts, L.S.B. Goldstein, Kinesin-mediated axonal transport of a membrane compartment containing b-secretase and presenilin-1 requires APP, Nature 414 (2001) 643–648.
4. S. Gunawardena, L.S.B. Goldstein, Disruption of axonal transport and neuronal viability by amyloid precursor protein mutations in drosophila, Neuron 32(2001) 389–401.
5. S. Roy, B. Zhang, V.M.Y. Lee, J.Q. Trojanowski, Axonal transport defects: a common theme in neurodegenerative diseases, Acta Neuropathol. 109 (2005)5–13.
6. S. Millecamps, J.P. Julien, Axonal transport deficits and neurodegenerative diseases, Nat. Rev. Neurosci. 14 (2013) 161–176.
7. T. Zech, S.D.J. Calaminus, L.M. Machesky, Actin on trafficking: could actin guide directed receptor transport?, Cell Adhes Migr. 6 (2012) 476–481.
8. L. Bard, C. Boscher, M. Lambert, R.-M. Mege, D. Choquet, O. Thoumine, Amolecular clutch between the actin flow and n-cadherin adhesions drives growth cone migration, J. Neurosci. 28 (2008) 5879–5890.422E.C. Qin et al./Acta Biomaterialia 90 (2019) 412–423
9. Z.-J. Tan, Y. Peng, H.-L. Song, J.-J. Zheng, X. Yu, N-cadherin-dependent neuron-neuron interaction is required for the maintenance of activity-induced dendrite growth, Proc. Natl. Acad. Sci. U.S.A. 107 (2010) 9873–9878.
10. W.J. Nelson, Regulation of cell-cell adhesion by the cadherin-catenin complex, Biochem. Soc. Trans. 36 (2008) 149–155.
11. R. Riehl, K. Johnson, R. Bradley, G.B. Grunwald, E. Cornel, A. Lilienbaum, C.E.Holt, Cadherin function is required for axon outgrowth in retinal ganglion cells in vivo, Neuron 17 (1996) 837–848.
12. K.J. Tomaselli, K.M. Neugebauer, J.L. Bixby, J. Lilien, L.F. Reichard, N-cadherin and integrins: two receptor systems that mediate neuronal process outgrowth on astrocyte surfaces, Neuron 1 (1988) 33–43.
13. J.L. Bixby, J. Lilien, L.F. Reichardt, Identification of the major proteins tha tpromote neuronal process outgrowth on schwann cells in vitro, J. Cell Biol. 107(1988) 353–361.
14. J.L. Bixby, R. Zhang, Purified N-cadherin is a potent substrate for the rapid induction of neurite outgrowth, J. Cell Biol. 110 (1990) 1253–1260.
15. D.L. Benson, H. Tanaka, N-cadherin redistribution during synaptogenesis in hippocampal neurons, J. Neurosci. 18 (1998) 6892–6904.
16. J. Arikkath, L.F. Reichardt, Cadherins and catenins at synapses: roles in synaptogenesis and synaptic plasticity, Trends Neurosci. 31 (2008) 487–494.
17. J.X. Chia, N. Efimova, T.M. Svitkina, Neurite outgrowth is driven by actin polymerization even in the presence of actin polymerization inhibitors, Mol.Biol. Cell. 27 (2016) 3695–3704.

18. L.D.M. Derycke, M.E. Bracke, N-cadherin in the spotlight of cell-cell adhesion, differentiation, invasion and signaling, Int. J. Dev. Biol. 48 (2004) 463–476.
19. V. Lemmon, S.M. Burden, H.R. Payne, G.J. Elmslie, M.L. Hlavin, Neurite growth on different substrates: permissive versus instructive influences and the role of adhesive strength, J. Neurosci. 12 (1992) 818–826.
20. B.D. Cosgrove, K.L. Mui, T.P. Driscoll, S.R. Caliari, K.D. Mehta, R.K. Assoian, J.A. Burdick, R.L. Mauck, N-cadherin adhesive interactions modulate matrix mechanosensing and fate commitment of mesenchymal stem cells, Nat.Mater. 15 (2016) 1297–1306.
21. L. Bian, M. Guvendiren, R.L. Mauck, J.A. Burdick, Hydrogels that mimic developmentally relevant matrix and N-cadherin interactions enhance MSC chondrogenesis, Proc. Natl. Acad. Sci. U.S.A. 110 (2013) 10117–10122.
22. M.Y. Kwon, S.L. Vega, W.M. Gramlich, M. Kim, R.L. Mauck, J.A. Burdick, Doseand timing of N-cadherin mimetic peptides regulate MSC chondrogenesis within hydrogels, Adv. Healthc. Mater. 7 (2018) 1701199.
23. J.C.M. Vega L., M.K. Lee, J.H. Jeong, C.E. Smith, K.Y. Lee, H.J. Chung, D.E. Leckband, H. Kong, Recapitulating cell-cell adhesion using N-cadherin biologically tethered to substrates, Biomacromolecules 15 (2014) 2172–2179.
24. J.C.M. Vega L., M.K. Lee, E.C. Qin, M. Rich, K.Y. Lee, D.H. Kim, H.J. Chung, D.E. Leckband, H. Kong, Three dimensional conjugation of recombinant N-cadherin to a hydrogel for in vitro anisotropic neural growth, J. Mater. Chem. B 4 (2016)6803–6811.
25. H. Tabdili, M. Langer, Q. Shi, Y.-C. Poh, N. Wang, D. Leckband, Cadherin-dependent mechanotransduction depends on ligand identity but not affinity, J. Cell Sci. 125 (2012) 4362–4371.
26. González-Mayorga, E. López-Dolado, M.C. Gutiérrez, J.E. Collazos-Castro, M.L. Ferrer, F. del Monte, M.C. Serrano, Favorable biological responses of neura lcells and tissue interacting with graphene oxide microfibers, ACS Omega 2(2017) 8253–8263.
27. R. Wang, Z. Wang, L. Millet, M.U. Gillette, A.J. Levine, G. Popescu, Dispersion-relation phase spectroscopy of intracellular transport, Opt. Express. 19 (2011)20571.
28. M. Mir, T. Kim, A. Majumder, M. Xiang, R. Wang, S.C. Liu, M.U. Gillette, S. Stice, G. Popescu, Label-free characterization of emerging human neuronal networks, Sci. Rep. 4 (2014) 4434.
29. G. Popescu, Quantitative Phase Imaging of Cells and Tissues, McGraw-Hill,2011.
30. Z. Wang, L. Millet, V. Chan, H. Ding, M.U. Gillette, R. Bashir, G. Popescu, Label-free intracellular transport measured by spatial light interference microscopy, J. Biomed. Opt. 16 (2011) 026019.
31. Y.J. Lee, P. Cintora, J. Arikkath, O. Akinsola, M. Kandel, G. Popescu, C. Best-Popescu, Quantitative assessment of neural outgrowth using spatial light interference microscopy, J. Biomed. Opt. 22 (2017) 066015.
32. M.E. Kandel, D. Fernandes, A.M. Taylor, H. Shakir, C. Best-Popescu, G. Popescu, Three-dimensional intracellular transport in neuron bodies and neurites investigated by label-free dispersion-relation phase spectroscopy, Cytom.Part A 91 (2017) 519–526.
33. Z. Wang, L. Millet, M. Mir, H. Ding, S. Unarunotai, J. Rogers, M.U. Gillette, G. Popescu, Spatial light interference microscopy (SLIM), Opt. Express. 19 (2011)797.

34. Bendali, L.H. Hess, M. Seifert, V. Forster, A.F. Stephan, J.A. Garrido, S. Picaud, Purified neurons can survive on peptide-free graphene layers, Adv. Healthc. Mater. 2 (2013) 929–933.
35. N. Li, X. Zhang, Q. Song, R. Su, Q. Zhang, T. Kong, L. Liu, G. Jin, M. Tang, G. Cheng, The promotion of neurite sprouting and outgrowth of mouse hippocampal cells in culture by graphene substrates, Biomaterials 32 (2011) 9374–9382.
36. V. Georgakilas, J.N. Tiwari, K.C. Kemp, J.A. Perman, A.B. Bourlinos, K.S. Kim, R. Zboril, Noncovalent functionalization of graphene and graphene oxide for energy materials, biosensing, catalytic, and biomedical applications, Chem.Rev. 116 (2016) 5464–5519.
37. S.Y. Park, J. Park, S.H. Sim, M.G. Sung, K.S. Kim, B.H. Hong, S. Hong, Enhanced differentiation of human neural stem cells into neurons on graphene, Adv.Mater. 23 (2011) 263–267.
38. W.C. Lee, C.H.Y.X. Lim, H. Shi, L.A.L. Tang, Y. Wang, C.T. Lim, K.P. Loh, Origin of enhanced stem cell growth and differentiation on graphene and grapheneoxide, ACS Nano 5 (2011) 7334–7341.
39. M. Lambert, F. Padilla, R.M. Mège, Immobilized dimers of N-cadherin-Fcchimera mimic cadherin-mediated cell contact formation: contribution of both outside-in and inside-out signals, J. Cell Sci. 113 (2000) 2207–2219.
40. A.K. Prakasam, V. Maruthamuthu, D.E. Leckband, Similarities between heterophilic and homophilic cadherin adhesion, Proc. Natl. Acad. Sci. 103(2006) 15434–15439.
41. C. Mattevi, G. Eda, S. Agnoli, S. Miller, K.A. Mkhoyan, O. Celik, D. Mastrogiovanni, G. Granozzi, E. Carfunkel, M. Chhowalla, Evolution of electrical, chemical, and structural properties of transparent and conductingchemically derived graphene thin films, Adv. Funct. Mater. 19 (2009) 2577–2583.
42. D.K. Owens, R.C. Wendt, Estimation of the surface free energy of polymers, J.Appl. Polym. Sci. 13 (1969) 1741–1747.
43. Das, B. Chakraborty, A.K. Sood, Raman spectroscopy of graphene on different substrates and influence of defects, Bull. Mater. Sci. 31 (2008) 579–584.
44. A.W. Koch, D. Bozic, O. Pertz, J. Engel, homophilic adhesion by cadherins, Curr.Opin. Struct. Biol. 9 (1999) 275–281.
45. Q. Shi, Y.-H. Chien, D. Leckband, Biophysical properties of cadherin bonds do not predict cell sorting, J. Biol. Chem. 283 (2008) 28454–28463.
46. S. Kaech, G. Banker, Culturing hippocampal neurons, Nat. Protoc. 1 (2006)2406–2415.
47. R.D. Fields, B. Stevens-Graham, New insights into neuron-glia communication, Science 298 (2002) 556–562.
48. B.A. Barres, The mystery and magic of Glia: a perspective on their roles in health and disease, Neuron 60 (2008) 430–440.
49. H.R. Payne, V. Lemmon, Glial cells of the O-2A lineage bind preferentially to N-cadherin and develop distinct morphologies, Dev. Biol. 159 (1993) 595–607.
50. P. Pittet, K. Lee, A.J. Kulik, J.-J. Meister, B. Hinz, Fibrogenic fibroblasts increase intercellular adhesion strength by reinforcing individual OB-cadherin bonds, J. Cell Sci. 121 (2008) 877–886.
51. N. Hirokawa, Y. Noda, Y. Tanaka, S. Niwa, Kinesin superfamily motor proteins and intracellular transport, Nat. Rev. Mol. Cell Biol. 10 (2009) 682–696.

52. W. Meng, Y. Mushika, T. Ichii, M. Takeichi, Anchorage of microtubule minus ends to adherens junctions regulates epithelial cell-cell contacts, Cell 135(2008) 948–959.
53. Chausovsky, A.D. Bershadsky, G.G. Borisy, Cadherin-mediated regulation of microtubule dynamics, Nat. Cell Biol. 2 (2000) 797–804.
54. A.F. Palazzo, C.H. Eng, D.D. Schlaepfer, E.E. Marcantonio, G.G. Gundersen, Localized stabilization of microtubules by integrin- and FAK-facilitated rho signaling, Science 303 (2004) 836–839.
55. Kamal, L.S. Goldstein, Connecting vesicle transport to the cytoskeleton, Curr.Opin. Cell Biol. 12 (2000) 503–508. E.C. Qin et al./Acta Biomaterialia 90 (2019) 412–423423